# Hybrid-Solid-State Electrolytes: Interface Strategy for Solid-State Lithium Metal Batteries

**Shuo Yan**

Thesis submitted to the University of Ottawa
in partial fulfillment of the requirements for the
Degree of Doctorate in Philosophy in Chemical Engineering

Department of Biological and Chemical Engineering
Faculty of Engineering
University of Ottawa

# Abstract

Growing adoption of electrified transportation (e.g., electric vehicles and electric aircraft) is promoting research efforts into renewable and clean energy storage technologies. Hence, in recent years there has been great interest in developing next-generation battery technologies such as solid-state lithium metal batteries (SS-LMBs) that when compared to existing liquid-based lithium-ion batteries (LIBs), provide a compelling potential to boost energy density (cell energy per mass or volume) and safety characteristics. Despite the promise, the practical application of SS-LMBs is dominantly impeded by the solid-solid interface challenges between solid-state electrolytes (SSEs) and battery electrodes. Hybrid solid-state electrolytes that combine bulk SSEs with a tiny amount of liquids (e.g., gel or liquid electrolyte) are proposed as an interim approach to improve the SSEs|battery electrode interfacial contacts. In a hybrid SS-LMBs, there are different interfaces (i.e., the two-dimensional boundary between bulk SSEs and bulk electrodes) and interphases (i.e., the three-dimensional layer that is a result of irreversible reactions between electrolyte and electrodes) that need to be investigated to unravel their roles in electrochemical performance of the cells. Herein, multiscale post-mortem techniques are used to study the interfaces and interphases between ceramic-based oxide SSEs (e.g., perovskites and garnets) and the two electrodes (e.g., Li-metal anodes and Ni-rich cathodes). The experiments reveal structural changes associated with evolutions in the chemical composition of solid-electrolyte interphase (SEI), cathode-electrolyte interphase (CEI), and solid-liquid electrolyte interphase (SLEI) during cycling in different cell configurations, and the results offer guidelines for designing physiochemically stable interphases and thus prolonging cycle life.

Chapter 1 introduces the background and motivation of this thesis, the thesis objective, and the thesis structure while Chapter 2 reviews the fundamentals of both liquid-state LIBs and SS-LMBs as well as explains various interface and interphase phenomena and challenges in different types of batteries. In Chapter 3, experimental methods and representative characterizations used in Chapters 4-7 are presented.

In Chapter 4, the anode interface in hybrid SS-LMBs between Li metal ($Li^0$) and perovskite-type SSEs ($Li_{0.29}La_{0.57}TiO_3$, LLTO) is studied. The electrochemical stability of LLTO SSEs coated with three poly

(ethylene oxide) (PEO)-based interfacial layers is also investigated. It is found that the gel PEO-lithium bis(trifluoromethanesulfonyl)imide (LiTFSI)-succinonitrile (SN) effectively prevents LLTO reduction against $Li^0$ while performing poorly in symmetric Li cells with a large Li nucleation overpotential.

Next, in Chapters 5 and 6, the cathode interface in hybrid SS-LMBs between Ni-rich $LiNi_{0.6}Mn_{0.2}Co_{0.2}O_2$ (NMC 622) cathode and garnet-type ($Li_{6.5}La_{2.9}Ba_{0.1}Zr_{1.4}Ta_{0.6}O_{12}$, LLBZTO) SSEs is explored. The results reveal the formation and chemical composition of two interphases (e.g., SLEI and CEI) after adding a tiny quantity (21 $\mu$L $cm^{-2}$, i.e., the absolute amount of liquid addition divided by the cathode surface area) of liquid electrolyte at the cathode interface. Additionally, the capacity fade mechanism in the SS-LMBs is reported, wherein the microstructural and chemical phase changes, oxygen vacancy formation associated with transition metal dissolution, as well as contributions from SLEI and CEI play key roles in the deterioration of battery performance.

Finally, Chapter 7 reports how the chemical composition of the liquid electrolyte affects the physicochemical properties of the SEIs in LIBs. High concentrations of LiTFSI and lithium nitrite ($LiNO_3$) are employed to create a concentrated precipitation electrolyte (CPE) and form an inorganic-rich (e.g., LiF, $Li_3N$, and $Li_2O$) SEI on the surface of $Li^0$ anodes. The precipitations in the CPE act as a reservoir for salting-out salts, leading to stabilization of the LiTFSI and $LiNO_3$ reduction on the $Li^0$ surface for stable cycling performance.

## Statement of contributions and co-authorship

I hereby declare that I am the lead author of all chapters and did not apply artificial intelligence to generate any content in this dissertation.

Chapter 1 was written solely by Shuo Yan while considering editorial comments and corrections by Prof. Arnaud Weck, Prof. Elena A. Baranova, and Dr. Yaser Abu-Lebdeh.

Chapter 2 is derived from a review paper published in *Batteries* and a book chapter published in *Encyclopedia of Solid-Liquid Interfaces (Elsevier)*. This chapter was solely written by Shuo Yan while considering editorial comments and corrections by the co-authors of the publications.

Chapter 3 was written solely by Shuo Yan while considering editorial comments and corrections by Prof. Arnaud Weck, Prof. Elena A. Baranova, and Dr. Yaser Abu-Lebdeh.

Chapter 4 is derived from a research paper published in *Frontiers in Chemistry*. This chapter was solely written by Shuo Yan while considering editorial comments and corrections by the co-authors of the publication. Shuo Yan wrote the first draft of the manuscript. Shuo Yan, Mr. Chae-Ho Yim, Dr. Ali Merati, and Dr. Yaser Abu-Lebdeh contributed to the conception and design of the study. Shuo Yan was responsible for electrolyte fabrication, interfacial modifications, symmetric Li cell assembly, material characterization (e.g., SEM, EDS, and XRD), and all electrochemical tests. Mr. Oltion Kodra contributed to XPS measurement and data fitting analysis.

Chapter 5 is derived from a research paper published in the *Journal of Physical Chemistry C*. This work was the first part of a collaboration with the University of Calgary, McMaster University, and Canadian Light Source Inc. Shuo Yan and Dr. Sara Abouali contributed equally to this work. This chapter was written primarily by Shuo Yan while considering additions and editorial comments by the co-authors of the publication. Shuo Yan was responsible for figures plotting and results discussion on STXM and XAS. Prof. Venkataraman Thangadurai and Dr. Sara Abouali designed the materials. Dr. Sara Abouali performed electrochemical experiments and contributed to figures plotting and results discussion on material characterizations and electrochemical performance. Mr. Travis Casagrande contributed to STXM sample

preparation via FIB lift-out. Dr. Jigang Zhou and Dr. Jian Wang conducted conventional-mode STXM and PCA characterizations and XAS analysis.

Chapter 6 is derived from a research paper published in the *Journal of Physical Chemistry C*. This work was the follow-up part of a collaboration with the University of Calgary, McMaster University, and Canadian Light Source Inc. This chapter was written solely by Shuo Yan while considering editorial comments and corrections by the co-authors of the publication. Shuo Yan, Mr. Chae-Ho Yim, and Dr. Yaser Abu-Lebdeh conceived and designed the work. Mr. Chae-Ho Yim contributed to the discussion of results and manuscript review. Prof. Venkataraman Thangadurai and Dr. Sara Abouali designed the materials and Dr. Sara Abouali performed electrochemical experiments. Dr. Jigang Zhou and Dr. Jian Wang conducted ptychography-mode STXM, PCA characterizations, and XAS analysis.

Chapter 7 is derived from a research paper submitted to the *Journal of Power Sources*. This chapter was written solely by Shuo Yan while considering editorial comments and corrections by the co-authors of the publication. Shuo Yan was responsible for electrolyte synthesis, coin-cell assembly, and all electrochemical tests. Mr. Chae-Ho Yim and Dr. Mohamed S.E. Houache contributed the results discussion and manuscript review. Mr. Jeff Fraser contributed to SEM imaging. Mr. Oltion Kodra contributed to XPS measurement and data fitting analysis. Ms. Gina Baird contributed to TGA and DSC tests. Dr. Martin Couillard contributed to (S)TEM and EDX imaging. Dr. Jaspreet Walia contributed to Raman spectroscopy characterization.

# Acknowledgements

I am ecstatic to collaboratively work on my thesis with diverse teams from different Canadian universities and national labs. My sincere gratitude goes out to my supervisors, Prof. Arnaud Weck (Weck'lab at MCG-uOttawa), Prof. Elena A. Baranova (Laboratory of Electrochemical Engineering at CHG-uOttawa), Dr. Yaser Abu-Lebdeh (Energy, Mining, and Environment Research Center, EME-NRC), and Dr. Ali Merati (Aerospace research center, AERO-NRC). I feel quite lucky to have had wholehearted mentorship throughout the PhD journey with the opportunity to get involved in a wide range of research projects. Thank you for taking the time to attend the weekly meetings and provide invaluable feedback from the very start. I also truly appreciate all of your support with more than 20 conferences, where I have improved both my confidence and presentation skills. More importantly, I appreciate all of your warm encouragement and insightful advice on my future career during my time at NRC and uOttawa.

I am really grateful that have had Mr. Chae-Ho Yim as my unofficial co-supervisor in the Battery Materials Innovation Team at EME-NRC. Mr. Yim has consistently provided guidance and assistance, especially with experimental design and conduct, as well as data analysis and discussion. He is an amazing researcher and a compassionate senior who guided me to learn from faults and grow from experiences. His advice has been crucial to my success during my PhD.

I would like to express my thanks to many research officers at EME-NRC whom I have worked with or who have helped me greatly during my PhD journey: Dr. Mohamed S.E. Houache, with whom I have collaborated closely since we first met at the LEE lab. He has been a huge helping hand to me, particularly with presentation preparation and speeches and we are quite productive when we work together. Dr. Zouina Karkar is another close collaborator who assisted me in acclimating to the lab and we had numerous fruitful discussions about the work. Mr. Oltion Kodra has been quite helpful with XPS measurement, and I would thank his patient training in XPS fitting analysis. Mr Jeff Fraser, Mr. Dave Kingston, Mr. Matthew Turnbull, and Dr. Martin Couillard are very professional electron microscopists who have been very supportive of SEM/EDX and (S)TEM/EDX imaging.

Aside from the EME-NRC, I would like to thank Dr. Vladimir Pankov for his assistance in the preparation and optimization of thin-film electrolytes via PVD, and Mr. Kayvan Separi who helped me put up instruments at AERO-NRC. Thanks to two outstanding COOP students, Benjamin Antaya, and Mackenzie Bauer, for your edits of the manuscripts.

I am of course also very appreciative of all of the group members at Prof. Weck's lab and Prof. Baranova's lab for their help throughout the past four years since my master's: Dr. Hilal Al-Salih, Dr. James Sturman, Asma Shubair, Najmeh Ahledel, Ju Wang, Dr. Ashwini Reddy Nallayagari, Dr. Jaspreet Walia, Xitong Xie, Katerina Luiza Monea, Graham Killaire, Arash Fellah Jahronmi, Frédéric Murphy, Sayed Ahmed Ebrahim, Hafsah Khan, Andrew Park, Shadia Khan. I appreciate you including me in all of the group events where I made so many wonderful friends. Working with Dr. Deliang Guo at Prof. Weck'lab is a pleasure, and he is very helpful in laser processing. Dr. Christopher Panaritis guided me in performing electrochemical experiments during the master project, and I really appreciate his assistance with data plotting and all the other meaningful suggestions.

It gives me great pleasure to work with Prof. Venkataraman Thangadurai and Dr. Sara Abouali from the University of Calgary, as well as Dr. Jigang Zhou and Dr. Jian Wang from Canadian Light Source Inc. Thanks for all of your suggestions and comments for improving the manuscripts. Special gratitude to Dr. Jigang Zhou who guided me many times on how to properly analyze STXM/XAS data.

Also, I would like to thank the members of the thesis evaluation committee including Prof. Benoît Lessard, Prof. Ghassan Jabbour, and Prof. David Bruce from the University of Ottawa as well as Prof. Lingzi Sang from the University of Alberta.

Finally, I would express my deep love to my parents and grandmother.

Thank you to everyone for the unlimited support at all times. We shared so many wonderful memories which I will always cherish while I pursue my career as a battery researcher!

# Table of Contents

# List of Figures

# List of Tables

# List of Abbreviations

| | |
|---|---|
| LIBs | Lithium-ion batteries |
| $Li^0$ | Lithium metal |
| NMC 811 | $LiNi_{0.8}Mn_{0.1}Co_{0.1}O_2$ |
| SSBs | Solid-state batteries |
| SSEs | Solid-state electrolytes |
| \| | Separates two phases between electrolyte and electrodes |
| LEs | Liquid electrolytes |
| LLTO | $La_{0.57}Li_{0.29}TiO_3$ |
| LLZO | $Li_7La_3Zr_2O_{12}$ |
| SEI | Solid-electrolyte interphase |
| NMC 622 | $LiNi_{0.6}Mn_{0.2}Co_{0.2}O_2$ |
| STXM | Scanning transmission X-ray microscopy |
| XAS | X-ray absorption spectroscopy |
| SLEI | Solid-liquid electrolyte interphase |
| CEI | Cathode-electrolyte interphase |
| CPE | Concentrated precipitation electrolyte |
| Li | Lithium |
| $LiMO_2$ | Lithium metal oxide |
| C | Carbon |
| $LiPF_6$ | Lithium hexafluorophosphate |
| LMBs | Lithium metal batteries |
| LUMO | Lowest unoccupied molecular orbital |
| HOMO | Highest energy molecular orbital |
| LEDC | Lithium ethylene dicarbonate |
| LiF | Lithium fluoride |
| CE | Coulombic efficiency |
| CPLi | Carboxylate-protected Li |
| LiTFSI | Lithium bis(trifluoromethane)sulfonimide |
| DOL | 1,3-dioxolane |
| DME | 1,2-dimethoxyethane |
| XPS | X-ray photoelectron spectroscopy |

| | |
|---|---|
| RPC | Reactive polymer composite |
| GO | Graphene oxide |
| $LiNO_3$ | Lithium nitrite |
| DMSO | Dimethyl sulfoxide |
| FEC | Fluoroethylene carbonate |
| LAGP | $Li_{1.3}Al_{0.3}Ti_{1.7}(PO_4)_3$ |
| PEO | Poly(ethylene oxide) |
| LPSCI | Lithium phosphorus sulfur chloride |
| NMC 532 | $LiNi_{0.5}Mn_{0.3}Co_{0.2}O_2$ |
| LNMO | $LiNi_{0.5}Mn_{1.5}O_4$ |
| NMC | $LiNi_xMn_yCo_z$ (x+y+z=1) |
| ATR-FTIR | Attenuated total reflection-fourier transform infrared |
| cryo-TEM | Cryogenic transmission electron microscopy |
| cryo-EM | Cryogenic electron microscopy |
| TOF-SIMS | Time-of-flight secondary-ion mass spectrometry |
| ROI | Region-of-interest |
| SS-LMBs | Solid-state lithium metal batteries |
| NASICON | $Na_{1+x}Zr_2Si_xP_{3-x}O_{12}$ ($0 \leq x \leq 3$) |
| TEM | Transmission electron microscopy |
| LiBOB | Lithium bis(oxalato)borate |
| ITO | Indium tin oxide |
| PET | Poly(ethylene terephthalate) |
| EIL | Exchange interlayer |
| CHG | Greenhouse gas |
| Ni-Cd | Nickel-cadmium |
| Pb-Acid | Lead-acid |
| $Ni-H_2$ | Nickel-hydrogen |
| Ag-Zn | Silver-zinc |
| SPEs | Solid polymer electrolytes |
| LISCON | $Li_{16-2x}A_x(BO_4)_4$, where $A^{2+}$ = Zn or Mg, $B^{4+}$ = Ge or Si, and $0<x<4$. |
| PAN | Poly(acrylonitrile) |
| PVDF | Poly(vinylidene fluoride) |
| G4 | Tetra(ethylene glycol dimethyl ether) |

| | |
|---|---|
| SS-LBs | Solid-state lithium batteries |
| SN | Succinonitrile |
| PC | Propylene carbonate |
| BC | Bacterial cellulose |
| RT | Room temperature |
| 1D | One dimensional |
| CSL | Coincidence-site lattices |
| EBSD-SEM | Electron backscatter diffraction-scanning electron microscopy |
| ESM | Electrochemical strain microscopy |
| SPS | Spark plasma sintering |
| LSTZ | $Li_{3/8}Sr_{7/16}Ta_{3/4}Zr_{1/4}O_3$ |
| PTFE | Poly(tetrafluoroethylene) |
| MSD | Mean square displacement |
| RF | Radio frequency |
| PLD | Pulsed laser deposition |
| STO | $SrTiO_3$ |
| PEG | Poly(ethylene glycol) |
| PVB | Poly(vinyl butyral) |
| BBP | Benzyl butyl phthalate |
| NMP | 1-methyl-2-pyrrolidinone |
| LTO | Lithium titanium oxide |
| LFP | $LiFePO_4$ |
| XRD | X-ray diffraction |
| PL | Poly(ethylene oxide)-lithium bis(trifluoromethanesulfonyl)imide |
| PLS | Poly(ethylene oxide)-lithium bis(trifluoromethanesulfonyl)imide-succinonitrile |
| LALZWO | $Li_{5.9}Al_{0.2}La_3Zr_{1.75}W_{0.25}O_{12}$ |
| CPAMEA | Cross-linked poly(ethylene glycol) methyl ether acrylate |
| PVDF-HFP | Poly(vinylidene fluoride-co-hexafluoropropylene) |
| Au | Gold |
| SEM | Scanning electron microscopy |
| EDS | Energy dispersive X-ray spectrometry |
| PXRD | Powder X-ray diffractometry |
| EIS | Electrochemical impedance spectroscopy |

| | |
|---|---|
| G-LLTO | Granular $La_{0.57}Li_{0.29}TiO_3$ |
| M-LLTO | Milled $La_{0.57}Li_{0.29}TiO_3$ |
| OCV | Open circuit voltage |
| P-LLTO | Poly(ethylene oxide) coated $La_{0.57}Li_{0.29}TiO_3$ |
| PL-LLTO | Poly(ethylene oxide)-lithium bis(trifluoromethanesulfonyl)imide coated $La_{0.57}Li_{0.29}TiO_3$ |
| PLS-LLTO | Poly(ethylene oxide)-lithium bis(trifluoromethanesulfonyl)imide-succinonitrile coated $La_{0.57}Li_{0.29}TiO_3$ |
| LLBZTO | $Li_{6.5}La_{2.9}Ba_{0.1}Zr_{1.4}Ta_{0.6}O_{12}$ |
| 2032 coin cell | Diameter = 20 mm, thickness = 3.2 mm |
| CLS | Canadian Light Source |
| FIB | Focused-ion beam |
| PCA | Principal component analysis |
| R | Resistance |
| EC | Ethylene carbonate |
| TM | Transition metal |
| S_01 | Slice 1 at the discharged state after 1 cycle |
| S_02 | Slice 1 at the discharged state after 28 cycles |
| ZP | Zone plate |
| OSA | Order sorting aperture |
| PMT | Photomultiplier tube |
| CMOS | Complementary metal oxide semiconductor |
| CCD | Charged couple devices |
| NMC_28 | $LiNi_{0.6}Mn_{0.2}Co_{0.2}O_2$ cathode at the discharged state after 1 cycle |
| NMC_01 | $LiNi_{0.6}Mn_{0.2}Co_{0.2}O_2$ cathode at the discharged state after 28 cycles |
| OD | Optical density |
| $LiNO_3$ | Lithium nitrite |
| HCEs | Highly-concentrated electrolytes |
| LHCEs | Localized highly-concentrated electrolytes |
| 1+1 | 1 mol $g^{-1}$ lithium bis(trifluoromethanesulfonyl)imide +1 wt.% lithium nitrile |
| 1+2 | 1 mol $g^{-1}$ LiTFSI+2 wt.% $LiNO_3$ |
| 2+2 | 2 mol $g^{-1}$ LiTFSI+2 wt.% $LiNO_3$ |
| 2+4 | 2 mol $g^{-1}$ LiTFSI+4 wt.% $LiNO_3$ |

| | |
|---|---|
| 4+2 | 4 mol $g^{-1}$ LiTFSI+2 wt.% $LiNO_3$ |
| HCl | Hydrochloric acid |
| CV | Cyclic voltammetry |
| DSC | Differential scanning calorimeter |
| HRTEM | High-resolution transmission electron microscope |
| ADF | Annular dark-filed |
| STEM | Scanning transmission electron microscopy |
| HAADF | High-angle annular dark-field |

# Chapter 1

# Introduction

## 1.1 Background and motivation

"Modern society is completely dependent on fossil fuels, so there is a huge incentive to find a replacement for the internal combustion engine", stated Dr. John Goodenough who is widely regarded as the father of today's lithium-ion batteries (LIBs).[1] Solar and wind power are two popular renewable energy sources; however, their intensity fluctuates with time and location. Renewable energy sources must therefore be stored and made available on demand.

Batteries potentially offer a long-term solution as a crucial enabler that facilitates renewable energy storage and generation. Electrifying transportation is currently leading global decarbonization; technical advancements and initiatives in portable devices and electric mobilities (e.g., electric vehicles and electric aircraft) heavily rely on rechargeable LIBs. Since Sony first marketed rechargeable LIBs (e.g., using graphitic carbon as anodes and layered oxides as cathodes) in 1991, many attempts have been made to optimize the overall LIBs chemistry (e.g., electrolyte, electrodes, current collectors, and separators).[2]

Dominating commercial cells only manage to sustain around 250 Wh $kg^{-1}$ (or 700 Wh $l^{-1}$), as illustrated in Figure 1.1(a) when compared to data from 2021 to 2023.[3] A primary goal propelling the development of next-generation LIBs is to maximize the attainable specific energy (cell energy per cell mass) and energy density (cell energy per cell volume). Battery 500 consortium funded by the US Department of Energy aims to produce cells with an energy density of 500 Wh $kg^{-1}$ (or almost 1 kWh $l^{-1}$).[3] By applying lithium metal ($Li^0$) anode and $LiNi_{0.8}Mn_{0.1}Co_{0.1}O_2$ (NMC 811) as the cathode, the specific energy is being approached to fabricate cells with 450 Wh $kg^{-1}$. The cell cost has simultaneously dropped from around USD$ 5,000 to USD$ 100 per kWh, as indicated in Figure 1.1(b).[3,4]

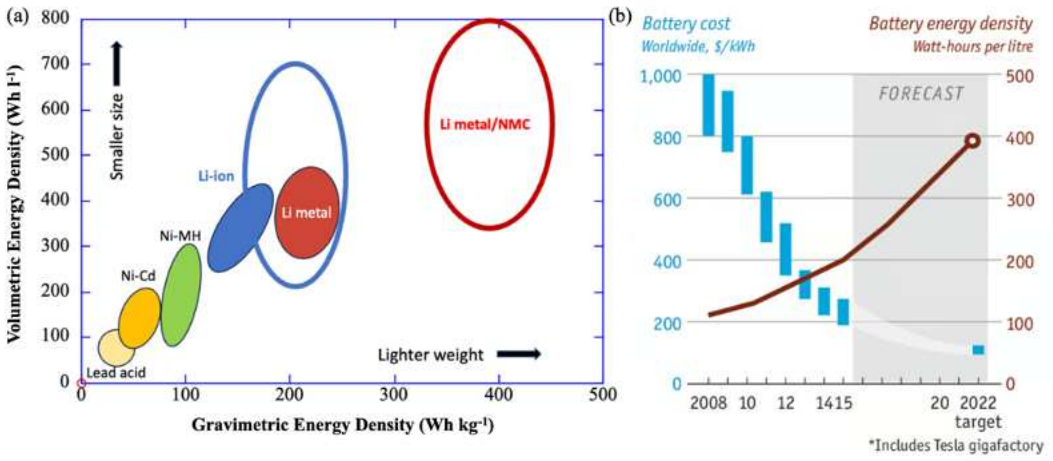


**Figure 1.1.** (a) Comparison of the energy densities of batteries reported in 2021 (closed circles) versus commercial cylindrical cells today (open circles). Image adapted from ref. [3].; (b) Cost reduction of lithium batteries and increase in energy density (Wh $l^{-1}$). Image adapted from ref. [4].

Solid-state batteries (SSBs) have been in the race to transform the science of safe and high energy-density storage systems. The SSB technology is compelling, with remarkable breakthroughs from commercial companies including Samsung, SolidPower, QuantumScape, and Toyota. Using solid-state electrolytes (SSEs) rather than flammable liquid electrolytes (LEs) results in improved safety and allows the incorporation of $Li^0$ anodes coupled with high-capacity cathodes (e.g., Ni-rich cathodes) inside the batteries.[5]

Nevertheless, there are numerous challenges that need to be overcome to reach the full potential of SSBs.[6] Among these are the lack of stable Li-ion conducting SSEs and the solid-solid interface between SSEs and electrodes. Furthermore, the large volume change of electrodes during cycling causes void formation at the interfaces that would block Li-ion migration.

## 1.2 Objectives

The overall objective of this dissertation is to investigate the interface and/or interphase phenomena with ceramic-based SSEs for the development of efficient and high-energy density solid-state batteries.

Among those reported SSE materials, perovskite-type ($La_{0.57}Li_{0.29}TiO_3$, LLTO) and garnet-type ($Li_7La_3Zr_2O_{12}$, LLZO) materials are some of the most researched because of their excellent thermal stability (>1000 °C) window, high shear modulus (e.g., ~60 GPa of LLZO), relatively high Li-ion conductivity at 25 ˚C (>$10^{-4}$ S $cm^{-1}$ versus <$10^{-5}$ S $cm^{-1}$ of most polymers), and wide electrochemical window (>5 V).[7,7] Furthermore, LLZO is relatively chemically stable when in contact with the $Li^0$ anode compared to LLTO.[7] As a result, both LLTO and LLZO SSEs were chosen as the candidates in this thesis.

To reach the above objective, four goals have been briefly explained and identified as follows:

1. The first goal is to design and fabricate highly conductive and dense ceramic-based oxide SSEs for SSBs. The current LLTO and LLZO SSEs, which are typically prepared by cold pressing followed by sintering (pellets are thicker than 200 $\mu$m), have a low intrinsic $Li^+$ conductivity (e.g., <$10^{-5}$ S $cm^{-1}$ at room temperature) with low relative density (e.g., <95%). Particularly, both sintering temperature and sintering time influence the density of SSEs.
2. Li can be intercalated into LLTO at voltages lower than 1.8 V, leading to the reduction of $Ti^{4+}$ cation and hence increased electronic conductivity. It is thus necessary to introduce coating layers upon LLTO and physically separate it from direct contact with Li. Herein, the second goal is to prevent the $Ti^{4+}$ cation reduction and study the electrochemical performance of LLTO SSEs while coated with different interfacial layers (e.g., metals, metal oxides, and polymers) against Li in symmetric Li cells.
3. The poor solid-solid contacts between SSEs and battery electrodes increase the impedance for Li-ion migration at the interfaces. The hybrid solid-state electrolyte approach has been suggested as an interim solution for the transition and implementation of SSBs as they contain a tiny amount of LE at the cathode interface to minimize the interfacial impedance. However, this approach is still in its infancy and the field urgently needs a deep understanding of the role of LE and related failure mechanisms on the battery performance.

Therefore, the third goal is to investigate the function of LE, identify different interphases, and reveal the failure mechanism of hybrid SSBs via synchrotron-based X-ray techniques.

4. The composition of LEs is essential to form a stable solid-electrolyte interphase (SEI) layer on the $Li^0$ surface. Hence, the last goal is to optimize the physicochemical properties of the SEI using a dual-anion concentrated Li-ion's LE when used as an additive at interfaces towards SSBs.

## 1.3 Thesis structure

This dissertation is arranged in the following manner.

In Chapter 2, an overview of the literature on the fundamentals of LIBs and SSBs is presented. Different solid-liquid interfaces in LIBs and solid-solid interfaces in SSBs are reviewed, respectively. This chapter is derived from a book chapter published in *Encyclopedia of Solid-Liquid Interfaces (Elsevier)* and a review paper published in *Batteries*.

In Chapter 3, experimental approaches are provided. It includes information on characterizations and techniques not covered in the experimental sections of the research papers.

Chapter 4 is derived from a research paper published in *Frontiers in Chemistry*. The effects of sintering temperature on the microstructure and Li-ion conductivity of LLTO are discussed. The chemical instability of LLTO again $Li^0$ anodes and related resolution strategies are reported. Supplementary information related to this paper is found in Appendix 1.

Chapters 5 and 6 are derived from two consecutive research papers published in the *Journal of Physical Chemistry C*. The role of liquid additives at the cathode interface between LLZO and $LiNi_{0.6}Mn_{0.2}Co_{0.2}O_2$ (NMC 622) cathode is revealed via scanning transmission X-ray microscopy (STXM) associated with X-ray absorption spectroscopy (XAS). The synergetic effects of solid-liquid electrolyte interphase (SLEI) and cathode-electrolyte interphase (CEI) on the capacity fade of SSBs are discussed. Supplementary information related to both papers is found in Appendix 2 and Appendix 3.

Chapter 7 is derived from a research paper submitted to the *Journal of Power Sources*. It reports a dual-anion concentrated precipitation electrolyte (CPE) for activating Li-ion transport capability and forming a robust SEI in advanced LIBs. Supporting information related to this paper is found in Appendix 4.

Chapter 8 contains conclusions and future work.

Appendix 5 includes a list of publications, conferences, and awards related to this dissertation.

## 1.4 References


1. Evarts, E.C. Lithium batteries: To the limits of lithium. *Nature*. **2015**, *526*, S93-S95.
2. Reddy, M.V.; Mauger, A.; Julien, C.M.; Paolella, A.; Zaghib, K. Brief history of early lithium-battery development. *Materials*. **2020**, *13*, 1884.
3. Whittingham, M.S.; Xiao, J. Fifty years of lithium-ion batteries and what is next? *MRS Bulletin*. **2023**, *48*, 1118-1124.
4. Asif, A.A.; Singh, R.; Majumder, A.J.A. The Paradigm Shifting Role of Solar Powered DC Nano-Grids in New Electrification and Replacement for Traditional Grid Distribution. *Clemson University Power Systems Conference (PSC)*. **2020**, 1-6.
5. Randau, S.; Weber, D.A.; Kötz, O.; Koerver, R.; Braun, P.; Weber, A.; Ivers-Tiffée, E.; Adermann, T.; Kulisch, J.; Zeier, W.G.; Richter, F.H. Benchmarking the performance of all-solid-state lithium batteries. *Nature Energy*. **2020**, *5*, 259-270.
6. Janek, J.; Zeier, W.G. Challenges in speeding up solid-state battery development. *Nature Energy*. **2023**, *8*, 230-240.
7. Yan, S.; Yim, C.H.; Pankov, V.; Bauer, M.; Baranova, E.; Weck, A.; Merati, A.; Abu-Lebdeh, Y. Perovskite solid-state electrolytes for lithium metal batteries. *Batteries*. **2021**, *7*, 75.

8. Abouali, S.; Yim, C.H.; Merati, A.; Abu-Lebdeh, Y.; Thangadurai, V. Garnet-based solid-state Li batteries: from materials design to battery architecture. *ACS Energy Letters*. **2021**, *6*, 1920-1941.

# Chapter 2

# Literature review

This chapter has been adapted from a book chapter published in *Encyclopedia of Solid-Liquid Interfaces (Elsevier)* (doi: 10.1016/B978-0323-85669-0.00129-X) and a review paper published in *Batteries* (doi: 10.3390/batteries7040075).

## 2.1 Liquid-state lithium-ion batteries

Using lithium (Li) batteries for renewable energy storage is a practical solution to cut greenhouse gas emissions at the industrial level of grid electrification and automotive transportation.[1] Sony was the first to introduce rechargeable lithium-ion batteries (LIBs) to the market in 1991. LIBs have been widely utilized in many commercial applications, such as electronic devices, electric or hybrid-electric vehicles, electric aircraft, and stationary energy storage systems.[2]

The energy density of LIBs with liquid electrolytes (LEs) commonly ranges from 100 Wh $kg^{-1}$ to 150 Wh $kg^{-1}$. As shown in Figure 2.1, a LIB has a graphite anode (e.g., mesocarbon microbeads, C), a Li metal oxide ($LiMO_2$, e.g., $LiCoO_2$) cathode, and an ion-conducting electrolyte embedded in a separator consisting of a solution of a Li salt (e.g., lithium hexafluorophosphate, $LiPF_6$) in a mixed organic solvent (e.g., ethylene carbonate/diethyl carbonate). A typical LIB configuration is based on the C|$LiPF_6$ in ethylene carbonate/diethyl carbonate|$LiMO_2$ (interpreted as: graphite anode|Li salts dissolved in organic solvents as LE|cathode, "|" separates two phases) and operates on the following chemical reaction:

$$yC+LiMO_2 \leftrightarrow Li_xC_y+Li(1-x)MO_2,\ x \approx 0.6,\ y = 6,\ \text{voltage} \approx 3.7\ V$$

The working principle of LIBs relies upon the Li-ions moving back and forth between the two electrodes within the battery during the charge/discharge process. Corresponding to the equation above, when the battery is charged, the Li-ions are extracted from the $LiMO_2$ cathode and transport through the $LiPF_6$-based electrolyte toward the graphite anode. Li-ions can insert (or intercalate)

into the layered structure of graphite to form $Li_xC_y$ ($x \approx 0.5$ and $y = 6$) and then the Li-ions return to the cathode when it is discharged (or recharged). The movement of the Li-ions creates free electrons that could drive electric devices.

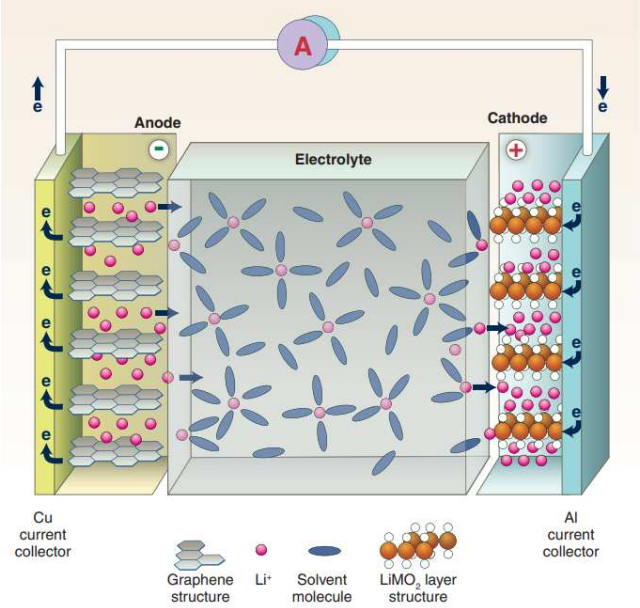


**Figure 2.1.** Schematic of a typical LIB. Image adapted from ref. [3].

However, the role of liquid-state LIBs in high-energy applications could be constrained by the limited electrochemical stability window and low-level energy densities (i.e., from 100 Wh $kg^{-1}$ to 150 Wh $kg^{-1}$). The electrochemical stability window is commonly referred to the potential difference between the cathodic and anodic limits (set by the reference of $Li/Li^+$) where the solvent is reduced and oxidized respectively. The electrolyte will react at the electrode interface outside of this window, causing undesired side reactions and thereby deteriorate battery performance.

Due to its ultrahigh theoretical specific capacity (3860 mAh $g^{-1}$) and lowest electrochemical potential (-3.04 V versus the standard hydrogen electrode), Li metal ($Li^0$) is alternatively applied as the anode to increase the energy density and expand the electrochemical stability window. In particular, when paired with different types of cathodes, the obtained Li metal batteries (LMBs) can dramatically increase energy density compared to the conventional LIBs.

The working principle of LMBs in the charge and discharge process is described as follows: (take the example of Li metal oxide as the cathode: $LiMO_2$)

Anode reaction: $xLi \leftrightarrow xLi^+ + xe^-$

Cathode reaction: $yLi(1-x)MO_2 + xLi^+ + xe^- \leftrightarrow LiMO_2$

The entire charge and discharge process is similar to the one in LIBs. During the charging process, the Li-ions are released from the layer-structured $LiMO_2$, which migrate through the electrolyte and electrically plate on the anode as Li. During the discharging process, the Li-ions are stripped from the anode and returned to the cathode side.

Traditional LMBs with LEs have a long history of safety issues due to electrolyte leakage and flammability. Furthermore, LEs have other significant limitations that have hampered further usage of LIBs at the industrial level. These issues include 1) narrow operating voltage (<5 V); 2) low energy density; 3) short cycling lifespan during the charge and discharge process; 4) Li dendrite formation and short circuit (e.g., fire hazard); and 5) high commercial cost.

## 2.2 Solid-liquid interphases in LIBs

Designing lithium batteries with steady ionic transport kinetics requires a thorough understanding of solid-liquid interphases. In this chapter, two typical interphases are briefly reviewed: solid-electrolyte interphase (SEI) and cathode-electrolyte interphase (CEI), which are mainly encountered in LIBs.

### 2.2.1 Solid-electrolyte interphases (SEI)

*In situ SEI formation and composition*

Utilizing a $Li^0$ anode in liquid systems creates severe issues related to Li dendrites formation and short circuits in the battery. In 1970, Dey et al. were the first to report that carbonated-based organic electrolytes could electrochemically decompose on the electrode to form a passivation layer.[4] Peled

named it a solid electrolyte interphase (SEI) because it acts as a solid electrolyte and functions as an electrical insulator and an ionic conductor.[5]

Goodenough et al. firstly proposed and simplified the SEI formation model.[6] The SEI layer forms when the redox potential of the electrodes lies outside the electrochemical window of the electrolyte, as indicated in Figure 2.2. The electrolyte is stable in the battery when the lowest unoccupied molecular orbital (LUMO) is higher than the Fermi energy of the anode; otherwise, the electrolyte is unstable and can be reduced by commonly-used anodes (e.g., silicon and $Li^0$ anodes). During the initial charging cycles, the SEI layer will accumulate at the anode|electrolyte interface via electrochemical reduction and the decomposition of electrolyte components.

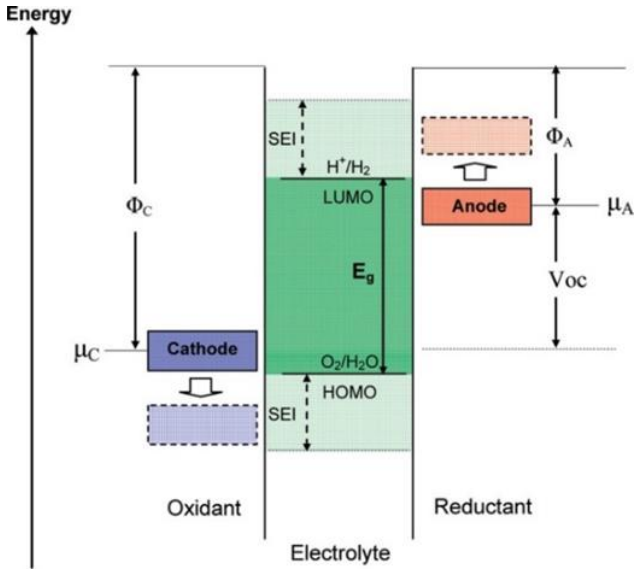


**Figure 2.2.** Schematic energy diagram of an aqueous electrolyte at open-circuit state. $\Phi_A$ and $\Phi_C$ are the anode and cathode work potentials. $E_g$ is the electrochemical stability window of the electrolyte. $V_{oc}$ is the open-circuit voltage. Image adapted from ref. [6]. Copyright @ 2010, American Chemical Society

The SEI composition strongly depends on the usage of different LEs. As illustrated in Figure 2.3(a), the initial SEI components for carbonated-based LEs (e.g., $LiPF_6$ in ethylene carbonate solvent) in LIBs are predominately made of reduction products from the salt and solvent, such as lithium ethylene dicarbonate (LEDC) and lithium fluoride (LiF). As shown in Figure 2.3(b) and (c), LEDC undergoes continuous decomposition reactions, resulting in an evolving SEI made up of partially

soluble organic species (e.g., semi-carbonates and polymers), as well as inorganic compounds (e.g., LiF, $Li_2O$, LiOH, and $Li_2CO_3$). The formation of a thicker SEI with a complex mixture corresponds to a change of SEI composition in the different cycling states, as depicted in Figure 2.3(d).

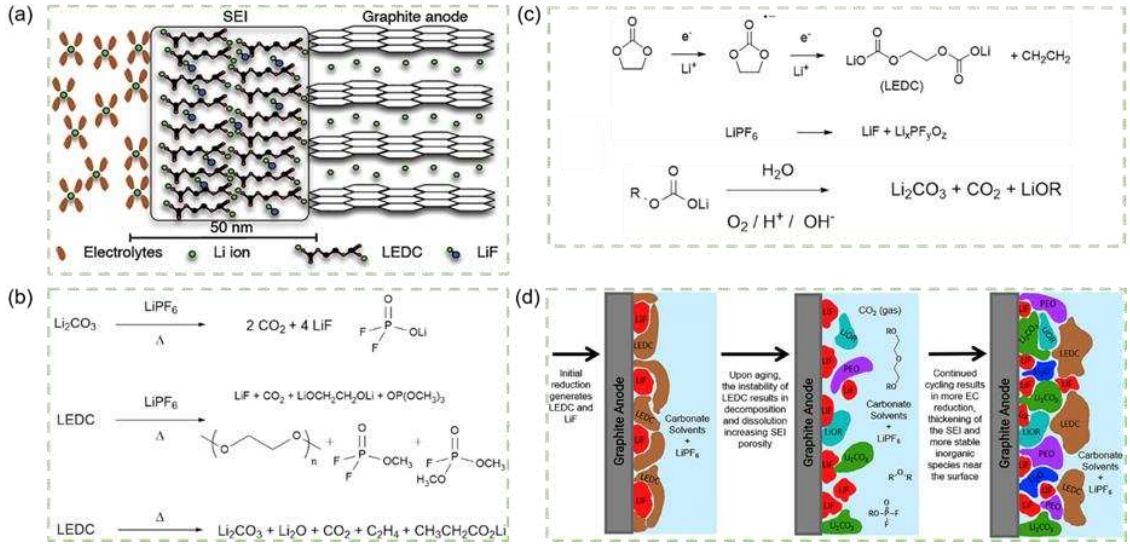


**Figure 2.3.** (a) The initial EC and $LiPF_6$ reduction reactions on the anode; (b-c) further decomposition reactions of LEDC and the evolution of SEI composition; and (d) a thicker SEI formation and evolution during the cycling. Image adapted from ref. [7]. Copyright @ 2019, Elsevier Inc.

*Unstable in situ SEI*

LMBs quickly fail in electrochemical performance because of the direct contact between the $Li^0$ anode and the electrolytes, leading to undesired interfacial reactions and unstable SEI formation. This unstable SEI film that initially forms on the $Li^0$ surface cannot maintain long-term Li plating/stripping process. This is mainly due to several properties of SEI:

1) The heterogeneous composition that led to a non-uniform Li-ions flux and subsequent Li dendrites formation;

2) The brittleness of SEI fails to withstand the volume expansion of $Li^0$;

3) Micro- or nano-structural changes during different thermal and electrochemical conditions.

Different dendrite morphologies (in Figure 2.4(a)) commonly appear when Li-ions move from electrolytes and deposit onto $Li^0$ under the external stimulus. Whisker-like Li dendrites are mostly observed in liquid-state LIBs but are less common in SSBs.[8] Besides, Li dendrite easily forms from mosaic SEI and grows upon the rough $Li^0$ surface, as shown in Figure 2.4(b).[9]

During further cycling, the Li stripping/plating process generally includes four steps (in Figure 2.4(c)): 1) the Li plating causes a volume expansion of $Li^0$, leading to the initial SEI crack; 2) Li dendrites grow to shoot out through the cracks; 3) Li stripping produces isolated Li (which is part of 'dead Li'), and SEI undergoes continuous fracture; 4) accumulated 'dead Li' forms a thick SEI and porous $Li^0$ anode.[10,11] Such an unstable SEI associated with Li dendrite causes excessive $Li^0$ and electrolyte consumption, which harm energy density and Coulombic efficiency (CE, the ratio of discharge capacity and charge capacity) of LMBs. Besides, the fractured and broken dendrites may lead to severe generation of 'dead Li' during cycling.

Generally, the failure mechanisms of a SEI could be categorized into three types: thermal, chemical, and mechanical failures. Thermal failure originates from the elevated internal temperature of the battery during the operation. In other words, SEI is chemically unstable and consistently evolves over cycling. The SEI components constantly change due to the extensive meta-stable SEI species. Increased concentration of decomposed salts might induce side reactions among the initial SEI components. The intense chemical reactions would damage the vulnerable SEI and cause battery failure. The tensile and compressive strains produced during cycling lead to the mechanical failure of SEI, which in turn cause fracture and breakage issues.

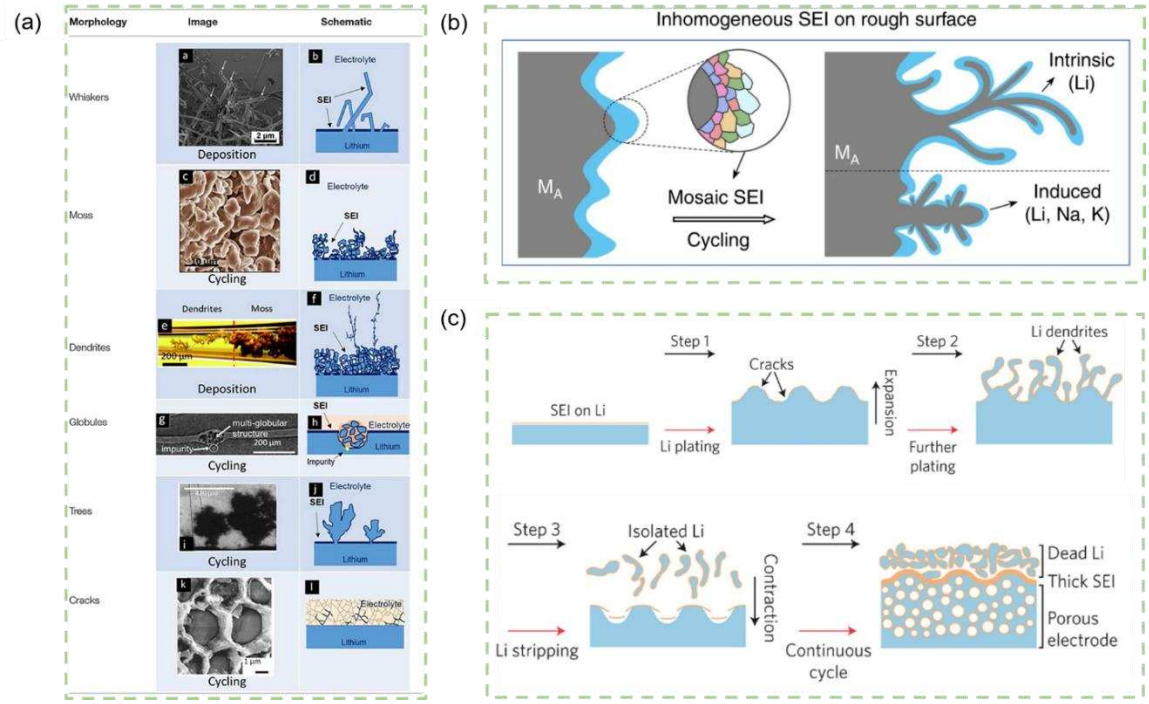


**Figure 2.4.** Schematic diagrams of: (a) various morphologies of electrodeposited lithium. Image adapted from ref. [8]. Copyright @ 2019, The Authors; (b) dendrite growth on rough anode surface. Image adapted from ref. [9]. Copyright @ 2018, Springer Nature Limited; (c) the Li stripping/plating process. Image adapted from ref. [11]. Copyright @ 2018, Elsevier Inc.

*Artificial in situ SEI*

$Li^0$ anode is a conversion-pattern host-less material that encounters infinite volume change during the plating/stripping process. This property inevitably leads to anode|electrolyte interface instability, causing a fractured or even collapsed SEI. The SEI serves multiple roles in determining the cycling performance of $Li^0$ anodes, which generally includes limiting side reactions at the interface and promoting uniform metal deposition by regulating the Li-ion flux.

An ideal SEI needs to have chemical stability, extraordinary Li-ion conductivity, and high modulus, simultaneously, and be a suitable buffer layer to block its direct contact with the electrolyte. Furthermore, the characteristics of SEI growth is a key indicator whether or not dendrites form. Many works have been directed toward the design of an artificial SEI for $Li^0$ anode. Two general requirements are necessary to establish a stable SEI: 1) SEI should have a structure with phase

uniformity; 2) SEI should be mechanically robust, displaying sufficient toughness to withstand the Li plating/stripping associated expansion/contraction.

Moreover, the chemical composition of the SEI can be manipulated by tailoring the electrolyte composition. Hence, based on the components of SEI, three major types of artificial SEIs are designed as 1) organic-rich; 2) inorganic-rich; and 3) hybrid (e.g., organic-inorganic).

Organic materials have great flexibility and excellent compatibility with electrodes, which allows for regulating Li-ion diffusion at the interface. Li carboxylate with low Young's modulus and high flexibility is promising to be applied as an artificial organic-rich SEI layer to suppress dendrite growth. However, the naturally formed SEI always has short $(CH_2)_2COOLi$; while long-chain carbonate tends to be less flexible. To address this issue, Kang et al. fabricated a carboxylate-protected Li (CPLi) by *in situ* spontaneous reaction between carboxylic acid of moderate carbon chain length (5 carbon atoms) and $Li^0$.[12] Compared to bare Li as shown in Figure 2.5, a uniform layer of CPLi with a thickness of 1 $\mu$m via spin coating could effectively avoid the dendrites formation in 1 M lithium bis(trifluoromethane)sulfonimide (LiTFSI) in 1,3-dioxolane/1,2-dimethoxyethane (DOL/DME, v/v=1:1) by extending the cycle life to over 1000h at 0.5 mA $cm^{-2}$.

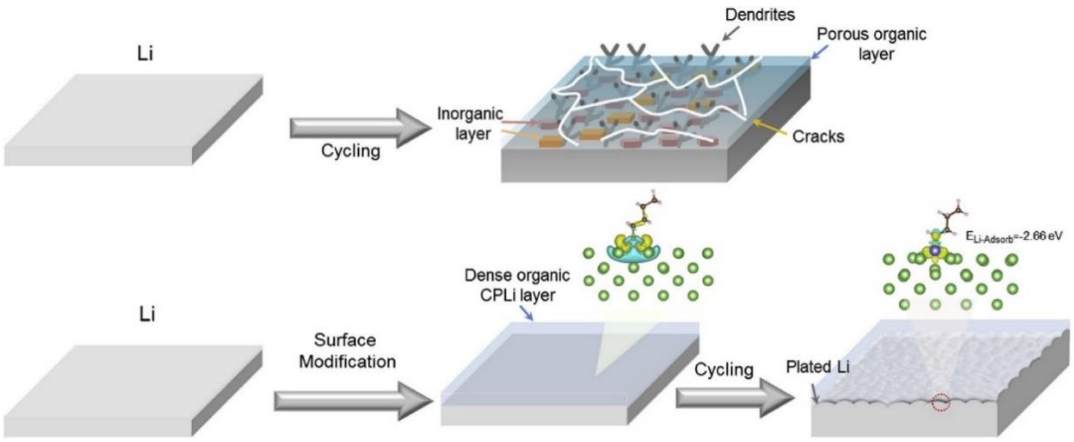


**Figure 2.5.** Schematic plots of SEI morphology comparison between bare Li and CPLi. The green and purple balls represent Li and the adsorbed Li atoms, respectively. Image adapted from ref. [12]. Copyright @ 2020, Elsevier B.V.

Compared to polymers, inorganics have a higher mechanical strength and ionic conductivity. Li et al. designed a $Li_3PO_4$-SEI layer by *in situ* reaction of polyphosphoric acid with $Li^0$ and its native SEI.[13] The uniform $Li_3PO_4$ could reduce the side reaction between $Li^0$ and the electrolyte, as evidenced by X-ray photoelectron spectroscopy (XPS) spectra of modified $Li^0$. Few electrolyte reduction products are on the surface at open-circuit potential or even after cycling.

Hybrid materials combine the merits of flexibility and rigidity from organics and inorganics, respectively, fabricating a multifunctional protection layer on the $Li^0$ anode. However, conventional organic-inorganic SEI cannot accommodate the volume change of the $Li^0$ anode. A novel hybrid (e.g., polymer-inorganic) artificial SEI layer reported by Gao et al. used a reactive polymer composite (RPC) as the SEI precursor. This SEI consists primarily of polymeric Li salts embedded within nanoparticles of LiF and graphene oxide (GO) nanosheets. The polymer–nanoparticle composite is dense and homogeneous, providing good passivation properties. Besides, the GO nanosheets confer mechanical strength and help prevent Li dendrite growth.[14] The addition of more inorganic salts (e.g., $LiPF_6$ and lithium nitrite, $LiNO_3$) into the electrolyte could increase the contact ion pair and aggregate solvates to form an inorganic-rich SEI. Liu et al. used the dimethyl sulfoxide (DMSO) as a $LiNO_3$ solubilizer to promote the preferential reduction of $NO_3^-$ ions.[15] $LiNO_3$-S electrolyte significantly stabilizes the Li deposition behavior compared to $LiNO_3$-free electrolyte.

*Artificial ex situ SEI*

The formation of an *ex situ* artificial SEI on $Li^0$ anode could be mainly carried out via deposition methods (e.g., chemical and physical vapor deposition) or solution casting. In general, a symmetric cell with LE is assembled and cycled. Afterward, the cell is disassembled and the *ex situ* artificial SEI on $Li^0$ anodes is obtained. Pre-cycling $Li^0$ with an optimized LE could initiate a robust SEI formation and thus significantly stabilize the $Li^0$|solid electrolyte interface. Compared to the *in situ* formed artificial SEI, the *ex situ* SEI has a precise thickness and composition. But the fabricated

coating layers cannot always maintain a sufficient contact with $Li^0$ during the cycling. Table 1 summarizes several artificial *ex situ* SEIs' properties along with battery performance.

**Table 1.** Selective artificial *ex situ* SEIs' properties along with battery performance.

| Salts | Solvent system | SSEs | SEI composition | Cell, cycling condition | Initial discharge capacity, capacity retention@cycles |
|---|---|---|---|---|---|
| **1M [1]LiTFSI, 1wt.% $LiNO_3$** | [2]DOL/[3]DME/[4]FEC (9:9:2, volume ratio) | [5]LAGP-[6]PEO | $Li_2CO_3$, LiOH, $Li_3N$, organic composites of $ROCO_2Li$, LiF | Li (SEI)\|[7]LFP, 0.1C | 147.2 mAh $g^{-1}$, 96 % @ 200 cycles[16] |
| **1M LiTFSI, 1wt.% $LiNO_3$** | DOL/DME/FEC (8:1:1, volume ratio) | LPSCl-PEO-LiTFSI | LiF, $Li_2CO_3$, $Li_3N$, organic composites of $ROCO_2Li$ | Li (SEI)\|$Al_2O_3$@NMC 532, 0.1C | 135.8 mAh $g^{-1}$, 89.3% @ 100 cycles[17] |

[1]Li bis-trifluoromethanesulfonimide, [2]1,3-dioxolane, [3]1,2-dimethoxyethane, [4]fluoroethylene carbonate, [5]$Li_{1.5}Al_{0.5}Ge_{1.5}(PO_4)_3$, [6]poly (ethylene oxide), [7]$LiFePO_4$

### 2.2.2 Cathode-electrolyte interphase (CEI)

The intimate coating layer that forms on the positive electrode is known as the *in situ* cathode-electrolyte interphase (CEI). The CEI, in contrast to the SEI, is generated by the oxidation process and decomposition of LEs.

*In situ CEI formation and composition*

The *in situ* CEI contains a high inorganic content (e.g., the decomposed LiF and $Li_2CO_3$ products from the LE), and it serves as an electronic insulator on the cathode layer.[18] A uniform and thin CEI layer can protect the cathode surface from being consumed and the corrosion of electrolyte by-products. Moreover, the CEI layer can reduce voltage polarization by inhibiting the side reactions of electrolytes. A CEI with an optimal chemical composition and structural stability is important to

increase the cutoff voltage of the cathodes beyond the oxidation stability of electrolytes. More work is required to stabilize the CEI formation and growth for different cathode chemistry.

With a high volumetric and gravimetric energy density of 3700 Wh $L^{-1}$ and 800 Wh $kg^{-1}$ (charged to 4.6 V (vs $Li/Li^+$), about 220 mAh $g^{-1}$), layered $LiCoO_2$ is competitive among various cathode candidates. A primary challenge of $LiCoO_2$ lies in the drastic structural change resulting from the repeated deep Li intercalation and/or de-intercalation reactions. The resulting mechanical damage during high voltage cycling is directly related to battery fatigue. The presence of the CEI layer on $LiCoO_2$ was firstly proved by Goodenough et al. in 1985.[19] The CEI layer presents dynamic evolution during battery cycling within the low-cut-off voltage range 4.2 V (vs. $Li/Li^+$), while a thicker CEI gradually accumulates with the increase of cycle number. When $LiCoO_2$ is charged up to 4.5 V (vs. $Li/Li^+$), the CEI layer becomes less stable and decomposes. Surface modification of $LiCoO_2$ with different oxides has been proposed to lower the high charge-transfer resistance by preventing the creation of the resistive CEI layer. Conventional coating materials such as $Li_4Ti_5O_{12}$, $LiNbO_3$, and $Li_2O$-$SiO_2$ generally have low Li-ion conductivities, which hinder the Li-ion migration at the interface.

Compared to $LiCoO_2$, spinel $LiNi_{0.5}Mn_{1.5}O_4$ (LNMO) shows a higher charge-discharge potential plateau at about 4.7 V (vs. $Li/Li^+$). Doping or surface modification have been considered as two efficient strategies to produce an inorganic-rich and chemically stable CEI to overcome the interfacial problems between LNMO and electrolytes.

As one of the high-voltage cathode materials, $LiNi_xMn_yCo_zO_2$, x+y+z=1 (NMC) series suffer from poor cycling performance and rapid capacity fade due to cation mixing and oxygen release from the surface. At the same time, a great quantity of Li residues (e.g., $Li_2O$ and LiOH) always accumulate on the surface and impact cycling.

Different strategies (e.g., CEI-forming additives and anti-oxidation solvents) have been applied to the LE formulation to establish a robust CEI. The surface modification of the cathode could avoid

the formation of the space-charge layer to some extent. Usually, the coating materials grow on the surface of the cathode particle and reach a crystalline state after high-temperature calcination, leading to moderate compatibility with the cathode. *In situ* depositing an amorphous artificial CEI with excellent structure compatibility and plasticity is another way to stabilize the cathode interface.

*CEI advanced characterizations*

A stable and conformal CEI helps improve CE and overall capacity retention of the battery. However, unlike the negative electrode (or anode) SEI, many aspects of CEI remain unclear due to the lack of effective tools to characterize the nano-scale structure. Therefore, advanced techniques such as *in situ* atomic force microscopy, an operando attenuated total reflection-fourier transform infrared (ATR-FTIR), and cryogenic transmission electron microscopy (cryo-TEM) have been used to analyze the CEI layer.[20]

Cui's group investigated the chemical nature of CEI via cryogenic electron microscopy (cryo-EM), and the sample preparation is shown in Figure 2.6(a).[21] In Figure 2.6(b) and (c), CEIs have a vastly different distribution and morphology on the electrode in different cycling states. Subsequent electrolyte decomposition would occur to form a continuous and conformal coating on the cathode particles. In addition, Manthiram's group used time-of-flight secondary-ion mass spectrometry (TOF-SIMS) to investigate the CEI and its cell performance on NMC cathodes. TOF-SIMS offers sub-nanometer surface sensitivity and ultra-high chemical selectivity associated with region-of-interest (ROI) analysis, enabling individual components to be observed independently. Besides, molecular dynamics simulation and machine learning have also been applied to investigate the solvation/desolvation within the structure of the CEI.

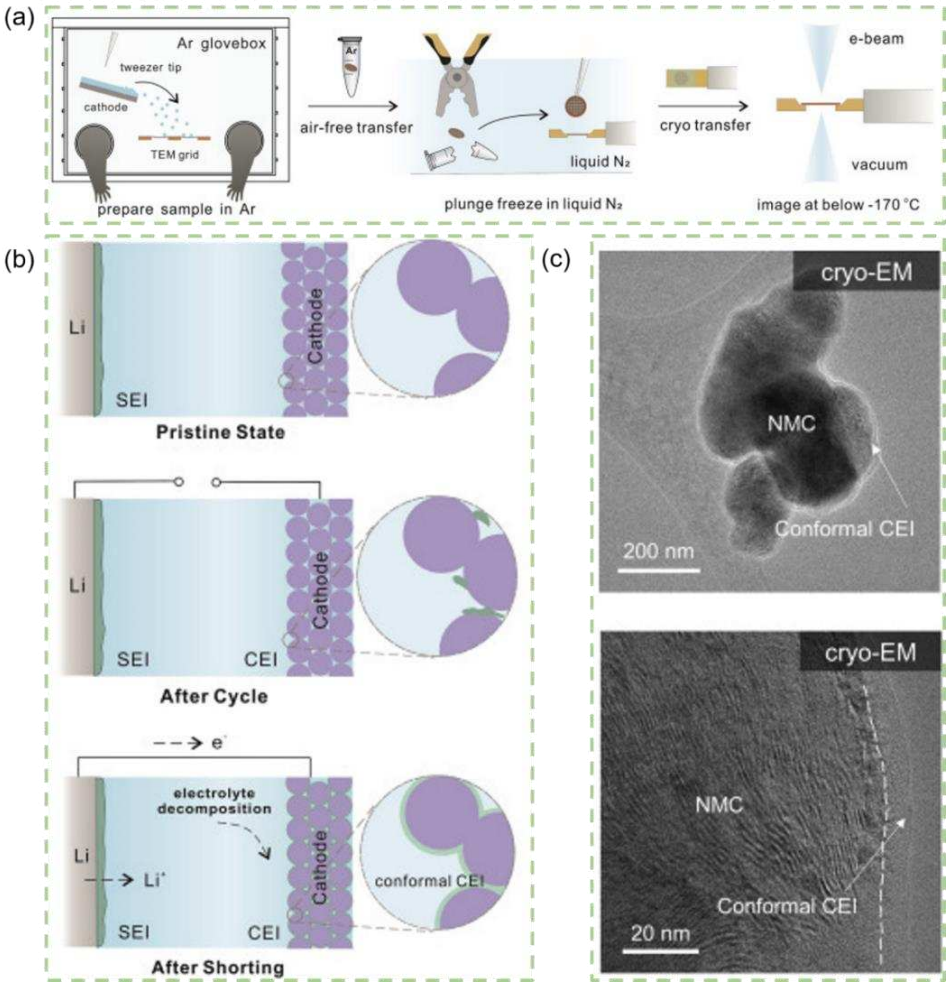


**Figure 2.6.** (a) Cryo-EM sample preparation; (b) CEI in different states of cycling; and (c) Cryo-EM images of conformal CEI formed on NMC electrodes. Image adapted from ref. [21]. Copyright @ 2020, The Authors.

## 2.3 Solid-state lithium metal batteries

Compared to liquid-state LIBs, solid-state lithium metal batteries (SS-LMBs) have attracted much attention due to their projected enhanced safety and higher energy density. SS-LMBs contain four basic components: cathode, anode, solid-state electrolyte (SSE), and current collectors.[22]

The anode, SSE, and cathode should all be void-free to attain high volumetric energy density. Additionally, the interfacial contact between the three layers must be sufficiently high to promote Li-ion conduction across the layers. This movement of ions in and out results in cathode volume

expansion and shrinkage. Therefore, the cathode must possess mechanical strength to resist internal cracking and delamination at the interface with SSEs.[23,25]

### 2.3.1 Ceramic solid-state electrolytes

One of the potential SS-LMB configurations uses ceramic SSEs (e.g., garnets, perovskites, etc.) with a $Li^0$ anode and high-capacity cathodes.[23] Compared to polymer SSEs, ceramic SSEs have a relatively higher ionic conductivity at room temperature of $10^{-3}$~$10^{-4}$ S $cm^{-1}$ and a wide range of electrochemical stability window over 5 V (vs. $Li/Li^+$) as indicated in Figure 2.7.[23,24]

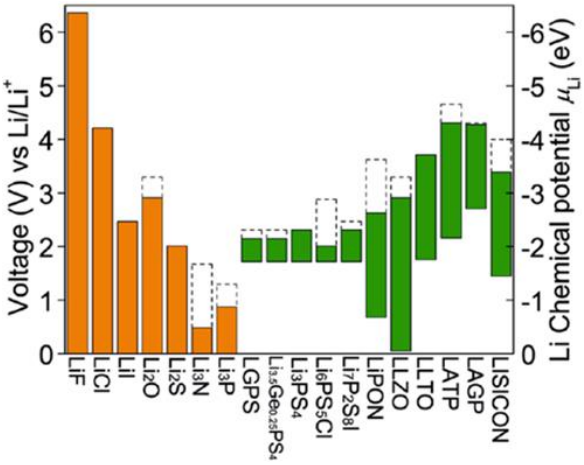


**Figure 2.7.** Electrochemical window (solid-colored bars) of representative inorganic SSEs. Image adapted from ref. [24].

Theoretically, ceramic SSEs with a high mechanical strength could prevent Li dendrite formation and thus avoid short circuits of the cell. At the same time, many works have pointed out that soft Li still has a chance to propagate along the grain boundary regions of SSEs (e.g., polycrystalline-structure oxides).[25,26]

*NASICON*

$Na_{1+x}Zr_2Si_xP_{3-x}O_{12}$ ($0 \leq x \leq 3$) (NASICON) have a rhombohedral structure with a space group of $R\bar{3}c$. The rhombohedral structure is shown in Figure 2.8 where $XO_4$ (e.g., $PO_4$ or $SiO_4$) tetrahedrons and $MO_6$ (e.g., $ZrO_6$) octahedrons are associated with each other to form a 3D framework for Li-ion

transportation. However, NASICON electrolytes possess poor chemical stability towards $Li^0$ anodes (e.g., $Ti^{4+}$ cations in $Li_{1.4}Al_{0.4}Ti_{1.6}(PO_4)_3$ can be reduced in direct contact with $Li^0$ anodes).[26]

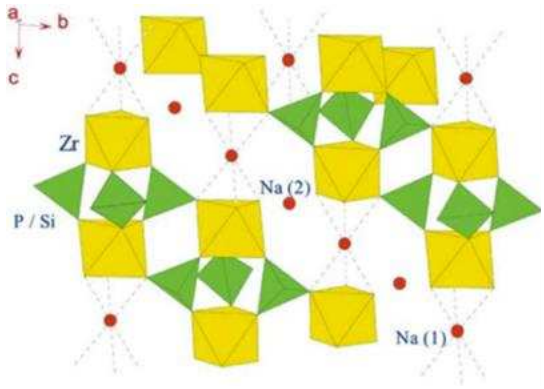


**Figure 2.8.** Crystal structure of NASICON-type oxides. Image adapted from ref. [26].

*Garnet*

The garnet structure has the general formula $A_3B_2(XO_4)_3$. A-sites are 8-fold coordinated, B-sites are 6-fold coordinated, and X-sites are 4-fold coordinated. In Li-conducting garnets, Li ions occupy the tetrahedral positions as in $Li_7La_3Zr_2O_{12}$ (LLZO) of Figure 2.9. Li ions can occupy tetrahedral 8a, and octahedral 16f and 32g sites. To obtain appreciable ionic conductivity at room temperature, more Li can be added into the crystal structure by adjusting the valence of the A and B cations.

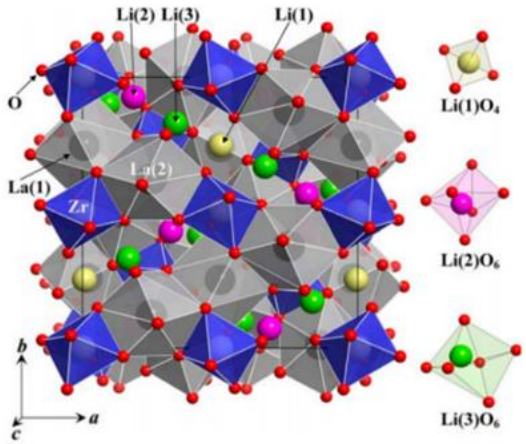


**Figure 2.9.** Crystal structure of a unit cell in a tetragonal LLZO. Shown on the right side are three different Li sites: 8a, 16f, and 32g. Image adapted from ref. [27].

There are two stable forms of LLZO available: the cubic and the tetragonal phases. The conductivity of the cubic LLZO (>$10^{-4}$ S $cm^{-1}$ at room temperature) is roughly two orders of magnitude higher than that of the tetragonal LLZO (>$10^{-6}$ S $cm^{-1}$ at room temperature). Therefore, it is strongly necessary to stabilize the cubic phase. High sintering temperatures (between 1000 ˚C and 1500 ˚C) is often required to obtain the more conductive cubic structure.[27]

Compared to NASICON, LLZO has better chemical stability against metallic Li and higher Li-ionic conductivity (>$10^{-4}$ S $cm^{-1}$ at room temperature). However, the ionic conductivity of cubic LLZO is decreased as a result of the structural collapse that frequently occurs along with the creation of second phases (e.g., $La_2Zr_2O_7$) during this high-temperature process. Numerous earlier researches have shown that it is possible to promote the stabilization of cubic-phase LLZO by adding doping elements.[28,29]

*Perovskite*

The perovskite structure has a general formula $ABO_3$. The cubic cell consists of A-site ions (e.g., alkaline-earth elements) at the corners, B ions (e.g., transition metal ions) at the centers, and oxygen atoms at the face-center positions. A-sites are in 12-fold coordination and B-sites are in 6-fold coordination ($BO_6$) that share corners with each other.[30]

Inaguam was the first to report $La_{2/3-x}Li_{3x}TiO_3$ (LLTO, $0.04<x<0.16$) with relatively high and total ionic conductivity of over $2 \times 10^{-5}$ S $cm^{-1}$. LLTO shows wider electrochemical windows of 8 V (vs. $Li/Li^+$) than LEs that allows them to pair with high-capacity cathode materials (e.g., Ni-rich NMC) to achieve a high energy density of SS-LMBs.[31] Additionally, the cost of LLTO fabrication is much lower than LLZO fabrication, making it more practical for commercialization. LLTO has many other advantages: 1) large ionic transference numbers (e.g., 0.5-0.9); 2) superior chemical and thermal stability (e.g., 4-1600 K) in air; and 3) environmental friendliness without any release of toxic gases during decomposition reactions.[32]

## 2.4 Solid-solid interfaces in SSBs

In SS-LMBs, the lack of intimate contact at the solid|solid interfaces between electrodes and ceramic SSEs results in high interfacial resistances. The interfacial resistance SS-LMBs can be described via the charge transport between electrodes and SSEs.[23] The term 'interface' combines contact condition, interphase formation, and energy status. The interfacial resistance that hinders Li-ion conductivity includes lattice mismatch, space charge regions, the formation of interphases, and the compatibility of $Li^0$ with the SSE interface. More details will be reviewed in the later sections. Moreover, the chemical reactivity at interfaces has adversely impacts on battery performance, including the poor rate capability and rapid battery fade during cycling.

### 2.4.1 Hybrid solid-state electrolyte approach

Increasing demand for SS-LMBs has prompted intensive research into fast ion transport at the interfaces between electrodes and electrolytes. Inspired by the ideal less resistive solid|liquid interfaces in liquid-based LIBs, a popular approach to overcome interfacial issues in SS-LMBs is by incorporating tiny amounts of liquids (e.g., LE, gel, ionic liquids, etc.) into the SSE|electrode interface to serve as an ionic bridge for fast Li-ion migration. Such a hybrid solid-electrolyte approach simultaneously improves the interfacial contact and suppresses Li dendrite growth, opening up a new route to design Li batteries with increased energy density and expanded cycle life. For conversion-type Li batteries (e.g., Li-S batteries), a hybrid electrolyte design combining a sulfide SSE and a liquid Li alloy solution anode could achieve a record-high current density of 17.78 mA $cm^{-2}$.

*SSE-gel*

Inorganic ceramic electrolytes and organic polymer electrolytes suffer from problems of poor physical contact and terrible chemical stability on interfaces between electrolytes and electrodes. Gel polymer electrolytes combine the advantages of LE solution and solid polymer electrolyte, demonstrating their ameliorative ionic conductivity and interfacial compatibility. One type of SSE-

gel hybrid electrolyte is constructed by preparing porous polymer films as hosts soaked with the liquid solution and then sandwiched between electrodes. The other is formed by interactions between ester groups inside the polymer skeleton and oxygen in functional groups of solvent molecules.

*SSE-liquid*

LE undergoes an *in situ* phase transformation inside the battery, going from a liquid state to a (quasi) solid state under thermal or electrical conditions. In Figure 2.10, it is shown that before a complete LE decomposition, LE with high mobility could easily fill the void space at the cathode interface and may potentially penetrate electrodes (e.g., porous cathodes); while following continuous LE decomposition, the newly-formed interphases (e.g., solid-liquid electrolyte interphase) maintain their $Li^+$ ionic conductivity.[33].

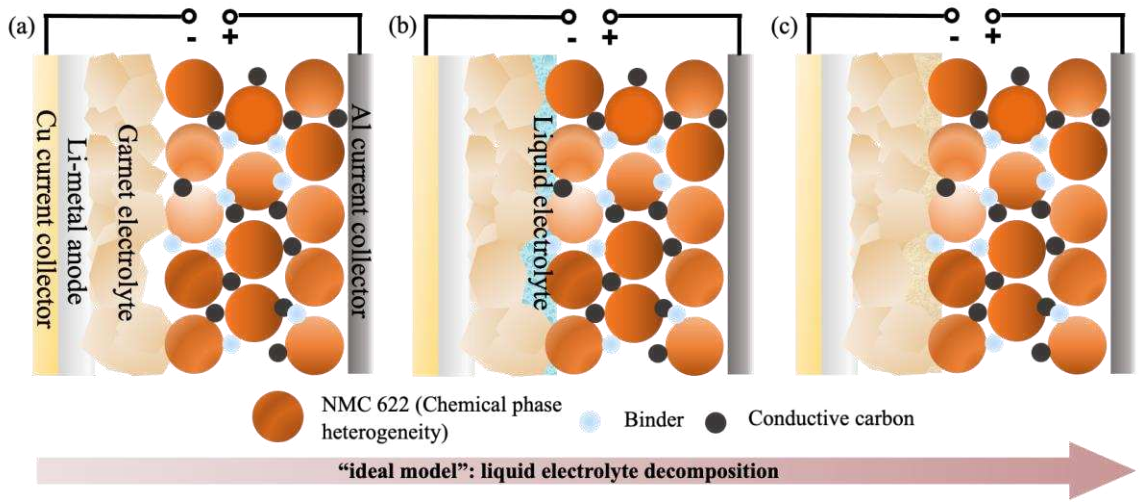


**Figure 2.10.** Schematic drawing of the "ideal model" hybrid solid-liquid approach: (a) less intimate solid-solid contact between ceramic SSE and electrodes; (b) LE is added at the cathode interface to improve the physical contact; and (c) LE is decomposed at the cathode interface under thermal or electrical conditions.

During the cycling process, the LE reacts chemically with SSE to establish a metastable solid-liquid electrolyte interphase (SLEI) at the SSE|electrodes interfaces, which usually combines decomposed

products from LE (e.g., inorganic species) with carbon-containing compounds (e.g., organic solvents). Numerous studies have investigated the structure and chemical composition of SLEI, as shown in Figure 2.11.[34-47] A better understanding of the SLEI function in the battery is essential to smartly design a robust SLEI.

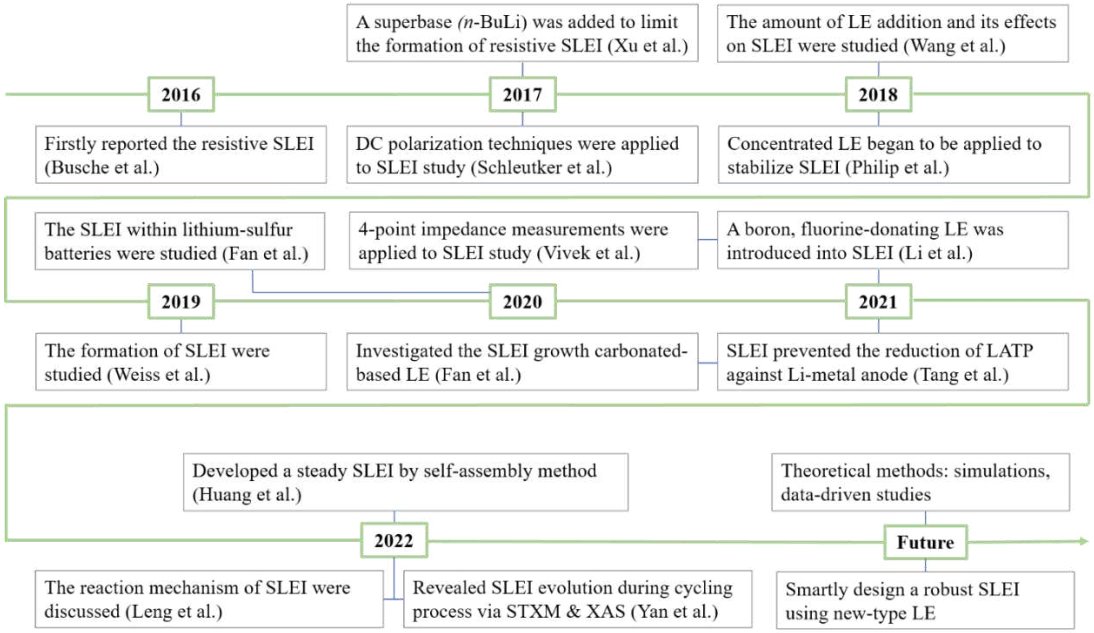


**Figure 2.11.** A roadmap of SLEI developments for solid-state lithium batteries.

The formation of SLEI starts when SSE is immersed with LE, and SLEI grows with immersion time increase during cycling.[45] The decomposition reaction may occur on the surface of SSE where it is exposed to LE, as shown in region I of Figure 2.12(a). However, a small amount of decay product was also observed at the fresh intergranular fracture surface along the grain boundary in region II. The thickness of SLEI is expanded, and the SSE surface becomes swelling from the prolonged immersion time, corresponding to the further decomposition reaction. In Figure 2.12(b) and (c), a homogenous and continuous SLEI (with an average thickness of around 40 nm) fully covers the SSE surface after 48h. This SLEI mainly consists of LiF and organic carbonate components, as supported by transmission electron microscopy (TEM) and XPS analysis in Figure 2.12(d-f).

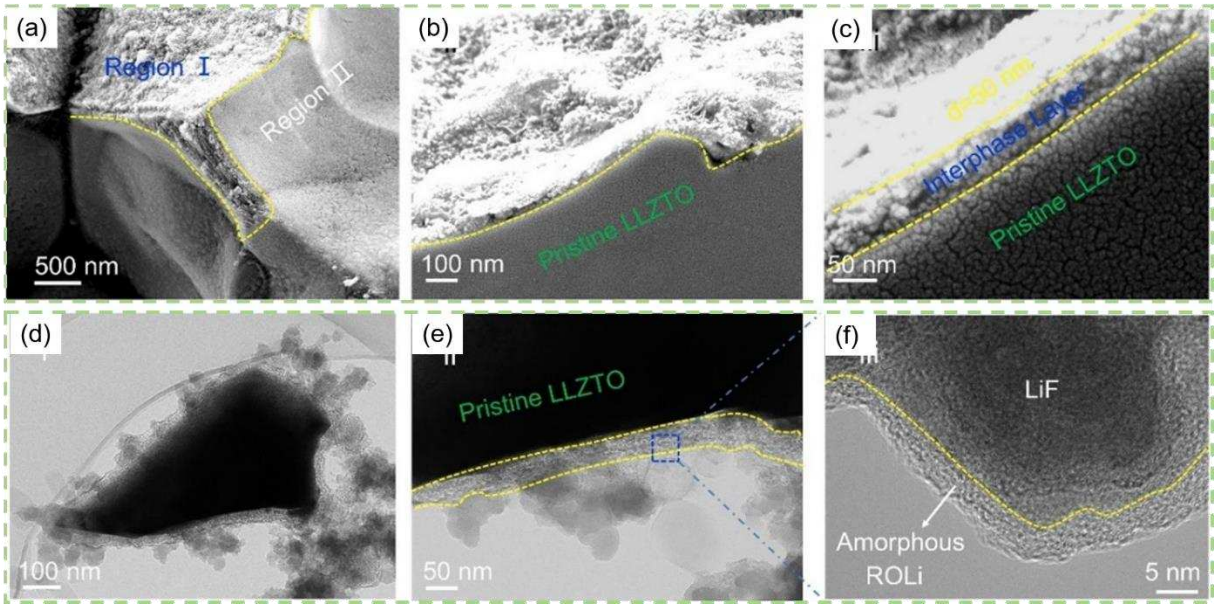


**Figure 2.12.** (a-c) Cross-sectional view SEM images of SSE; and (d-f) TEM images of SSE particles. Image adapted from ref. [45]. Copyright @ 2022, Elsevier B.V.

Specifically, several driving forces have been proposed as being responsible for the formation of the SLEI, including ion solvation, charge carrier re-distribution, and LE decomposition triggered by the Lewis acidity of SSE. Besides, SLEI significantly impacts the structural stability of electrodes, interfacial stability, and Li-ion migration. However, this SLEI with low conductivity generates a significant ohmic loss in the battery, which causes a rapid fade in battery capacity. Figure 2.13 shows that the thickness of SLEI increases over time in response to a resistive SLEI formation, which increases the interfacial resistance of Li-ion transfer. A hopping ion-conduction mechanism for ionic transport across SLEI was reported by Busche et al. [48] Solvated ions in the LE transit into SSE by desolvation and then migration through SLEI against a large energy barrier (depicted in Figure 2.13 as $E_{A,\,SLEI}$).

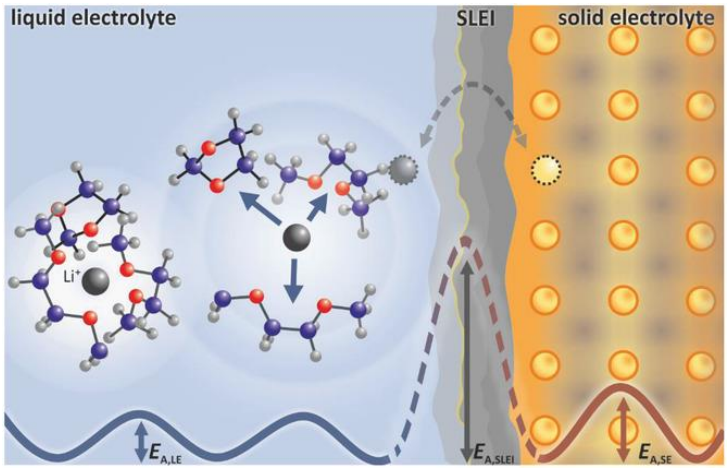


**Figure 2.13.** Schematic ion-conduction mechanism of SLEI. Image adapted from ref. [48]. Copyright @ 2020, The Authors.

Due to the complexity of the interfacial phenomena and the infancy of this research topic, it is still difficult to fully comprehend how SLEI affects ionic migration. More importantly, the electrodes need to be sufficiently wetted with a proper amount to improve the chemical and electrochemical compatibility at the interfaces. In addition, a lack of high-resolution characterization methods makes it hard to trace and probe SLEI during cycling.

*The interphase between SSEs and $Li^0$ anodes*

SSE is difficult to be used in commercial Li batteries due to its inherent rigidity, which leads to poor contact between SSEs and $Li^0$ anodes. In addition, some ceramic SSEs are chemically unstable with $Li^0$ due to the reduction of transition metal cations (e.g., $Ti^{4+}$ ion reduction in perovskites and NASICON). As a result, the addition of LE at the SSE|$Li^0$ interface could wet the interface to minimize the interfacial resistance and form an SLEI to suppress the side reactions at the interface. However, LEs are limited by their inherent thermodynamic instability against $Li^0$ anodes. Super-concentrated 'solvent-in-salt' solvates are considered safer than conventional LEs because the solvent molecules are coordinated to the salt, thereby limiting side reactions between the solvent and the $Li^0$. Philip et al. reported the hybrid electrolyte for LMBs by adding a highly fluorinated ether-modified solvate to the surface of NASICON-type pellets.[38] The permeation of concentrated

LE highly relates to its viscosity and the porosity of SSE. Optimizing the LE composition could reduce the cell resistivity that originates from the formation of SLEI.

A superbase (e.g., *n*-BuLi) is introduced into commercial LE to suppress the $Li^+/H^+$ exchange on the garnet surface. Hence, LE decomposition and the formation of resistive SLEI can be inhibited. Three primary benefits could be gained from *n*-BuLi addition: (1) this Lewis base additive may retard the decomposition reaction of LE; (2) it is highly proton withdrawing and suppress side reactions; and (3) it lithiates the SSE|LE interface and consequently improves the interfacial conductivity.[35]

The solubility of Li-salts in the solvent and the solvation effect can influence the stability and solidification of SLEI. For example, Fan et al. used DME-based LE that could form a more stable and compact SLEI with $Li_2S$-$P_2S_5$ glass-ceramic SSEs due to the stronger $Li_3PS_4$ solvation effect of DME than that of DOL.[40,41] Meanwhile, the corrosion effect of DME on the $Li_2S-P_2S_5$ was weaker than that of DOL.

*The interphase between SSEs and cathodes*

The incompatibility caused by the inherent chemical and electrochemical reactivity at the cathode|SSE interface has usually been overlooked. However, when coupling with NMC cathodes, there are inevitable side reactions that deteriorate interfacial stability, owing to the addition of commercial liquid electrolyte. Additionally, the aggregation of space charge still exists across the cathode|SSE interface, which is liable to hinder ionic transportation.

To improve the electrochemical compatibility between SSE and LE, Li et al. applied LE with dual-salts (95 mol% LiTFSI: 5 mol% lithium bis(ethanedioato)borate (LiBOB),) between garnet-based SSE and NMC 622 cathode.[42] The addition of LiBOB in highly fluorinated solvents can reduce the amount of highly resistive LiF species in SLEI, which not only accelerates ion transport kinetics at the SE|cathode interface but also reinforces interfacial thermodynamic stability.

To prevent $Li^+$ from being trapped in decomposed LE or turned into SLEI species, Kim et al. proposed a key feature of hybrid cell with polymer SSE and LE: "$Li^+$ caging" process during charge/discharge as shown in Figure 2.14(a) and (b).[49] Polymer SSE as a solid electrolyte and separator enables the caging of lithium ions inside the battery, possibly by changing their linearity in the polymer chain and crystallinity during cycling. The embedded structure of Indium tin oxide (ITO) behind the polymer (e.g., poly(ethylene terephthalate), PET) can give rise to electrolyte resistance as it shields the large contact area between the cathode|SSE yet allows $Li^+$ to diffuse into PET/ITO through the LE. No decomposed LE or SLEI species were identified close to the PET surface. Besides, Huang et al. found that an ion exchange interlayer (EIL) forms between SLEI and garnet SSE due to *in situ* $Li^+/H^+$ ion exchange and pointed out the importance of stabilizing the EIL, as plotted in Figure 2.14(c).[46] The acidic molecule treatments can controllably restrict the exchange depth and efficiently protect SSE from further decomposition.

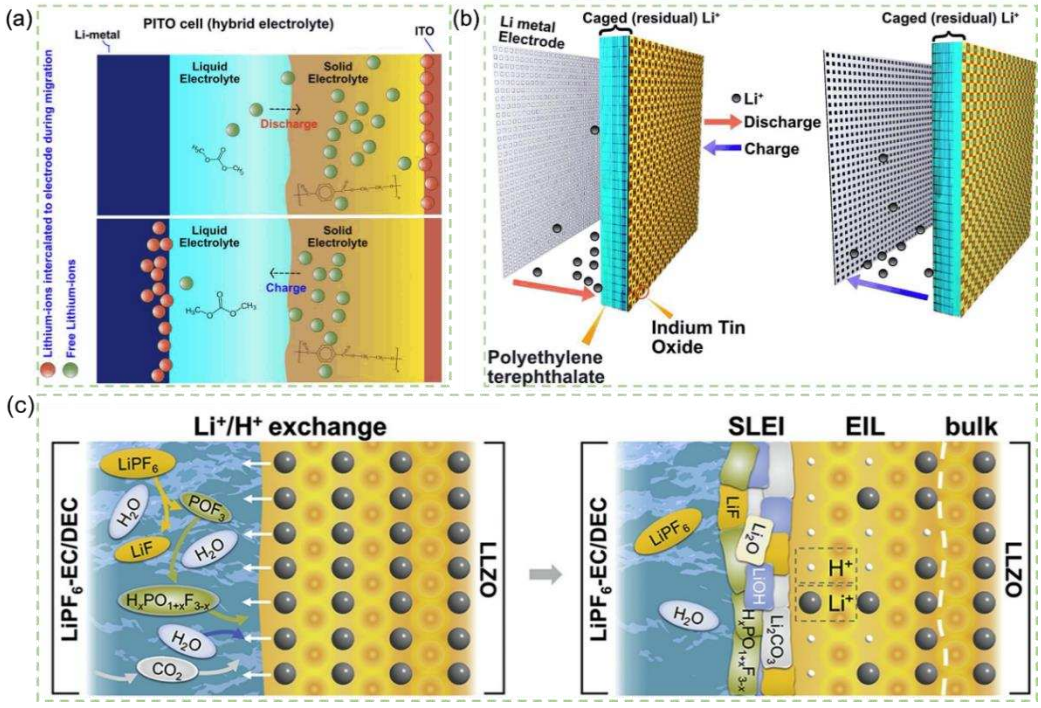


**Figure 2.14.** Schematic drawings of: (a) a hybrid cell design; (b) $Li^+$ caging process in PET on charge and discharge. Image adapted from ref. [49]. Copyright @ 2021, IOP Publishing; and (c)

$Li^+/H^+$ exchange at the LE|SSE interface and interfacial composition at an equilibrium state. Image adapted from ref. [46]. Copyright @ 2022, Elsevier Inc.

## 2.5 Review of perovskite SSEs for LMBs

This section has been adapted from a review paper published in *Batteries* (doi: 10.3390/batteries7040075).

### 2.5.1 Introduction

Electrifying transportation and expanding the use of renewable energy sources require a transformative energy storage technology.[50-55] Rechargeable lithium-ion batteries (LIBs) represent one of the most promising energy storage technologies.[51,56-60] LIBs have a much higher energy density than conventional Nickel-Cadmium (Ni-Cd), Lead-Acid (Pb-Acid), Nickel-Hydrogen (Ni-$H_2$), and Silver-Zinc (Ag-Zn) batteries presented in Ragone plot (in Figure 2.15).[61,62,63]

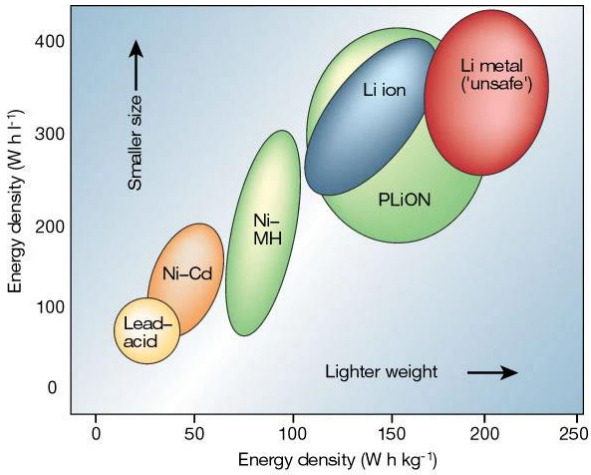


**Figure 2.15.** Ragone plot of lithium batteries. Image adapted from ref. [64]. Copyright@2011 Springer Nature Limited

However, high flammability and low thermal stability of organic liquid-state electrolytes are the major concerns for conventional LIBs.[65,66,67,68] These issues can potentially be addressed by replacing liquid-state electrolytes with non-flammable solid-state electrolytes (SSEs).[69,70,71] The cells combined with SSEs could be operated at a wider temperature range with an improved reactions kinetics at the cathode and anode. Furthermore, SSEs with wider electrochemical are

more adaptable to high-capacity cathode materials (e.g., Ni-rich oxide ceramic cathodes) and Li-metal anodes, which can enhance the energy density (up to 70%) and cycling performance of the cells.[72,73]

SSEs generally comprise polymers, inorganics (e.g., ceramic-based oxides) and their hybrids of electrolytes. Free-standing solid polymer electrolytes (SPEs) could be prepared using the proper crosslinkers followed by photo-polymerization as an *in situ* approach.[74-83] Gel SPEs are capable of forming good interfacial contact with electrodes.[74,75,84] Both Li et al. and Yao et al. provided an overview of current developments on the SPEs for LBs.[85,86] The ionic conduction of SPEs is achieved by ions hopping from one coordinating sites to another under an electrical field assisted by segmental motion of polymer chains in an amorphous phase above the glass transition temperature. Unfortunately, most SPEs have low ionic conductivity at room temperature.[72]

The primary inorganic oxides SSEs are perovskites, garnets, NASICONs, and LISICONs. Cao et al. comprehensively reviewed inorganic SSEs for LBs.[87] Similar to perovskites, hybrid polymer-ceramic systems utilize ceramic fillers with garnets (LLZO) as a dispersant into the polymer matrix (e.g., poly(ethylene oxide) (PEO)-based, poly(acrylonitrile) (PAN)-based, and poly(vinylidene fluoride) (PVDF)-based, etc.).[78,94,95,96,98,99] Goodenough et al. fabricated low-cost hybrid PEO-LLZO electrolytes and applied in $LiFePO_4$|Li cells that delivered high discharge capacity of 139.1 mAh $g^{-1}$ with capacity retention of 93.6% after 100 cycles.[89] Falco et al. innovatively prepared cross-linked hybrid electrolytes to enhance ionic conductivity by mixing LLZO, lithium bis(trifluoromethanesulfonyl)imide (LiTFSI), tetra(ethylene glycol dimethyl ether) (G4) together under UV-light.[90,91] The fabricated hybrid electrolytes have an improved ionic conductivity of $10^{-4}$ S $cm^{-1}$ at 20 ˚C. Passerini's group reported UV cross-linked PEO polymer electrolytes with ionic liquids.[92,93] The room-temperature ionic conductivity could reach nearly $10^{-3}$ S $cm^{-1}$.

As shown in Figure 2.16, we reviewed the progress of all-ceramic LLTO electrolytes in solid-state lithium batteries (SS-LBs). Many investigations have been done on LLTO composite SSEs and

related electro-chemical performance for selected electrolytes are presented in Table 2. However, hybrid electrolytes still suffer safety issues due to the flammability of the organic polymers. There is only a few research working on all-ceramic electrolytes in SS-LBs applications.

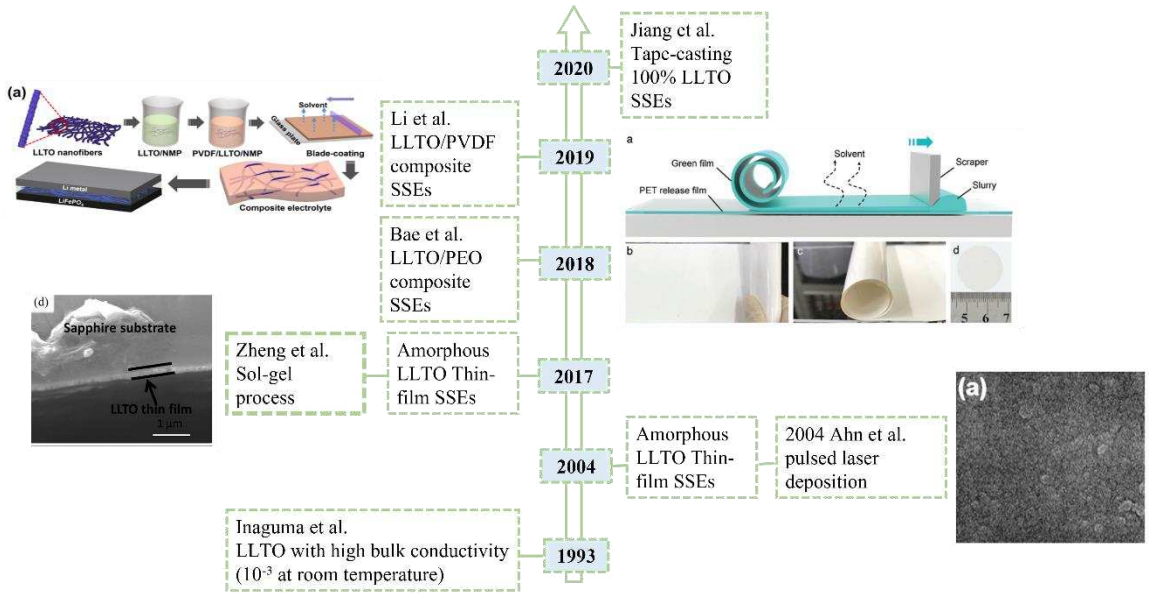


**Figure 2.16.** Timeline for the development of typical LLTO SSEs in SS-LBs.

**Table 2.** Summary of electrochemical performance for selected LLTO SSEs in SS-LBs.

| SSEs composition | Anode\|Cathode | Ionic conductivity (S $cm^{-1}$) | Discharge capacity/Charging rate/Cycle number (capacity retention rate) |
|---|---|---|---|
| LLTO/[1]PAN/[2]SN[94] | Li\|$LiFePO_4$ | $2.20\times10^{-3}$ at 30 °C | 151mAh $g^{-1}$/0.5C/150 (data unavailable) |
| LLTO/[3]PEO/LiTFSI/SN[95] | Li\|NMC 532 | $>10^{-3}$ at 55 °C | 143.2 mAh $g^{-1}$/0.05C/30 (data unavailable) |
| LLTO/PEO[96] | Li\|$LiFePO_4$ | $3.31\times10^{-4}$ at [7]RT | 147 mAh $g^{-1}$/0.1C/100 (~98%) |
| 15 wt.% LLTO/[4]PVDF[97] | Li\|$LiFePO_4$ | $5.3\times10^{-4}$ at 25 °C | 121 mAh $g^{-1}$/1C/100 (~99%) |
| LLTO/PEO/LiTFSI[98] | Li\|$LiFePO_4$ | $1.3\times10^{-4}$ at 60 °C | 144.6 mAh $g^{-1}$/1C/100 (~96%) |
| LLTO/PEO/LiTFSI[99] | Li\|$LiFePO_4$ | $1.6\times10^{-4}$ at 60 °C | 135 mAh $g^{-1}$/2C/300 (79%) |
| 5 wt.% LLTO/PEO/LiTFSI[100] | Li\|$LiFePO_4$ | $3.63\times10^{-4}$ at 60 °C | 123 mAh $g^{-1}$/0.5C/100 (94%) |
| 8 wt.% LLTO/PEO/[5]PC/LiTFSI[101] | Li\|$LiFePO_4$ | $4.72\times10^{-4}$ at 60 °C | 135 mAh $g^{-1}$/0.5C/100 (96%) |
| 3 wt.% LLTO/PEO/$LiClO_4$[102] | Li\|$LiFePO_4$ | $4.01\times10^{-4}$ at 60 °C | 140 mAh $g^{-1}$/1C/100 (92.4%) |
| LLTO/[6]BC[103] | Li\|$LiFePO_4$ | $1.54\times10^{-3}$ at RT | 151.7 mAh $g^{-1}$/0.2C/100 (98.5%) |
| Sr/Ta co-doped LLTO[104] | Li\|$LiFePO_4$ | $1.40\times10^{-4}$ at 25 °C | 83.8 mAh $g^{-1}$/0.1C/80 (89%) |

[1]Poly(acrylonitrile), [2]Succinonitrile, [3]Poly(ethylene oxide), [4]Poly(vinylidene fluoride), [5]Propylene carbonate, [6]Bacterial Cellulose, [7]Room Temperature

Compared to SPEs, perovskites usually demonstrate relatively higher Li-ion conductivities (e.g., $10^{-3}$~$10^{-4}$ S cm$^{-1}$ at room temperature) as shown in Figure 2.17(a) and lower electronic conductivity (e.g., $10^{-8}$ S cm$^{-1}$ at room temperature).[70] Inaguam et al. was the first to report LLTO electrolytes with relatively high bulk ionic conductivity (e.g., $1\times10^{-3}$ S cm$^{-1}$ at room temperature) and total ionic conductivity (e.g., >2 $\times10^{-5}$ S cm$^{-1}$ at room temperature).[105] Figure 2.17(b) shows the Arrhenius plots of the ionic conductivities of the perovskite compared with other ceramic SSEs. LLTO has been widely used as an additive within polymers to form composited electrolytes for ionic conductivities enhancement.

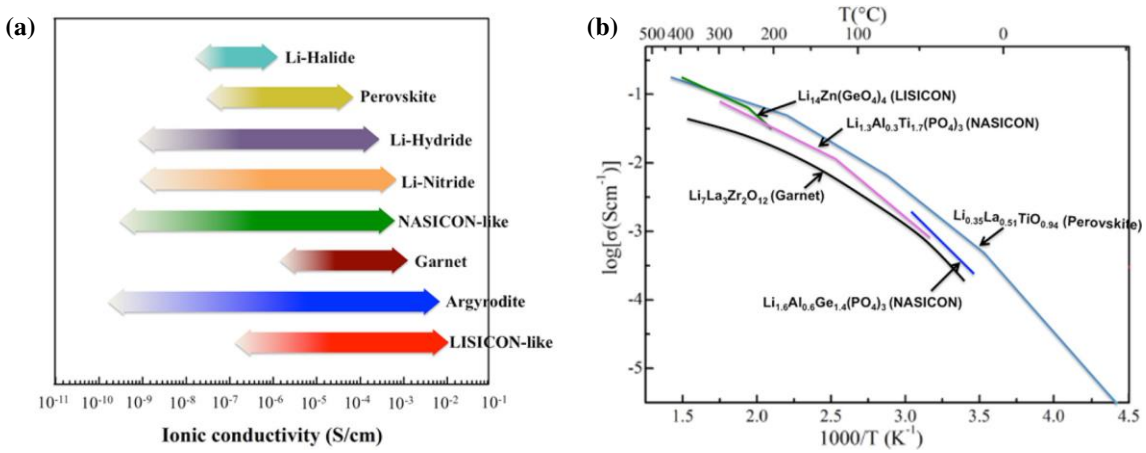


**Figure 2.17.** (a) Typical SSEs with highly ionic conductivities at room temperature; and (b) ionic conductivities of selected SSEs with elevated temperature. Images adapted from ref. [106]. Copyright@2017 American Chemical Society

LLTO SSEs have many advantages: 1) large ionic transference numbers (e.g., 0.5-0.9); 2) superior chemical and thermal stability in air; and 2) environmentally friendly without any release of toxic gases during decomposition reactions. Furthermore, LLTO shows a wide electrochemical window of 5 V (vs. Li/Li$^+$) that increase their adaptiveness to high-voltage cathode materials and if combined with Li-metal anodes. Also, LLTO exhibits excellent thermal stability that provide potential applications even at extreme conditions.[64]

Nonetheless, a number of obstacles prevent LLTO SSEs from being applied in practical SS-LBs. Initially, the large grain boundary resistance lowers the total ionic conductivity below $10^{-5}$ S cm$^{-1}$

at room temperature.[70] Second, LLTO is chemically unstable in direct contact with Li metal ($Li^0$). Li can be intercalated into LLTO at voltages lower than around 1.8 V, resulting in the reduction of $Ti^{4+}$ cations and increased electronic conductivity.[107] Thirdly, it is challenging to fabricate and integrate LLTO in batteries due to its brittle nature. Additionally, de-lamination of the ceramic SSEs may occur as a result of internal volume changes that during battery operation, hence harming the battery lifetime.[108]

In this review, we analyzed the origins of large grain boundary resistance for LLTO and provided potential solutions. We got an insight to the chemical instability of LLTO when contacting $Li^0$ anode. Furthermore, we presented the tape-casting fabrication methods and electrochemical performances for LLTO SSEs SS-LBs.

### 2.5.2 Crystal structure/composition of LLTO and relationship to ionic conductivity

With an $ABO_3$ structure (in Figure 2.18(a)), the perovskite $La_{2/3-x}Li_{3x}TiO_3$ (LLTO)-family ($0.04<x<0.16$) has oxygen octahedrally coordinated with Li-ions, La-ions, and vacancies occupying the A sites and Ti-ions occupying B sites.[70,71] Different x values of both Li ions and La ions lead to distorted structures which originates from the unequal distribution of vacancies and displaced cations. The stable structure could be preserved when the x value is between 0.04 and 0.16.

Cubic and tetragonal LLTO display a lattice structure with the stacking of La-rich and La-poor regions (in Figure 2.18(b)) to maintain high bulk conductivity. Figure 2.18 (c) indicates the crystal structure of the tetragonal-type perovskite with the lattice parameter of a = 3.8 Å for cubic unit cell.[109] Inaguma and Itoh demonstrated that the ionic conductivity of LLTO has a parabolic dependency on x values due to variations in the Li ions to vacancy concentration and the formation of low activation energy Li-ion pathways controlled by site percolation and bottleneck size.[110] As seen in in Figure 2.18(d), the bottleneck structure of perovskites consists of 12-fold coordinated with corner-shared oxygen.

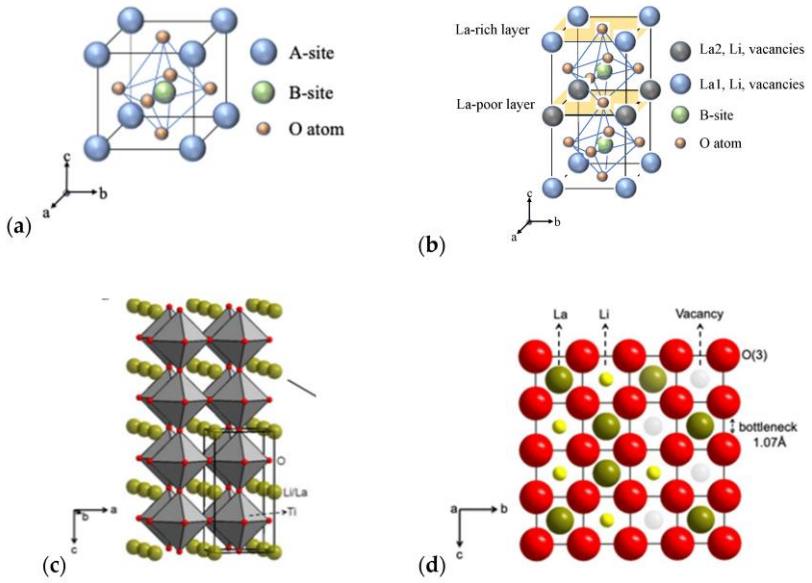


**Figure 2.18.** (a) $ABO_3$ structure; (b) La-rich and La-poor regions; (c) crystal structure of (*P4/mmm)*-type LLTO; and (d) bottleneck structure of 12-fold coordinated with oxygen ions. Images adapted from ref. [109].

Great efforts have been made on LLTO-based electrolytes to gain a better understand of how chemical composition, crystal structure, and synthetic methods influence Li-ion conductivity. Table 3 shows the summary of room-temperature ionic conductivities for selected LLTO SSEs with x values of Li ions.

**Table 3.** Summary of selected LLTO SSEs in ionic conductivities.

| Composition | Space group | Conductivity at RT (S $cm^{-1}$) | Synthesis method |
|---|---|---|---|
| **Type I: pure LLTO SSEs** | | | |
| $La_{0.61}Li_{0.17}TiO_3$ | *Cmmm* | 3.76 x $10^{-4}$ | Pulsed laser deposition[111] |
| $La_{0.5}Li_{0.5}TiO_3$ | *P4/mmm* | 3.52 x $10^{-7}$ | Spin coating[112] |
| | *P4/mmm* | 7.2 x $10^{-7}$ | Microwave sintering method[113] |
| **Type II: composite LLTO SSEs** | | | |
| $La_{0.5}Li_{0.5}TiO_3$/nano-Ag | *Pm3m* | 2.8 x $10^{-5}$ | Sol-gel processing[114] |
| $La_{0.5}Li_{0.5}TiO_3$/silica | *P4/mmm* | 1 x $10^{-4}$ | Wet chemical method[115] |
| Sr-doped $La_{0.56}Li_{0.33}TiO_3$ | *Pm3m* | 9.51 x $10^{-4}$ | Sol-gel processing[116] |
| Y-doped $La_{0.46}Li_{0.33}TiO_3$ | *P4/mmm* | 1.95 x $10^{-3}$ | Sol-gel processing[117] |
| Nb-doped $La_{0.5}Li_{0.5}TiO_3$ | *P4/mmm* | 1.04 x $10^{-4}$ | Solid-state reaction method[118] |
| Sr/Co-doped $La_{0.557}Li_{0.33}TiO_3$ | *Pm$\bar{3}$m* | 1.4 x $10^{-4}$ | Solid-state reaction method[104] |

### 2.5.3 Challenges for LLTO SSEs

*Low total ionic conductivity*

Despite numerous appealing properties, the high grain boundary resistance of LLTO causes it to have an inferior total ionic conductivity than liquid electrolytes.[119] The total ionic conductivity is governed by both grains and grain boundaries. Researchers have attempted to improve the total ionic conductivity by the modification of the morphology of LLTO particles or the grain boundary composition.

Compared with LLTO particles, one dimensional LLTO nanofibers with high surface-to-volume ratios can increase the number of continuous ion-conducting pathways.[119,120] Figure 2.19 depicts the difference of Li-ion pathways when using LLTO nanoparticles and nanofibers (e.g., random or well-aligned type). In contrast to the isolated nanoparticles in Figure 2.19(a), random nanowires could provide continuous fast pathways for Li-ion migration. When compared to random nanowires in Figure 2.19(b), well-aligned nanowires in Figure 2.19(c) are free of crossing junctions. According to Liu et al., 1D LLTO nanowire fillers can facilitate the formation of ionic conduction networks in the polyacrylonitrile-$LiClO_4$ matrix and thus enhance the total ionic conductivity by three orders of magnitude than using nanoparticles.[121]

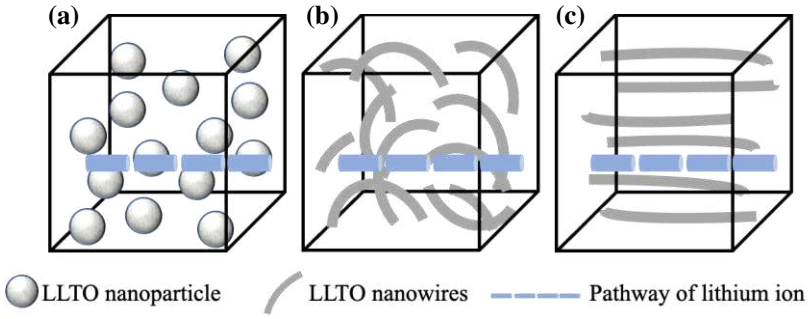


**Figure 2.19.** Schematic images of pathways of Li ions when LLTO as: (a) isolated nanoparticles; (b) random nanowires; and (c) well-aligned nanowires. Image adapted from ref. [121].

*Large grain boundary resistance*

When some LLTO matrices consist of structural and chemical deviations, lattice mismatch appears to offset the random orientation of neighboring coarse LLTO grains.[122] Lattice mismatch refers to the mismatch between LLTO grain boundaries that is composed of a Ti-O binary compound with a 2-3 unit-cell thickness (in Figure 2.20). It is not energetically favorable for Li-ion accommodation or migration, hence resulting in large grain boundary resistance.

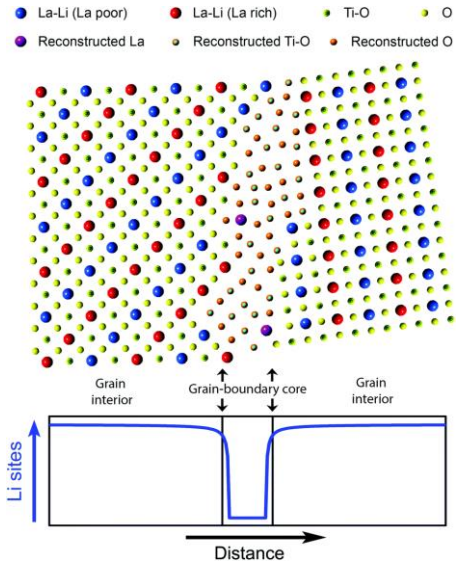


**Figure 2.20.** Schematic image of lattice mismatch. Image adapted from ref. [122].


Sasano et al. proposed that the grain-boundary conductivity can be enhanced by increasing the quantity of coincidence-site lattices (CSL) at the grain boundaries.[123] The index Σ is introduced for the geometric CSL of the grain boundary; the smaller Σ value means the higher lattice coincidence of the grain boundaries. For instance, the grain boundaries are regarded as random regions when Σ values exceed 29. As the closed square marked in Figure 2.21(a), electron backscatter diffraction in scanning electron microscopy (EBSD-SEM) with crystallographic orientation map and electrochemical strain microscopy (ESM) loop area map are measured at the same region. In Figure 2.21(b), CSL at the grain boundaries are smaller than random regions which have fewer composition deviations and structural distortions. Furthermore, the higher ESM signal intensity is

correlated with the higher Li-ion conductivity of the grain boundaries (as black arrowheads pointed out in Figure 2.21(b) and (c)).

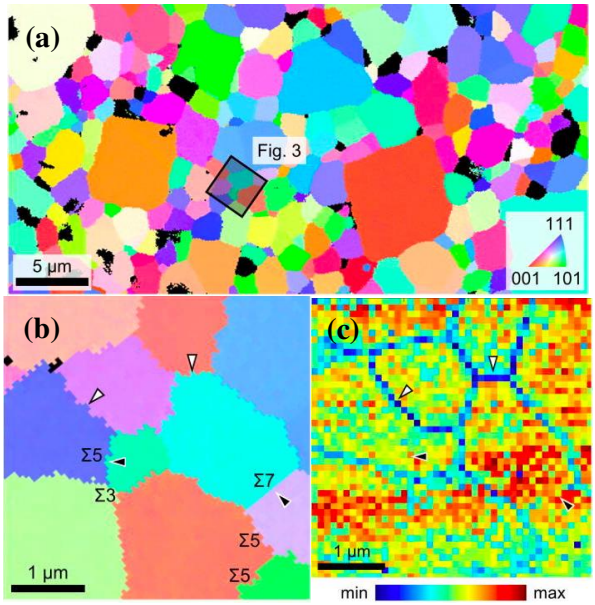


**Figure 2.21.** (a) EBSD-SEM crystallographic orientation map for LLTO; (b) the enlarged area from the black-square; and (c) ESM loop area map at the voltage of 20 V. Image adapted from ref. [123]. Copyright@2020 AIP Publishing LLC.

In addition to lattice mismatch, the 90° domain boundary that exists between adjacent La-rich regions (in Figure 2.22) is another feature leading to the large grain boundary resistance.[124] Moriwake et al. reported that an extremely high activation energy ($E_a$ = 3.58 eV) of Li-ion migration in the 90° domain boundaries.[124,125]

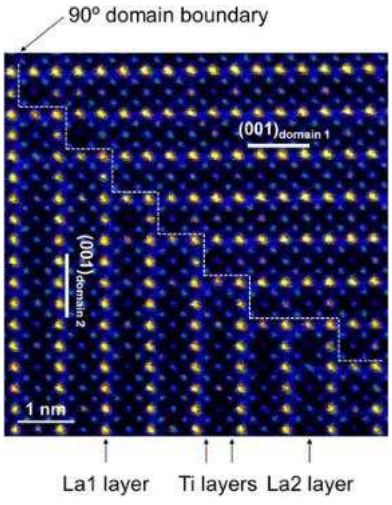

**Figure 2.22.** Schematic image of 90˚ domain boundary. Image adapted from ref. [124]. Copyright@2014 Elsevier B.V.

As previously indicated, one practical approach to lower the grain boundary resistance would alter the composition of the LLTO grain boundaries. Introducing dopant elements into the A-sites and/or B-sites in the crystalline structure of LLTO would create more point defects. Another method is to "fill up" the LLTO grain boundaries with an amorphous layer or valence ions (e.g., $Ag^+$ ions as shown in Figure 2.23).[115] Mei et al. added an amorphous glassy silica layer to the LLTO grain boundaries, which decreased the grain boundary resistance and thus enhanced the total ionic conductivity up to over $1\times10^{-4}$ S $cm^{-1}$ at room temperature.[126]

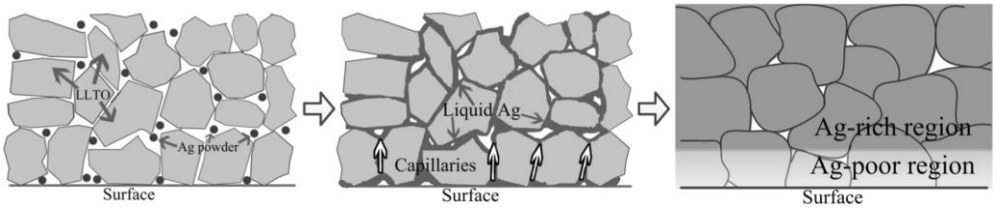


**Figure 2.23.** Schematic images of introducing $Ag^+$ into LLTO grain boundaries. Image adapted from ref. [115]. Copyright@2019 Springer Nature Switzerland AG

Regarding the pellet fabrication, researchers have employed hot-press techniques (e.g., spark plasma sintering (SPS)) to densify LLTO SSEs for grain conductivity improvememt.[127,128] SPS can reach higher heating rates (up to 600 °C $min^{-1}$) in a shorter period of time (e.g., 0-10 min in most circumstances) than most of conventional hot pressing. The hot-pressed $Li_{3/8}Sr_{7/16}Ta_{3/4}Zr_{1/4}O_3$ (LSTZ) SSEs, with a relative density of 96.7%, the ratio of the density of a substance to the density of a given reference, had higher bulk ionic conductivity (e.g., $4.1\times10^{-4}$ S $cm^{-1}$ at 25 °C) and compressive strength.[129] Mei et al. prepared LLTO SSEs via SPS, yielding highly dense (e.g., relative density of over 97%) and finely grained (e.g., grain size of 2 μm) LLTO pellets with an enhanced room-temperature ionic conductivity exceeding $10^{-3}$ S $cm^{-1}$.[130]

### 2.5.4 Chemical instability of LLTO SSEs against Li metal

*$Ti^{4+}$ cations reduction*

Studies using X-ray photoelectron spectroscopy (XPS) confirm that LLTO reacts easily with Li metal and changes color from pristine white to deep black due to the reduction of $Ti^{4+}$ cations to lower oxidation state species. Additionally, this leads to the formation of oxygen vacancies, which makes the interface highly electronically conductive and unsuitable for use as an electrolyte for SS-LBs.[131] Galvez-Aranda et al. revealed that $Ti^{4+}$-ions reduction takes place at the LLTO|$Li^0$ interface.[132] The reaction rate at the interface between LLTO and $Li^0$ increases as the applied external electric field increases. Wenzel et al. applied *in situ* XPS to study how LLTO reacted with $Li^0$.[133] Figure 2.24 displays high-resolution spectra for the Ti 2p, La 3d and O 1s of LLTO after depositing different amount of Li. It is evident that the lithiation process directly impacts the reduction state of $Ti^{4+}$ ions. The color shifts of LLTO electrolyte during the lithiation process is depicted in Figure 2.25. The increased deposition times have no effect on La 3d and all specific peaks remain unchanged. While $Ti^{4+}$-ions can be even greatly reduced to metallic titanium $Ti^0$ when depositing time reaches 300 min. The formation of metallic Ti would increase the electronic conductivity of LLTO.

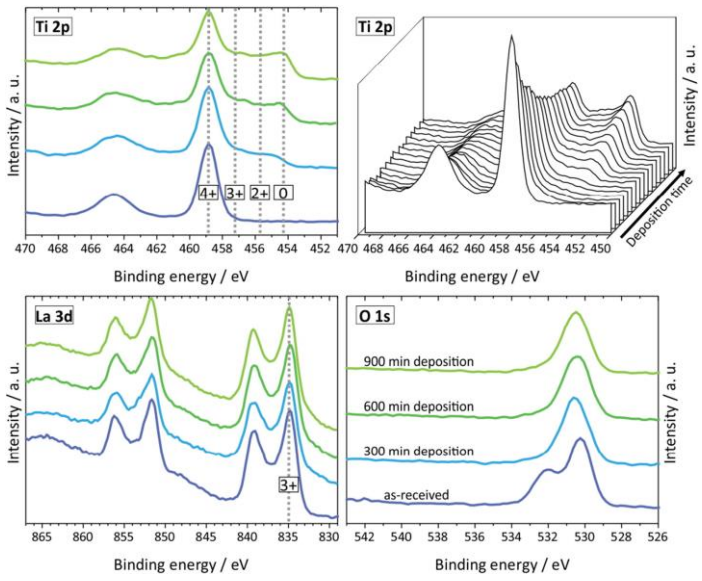


**Figure 2.24.** The Ti 2p, La 3d and O 1s detailed spectra for four different deposition times (different amounts of deposited Li metal). Images adapted from ref. [133]. Copyright@2015 Elsevier B.V.

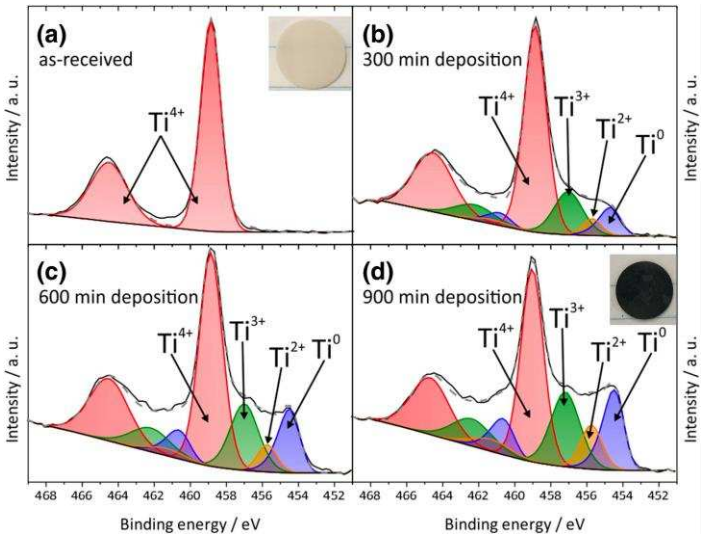


**Figure 2.25.** XPS detailed spectra of four Ti oxidation states for four different deposition times. Image adapted from ref. [133]. Copyright@2015 Elsevier B.V.

However, only a few studies discuss solutions for addressing $Ti^{4+}$-ions reduction problem for LLTO SSEs. To prevent $Ti^{4+}$-ions reduction and achieve a sufficient interfacial contact against $Li^0$, poly(vinylidene fluoride)-*block*-poly(tetrafluoroethylene) (PVDF-b-PTFE) polymer matrix was combined with LLZO and LLTO nanofibers.[131] The assembled battery exhibited a high initial discharge capacity of 150 mAh $g^{-1}$ and retained 127 mAh $g^{-1}$ over 550 cycles. The Coulombic efficiency was always more than 99.5% during cycling. Besides, in symmetric Li cells (e.g., Li|LLTO|Li), metal or metal oxides is effective as a protective layer against $Li^0$ for Li-ion conductivity measurements. [134,135,136]

*Formation of lithium-oxide and lanthanum-oxide phase*

The formation of Li-oxide and La-oxide occurs when LLTO is in contact with $Li^0$.[132] According to a mean square displacement (MSD) analysis, the oxygen atoms continue to migrate at the constant positive rate toward the $Li^0$ anode. When applying an external electric field, the formation of both oxides is accelerated (in Figure 2.26).

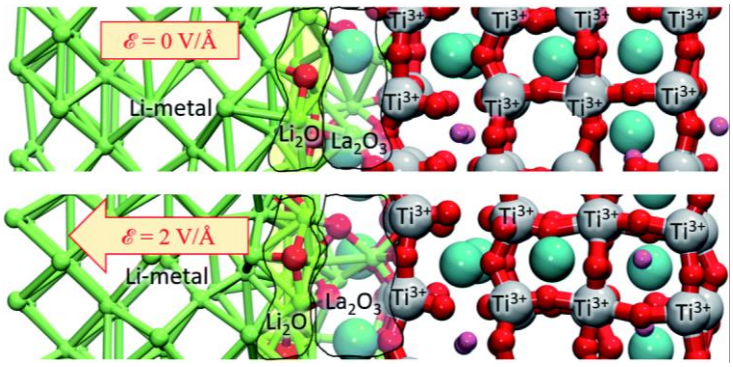


**Figure 2.26.** Structures of both oxides at 10ps (atomic Bader charges) with and without the application of an external electric field (ab initio molecular dynamics study). Image adapted from ref. [132]. Copyright@The Royal Society of Chemistry 2020

### 2.5.5 Fabrication of LLTO SSEs

*Thin-film LLTO*

Fabricating thin-film LBs with a pure LLTO matrix would be effective to enhance ionic conductivity. Batteries with thin-film LLTO electrolytes have large active surface areas and smaller volumes, leading to increase the charge rates by decreasing Li-ion diffusion lengths. However, crystalline thin-film LLTO electrolytes still have high grain boundary resistance and are chemically unstable contacting with $Li^0$. These problems could be effectively resolved by either a substituting an amorphous phase for the crystalline LLTO or adjusting the orientation of LLTO grains.

The structure of amorphous LLTO films is open and disordered. They can be prepared by chemical solution methods (e.g., sol-gel process) or physical vapour deposition techniques (e.g., radio frequency (RF) magnetron sputtering, pulsed laser deposition (PLD), electron-beam (e-beam) evaporation).[112,137,138,139,140,141] By using RF magnetron sputtering, Xiong et al. were able to obtain amorphous LLTO thin films at annealing temperatures below 400 °C.[138]

The orientational growth of LLTO thin films significantly affects the size of the LLTO lattices. Epitaxial growth of LLTO thin films on single crystal substrates can be prepared by e-beam evaporation, resulting in uniform LLTO grains without obvious pinholes or cracks.[142] For example, the epitaxial growth of LLTO thin films on the (100) and (111)-oriented $SrTiO_3$ (STO) substrates

have reduced lattice and thermal strains, which is beneficial to enhance the ionic conductivity and stability.[143]

*Tape-casting LLTO*

Physical vapour deposition methods can produce thin layers, however they are frequently costly or have limited scalability.[144] The commonly used cold-pressed pellets have thickness limitations around 200 μm, while the pellets remain brittle.[145,146] This problem could be solved by implementing the tape-casting technology to cast thin-film electrolytes with a thickness below 200 μm.

Tape casting refers to a slurry casting on a carrier film, has proven successful in producing thin-film electrolytes and layered ceramic structures. The slurry usually consists of ceramics, binders, plasticizers, and dispersants. The green tape is generated by moving the doctor blade with a certain height over the poured slurry. The thickness of tapes could shrink to less than 100 μm at which point sintering will be followed to enhance the densification.[147.148,149]

A high-quality green tape before sintering should meeting certain requirements, including the following: (1) no agglomeration and cracks after evaporating the solvent; (2) microstructural homogeneity; (3) free-standing from the carrier film; and (4) good lamination ability and mechanical strength.[148,149,150]

To prepare satisfactory tape-casting electrolytes, several rules need be considered: (1) control the viscosity the slurry by optimizing the ratio of ceramics, binder, plasticizer, dispersant, and solvent; (2) modify the drying conditions to obtain a flat green tape; and (3) set the proper sintering temperature and duration for removing binder removal and densifying the tapes. Table 4 summarizes green tape preparations and casting/sintering parameters. A ball mill is typically used to a obtain homogeneous slurry. Laminating green tapes in multiple layers prior to sintering could effectively enhance mechanical strength and packing integrity.

**Table 4.** Summary of preparations for green tapes and casting/sintering parameters.

| Preparations for green tapes | Casting parameters | Sintering conditions |
|---|---|---|
| (1) Dissolved dispersant (Zschimmer & Schwarz KM 3014) in ethanol;<br>(2) Added LLTO powder;<br>(3) Mixed plasticizer [1]PEG 400 and binder [2]PVB with solution above[151] | Casting gap = 200 $\mu$m<br>Casting speed = 5 mm $s^{-1}$ | 950 ˚C/1000 ˚C/1050 ˚C/1100 ˚C for 1h in air |
| 30wt.% LLTO<br>30wt.% acetylacetone<br>22wt.% isopropanol<br>9wt.% poly(methyl-methacrylate)<br>2 wt.% dibutyl phthalate<br>2wt.% hallotannin<br>5wt.% PEG 4000[152] | Cast substrate: polished $\alpha$-$Al_2O_3$<br>Cast speed = 0.1 mm $s^{-1}$ | 1000 ˚C-1350 ˚C for 2h in air |
| (1) Mixed LLTO powder into ethanol;<br>(2) Added acrylic resin as a dispersant;<br>(3) Added binder PVB and plasticizer diisononyl phthalate[153] | Casting gap = 50-500 $\mu$m<br>Casting speed = 5 mm $s^{-1}$ | 900 ˚C/1000 ˚C for 1h in air |
| Lack of details[154] | Casting gap = <200 $\mu$m | 1200 ˚C for 12h in air |
| (1) Dissolved [5]PVDF and $LiClO_4$ (at a weight ratio of 6:1) in [6]NMP solvent;<br>(2) Added 15/45/75wt.% LLTO powder into above solution[155] | Casting gap = 50-150 $\mu$m | No sintering process |
| 51.2 wt.% LLTO<br>1.3wt% triethanolamine<br>10.7wt. % PVB<br>6.1wt.% [3]BBP<br>30.7wt.% ethanol[156] | Cast substrate = [4]PET film<br>Casting speed = 10 mm $s^{-1}$ | 500˚C for 2h + 1050˚C for 2h + 1260˚C for 12h in air |

[1]Poly(ethylene glycol), [2]Poly(vinyl butyral), [3]Benzyl butyl phthalate, [4]Poly(ethylene terephthalate), [5]Poly(vinylidene fluoride), [6]1-methyl-2-pyrrolidinone

There are not many reports of thin-film LLTO electrolytes fabrication using tape casting method. A number of factors, such as the dispersant concentration, the particle size of the dispersant, the ratio of binder to plasticizer, the total amount of binder and plasticizer, and the drying conditions, needs to be optimized. Schrökert et al. found a dispersant concentration of dispersant (e.g., 2 wt.%) was optimal to obtain a homogenous slurry.[151] High-quality tapes were produced from a slurry containing 15 wt.% of binder and plasticizer (the binder-plasticizer ratio was set at 2:1) under the fast-drying conditions.

It is important to improve the ionic conductivity of tape-casting LLTO SSEs.[152] Schiffmann et al. casted LLTO tapes and then co-sintered it with LTO anode as shown in Figure 2.27(a) and (b).[153]

LLTO tapes with a thickness of only around 25 μm maximize the ionic conductivity near $10^{-3}$ S $cm^{-1}$ (in Figure 2.27(c)). Employing a lamination process guarantees that during co-sintering, a close and homogeneous interfacial contact between LLTO and LTO.

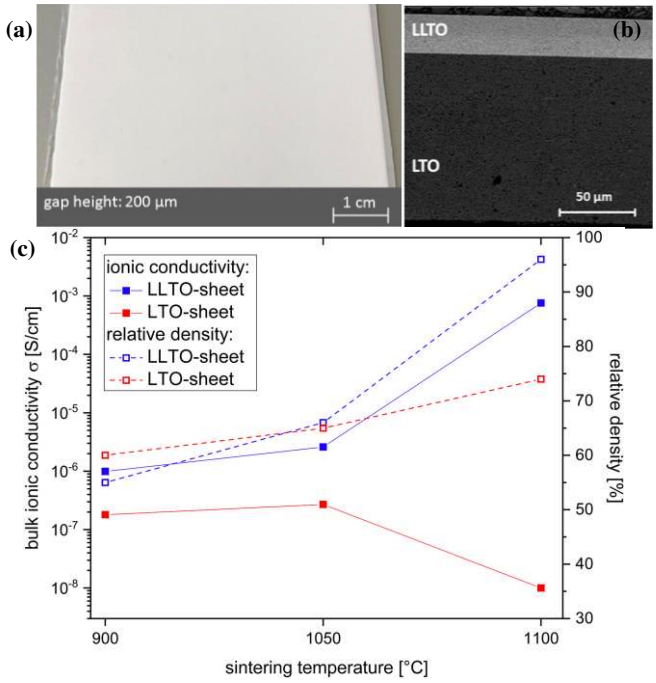


**Figure 2.27.** Schematic images of (a) LLTO green tapes; (b) microstructure of the cross section and interface between LLTO and LTO electrode sintered at 1100 °C for 1h; and (c) plot of the real resistance for sintered LLTO. Imaged adapted from ref. [153]. Copyright@2019 Elsevier B.V.

Jiang et al. fabricated a free-standing tape-casting LLTO film with a reduced thickness of 41 μm (designated as LLTO-41).[156] Figure 2.28 indicates the fabrication of tape-casting approach and related electrochemical performance. Comparing the total Li ionic conductivity to a thick cold-pressed LLTO pellet, the value of LLTO-41 was improved to $2.0\times10^{-5}$ S $cm^{-1}$. The aid of PEO electrolyte coating in the symmetric Li cells could avoid reduction of Ti element and improve the interfacial contact between Li metal and electrolyte. In this way, the total resistance of a symmetrical cell was reduced to about 2250 Ω. Li|LLTO-41|$LiFePO_4$ (LFP) cell was successfully assembled and exhibited stable battery performance at different charge/discharge rates. The initial

discharge capacity of was 145 mAh $g^{-1}$ at current density of 0.1C with a capacity retention of 86.2% after 50 cycles.

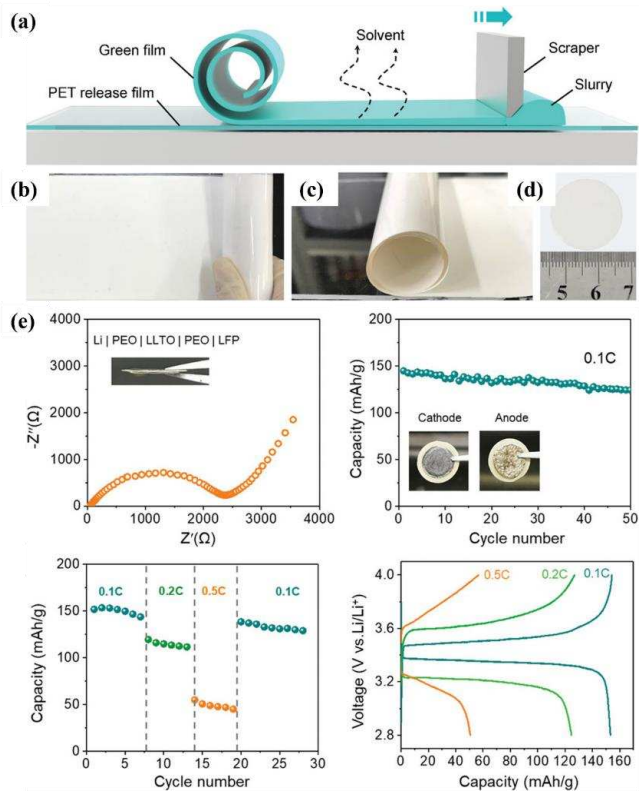


**Figure 2.28.** Schematic images of (a-d) Tape-casting method; and (e) electrochemical performance of Li|LFP cell. Images adapted from ref. [156]. Copyright@2019 John Wiley & Sons, Inc.

## 2.6 Conclusions and perspectives

The formation of stable interphases (e.g., SEI, SLEI, and CEI) in lithium batteries is critical to achieving high-energy density and long cycle life. Based on the progressive understanding of the structural and chemical properties of the different interphases, great progress has been made in designing and fabricating artificial interphases with improved stability. We concluded that more focus should be directed on the following topics to maximize the benefits of the interphases and minimize their negative impacts on battery performance:

1. The need to establish a database that guides the formation of a robust layer of the less-studied interphases (e.g., SLEI and CEI) using advanced characterizations and simulations.

2. Particularly for SSBs, it is imperative to comprehend the dynamics of ionic transport across the interphases.
3. The requirement to rationally adjust the electrolyte components to expand the lifespan of batteries. This is critical for SSBs as they can potentially enhance safety and energy densities in comparison to commercial LIBs with flammable electrolytes.

The interfacial challenges in SSBs seriously impact battery performance and hamper their commercialization. Solid-liquid hybrid electrolytes display great potential for solving the inferior physical/electrochemical contacts between electrodes and mass-producing SSEs through wet-chemistry routes. Despite the merits of this strategy, rationally designing a chemically stable and less resistive solid-liquid electrolyte interphase (SLEI) is a crucial future step. However, no previous critical review has been accessed for SLEI, though, thus additional efforts are urgently needed on hybrid electrolyte optimization. Some perspectives on this are provided below.

1. LE addition optimization: The proper quantity of LE is needed to wet the interface adequately. Furthermore, it is crucial to minimize the liquid content that remains after decomposition. It would be challenging to precisely quantify the residual liquid content after cycling when disassembling the cell.
2. A deep understanding of the SLEI: To sustain battery cycling efficiency, the formed SLEI should have low resistivity and excellent stability. However, with the addition of a complex LE (e.g., a liquid system with multiple additives), it is difficult to probe and understand the SLEI evolution during cycling.
3. Careful evaluation of battery safety and durability: Safety is a concern when using the hybrid solid-state electrolyte interfacial approach in SSBs, even when a tiny amount of liquid addition is added. Therefore, comprehensive monitoring of battery safety assisted with theoretical modeling is required to demonstrate and/or enhance the battery reliability.

After reviewing the issues of interface and interphases, SSEs (e.g., LLTO) still have face numerous obstacles to be overcome at different levels, including material design and synthesis with required properties, processing, and a stable performance in SSBs.

1. At the material level: SSEs suffered from high grain boundary resistance that limits total ionic conductivity. Several approaches have been adopted to address this issue such as microstructural engineering of grains or introducing amorphous phase into grain boundary, which have been found to decrease grain boundary resistance and thus enhance total conductivity. Another strategy is to fabricate amorphous or single crystalline films. Additionally, a variety of methods have been followed to improve total ionic conductivities of crystalline SSEs:
    a) Doping: dopants such as Sr, Y, Nb, etc. could modify the crystal structure of LLTO and increase the ionic conductivity over $10^{-4}$ S $cm^{-1}$ at room temperature.
    b) Nano-structuring: we have reviewed that implementing well-aligned 1D SSE materials in nanoscale morphology can facilitate Li-ion migration. Based on this idea, fabricating 3D vertically aligned channels in all-ceramic SSEs may be effective in attaining high ionic conductivity without the usage of flammable polymeric components as the matrix.
2. Fabrication and mass processing of all-ceramic SSBs: Tape casting technology is very compatible with existing roll-to-roll battery manufacturing processes; a lot of research is focused on its application in SSBs to make thin films (thickness is less than 100 μm). Optimization of the slurry recipe and sintering conditions is essential to obtain a good quality of final tapes. However, it is still challenging to fabricate large-scale tape-casting films for SSBs.
3. Li loss during sintering: thin films always need to be sintered at high temperatures (e.g., >1000 ˚C) to be further densified. To counteract undesired Li loss (Li evaporates

apparently over 900˚C) in all-ceramic SSEs, researchers typically surround green tapes with the mother powder during sintering to reduce any further Li losses from electrolytes, but Li sublimation still occurs. Introducing low melting point phases (also called sintering aids) could be acceptable for processing electrolytes with improved sinterability and density.

4. Capability with Li-metal anodes. Battery assembly and manufacturing based on all-ceramic SSEs is another important consideration for high energy-density SSBs. The following issues need to be addressed:
    a) Compatibility with Li metal: For instance, the poor contact between Li metal and LLTO SSEs. Li metal reacts easily with $Ti^{4+}$ cations inside LLTO. Thus, it is essential to modify the surface of LLTO SSEs. Some researchers have employed protective layers including metal or metal oxides or polymers for LLZO SSEs. Moreover, the addition of LEs could be one compromising way to improve interfacial contact.
    b) Mechanical strength and stacking pressure: The brittleness of all-ceramic thin films makes battery assembly challenging. A proper stacking pressure needs to be applied that could maintain good contact among layers but cause no damage to SSEs. Applying buffer layers during the assembly (e.g., Ni-coated sponge) may help to prevent SSEs from cracking and fracture.

Finally, ceramic-based oxides are promising SSEs materials with a potential use in SSEs. However, like all other prospective materials (e.g., phosphates, sulfides, and halides), it has many drawbacks that currently hamper their practical development in SSBs. Nevertheless, intensive research into innovative strategies to overcome these challenges can lead to its adoption into high-energy SSBs.

## 2.7 References


1. Pervez, S. A.; Cambaz, M. A.; Thangadurai, V.; Fichtner, M. Interface in Solid-state Lithium Battery: Challenges, Orogress, and outlook. *ACS applied materials & interfaces*. **2019**, *11*, 22029-22050.
2. Houache, M.S.; Yim, C.H.; Karkar, Z.; Abu-Lebdeh, Y. On the Current and Future Outlook of Battery Chemistries for Electric Vehicles—Mini Review. *Batteries*. **2022**, *8*, 70.
3. Dunn, B.; Kamath, H.; Tarascon, J.M. Electrical energy storage for the grid: a battery of choices. *Science*. **2011**, *334*, 928-935.
4. Dey, A. N.; Sullivan, B. P. The Electrochemical Decomposition of Propylene Carbonate on Graphite. *Journal of The Electrochemical Society*. **1970**, *117*, 222.
5. Peled, E. The Electrochemical Behavior of Alkali and Alkaline Earth Metals in Nonaqueous Battery Systems—the Solid Electrolyte Interphase Model. *Journal of The Electrochemical Society*. **1979**, *126*, 2047.
6. Goodenough, J. B.; Kim, Y. Challenges for Rechargeable Li Batteries. *Chemistry of materials*. **2010**, *22*, 587-603.
7. Heiskanen, S.K.; Kim, J.; Lucht, B.L. Generation and Evolution of the Solid Electrolyte Interphase of Lithium-ion Batteries. *Joule*. **2019**, *3*, 2322-2333.
8. Frenck, L.; Sethi, G. K.; Maslyn, J. A.; Balsara, N. P. Factors that control the formation of dendrites and other morphologies on lithium metal anodes. *Frontiers in Energy Research*. **2019**, *7*, 115.
9. Gu, Y.; Wang, W. W.; Li, Y. J.; Wu, Q. H.; Tang, S.; Yan, J. W.; Zheng, M.S.; Wu, D.Y.; Fan, C.H.; Hu, W.Q.; Mao, B. W. Designable Ultra-smooth Ultra-thin Solid-electrolyte Interphases of Three Alkali Metal Anodes. *Nature communications*. **2018**, *9*, 1-9.
10. Lin, D.; Liu, Y.; Cui, Y. Reviving the Lithium Metal Anode for High-energy Batteries. *Nature nanotechnology*. **2017**, *12*, 194-206.

11. Wang, L.; Zhou, Z.; Yan, X.; Hou, F.; Wen, L.; Luo, W.; Liang, J.; Dou, S.X. Engineering of Lithium-metal Anodes towards A Safe and Stable Battery. *Energy Storage Materials*. **2018**, *14*, 22-48.
12. Kang, D.; Sardar, S.; Zhang, R.; Noam, H.; Chen, J.; Ma, L.; Liang, W.; Shi, C.; Lemmon, J.P. In-situ Organic SEI Layer for Dendrite-free Lithium Metal Anode. *Energy Storage Materials*. **2020**, *27*, 69-77.
13. Liu, J.; Liu, T.; Pu, Y.; Guan, M.; Tang, Z.; Ding, F.; Xu, Z.; Li, Y. Facile Synthesis of NASICON-type Li 1.3 Al 0.3 Ti 1.7 (PO 4) 3 Solid Electrolyte and its Application for Enhanced Cyclic Performance in Lithium ion Batteries through the Introduction of An Artificial Li 3 PO 4 SEI layer. *RSC Advances*. **2017**, *7*, 46545-46552.
14. Gao, Y.; Yan, Z.; Gray, J.L.; He, X.; Wang, D.; Chen, T.; Huang, Q.; Li, Y.C.; Wang, H.; Kim, S.H.; Mallouk, T.E. Polymer–inorganic Solid–electrolyte Interphase for Stable Lithium Metal Batteries under Lean Electrolyte Conditions. *Nature materials*. **2019**, *18*, 384-389.
15. Liu, S.; Ji, X.; Piao, N.; Chen, J.; Eidson, N.; Xu, J.; Wang, P.; Chen, L.; Zhang, J.; Deng, T.;Hou, S. An Inorganic-rich Solid Electrolyte Interphase for Advanced Lithium-metal Batteries in Carbonate Electrolytes. *Angewandte Chemie International Edition*. **2021**, *60*, 3661-3671.
16. Hou, G.; Ma, X.; Sun, Q.; Ai, Q.; Xu, X.; Chen, L.; Li, D.; Chen, J.; Zhong, H.; Li, Y.; Xu, Z. Lithium Dendrite Suppression and Enhanced Interfacial Compatibility Enabled by an Ex Situ SEI on Li Anode for LAGP-based All-solid-state Batteries. *ACS applied materials & interfaces*. **2018**, *10*, 18610-18618.
17. Yi, J.; Zhou, D.; Liang, Y.; Liu, H.; Ni, H.; Fan, L. Z. Enabling High-performance All-solid-state Lithium Batteries with High Ionic Conductive Sulfide-based Composite Solid Electrolyte and Ex-situ Artificial SEI Film. *Journal of Energy Chemistry*. **2021**, *58*, 17-24.

18. Duncan, H.; Abu-Lebdeh, Y.; Davidson, I.J. Study of the Cathode–electrolyte Interface of LiMn1. 5Ni0. 5O4 Synthesized by A Sol–gel Method for Li-ion Batteries. *Journal of the Electrochemical Society*. **2010**, *157*, A528.
19. Thomas, M. G. S. R.; Bruce, P. G.; Goodenough, J. B. Lithium Mobility in the Layered Oxide Li1− xCoO2. *Solid State Ionics*. **1985**, *17*, 13-19.
20. Xu, J. Critical Review on Cathode–electrolyte Interphase toward High-Voltage Cathodes for Li-Ion Batteries. *Nano-Micro Letters*. **2022**, *14*, 1-22.
21. Zhang, Z.; Yang, J.; Huang, W.; Wang, H.; Zhou, W.; Li, Y.; Li, Y.; Xu, J.; Huang, W.; Chiu, W.; Cui, Y. Cathode-electrolyte Interphase in Lithium Batteries Revealed by Cryogenic Electron Microscopy. *Matter*. **2021**, *4*, 302-312.
22. Baek, S. W.; Honma, I., Kim, J.; Rangappa, D. Solidified Inorganic-organic Hybrid Electrolyte for All Solid State Flexible Lithium Battery. *Journal of Power Sources*. **2017**, *343*, 22-29.
23. Sun, C.; Liu, J.; Gong, Y.; Wilkinson, D.P.; Zhang, J. Recent Advances in All-solid-state Rechargeable Lithium Batteries. *Nano Energy*. **2017**, *33*, 363-386.
24. Lotsch, B. V.; Maier, J. Relevance of solid electrolytes for lithium-based batteries: A realistic view. *Journal of Electroceramics*. **2017**, *38*, 128-141.
25. Liu, S.; Ji, X.; Piao, N.; Chen, J.; Eidson, N.; Xu, J.; Wang, P.; Chen, L.; Zhang, J.; Deng, T.; Hou, S. An Inorganic-rich Solid Electrolyte Interphase for Advanced Lithium-metal Batteries in Carbonate Electrolytes. *Angewandte Chemie International Edition*. **2021**, *60*, 3661-3671.
26. Zheng, F.; Kotobuki, M.; Song, S.; Lai, M.O.; Lu, L. Review on Solid Electrolytes for All-solid-state Lithium-ion Batteries. *Journal of Power Sources*. **2018**, *389*, 198-213.

27. Raju, M. M.; Altayran, F.; Johnson, M.; Wang, D.; Zhang, Q. Crystal Structure and Preparation of Li7La3Zr2O12 (LLZO) Solid-State Electrolyte and Doping Impacts on the Conductivity: An Overview. *Electrochem*. **2021**, *2*, 390-414.
28. Tsai, C. L.; Yu, S.; Tempel, H.; Kungl, H.; Eichel, R. A. All-ceramic Li Batteries based on Garnet Structured Li7La3Zr2O12. *Materials Technology*. **2020**, *35*, 656-674.
29. Shin, D.O.; Oh, K.; Kim, K.M.; Park, K.Y.; Lee, B.; Lee, Y.G.; Kang, K. Synergistic Multi-doping Effects on the Li7La3Zr2O12 Solid Electrolyte for Fast Lithium ion Conduction. *Scientific reports*. **2015**, *5*, 1-9.
30. Yan, S.; Yim, C.H.; Pankov, V.; Bauer, M.; Baranova, E.; Weck, A.; Merati, A.; Abu-Lebdeh, Y. Perovskite Solid-State Electrolytes for Lithium Metal Batteries. *Batteries*. **2021**, *7*, 75.
31. Inaguma, Y.; Liquan, C.; Itoh, M.; Nakamura, T.; Uchida, T.; Ikuta, H.; Wakihara, M. High Ionic Conductivity in Lithium Lanthanum Titanate. *Solid State Communications*. **1993**, *86*, 689-693.
32. Sun, Y.; Guan, P.; Liu, Y.; Xu, H.; Li, S.; Chu, D. Recent Progress in Lithium Lanthanum Titanate Electrolyte towards All Solid-state Lithium ion Secondary Battery. *Solid State and Materials Sciences*. **2019**, *44*, 265-282.
33. Bi, Z.; Guo, X. Solidification for Solid-state Lithium Batteries with High Energy Density and Long Cycle Life. *Energy Mater*. **2022**, *2*, 200011.
34. Busche, M. R.; Drossel, T.; Leichtweiss, T., Weber, D. A.; Falk, M.; Schneider, M.; Reich, M-L.; Sommer, H.; Adelhelm, P.; Janek, J. Dynamic Formation of A Solid-liquid Electrolyte Interphase and its Consequences for Hybrid-battery Concepts. *Nature chemistry*. **2016**, *8*, 426-434.

35. Xu, B.; Duan, H.; Liu, H.; Wang, C. A.; Zhong, S. Stabilization of Garnet/liquid Electrolyte Interface Using Superbase Additives for Hybrid Li Batteries. *ACS Applied Materials & Interfaces*. **2017**, *9*, 21077-21082.

36. Schleutker, M.; Bahner, J.; Tsai, C. L.; Stolten, D.;Korte, C. On the Interfacial Charge Transfer between Solid and Liquid Li+ Electrolytes. *Physical Chemistry Chemical Physics*. **2017**, *19*, 26596-26605.

37. Wang, C.; Sun, Q.; Liu, Y.; Zhao, Y.; Li, X.; Lin, X.; Banis, M.N.; Li, M.; Li, W.; Adair, K.R.; Wang, D. Boosting the Performance of Lithium Batteries with Solid-liquid Hybrid Electrolytes: Interfacial Properties and Effects of Liquid Electrolytes. *Nano Energy*. **2018,** *48*, 35-43.

38. Philip, M. A.; Sullivan, P. T.; Zhang, R.; Wooley, G. A.; Kohn, S. A.; Gewirth, A. A. Improving Cell Resistance and Cycle Life with Solvate-coated Thiophosphate Solid Electrolytes in Lithium Batteries. *ACS Applied Materials & Interfaces*. **2018**, *11*, 2014-2021.

39. Weiss, M.; Seidlhofer, B.K.; Geiß, M.; Geis, C.; Busche, M.R.; Becker, M.; Vargas-Barbosa, N.M.; Silvi, L.; Zeier, W.G.; Schröder, D.; Janek, J. Unraveling the Formation Mechanism of Solid–Liquid Electrolyte Interphases on LiPON Thin Films. *ACS applied materials & interfaces*. **2019**, *11*, 9539-9547.

40. Fan, B.; Xu, Y.; Ma, R.; Luo, Z.; Wang, F.; Zhang, X.; Ma, H.; Fan, P.; Xue, B.; Han, W. Will Sulfide Electrolytes be Suitable Candidates for Constructing a Stable Solid/Liquid Electrolyte Interface?. *ACS Applied Materials & Interfaces*. **2020**, *12*, 52845-52856.

41. Fan, B.; Li, W.; Luo, Z.; Zhang, X.; Ma, H.; Fan, P.; Xue, B. Stabilizing Interface between Li2S–P2S5 Glass-Ceramic Electrolyte and Ether Electrolyte by Tuning Solvation Reaction. *ACS Applied Materials & Interfaces*. **2021**, *14*, 933-942.

42. Li, X.; Cong, L.; Ma, S.; Shi, S.; Li, Y.; Li, S.; Chen, S.; Zheng, C.; Sun, L.; Liu, Y.; Xie, H. Low Resistance and High Stable Solid–liquid Electrolyte Interphases Enable High-voltage Solid-state Lithium Metal Batteries. *Advanced Functional Materials*. **2021**, *31*, 2010611.
43. Tang, J.; Wang, L.; You, L.; Chen, X.; Huang, T.; Zhou, L.; Geng, Z.; Yu, A. Effect of Organic Electrolyte on the Performance of Solid Electrolyte for Solid–liquid Hybrid Lithium Batteries. *ACS Applied Materials & Interfaces*. **2021**, *13*, 2685-2693.
44. Vivek, J. P.; Meddings, N.; Garcia-Araez, N. Negating the Interfacial Resistance between Solid and Liquid Electrolytes for Next-Generation Lithium Batteries. *ACS Applied Materials & Interfaces*. **2021**, *14*, 633-646.
45. Leng, J.; Wang, H.; Li, Y.; Xiao, Z.; Wang, S.; Zhang, Z.; Tang, Z. Insight into the Solid-liquid Electrolyte Interphase between Li6. 4La3Zr1. 4Ta0. 6O12 and LiPF6-based Liquid Electrolyte. *Applied Surface Science*. **2022**, *575*, 151638.
46. Huang, L.; Fu, H.; Duan, J.; Wang, T.; Zheng, X.; Huang, Y.; Zhao, T.; Yu, Q.; Wen, J.; Chen, Y.; Sun, D. Negating Li+ Transfer Barrier at Solid-liquid Electrolyte Interface in Hybrid Batteries. *Chem*. **2022**, *8*, 1928-1943.
47. Yan, S.; Abouali, S.; Yim, C.H.; Zhou, J.; Wang, J.; Baranova, E.A.; Weck, A.; Thangadurai, V.; Merati, A.; Abu-Lebdeh, Y. Revealing the Role of Liquid Electrolytes in Cycling of Garnet-Based Solid-State Lithium-Metal Batteries. *The Journal of Physical Chemistry C*. **2022**, *126*, 14027-14035.
48. Busche, M.R.; Weiss, M.; Leichtweiss, T.; Fiedler, C.; Drossel, T.; Geiss, M.; Kronenberger, A.; Weber, D.A.; Janek, J. The Formation of the Solid/Liquid Electrolyte Interphase (SLEI) on NASICON-Type Glass Ceramics and LiPON. *Advanced Materials Interfaces*. **2020**, *7*, 2000380.

49. Kim, T.; Son, D. Y.; Ono, L. K.; Jiang, Y.; Qi, Y. A Solid–liquid Hybrid Electrolyte for Lithium Ion Batteries enabled by A Single-body Polymer/indium Tin Oxide Architecture. *Journal of Physics D: Applied Physics*. **2021**, *54*, 475501.

50. Denholm, P.; Kulcinski, G. L. Life cycle energy requirements and greenhouse gas emissions from large scale energy storage systems. *Energy Conversion and Management*. **2004**, *45*, 2153-2172.

51. Goodenough, J. B.; Kim, Y. Challenges for rechargeable Li batteries. *Chemistry of materials*. **2010**, *22*, 587-603.

52. Goodenough, J. B.; Park, K. S. The Li-ion rechargeable battery: a perspective. *Journal of the American Chemical Society*. **2013,** *135*, 1167-1176.

53. Larcher, D.; Tarascon, J. M. Towards greener and more sustainable batteries for electrical energy storage. *Nature Chemistry*. **2015**, *7*, 19-29.

54. Liang, Y.; Su, J.; Xi, B.; Yu, Y.; Ji, D.; Sun, Y.; Cui, C.; Zhu, J. Life cycle assessment of lithium-ion batteries for greenhouse gas emissions. *Resources, conservation and recycling*. **2017**, *117*, 285-293.

55. Liu, J.; Bao, Z.,; Cui, Y.; Dufek, E. J.; Goodenough, J. B.; Khalifah, P.; Li, Q.; Liaw, B.Y.; Liu, P.; Manthiram, A.; Zhang, J. G. Pathways for practical high-energy long-cycling lithium metal batteries. *Nature Energy*. **2019**, *4*, 180-186.

56. Dehghani-Sanij, A. R.; Tharumalingam, E.; Dusseault, M. B.; Fraser, R. Study of energy storage systems and envi-ronmental challenges of batteries. *Renewable and Sustainable Energy Reviews*. **2019**, *104*, 192-208.

57. Yang, Z.; Zhang, J.; Kintner-Meyer, M. C.; Lu, X.; Choi, D.; Lemmon, J. P.; Liu, J. Electrochemical energy storage for green grid. *Chemical reviews*. **2011**, *111*, 3577-3613.

58. Ciez, R. E.; Whitacre, J. F. Examining different recycling processes for lithium-ion batteries. *Nature Sustainability*. **2019**, *2*, 148-156.

59. Ellingsen, L. A. W.; Hung, C. R.; Strømman, A. H. Identifying key assumptions and differences in life cycle as-sessment studies of lithium-ion traction batteries with focus on greenhouse gas emissions. *Transportation Research Part D: Transport and Environment*. **2017**, *55*, 82-90.

60. Nishi, Y. Lithium ion secondary batteries; past 10 years and the future. *Journal of Power Sources*. **2001**, *100*, 101-106.

61. Tariq, M.; Masood, A. I.; Gajanayake, C. J.; Gupta, A. K. Aircraft batteries: current trend towards more electric air-craft. *IET Electrical Systems in Transportation*. **2016**, *7*, 93-103.

62. Lee, J. W.; Anguchamy, Y. K.; Popov, B. N. Simulation of charge–discharge cycling of lithium-ion batteries under low-earth-orbit conditions. *Journal of Power Sources*. **2006**, *162*, 1395-1400.

63. Ratnakumar, B. V.; Smart, M. C.; Kindler, A.; Frank, H.; Ewell, R.; Surampudi, S. Lithium batteries for aerospace applications: 2003 Mars Exploration Rover. *Journal of power sources*. **2003**, *119*, 906-910.

64. Tarascon, J. M.; Armand, M. Issues and challenges facing rechargeable lithium batteries. *Nature*. **2011**, *414*, 359-267.

65. Scrosati, B.; Garche, J. Lithium batteries: Status, prospects and future. Journal of power sources. **2010**, *195*, 2419-2430.

66. Quartarone, E.; Mustarelli, P. Electrolytes for solid-state lithium rechargeable batteries: recent advances and per-spectives. *Chemical Society Review*s. **2011**, *40*, 2525-2540.

67. Chen, S.; Wen, K.; Fan, J.; Bando, Y.; Golberg, D. Progress and future prospects of high-voltage and high-safety electrolytes in advanced lithium batteries: from liquid to solid electrolytes. *Journal of Materials Chemistry A*. **2018**, *6*, 11631-11663.

68. Zhang, H.; Zhao, H.; Khan, M. A.; Zou, W.; Xu, J.; Zhang, L.; Zhang, J. Recent progress in advanced electrode materials, separators and electrolytes for lithium batteries. *Journal of Materials Chemistry A*. **2018**, *6*, 20564-20620.

69. Ozdemir, U.; Aktas, Y. O.; Vuruskan, A.; Dereli, Y.; Tarhan, A. F.; Demirbag, K.; Erdem, A.; Kalaycioglu, G.D.; Ozkol, I.; Inalhan, G. Design of a commercial hybrid VTOL UAV system. *Journal of Intelligent & Robotic Systems*. **2014**, *74*, 371-393.

70. Sun, Y.; Guan, P.; Liu, Y.; Xu, H.; Li, S.; Chu, D. Recent Progress in Lithium Lanthanum Titanate Electrolyte towards All Solid-State Lithium Ion Secondary Battery. *Critical Reviews in Solid State and Materials Sciences*. **2019**, *44*, 265-282.

71. Sun, C.; Liu, J.; Gong, Y.; Wilkinson, D. P.; Zhang, J. Recent advances in all-solid-state rechargeable lithium batteries. Nano Energy. **2017**, *33*, 363-386.

72. Mauger, A.; Julien, C. M.; Paolella, A.; Armand, M.; Zaghib, K. Building better batteries in the solid state: a re-view. *Materials*. **2019**, *12*, 3892.

73. DRIVE, U. Electrochemical Energy Storage Technical Team Roadmap (September 2017).

74. Lv, F.; Wang, Z.; Shi, L.; Zhu, J.; Edström, K.; Mindemark, J.; Yuan, S. Challenges and development of composite solid-state electrolytes for high-performance lithium ion batteries. *Journal of Power Sources*. **2019**, *441*, 227175.

75. Guan, X.; Wu, Q.; Zhang, X.; Guo, X.; Li, C.; Xu, J. In-situ crosslinked single ion gel polymer electrolyte with superior performances for lithium metal batteries. *Chemical Engineering Journal*. **2020**, *382*, 122935.

76. Tan, S.; Walus, S.; Hilborn, J.; Gustafsson, T.; Brandell, D. Poly (ether amine) and cross-linked poly (propylene oxide) diacrylate thin-film polymer electrolyte for 3D-microbatteries. *Electrochemistry Communications*. **2010**, *12*, 1498-1500.

77. Scheers, J.; Fantini, S.; Johansson, P. A review of electrolytes for lithium–sulphur batteries. *Journal of Power Sources*. **2014**, *255*, 204-218.

78. Mindemark, J.; Lacey, M. J.; Bowden, T.; Brandell, D. Beyond PEO—Alternative host materials for Li+-conducting solid polymer electrolytes. *Progress in Polymer Science*. **2018**, *81*, 114-143.

79. Stepniak, I.; Andrzejewka, E.; Dembna, A.; Galinski, M. Characterization and application of N-methyl-N-propylpiperidinium bis (trifluoromethanesulfonyl) imide ionic liquid–based gel polymer electrolyte prepared in situ by photopolymerization method in lithium ion batteries. *Electrochimica Acta*. **2014**, *121*, 27-33.

80. Röchow, E. T.; Coeler, M.; Pospiech, D.; Kobsch, O.; Mechtaeva, E.; Vogel, R.; Voit, B.; Nikolowski, K.; Wolter, M. In Situ Preparation of Crosslinked Polymer Electrolytes for Lithium Ion Batteries: A Comparison of Monomer Sys-tems. *Polymers*. **2020**, *12*, 1707.

81. Ma, C.; Cui, W.; Liu, X.; Ding, Y.; Wang, Y. In situ preparation of gel polymer electrolyte for lithium batteries: Progress and perspectives. *InfoMat*. **2022**, *4*, e12232.

82. Zaghib, K.; Zhu, W.; Kaboli, S.; Demers, H.; Trudeau, M.; Paolella, A.; Guerfi, A.; Julien, C.M.; Mauger, A.; Armand, M.; Goodenough, J. B. In Operando and in Situ techniques for Intercalation Compounds in Li-Ion and All-Solid-State Batteries. *ECS Meeting Abstracts*. **2020**, *1*, 16.

83. Mindemark, J.; Sun, B.; Törmä, E.; Brandell, D. High-performance solid polymer electrolytes for lithium batteries operational at ambient temperature. *Journal of Power Sources*. **2015**, *298*, 166-170.

84. Wu, H.; Yu, G.; Pan, L.; Liu, N.; McDowell, M. T.; Bao, Z.; Cui, Y. Stable Li-ion battery anodes by in-situ polymeri-zation of conducting hydrogel to conformally coat silicon nanoparticles. *Nature communications*. **2013**, *4*, 1-6.

85. Li, S.; Zhang, S. Q.; Shen, L.; Liu, Q.; Ma, J. B.; Lv, W.; He, Y.B.; Yang, Q. H. Progress and perspective of ceramic/polymer composite solid electrolytes for lithium batteries. *Advanced Science*. **2020**, *7*, 1903088.

86. Yao, P.; Yu, H.; Ding, Z.; Liu, Y.; Lu, J.; Lavorgna, M.; Wu, J.; Liu, X. Review on polymer-based composite electrolytes for lithium batteries. *Frontiers in chemistry*. **2019**, *7*, 522.

87. Cao, C.; Li, Z. B.; Wang, X. L.; Zhao, X. B.; Han, W. Q. Recent advances in inorganic solid electrolytes for lithium batteries. *Frontiers in Energy Research*. **2014**, *2*, 25.

88. Yu, X.; Manthiram, A. A review of composite polymer-ceramic electrolytes for lithium batteries. *Energy Storage Materials.* **2021**, *34*, 282-300.

89. Chen, L.; Li, Y.; Li, S. P.; Fan, L. Z.; Nan, C. W.; Goodenough, J. B. PEO/garnet composite electrolytes for solid-state lithium batteries: From "ceramic-in-polymer" to "polymer-in-ceramic". *Nano Energy*. **2018**, *46*, 176-184.

90. Falco, M.; Castro, L.; Nair, J. R.; Bella, F.; Bardé, F.; Meligrana, G.; Gerbaldi, C. UV-cross-linked composite polymer electrolyte for high-rate, ambient temperature lithium batteries. *ACS Applied Energy Materials*. **2019**, *2*, 1600-1607.

91. Falco, M.; Simari, C.; Ferrara, C.; Nair, J. R.; Meligrana, G.; Bella, F.; Nicotera, I.; Mustarelli, P.; Winter, M.; Gerbaldi, C. Understanding the effect of UV-induced cross-linking on the physicochemical properties of highly performing PEO/LiTFSI-based polymer electrolytes. *Langmuir*. **2019**, *35*, 8210-8219.

92. Shin, J. H.; Henderson, W. A.; Passerini, S. PEO-based polymer electrolytes with ionic liquids and their use in lithium metal-polymer electrolyte batteries. *Journal of the Electrochemical Society*. **2005**, *152*, A978.

93. Kim, G. T.; Appetecchi, G. B.; Carewska, M.; Joost, M.; Balducci, A.; Winter, M.; Passerini, S. UV cross-linked, lith-ium-conducting ternary polymer electrolytes containing ionic liquids. *Journal of Power Sources*. **2010**, *195*, 6130-6137.

94. Bi, J.; Mu, D.; Wu, B.; Fu, J.; Yang, H.; Mu, G.; Zhang, L.; Wu, F. 2020. A hybrid solid electrolyte Li0.33La0.557TiO3/poly (acylonitrile) membrane infiltrated with a

succinonitrile-based electrolyte for solid state lithium-ion batteries. *Journal of Materials Chemistry A*. **2020**, *8*, 706-713.

95. Al-Salih, H.; Huang, A.; Yim, C. H.; Freytag, A. I.; Goward, G. R.; Baranova, E.; Abu-Lebdeh, Y. A Polymer-Rich Quaternary Composite Solid Electrolyte for Lithium Batteries. *Journal of The Electrochemical Society*. **2020**, *167*, 070557.
96. Yan, C.; Zhu, P.; Jia, H.; Zhu, J.; Selvan, R. K.; Li, Y.; Dong, X.; Du, Z.; Angunawela, l.; Wu, N.; Dirican, M. High-Performance 3-D Fiber Network Composite Electrolyte Enabled with Li-Ion Conducting Nanofibers and Amorphous PEO-Based Cross-Linked Polymer for Ambient All-Solid-State Lithium-Metal Batteries. *Advanced Fiber Materials*. **2019**, *1*, 46-60.
97. Li, B.; Su, Q.; Yu, L.; Wang, D.; Ding, S.; Zhang, M.; Du, G.; Xu, B. Li0. 35La0. 55TiO3 Nanofibers Enhanced Poly (vi-nylidene fluoride)-Based Composite Polymer Electrolytes for All-Solid-State Batteries. *ACS Applied Materials & Interfaces*. **2019**, *11*, 42206-42213.
98. Liu, K.; Wu, M.; Wei, L.; Lin, Y.; Zhao, T. A composite solid electrolyte with a framework of vertically aligned perovskite for all-solid-state Li-metal batteries. *Journal of Membrane Science.* **2020**, *610*, 118265.
99. Liu, K.; Zhang, R.; Sun, J.; Wu, M.; Zhao, T. Polyoxyethylene (PEO)|PEO–Perovskite| PEO Composite Electrolyte for All-Solid-State Lithium Metal Batteries. *ACS Applied Materials & Interfaces*. **2019**, *11*, 46930-46937.
100. Zhu, L.; Zhu, P.; Fang, Q.; Jing, M.; Shen, X.; Yang, L. 2018. A novel solid PEO/LLTO-nanowires polymer composite electrolyte for solid-state lithium-ion battery. *Electrochimica Acta*. **2018**, *292*, 718-726.
101. Zhu, L.; Zhu, P.; Yao, S.; Shen, X.; Tu, F. High-performance solid PEO/PC/LLTO-nanowires polymer composite electrolyte for solid-state lithium battery. *International Journal of Energy Research*. **2019**, *43*, 4854-4866.

102. He, K. Q.; Zha, J. W.; Du, P.; Cheng, S. H. S.; Liu, C.; Dang, Z. M.; Li, R. K. Tailored high cycling performance in a solid polymer electrolyte with perovskite-type Li0.33La0.557TiO3 nanofibers for all-solid-state lithium-ion batteries. *Dalton Transactions*. **2019**, *48*, 3263-3269.

103. Ding, C.; Fu, X.; Li, H.; Yang, J.; Lan, J. L.; Yu, Y.; Zhong, W.H.; Yang, X. An Ultrarobust Composite Gel Electrolyte Stabilizing Ion Deposition for Long-Life Lithium Metal Batteries. *Advanced Functional Materials*. **2019**, *29*, 1904547.

104. Li, R.; Liao, K.; Zhou, W.; Li, X.; Meng, D.; Cai, R.; Shao, Z. Realizing fourfold enhancement in conductivity of perovskite Li0. 33La0. 557TiO3 electrolyte membrane via a Sr and Ta co-doping strategy. *Journal of Membrane Science*. **2019**, *582*, 194-202.

105. Inaguma, Y.; Liquan, C.; Itoh, M.; Nakamura, T.; Uchida, T.; Ikuta, H.; Wakihara, M. High ionic conductivity in lithium lanthanum titanate. *Solid State Communications*. **1993**, *86*, 689-693.

106. Meesala, Y.; Jena, A.; Chang, H.; Liu, R. S. Recent advancements in Li-ion conductors for all-solid-state Li-ion batteries. *ACS Energy Letters*. **2017**, *2*, 2734-2751.

107. Chen, C. H.; Amine, K. Ionic conductivity, lithium insertion and extraction of lanthanum lithium titanate. *Solid State Ionics*. **2001**, *144*, 51-57.

108. Deng, D. Li-ion batteries: basics, progress, and challenges. *Energy Science & Engineering*. **2015**, *3*, 385-418.

109. Kokal, I. **2012**. Solid State Electrolytes for All Solid State 3D Lithium ion Batteries (Doctoral dissertation, Ph. D. Thesis, Eindhoven University of Technology, Eindhoven).

110. Inaguma, Y.; Itoh, M. Influences of carrier concentration and site percolation on lithium ion conductivity in perovskite-type oxides. *Solid State Ionics*. **1996**, *86*, 257-260.

111. Kim, S.; Hirayama, M.; Cho, W.; Kim, K.; Kobayashi, T.; Kaneko, R.; Suzuki K. Kanno, R. Low temperature synthesis and ionic conductivity of the epitaxial Li0.17La0.61TiO3 film electrolyte. *CrystEngComm*. **2014**, *16*, 1044-1049.

112. Abhilash, K. P.; Sivaraj, P.; Selvin, P. C.; Nalini, B.; Somasundaram, K. Investigation on spin coated LLTO thin film nano-electrolytes for rechargeable lithium ion batteries. *Ceramics International*. **2015**, *41*, 13823-13829.

113. Geng, H. X.; Mei, A.; Dong, C.; Lin, Y. H.; Nan, C. W. Investigation of structure and electrical properties of Li0.5La0.5TiO3 ceramics via microwave sintering. *Journal of alloys and compounds*. **2009**, *481*, 555-558.

114. Jiang, Y.; Huang, Y.; Zhou, Y.; Zhu, X. Enhancement of ionic conductivity in Li0.5La0.5TiO3 with Ag nanoparticles. *Journal of Materials Science*. **2020**, *55*, 3750-3759.

115. Mei, A.; Wang, X. L.; Lan, J. L.; Feng, Y. C.; Geng, H. X.; Lin, Y. H.; Nan, C. W. Role of amorphous boundary layer in enhancing ionic conductivity of lithium–lanthanum–titanate electrolyte. *Electrochimica acta*. **2010**, *55*, 2958-2963.

116. Zhang, S.; Zhao, H.; Guo, J.; Du, Z.; Wang, J.; Świerczek, K. Characterization of Sr-doped lithium lanthanum titanate with improved transport properties. *Solid State Ionics*. **2019**, *336*, 39-46.

117. Lee, S. J.; Bae, J. J.; Son, J. T. Structural and Electrical Effects of Y-doped Li0.33La0.56−xYxTiO3 Solid Electrolytes on All-Solid-State Lithium-Ion Batteries. *Journal of the Korean Physical Society*. **2019**, *74*, 73-77.

118. Jiang, Y.; Huang, Y.; Hu, Z.; Zhou, Y.; Zhu, J.; Zhu, X. Effects of B-site ion (Nb5+) substitution on the microstructure and ionic conductivity of Li0.5La0.5TiO3 solid electrolytes. *Ferroelectrics*. **2020**, *554*, 89-96.

119. Liu, W.; Liu, N.; Sun, J.; Hsu, P. C.; Li, Y.; Lee, H. W.; Cui, Y. Ionic conductivity enhancement of polymer electrolytes with ceramic nanowire fillers. *Nano letters*. **2015**, *15*, 2740-2745.

120. Zhu, P.; Yan, C.; Dirican, M.; Zhu, J.; Zang, J.; Selvan, R. K.; Chuang, C.C.; Jia, H.; Li, Y.; Kiyak, Y.; Wu, N. 2018. Li0.33La0.557TiO3 ceramic nanofiber-enhanced polyethylene oxide-based composite polymer electrolytes for all-solid-state lithium batteries. *Journal of Materials Chemistry A*. **2018**, *6*, 4279-4285.

121. Liu, W.; Lin, D.; Sun, J.; Zhou, G.; Cui, Y. Improved lithium ionic conductivity in composite polymer electrolytes with oxide-ion conducting nanowires. *ACS nano*. **2016**, *10*, 11407-11413.

122. Ma, C.; Chen, K.; Liang, C.; Nan, C. W.; Ishikawa, R.; More, K.; Chi, M. Atomic-scale origin of the large grain-boundary resistance in perovskite Li-ion-conducting solid electrolytes. *Energy & Environmental Science*. **2014**, *7*, 1638-1642.

123. Sasano, S.; Ishikawa, R.; Kawahara, K.; Kimura, T.; Ikuhara, Y. H.; Shibata, N.; Ikuhara, Y. 2020. Grain boundary Li-ion conductivity in (Li0.33La0.56)TiO3 polycrystal. *Applied Physics Letters*. **2020**, *116*, 043901.

124. Moriwake, H.; Gao, X.; Kuwabara, A.; Fisher, C. A.; Kimura, T.; Ikuhara, Y. H.; Kohama, K.; Tojigamori, T.; Ikuhara, Y. Domain boundaries and their influence on Li migration in solid-state electrolyte (La, Li)TiO3. *Journal of Power Sources*. **2015**, *276*, 203-207.

125. Takatori, K.; Kadoura, H.; Matsuo, H.; Tani, T. Microstructural analyses and improved ionic conductivity of La0.62Li0.16TiO3 ceramics prepared by a reactive-templated grain growth (RTGG) process. *Journal of the European Ceramic Society*. **2019**, *39*, 384-388.

126. Mei, A.; Wang, X. L.; Feng, Y. C.; Zhao, S. J.; Li, G. J.; Geng, H. X.; Lin, Y. H; Nan, C. W. Enhanced ionic transport in lithium lanthanum titanium oxide solid state electrolyte by introducing silica. *Solid State Ionics*. **2008**, *179*, 2255-2259.

127. Leyet, Y.; Guerrero, F.; Anglada-Rivera, J.; Martinez, I.; Amorin, H.; Romaguera-Barcelay, Y.; Poyato, R.; Gallardo-Lopez, A. Obtention of Li3xLa2/3−xTiO3 ceramics from amorphous nanopowders by spark plasma sintering. *Ferroelectrics*. **2016**, *498*, 62-66.

128. Kali, R.; Mukhopadhyay, A. Spark plasma sintered/synthesized dense and nanostructured materials for solid-state Li-ion batteries: Overview and perspective. *Journal of Power Sources*. **2014**, *247*, 920-931.

129. Luo, J.; Zhong, S.; Huang, Z.; Huang, B.; Wang, C. A. High Li+-conductive perovskite Li3/8Sr7/16Ta3/4Zr1/4O3 electrolyte prepared by hot-pressing for all-solid-state Li-ion batteries. *Solid State Ionics*. **2019**, *338*, 1-4.

130. Mei, A.; Jiang, Q. H.; Lin, Y. H.; Nan, C. W. Lithium lanthanum titanium oxide solid-state electrolyte by spark plasma sintering. *Journal of alloys and compounds*. **2009**, *486*, 871-875.

131. Liu, S.; Zhao, Y.; Li, X.; Yu, J.; Yan, J.; Ding, B. Solid-State Lithium Metal Batteries with Extended Cycling Enabled by Dynamic Adaptive Solid-State Interfaces. *Advanced Materials*. **2021**, *33*, 2008084.

132. Galvez-Aranda, D. E.; Seminario, J. M. Solid electrolyte interphase formation between the Li0.29La0.57TiO3 solid-state electrolyte and a Li-metal anode: an ab initio molecular dynamics study. *RSC Advances*. **2020**, *10*, 9000-9015.

133. Wenzel, S.; Leichtweiss, T.; Krüger, D.; Sann, J.; Janek, J. Interphase formation on lithium solid electrolytes—An in situ approach to study interfacial reactions by photoelectron spectroscopy. *Solid State Ionics*. **2015**, *278*, 98-105.

134. Wang, C.; Gong, Y.; Liu, B.; Fu, K.; Yao, Y.; Hitz, E.; Li, Y.; Dai. J.; Xu, S.; Luo, W.; Hu, L. 2017. Conformal, nanoscale ZnO surface modification of garnet-based solid-state electrolyte for lithium metal anodes. *Nano letters*. **2017**, *17*, 565-571.

135. Han, X.; Gong, Y.; Fu, K. K.; He, X.; Hitz, G. T.; Dai, J.; Pearse, A.; Liu, B.; Wang, H.; Rubloff, G.; Hu, L. Negating interfacial impedance in garnet-based solid-state Li metal batteries. *Nature materials*. **2017**, *16*, 572-579.

136. Fu, K. K.; Gong, Y.; Liu, B.; Zhu, Y.; Xu, S.; Yao, Y.; Luo, W.; Wang, C.; Lacey, S.D.; Dai, J.; Hu, L. Toward garnet electrolyte–based Li metal batteries: An ultrathin, highly effective, artificial solid-state electrolyte/metallic Li interface. *Science Advances*. **2017**, *3*, 1601659.

137. Zheng, Z.; Fang, H.; Yang, F.; Liu, Z.K.; Wang, Y. Amorphous LiLaTiO3 as solid electrolyte material. *Journal of The Electrochemical Society*. **2014**, *161*, A473-A479.

138. Xiong, Y.; Tao, H.; Zhao, J.; Cheng, H.; Zhao, X. Effects of annealing temperature on structure and opt-electric properties of ion-conducting LLTO thin films prepared by RF magnetron sputtering. *Journal of Alloys and Compounds*. **2011**, *509*, 1910-1914.

139. Ahn, J. K.; Yoon, S. G. Characteristics of perovskite (Li0.5La0.5)TiO3 solid electrolyte thin films grown by pulsed laser deposition for rechargeable lithium microbattery. *Electrochimica acta.* **2004**, *50*, 371-374.

140. Ohnishi, T.; Takada, K. Synthesis and orientation control of Li-ion conducting epitaxial Li0.33La0.56TiO3 solid electrolyte thin films by pulsed laser deposition. *Solid State Ionics*. **2012**, *228*, 80-82.

141. Dinh, N. N.; Long, P. D. Characteristics of lithium lanthanium titanate thin films made by electron beam evaporation from nanostructured La0.67-xLi3xTiO3 target. *ASEAN Journal on Science and Technology for Development*. **2008**, *25*, 243-250.

142. Li, C. L.; Zhang, B.; Fu, Z. W. Physical and electrochemical characterization of amorphous lithium lanthanum titanate solid electrolyte thin-film fabricated by e-beam evaporation. *Thin solid films*. **2006**, *515*, 1886-1892.

143. Zheng, Z.; Zhang, Y.; Song, S.; Wang, Y. Sol–gel-processed amorphous inorganic lithium ion electrolyte thin films: sol chemistry. *RSC advances*. **2017**, *7*, 30160-30165.

144. Schröckert, F.; Schiffmann, N.; Bucharsky, E. C.; Schell, K. G.; Hoffmann, M. J. Tape casted thin films of solid electrolyte Lithium-Lanthanum-Titanate. *Solid State Ionics.* **2018**, *328*, 25-29.

145. Gao, K.; He, M.; Li, Y.; Zhang, Y.; Gao, J.; Li, X.; Cui, Z.; Zhan, Z.; Zhang, T. Preparation of high-density garnet thin sheet electrolytes for all-solid-state Li-Metal batteries by tape-casting technique. *Journal of Alloys and Compounds*. **2019**, *791*, 923-928.

146. Chen, F.; Yang, D.; Zha, W.; Zhu, B.; Zhang, Y.; Li, J.; Gu. Y.; Shen, Q.; Zhang, L.; Sadoway, D. R. Solid polymer electrolytes incorporating cubic Li7La3Zr2O12 for all-solid-state lithium rechargeable batteries. *Electrochimica Act*a. **2017**, *258*, 1106-1114.

147. Jonson, R. A.; McGinn, P. J. Tape casting and sintering of Li7La3Zr1.75Nb0.25Al0.1O12 with Li3BO3 additions. *Solid State Ionics*. **2018**, *323*, 49-55.

148. Hotza, D.; Greil, P. Aqueous tape casting of ceramic powders. Materials Science and Engineering: A. **1995**, *202*, 206-217.

149. Nishihora, R. K.; Rachadel, P. L.; Quadri, M. G. N.; Hotza, D. Manufacturing porous ceramic materials by tape casting—A review. *Journal of the European Ceramic Society*. **2018**, *38*, 988-1001.

150. Liu, Z.; Wang, Y.; Li, Y. Combinatorial study of ceramic tape-casting slurries. *ACS combinatorial science*. **2012**, *14*, 205-210.

151. Schröckert, F.; Schiffmann, N.; Bucharsky, E. C.; Schell, K. G.; Hoffmann, M. J. Tape casted thin films of solid electrolyte Lithium-Lanthanum-Titanate. Solid State Ionics, **2018**, *328*, 25-29.

152. Jiménez, R.; Del Campo, A.; Calzada, M. L.; Sanz, J.; Kobylianska, S. D.; Solopan, S. O.; Belous, A. G. Lithium La0. 57Li0. 33TiO3 perovskite and Li1.3Al0.3Ti1.7(PO4)3(Li-

NASICON) supported thick films electrolytes prepared by tape casting meth-od. *Journal of The Electrochemical Society*. **2016**, *163*, A1653.

153. Schiffmann, N.; Schröckert, F.; Bucharsky, E. C.; Schell, K. G.; Hoffmann, M. J. Development and characterization of half-cells based on thin solid state ionic conductors for Li-ion batteries. *Solid State Ionics*. **2019**, *333*, 66-71.
154. Zhang, H.; Liu, X.; Qi, Y.; Liu, V. On the La2/3−xLi3xTiO3/Al2O3 composite solid-electrolyte for Li-ion conduction. *Journal of Alloys and Compounds*. **2013**, *577*, 57-63.
155. Li, B.; Su, Q.; Yu, L.; Dong, S.; Zhang, M.; Ding, S.; Du, G.; Xu, B. Ultrathin, flexible, and sandwiched structure composite polymer electrolyte membrane for solid-state lithium batteries. *Journal of Membrane Science*. **2021**, *618*, 118734.
156. Jiang, Z.; Wang, S.; Chen, X.; Yang, W.; Yao, X.; Hu, X.; Han, Q.; Wang, H. Tape-Casting Li0.34La0.56TiO3 Ceramic Electrolyte Films Permit High Energy Density of Lithium-Metal Batteries. *Advanced Materials*. **2020**, *32*, 1906221.

# Chapter 3

# Experiments and characterizations

## 3.1 Experimental approach

### 3.1.1 SSEs preparation

In this study, we used two approaches (uniaxial cold-pressing and isostatic cold-pressing) to fabricate SSE pellets. The first step for both approaches is to press powder into non-sintered electrolytes (also called green pellets). The second step is to identify the optimal temperature to sinter the green pellets. A proper sintering temperature is beneficial to fabricate crystalline SSEs with a dense microstructure. For instance, the green LLTO pellets were sintered at different temperatures (960 ˚C, 1050 ˚C, and 1170 ˚C) for 12h in air. Extra powder of LLTO was placed at the surface of the pellet during sintering to compensate for Li loss (Li will evaporate after 900 ˚C). The sintering process enhances the densification of LLTO pellets and thus improves the total ionic conductivity. In Figure 3.1, uniaxial cold-pressing needs a high pressure (200 MPa is used in this study) to obtain voids-free SSEs. On the other hand, isostatic cold-pressing can reach a higher density with a lower pressure (<100 MPa).

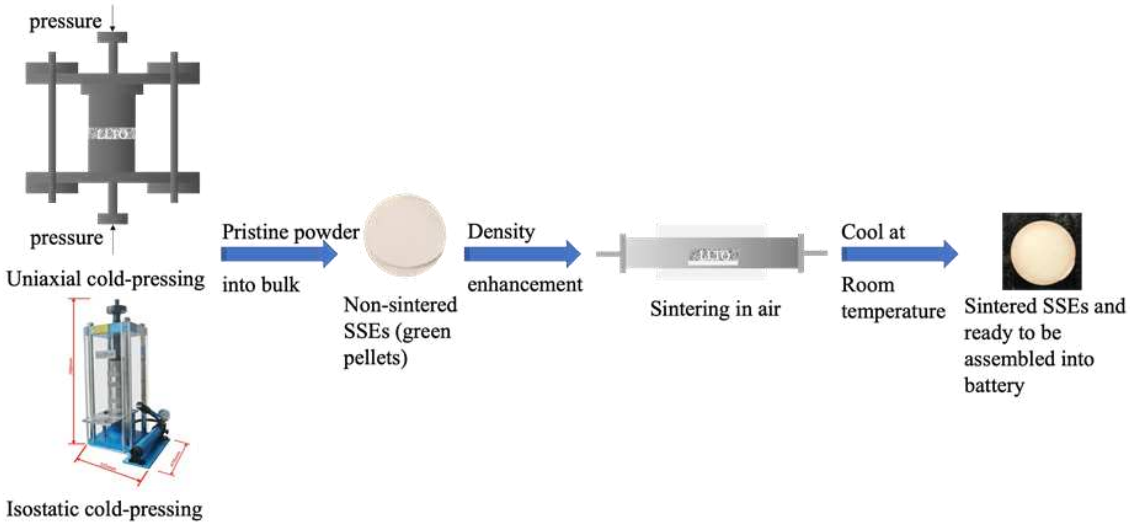


**Figure 3.1.** LLTO preparation via two types of cold-pressing followed by sintering.

### 3.1.2 Electrodes preparation

Lithium metal ($Li^0$) foil has the highest theoretical capacity (3860 mAh $g^{-1}$) among metals and thus was used as the anode in this study. Commercial $Li^0$ foils with different thicknesses (e.g., 25 $\mu$m and 250 $\mu$m) supplied from MTI Corp. were stored inside an Argon-filled glovebox to avoid oxidation and were then cut into discs (portable manual punching cutter supplied from MTI Corp., 10 mm in diameter) for battery assembly.

Lithium iron phosphate ($LiFePO_4$, LFP) is the representative cathode material. Its specific capacity (around 170 mAh $g^{-1}$) is higher than that of the related lithium cobalt oxide (around 140 mAh $g^{-1}$). Because of its low cost, low toxicity, and long-term stability, it was used for this study. A commercial cathode sheet (83 $\mu$m in thickness) was cut into discs (portable manual punching cutter supplied from MTI Corp., 12 mm in diameter) for battery assembly.

### 3.1.3 Battery assembly

*Symmetric Li cell*

A symmetric Li cell was assembled in a 2325-type coin cell (the diameter is 23 mm and the height is 2.5 mm). 2325-type coin cells contain stainless steel caps and cans that seal the battery. A spring and a stainless-steel spacer were used to increase the stacking pressure among layers. LLTO sandwiched by $Li^0$ foils was assembled in the middle, as shown in Figure 3.2. The symmetric cell was used to study the chemical stability of LLTO against $Li^0$. All assemblies were done inside an Argon-filled glovebox.

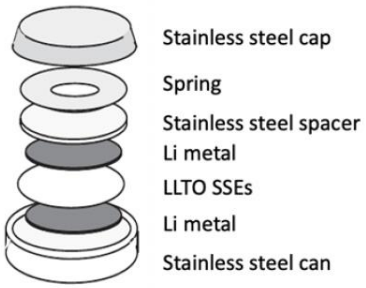

**Figure 3.2.** Schematic of a symmetric Li cell design.

*Battery cell*

A battery cell design as shown in Figure 3.3 consists of a $Li^0$ anode, SSE, and a cathode (e.g., $LiFePO_4$, LFP), and was used to investigate the battery charge/discharge performance. All layers were assembled in a 2325-type coin cell in an Argon-filled glovebox.

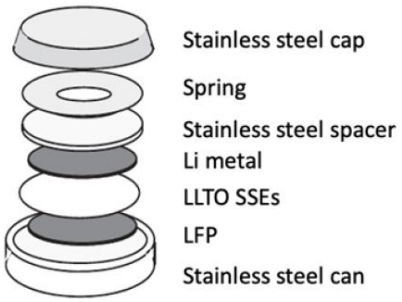


**Figure 3.3.** Schematic of a battery cell design.

## 3.2 Materials characterization

*X-ray diffraction*

The technique of X-ray diffraction (XRD) is used to determine the structure of a crystal. A beam of incident X-rays irradiates the sample and is subsequently diffracted in many directions by the crystalline structure.[1]

*X-ray photoelectron spectroscopy*

Photoelectron spectroscopy is based on the external photoelectric effect, where illumination of a sample with photons of defined energy larger than the ionization energy causes electrons to be emitted from the sample.[1] The method is known as X-ray photoelectron spectroscopy (XPS) when X-ray is used as excitation source. The detection depth of XPS is around 20 Å, only several atomic layers on the surface of the material. The *ex situ* XPS is commonly used to detect the chemical and electronic properties of interfaces in SSBs. In this study, XPS peaks were fitted using CasaXPS

software (version 2.3.25) with Shirley BG and all spectra were calibrated with respect to C 1s (at 285.0 eV).

### 3.2.1 Interphase characterization

*Scanning transmission X-ray microscopy and X-ray absorption spectroscopy*

Scanning transmission X-ray microscopy (STXM) is a type of soft X-ray synchrotron-based spectromicroscopy. The ambient-STXM facility used in this study is available on beamline:10ID-spectromicroscopy at the Canadian Light Source. STXM is highly adaptive with X-ray absorption spectroscopy (XAS) to determine the two-dimensional/three-dimensional local chemical and morphological structure in bulk/surface with a spatial resolution of ~30 nm in the conventional mode and ~10 nm in the ptychography-mode (the set-up components are illustrated in Figure 3.4).[2,3] Dry and wet samples can both be measured in a helium environment or in vacuum from rough to ~$10^{-6}$ Torr.

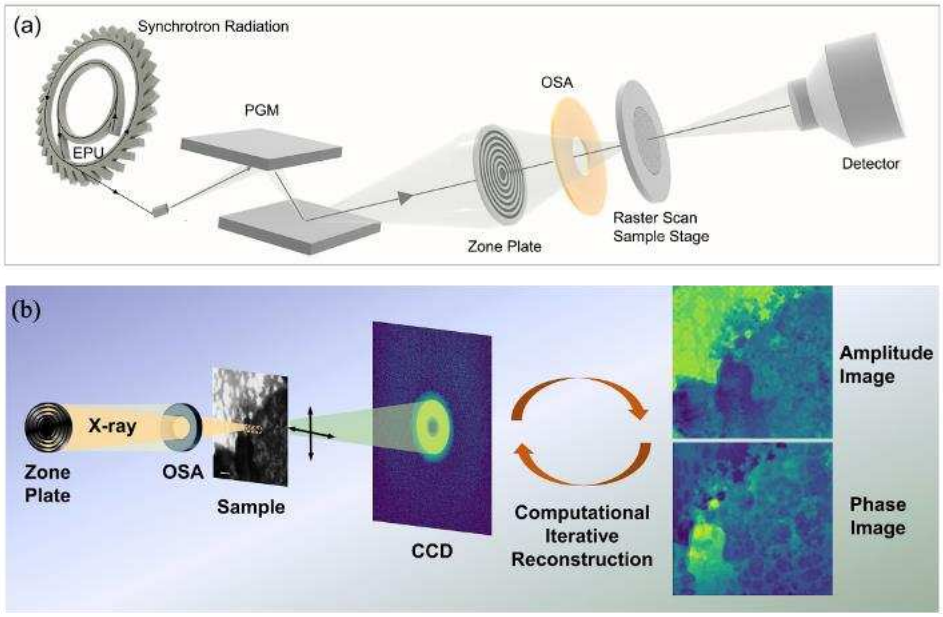


**Figure 3.4.** Schematic of (a) conventional-mode and (b) ptychography-mode STXM with the data reconstruction method. Image adapted form ref. [3].

## 3.3 Electrochemical characterization

*Electrochemical impedance spectroscopy*

Electrochemical impedance spectroscopy (EIS) analysis is a technique that measures resistance by monitoring the current response while an alternating voltage is applied to an electrochemical cell. Two-electrode electrochemical cells with SSEs are usually modeled with the equivalent circuit shown in Figure 3.5. The electrical circuit is described using the Nyquist plot obtained from (Solartron, SI 1260) with a frequency ranging from 1 MHz to 0.01 Hz and an amplitude of 50 mV. For low values of test frequency, the dominant effect is ion diffusion and the plot produced is essentially a straight line with a slope of 45˚. At high frequencies, where the diffusion time constant is much longer than the single period, the plot is described by a semi-circle with its diameter given by the charge transfer resistance $R_{ct}$. $R_s$ is considered as the bulk resistance of SSEs. The bulk ionic conductivity of SSEs was calculated following the formula $\sigma = L/R_sS$, where R is the impedance for the fitted results in Nyquist plots, L is the ceramic thickness, and S is the effective contact area between the electrolyte and electrodes.[4]

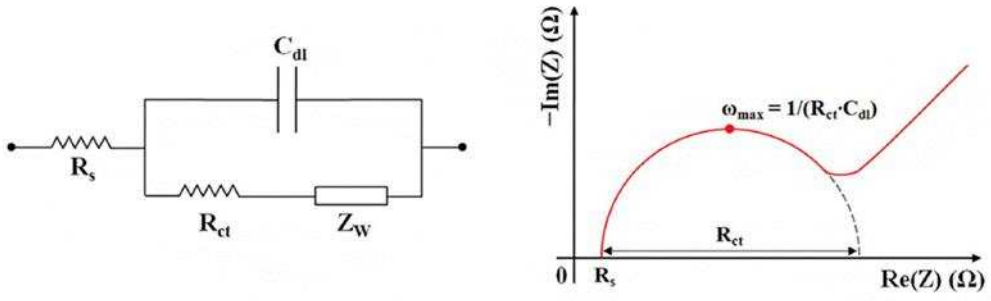


**Figure 3.5.** EIS equivalent circuit (left) and Nyquist plot (right). Image adapted form ref. [4].

*Galvanostatic charge/discharge*

One common way to characterize the performance of lithium batteries (e.g., battery lifetime, long-term stability, etc.) is to measure the amount of charge stored and delivered during charge and discharge. The galvanostatic test is conducted during various cycles at different current rates to measure the amount of charge stored and delivered during charge and discharge. During the

galvanostatic cycling of batteries, the charge and discharge currents are expressed as a C-rate, calculated from the battery's nominal capacity (the battery's capacity can be fully charged). For example, 1C means complete charging or discharging the battery in one hour.

## 3.4 References


1. Li, Y.; Gao, Z.; Hu, F.; Lin, X.; Wei, Y.; Peng, J.; Yang, J.; Li, Z.; Huang, Y.; Ding, H. Advanced characterization techniques for interface in all-solid-state batteries. *Small Methods*. **2020**, *4*, 2000111.
2. Zhou, J.; Wang, J. Applications of Soft X-ray Spectromicroscopy in Energy Research from Materials to Batteries. *Advanced X-ray Imaging of Electrochemical Energy Materials and Devices*. **2021**, 141-178.
3. Wang, J.; Li, J. H. Scanning transmission x-ray microscopy at the Canadian Light Source: Progress and selected applications in geosciences. *At. Spectrosc*. **2022**, *43*, 84-98.
4. Grossi, M.; Riccò, B. Electrical impedance spectroscopy (EIS) for biological analysis and food characterization: A review. *Journal of sensors and sensor systems*. **2017**, *6*, 303-325.

# Chapter 4

# Engineered interfaces between perovskite $La_{2/3x}Li_{3x}TiO_3$ electrolyte and Li metal for solid-state batteries

This chapter has been adapted from a research paper published in *Frontiers in Chemistry* (doi: 10.3389/fchem.2022.966274).

## 4.1 Abstract

Perovskite $La_{2/3x}Li_{3x}TiO_3$ (LLTO) materials are promising solid-state electrolytes for lithium metal batteries (LMBs) due to their intrinsic fire-resistance, high bulk ionic conductivity, and wide electrochemical window. However, their commercialization is hampered by high interfacial resistance, dendrite formation, and instability against Li metal. To address these challenges, we first prepared highly dense LLTO pellets with enhanced microstructure and high bulk ionic conductivity of $2.1\times10^{-4}$ S $cm^{-1}$ at room temperature. Then, the LLTO pellets were coated with three polymer-based interfacial layers, including pure (polyethylene oxide) (PEO), dry polymer electrolyte of PEO-LITFSI (lithium bis(trifluoromethanesulfonyl)imide) (PL), and gel PEO-LiTFSI-SN (succinonitrile) (PLS). It is found that each layer has impacted the interface differently; the soft PLS gel layer significantly reduced the total resistance of LLTO to a low value of 84.88 ohm $cm^{-2}$. Interestingly, PLS layer has shown excellent ionic conductivity but performs inferior in symmetric Li cells. On the other hand, the PL layer significantly reduces lithium nucleation overpotential and shows a stable voltage profile after 20 cycles without any sign of Li dendrite formation. This work demonstrates that LLTO electrolytes with denser microstructure could reduce the interfacial resistance and when combined with polymeric interfaces show improved chemical stability against Li metal.

## 4.2 Introduction

Solid-state lithium metal batteries (LMBs) using lithium (Li) metal as anode chemistry are promising alternative energy sources with improved safety and increased energy densities.[1,2,3,4,5] Solid-state electrolytes (SSEs) permit reliable safety for LMBs due to their non-flammable, solid feature, and the wider electrochemical window (>5 V vs $Li/Li^+$).[6]

Among reported solid-state electrolyte (SSE) materials, perovskite-type ($ABO_3$) LLTO exhibits high bulk ionic conductivity, good stability in a dry or humid atmosphere and a wide operating temperature range.[6,7,8,9] However, the low sinterability (interpreted as a long period of sintering at a high temperature over 1000 ˚C) leads to significant Li loss, further resulting in a decreased lower total ionic conductivity. Simply modifying the sintering conditions risks reducing the density of electrolytes. To maintain good sinterability and density, scholars typically add additional Li (e.g., excess of pristine powders and low-melting points salts during solid-state processing).[10,11,12] However, the produced second phase may increase the grain boundary resistance.

In addition, the resistive and inhomogeneous interfacial contact against Li metal results in high interfacial resistance in the range of $10^2$ ohm $cm^{-2}$ to $10^3$ ohm $cm^{-2}$.[13,14,15] High interfacial resistance due to poor contact results in a large overpotential during the charge and discharge cycling process. Various strategies of surface treatments on ceramic electrolytes have been investigated to improve the interfacial contact. Table 5 presents selected interfaces on ceramic electrolytes and performance in symmetric Li cells.

**Table 5.** Summary of selected interfaces on ceramic electrolytes and performance in symmetric lithium cells.

| **Interface** | **Ceramic SSEs** | **Interface resistance (ohm $cm^{-2}$)** | **Stable potential (mV)** |
|---|---|---|---|
| **Gold (Au)[16]** | Ta-doped $Li_7La_3Zr_2O_{12}$ | Reduced from 1500 to 380 | ~22 at 0.5 mA $cm^{-2}$ |

| | | | |
|---|---|---|---|
| **20nm germanium (Ge)[17]** | $Li_{6.85}La_{2.9}Ca_{0.1}Zr_{1.75}Nb_{0.25}O_{12}$ | Reduced from 900 to 115 | ~25 at 0.05 mA $cm^{-2}$ |
| **$Al_2O_3$[18]** | $Li_7La_{2.75}Ca_{0.25}Zr_{1.75}Nb_{0.25}O_{12}$ | Reduced from 1710 to 1 | 22 at 0.2 mA $cm^{-2}$ |
| **ZnO[19]** | $Li_{6.75}La_{2.75}Ca_{0.25}Zr_{1.75}Nb_{0.75}O_{12}$ | 20 | 6.5 at 0.1 mA $cm^{-2}$ |
| **Graphite[20]** | $Li_{5.9}Al_{0.2}La_3Zr_{1.75}W_{0.25}O_{12}$ | Reduced from 1350 to 105 | 6 at 50 $\mu$A $cm^{-2}$ |
| **PEO[21]** | $Li_{0.34}La_{0.56}TiO_3$ | 549 | 100 at 0.1 mA $cm^{-2}$ |
| **PEO/LiTFSI (O/Li mole ratio of 8:1)[22]** | $Li_{6.4}La_2Zr_{1.4}Ta_{0.6}O_{12}$ | Data is no available | 50 at 0.1 mA $cm^{-2}$ |
| **Cross-linked poly(ethylene glycol) methyl ether acrylate-LiTFSI-$Al_2O_3$[23]** | $Li_{1.3}Al_{0.3}Ti_{1.7}(PO_4)_3$ | Data is not available | 500 |
| **PAN/10 wt.% $LiClO_4$[24]** | Li-ion-conducting glass ceramic | Data is not available | 150 at 0.3 $\mu$A $cm^{-2}$ |
| **PVDF-HFP[25]** | $Li_7La_{2.75}Ca_{0.25}Zr_{1.75}Nb_{0.25}O_{12}$ | Reduced from 1400 to 214 | 125 at 125 $\mu$A $cm^{-2}$ |
| **PLS gel membrane (this work)** | $La_{0.57}Li_{0.29}TiO_3$ | Reduced to 84.88 for pellet | 7.25 at 0.04 mA $cm^{-2}$ |

One approach is to introduce another metallic layer between the Li metal and ceramic electrolytes such as Au, Ge, etc.[16,17] Alternatively, Fu et al. applied an aluminum metal coating on garnet and reduced the interfacial resistance by more than one order of magnitude.[13] A metallic layer tends to alloy with Li metal, which could improve the wettability of ceramic SSEs though they are still solid and hence, cannot ensure impeccable interfacial contact. To further enhance the contact against electrodes, metal oxides consisting of $Al_2O_3$, ZnO, and graphite are widely used to modify the surface of electrolytes.[18,19,20] Han et al. deposited atomic-layer of $Al_2O_3$ on garnet electrolyte, allowing the interfacial resistance to be reduced to only 1 ohm $cm^{-2}$.[18] However, the above-mentioned metal oxides are generally deposited by complicated and expensive methods. The resistance between hard ceramic grains within the electrolyte is still large. Compared with metal or

metal oxides, utilizing soft polymers (e.g., poly(ethylene oxide) (PEO), poly(acrylonitrile) (PAN), poly(vinylidene fluoride) (PVDF), etc.) as interfacial layers increases ionic conductivity and enhances the contact among neighboring grains by filling the voids and grain boundary regions.[26,27] Specifically, PEO has been widely used for composite electrolytes to provide flexibility but suffers low room temperature conductivity (e.g., $10^{-6}$-$10^{-8}$ S $cm^{-1}$) partly due to its high degree of crystallinity below its melting point (~60 ˚C). The addition of Li salts such as lithium bis(trifluoromethanesulfonyl)imide (LiTFSI), tends to reduce PEO crystallinity and enhance conductivity by facilitating lithium-ion transport. Al-Salih et al. published on polymer-rich electrolytes (e.g., the mass ratio of PEO:LiTFSI is 70%:30%) with ionic conductivity of over $10^{-3}$ S $cm^{-1}$ at 55 ˚C.[28] As an effective ionizer, succinonitrile's (SN) high dielectric nature can separate Li ions from LiTFSI and further boost ionic conductivity. Observed room temperature ionic conductivity could reach the magnitude of $10^{-3}$ S $cm^{-1}$ by optimizing the mass ratio to 35% PEO:30% LiTFSI:35% SN.[29] They have also shown successful cycling in oxide-based cathodes up to 4.1 V (vs. $Li/Li^+$) compared to the conventional, phosphate-based cathode limited by PEO stability above 3.7 V (vs. $Li/Li^+$).

To date, only a few articles have proposed microstructural and interfacial modifications to perovskite-based electrolytes. The main problem with perovskite-based electrolytes is that $Ti^{4+}$ cation is chemically unstable in the presence of Li-metal anode, and thus it is essential to introduce protective layers to avoid direct contact. Jiang et al. applied PEO films between LLTO and electrodes in a cell of Li|PEO|LLTO|PEO|$LiFePO_4$ (LFP) that exhibited good electrochemical performance. The initial discharge capacity reached 145 mAh $g^{-1}$ at a current density of 0.1C and capacity retention was 86.2% after 50 cycles.[21]

In this work, we have first prepared dense LLTO electrolyte materials with improved microstructure and high bulk ionic conductivity by mixing and optimizing the weight ratios between granular and milled LLTO powders at different sintering temperatures. We have then

identified optimal interfacial layers of PEO-based gel membranes for LLTO electrolytes, including 100 wt.% PEO (P), 70 wt.% PEO/30 wt.% LiTFSI (PL), and 35 wt.% PEO/30 wt.% LiTFSI/35 wt.% SN (PLS). The optimal interfacial layer for LLTO is expected to provide efficient protection against Li metal and reserve good ionic conductivity. Electrochemical Impedance spectroscopy was performed to evaluate the conductivity of pristine and coated LLTO pellets. Symmetric Li cells and Ohm's law were used to explore and analyze the possible mechanism of coated LLTO electrolytes for the improved stability with Li metal.

## 4.3 Materials and methods

### 4.3.1 Electrolyte fabrication

Pristine $La_{0.57}Li_{0.29}TiO_3$ (TOHO TITANIUM, Co., Ltd.) powders including granular (G-LLTO, D50 = 50 μm) and milled (M-LLTO, D50 = 1 μm) type were stored under inert conditions in an argon-filled glovebox. To prepare mixed LLTO powders, G-LLTO and M-LLTO powders with an optimized weight ratio of 70:30 was dispersed in 2-propanol to acquire a homogenous suspension. After vigorous stirring at 2000 rpm for 30 mins (THINKY mixer), the mixture was dried in a 70 ˚C oven overnight to remove the solvent.

The LLTO powder was then uniaxially cold-pressed followed by sintering at high temperature. The mixed powder was molded in a stainless-steel die (15.6 mm in diameter) and then pressed with a pressure of 200 MPa for 4 mins. The cold-pressed pellet was fully covered with mother powder (e.g., 5 wt.% with respect to the total weight of cold-pressed pellet) and then was sintered at 1170 ˚C for 12 h in air. The mother powder was added to compensate for any lithium loss (or evaporation of lithium compounds such as lithium oxides) at the high-temperature sintering process. The heating and cooling rate were 10 ˚C/min and 2 ˚C/min, respectively. The sintered electrolyte was cut into about 0.7 mm thick slices (the minimum thickness to keep the cut-off pellets complete) by a low-speed diamond saw (MTI Co., Ltd) and then stored in an argon-filled glovebox.

### 4.3.2 Interfacial modifications

Poly (ethylene oxide) (PEO, average molecular weight of 600,000) was dispersed in acetonitrile to acquire a pure PEO (P) solution. PEO and lithium bis(trifluoromethanesulfonyl)imide (LiTFSI) with a weight ratio of 70:30 was mixed in acetonitrile to get PEO-LiTFSI (PL) solution. A weight ratio of among PEO, LiTFSI, and succinonitrile (SN) of 35:30:35 in acetonitrile was used to make the gel membrane (PLS) solution. Each solution was dropped two times on both sides of LLTO pellets. The coated pellets were dried in air at room temperature to remove the solvent.

### 4.3.3 Symmetric Li cells assembly

Symmetric Li cells of LLTO pellets with and without coating were fabricated in an argon-filled glovebox to investigate the process of Li plating/stripping and evaluate its long-term cycling stability. Two Li foils were sandwiched on both sides of coated LLTO in a 2325-type coin cell.

### 4.3.4 Material characterization

The morphology of the pristine powder and prepared pellets were observed by scanning electron microscopy (Zeiss Gemini SEM 500) and energy dispersive X-ray spectrometry (EDS, Bruker). The crystalline phase was confirmed by powder X-ray diffractometry (PXRD, Rigaku, Ultima IV) with a copper source and one diffracted beam monochromator, operating at 40 kV and 44 mA. The pellets were scanned in the $2\theta$ range from 10 degrees to 60 degrees with a scan rate of 2 degrees/min. X-ray photoelectron spectroscopy (XPS) analyses were carried out using an Axis Ultra DLD spectrometer (Kratos Analytical, Manchester, UK) with monochromatized Al K$\alpha$ X-rays.

### 4.3.5 Electrochemical characterization

The resistance of pellets was measured via electrochemical impedance spectroscopy (EIS) by impedance/gain-phase analyzer (Solartron, SI 1260) with a frequency ranging from 1 MHz to 0.01 Hz (the amplitude was 50 mV) from room temperature to 60 ˚C. For uncoated LLTO pellets, an

Au/Pd layer was sputtered on both sides before the test. Coated LLTO pellets were tested directly without Au/Pd coating layer. The bulk ionic conductivity was calculated following the formula $\sigma$ = L/RS, where R is the impedance for the fitted results in Nyquist plots, L is the ceramic thickness, and S is the effective surface area of the electrolyte. The galvanostatic charge/discharge characteristics for symmetric Li cell were measured between -4.5 V and 4.5 V with current densities of 0.01 mA $cm^{-2}$, 0.02 mA $cm^{-2}$ and 0.04 mA $cm^{-2}$ at 60 ˚C using a potentiostat (Biologic Sciences Instruments).

## 4.4 Results and discussion

### 4.4.1 Characterization of LLTO powders and pellets

LLTO powders exhibit different morphologies, as shown in Supplementary Figure 1. The shape of the secondary particle for granular powder (designated as G-LLTO) is spherical (in Figure A9.1(A)). For milled powder (designated as M-LLTO), each secondary particle is more angular than G-LLTO (in Figure A9.1(B)). The secondary particles (with size of ~40 $\mu$m) comprise of agglomerated primary particles with smaller sizes of ~0.5 $\mu$m. Note that each secondary particle for M-LLTO appears to represent one primary particle. To enhance the sinterability of dense LLTO, G-LLTO and M-LLTO powders with various weight ratios are mixed and investigated. The optimization of the weight ratio between G-LLTO and M-LLTO powders is 70:30. While regarding to the mixed powder, each secondary particle contains larger primary LLTO particles surrounded by smaller primary particles. The secondary particle of mixed powder has the average particle size of ~1 $\mu$m as indicated in Figure A9.1(C).

The mixed LLTO electrolytes (70 wt.% of G-LLTO and 30 wt.% of M-LLTO) show the highest densification after sintering at 1170 ˚C for 12h in air, compared with its single components as shown in Figure A9.2. Furthermore, the SEM images for LLTO with the optimization of sintering temperatures is exhibited in Figure A9.3. Green mixed pellets are sintered at 960 ˚C, 1050 ˚C, and 1170 ˚C for 12h in air atmosphere. Elevated sintering temperatures thus accelerate the growth of

LLTO grains. The densification is enhanced with increased sintering temperature at the same time. As a result, the mixed LLTO pellets show void-free surface and indicate the highest densification after sintering at 1170 ˚C. However, the sintering temperature cannot be too high as Li would be lost during the sintering process (Li starts to be sublimated at temperatures above 900 ˚C).[10]

In the insets of Figure 4.1, the sintered electrolytes have a light-yellow color on the surface. The surface of sintered LLTO pellets without any polishing is dense but relatively rough. The sintered pellets using G-LLTO and M-LLTO, respectively (in Figure 4.1(A) and (B)), indicate grains growth in different degrees. Most LLTO neighboring grains for mixed LLTO in Figure 4.1(C) have better contacts without significant porosity at 1170 ˚C. The dense microstructure of the LLTO electrolytes could enable a homogeneous current distribution and prevents Li dendrite penetration during the cycling process.[16]

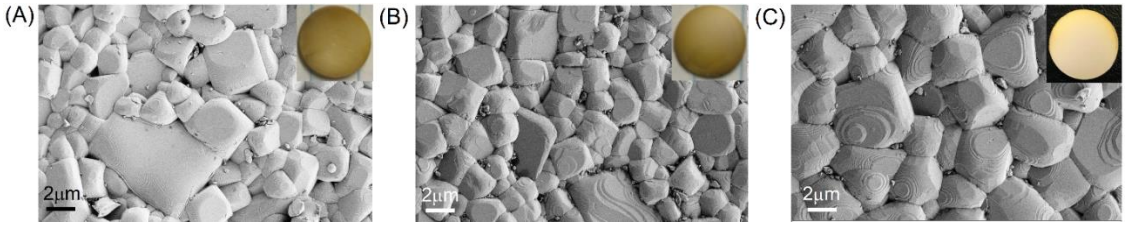


**Figure 4.1.** SEM pictures of sintered pellets (without polishing at 1170 ˚C for 12h in air): (A) G-LLTO; (B) M-LLTO; and (C) mixed LLTO.

Figure 4.2 shows that the color of sintered LLTO pellets changes from white to dark gray and then to a deep black over time when bring in contact with Li metal. To avoid the exposure of Li metal to air, LLTO with Li-metal foil is sealed in glass containers filled with inert Argon atmosphere. It is clear that white LLTO is very sensitive to reduction and takes place in less than 5 mins. Initially, white LLTO electrolytes would turn black after contacting with Li after 90 mins. The SEM micrograph in Figure A9.4 shows that the surface of the white and black LLTO pellet is not flat. The roughness of both pellets depends on the cut-off procedure via low-speed diamond saw. This result supports that color change of LLTO has no apparent effect on the surface morphology of pellets.

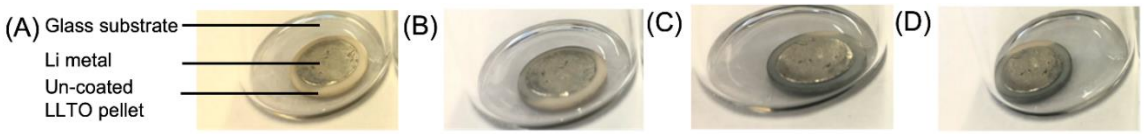


**Figure 4.2.** Photographs of un-coated LLTO contacts with Li metal after: (A) 5 mins; (B) 30 mins; (C) 60 mins; and (D) 90 mins.

The XRD patterns of all pellets are plotted in Figure 4.3 and match to a perovskite $ABO_3$ superstructure (tetragonal structure JCPDS #87-0935).[31,32] Figure 4.3(A) proves that the bulk structure of white LLTO remains unchanged after mixing G-LLTO and M-LLTO powder. Figure 4.3(B) also validates that sintering at 1170 ˚C for 12h in air does not affect tetragonal structure of black LLTO (when it is in contact with Li metal). Also, the LLTO structure would be changed from tetragonal to cubic after sintering over 1500 ˚C.

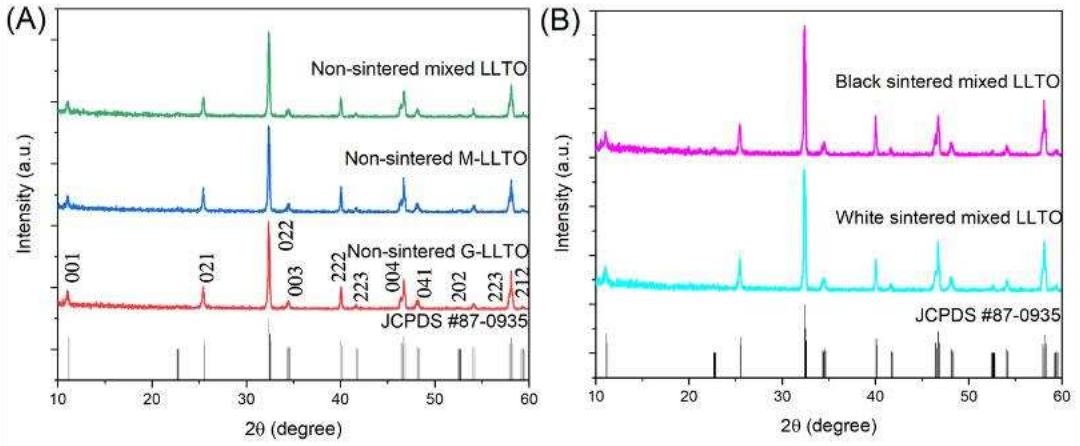


**Figure 4.3.** 2D stacked XRD spectra of: (A) non-sintered LLTO pellets; and (B) sintered mixed LLTO pellets.

### 4.4.2 Ionic conductivity of sintered LLTO pellets

Figure 4.4 compares EIS curves of sintered un-coated LLTO pellets. The resulting Nyquist plots contain one semicircle and an inclined straight line. In Figure 4.4(A), the calculated bulk ionic conductivity of the G-LLTO pellet is $4.7\times10^{-5}$ S $cm^{-1}$ at room temperature. Because of the decreased particle size, the bulk ionic conductivity of M-LLTO electrolyte increases to $1.8\times10^{-4}$ S $cm^{-1}$. Mixed LLTO electrolyte presents the highest bulk conductivity of $2.1\times10^{-4}$ S $cm^{-1}$ at room

temperature as calculated from Figure 4.4(B). This enhancement might be attributed to the presence of smaller secondary particles within the grains of G-LLTO powder, which minimizes grain boundary resistance and increases the contact area between neighboring grains.[33] The ionic conductivity of the mixed electrolyte increases with temperature and follows an Arrhenius behavior as indicated in Figure 4.4(C) with an activation energy of 0.23 eV.

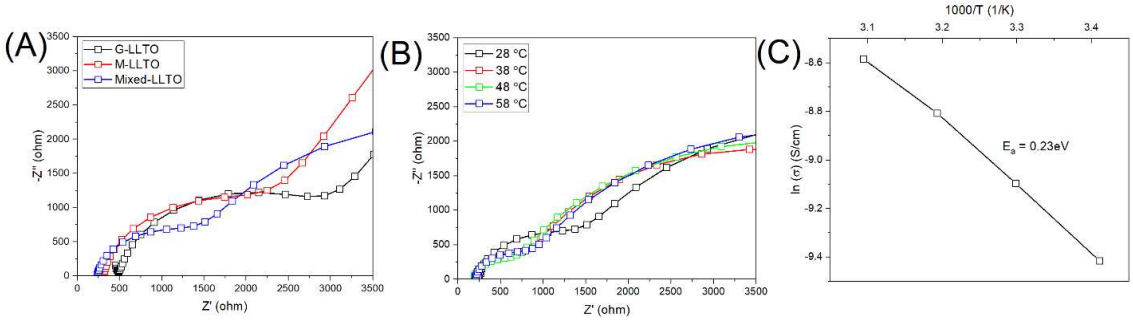


**Figure 4.4.** (A) AC impedance spectra of sintered un-coated LLTO pellets at room temperature; (B) Nyquist plot of sintered mixed LLTO pellet during 28 ˚C-58 ˚C; and (C) Arrhenius plot of sintered mixed LLTO pellet during 28 ˚C-58 ˚C. Fitting circuit is (R1CPE1)(CPE2). R and CPE represent the resistor and the constant phase element, respectively.

### 4.4.3 Instability of LLTO electrolytes against Li-metal

To further confirm the composition and chemical nature of black sintered LLTO pellets, XPS analysis is conducted on the collected black samples and the results are shown in Figure 4.5. The XPS spectra shown in Figure 4.5(A) consist of major peaks assigned to Li 1s, La 3d, Ti 2p, O1 1s, and C 1s. C 1s peak at 284.8 eV is used as a reference peak for calibration. High-resolution peaks of La 3d 3/2, La 3d 5/2, and O 1s are shown in Figure 4.5(B) and (C), respectively. In Figure 4.5(D), the Ti 2p core spectrum reveals two main components: the peaks around 458.6 eV and 463.3 eV are associated with $Ti^{4+}$ cations.[34,35] The atomic content of $Ti^{4+}$ species on the surface of the black sample is 84.48 %. For black LLTO pellets, $Ti^{4+}$ species are heavily reduced to the lower valence of Ti ions after assembling with Li metal, corresponding to the peak around 460.5 eV that is associated with $Ti^{2+}$ species.[35,36]

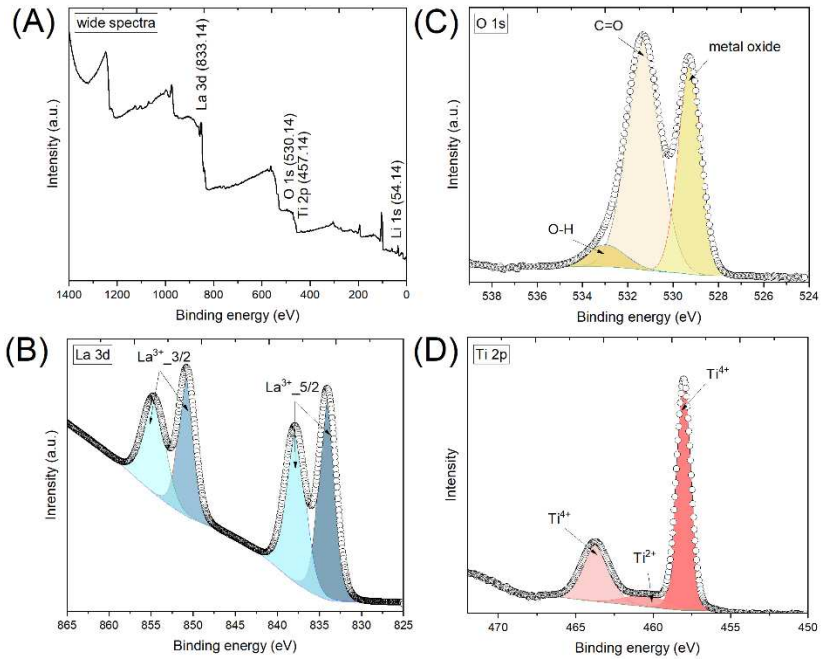


**Figure 4.5.** XPS spectra of black sintered LLTO pellet: (A) wide survey (pass energy = 80 eV); high-resolution scans (pass energy = 20 eV) of (B) La 3d region; (C) O 1s region; and (D) Ti 2p region.

### 4.4.4 Resistance of coated LLTO electrolytes

The two sides of sintered mixed LLTO pellets (non-polished) are coated with PEO-based gel membranes. The SEM images for the morphology of coated-LLTO with each interfacial layer are shown in Figure A9.5. LLTO pellets modified by PEO-based gel films are smooth and uniform. PEO-based gel can be observed in the cracks and porosities of LLTO pellets and can thus provide effective pathways for Li-ion transportation even if the ceramic pellet cracks during cell assembly. High-resolution EDX mapping in insets of Figure A9.5 exhibits a continuous and conformal coating of polymer on the surface of LLTO pellets, enabling effective protection of LLTO pellets from $Ti^{4+}$ cation reduction.

The AC impedance results of coated LLTO electrolytes during testing at 30 ˚C-60 ˚C are illustrated in Figure 4.6. The high-frequency semicircle in all curves is attributed to the total resistance of the coated electrolytes. Compared to the total resistance PEO-LLTO and PEO-LiTFSI (PL)-LLTO as shown in Figure 4.6(A) and (B), the value of PEO-LiTFSI-SN (PLS)-LLTO in Figure 4.6(C) is the

smallest (84.88 ohm $cm^{-2}$ at 60 ˚C) because the gel electrolyte has high ionic conduction compared with PEO or PL. Thus, it is verified that PLS with a weight ratio of 35%:30%:35% enables more lithium-ion pathways and enhances the polymer membrane's ionic conductivity.

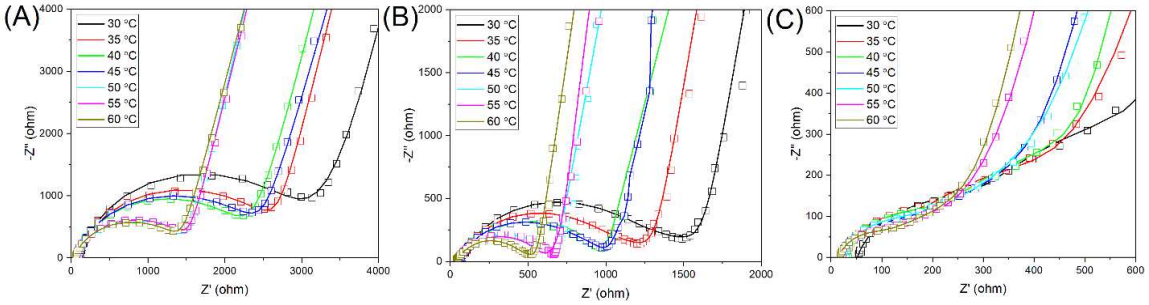


**Figure 4.6.** Nyquist plots of LLTO pellets during 30 ˚C-60 ˚C coated by: (A) PEO; (B) PEO-LiTFSI; and (C) PEO-LiTFSI-SN.

To determine the total activation energy for Li-ion migration, temperature-dependent measurements are obtained at the same frequency range (1 MHz-0.01 Hz) by changing the temperature from 30 ˚C to 60 ˚C as plotted in Figure A9.5. The calculated activation energy for each coated-LLTO is listed in Table A7. PL-LLTO has the lowest activation energy of 14.85 kJ $mol^{-1}$, as shown by the reduced interfacial resistance mentioned before. Compared to PEO only, the introduction of LiTFSI salt is helpful to reduce the activation energy and increase the ionic conductivity. For PLS-LLTO, it is obvious that after 55 ˚C, the slope of the line decreased due to the reduction of activation energy. The slope change at higher temperatures is possibly due to "melting" phase transition of SN and PEO. Nevertheless, $Li^+$ mobility is restricted at lower temperatures.[37] We assume that the increase in activation energy for PLS is due to the phase transition of SN to the plastic solid phase. As a result, PLS-LLTO increases the total resistance and brings on a higher energy barrier for lithium-ion transport. We would test PLS-LLTO in symmetric Li cells to further verify this hypothesis in the Section 4.4.5.

### 4.4.5 Performance of symmetric Li|coated-LLTO|Li cell

Figure A9.7 exhibits the color of coated LLTO pellets after cycling in symmetric cells. PEO membrane cannot protect LLTO well due to several darker grey dots (in Figure A9.7(A)). The black circle in the middle of the P coated-LLTO and PL coated-LLTO (in Figure A9.7(B)) pellets is Li foil. In contrast, Li foil is absent on the surface of PLS coated-LLTO as evidenced by Figure A9.7(C). It may be due to the softness change of the gel membranes at room temperature. The separation of Li-metal foil from PLS coated-LLTO could also indicate increased interfacial resistance. Moreover, partial Ti reduction increases the total resistance of LLTO pellets. Compared to the ineffective coating of PEO, the color of PL or PLS coated-LLTO remains unchanged. Hence, it is proved that PL and PLS could protect LLTO against Li metal.

Galvanostatic charge/discharge testing in symmetric Li cells (cell configuration is added in Figure 4.7 inset) are performed to evaluate the interfacial stability and voltage polarization at 60 ˚C. The time-dependent voltage profile of the Li|gel-LLTO|Li cells are plotted and analyzed. LLTO coated by three gel membranes perform relatively stable plots without noise compared to un-coated LLTO as plotted in Figure A9.8, as evidenced by which a better interfacial contact between coated-LLTO and Li. Besides, the flat voltage plateau with a small variation for three cells with coated-LLTO is support of the excellent interfacial stability.[38] The open circuit voltage (OCV) is around 1.5 V and drops down to 0 V after resting for 12h. To study the reason why the OCV is not 0 V, the assembled cell is rested for 12h and 24h before cycling to investigate the difference. Voltage differences with the other cells studied here may be due to good $Li^+$ conduction of gel electrolytes. The interface activation process can be seen from the voltage profile of the stripping-plating cycle, where the voltage decreases in the first 20h and then becomes relatively stable.[39] The related tiny noise in the voltage profile is attributed to localized voids forming at the Li|coated layers interface as Li is stripped away from the anode; the voids likely formed because of insufficient pressure applied to the symmetric cell during cycling.[40] Small asymmetry of the whole profile could be related to the still inefficient transition pathways and partial distortion between coating layers and LLTO.[41]

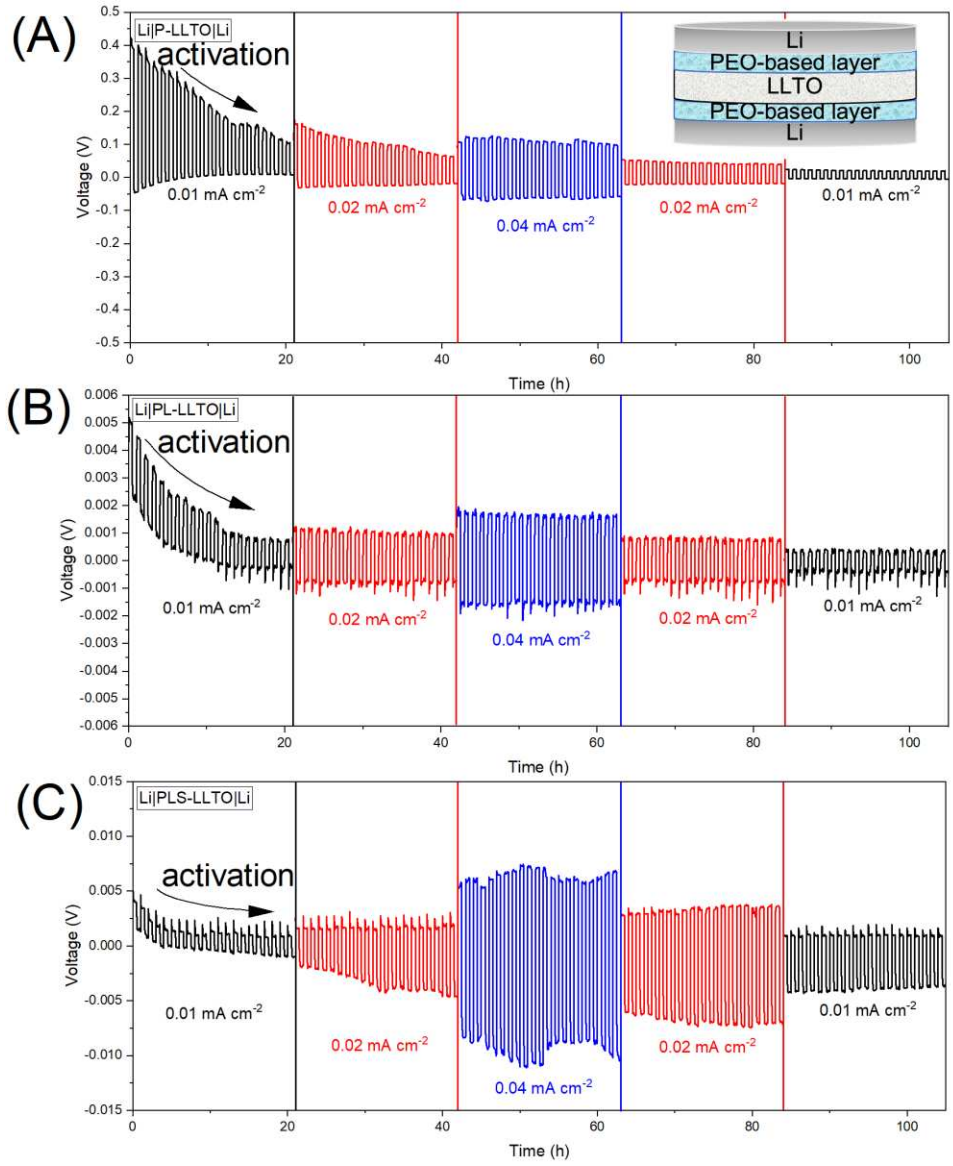


**Figure 4.7.** Cycling performance of symmetric Li cells at different current densities (tested at 60°C) and LLTO was coated by: (A) PEO; (B) PEO-LiTFSI; and (C) PEO-LiTFSI-SN.

Compared to the overpotential for un-coated LLTO at a current density of 0.04 mA $cm^{-2}$, PEO coated-LLTO (P-LLTO) pellet has a larger value as represented in Figure 4.7(A). This may be due to PEO degradation during the cycling at different current densities. Besides, as confirmed by the color change of PEO-LLTO pellet after cycling (in Figure A9.7(A)) the reduction of LLTO might affect the interfacial stability against Li and increase the total cell resistance.[42] In comparison, the overpotential is only 1.7 mV at a current density of 0.04 mA $cm^{-2}$ for PL-LLTO pellet as indicated

in Figure 4.7(B). The smallest value of overpotential with the stable trend and mitigated noise suggests enhanced interface stability and favored electrochemical reaction with Li-metal anode.[39] The hysteresis change in voltage trace implies that the voltage shape after extended cycling cannot be fully captured by morphology-driven reaction kinetics.[41] Regarding the reversible behavior of gel-LLTO for Li stripping and plating, the profile indicates stable performance when the current density is dropped down to the original value of 0.01 mA $cm^{-2}$.

The larger overpotential value for PLS-LLTO pellet as shown in Figure 4.7(C) proves our assumption based on its higher activation energy during 30 ˚C-60 ˚C. PLS with SN brings on increased interfacial resistance against Li metal. This claim agrees with the observation for cycled PLS coated-LLTO (from opened symmetric Li cell in Figure A9.7(C)) that Li metal is completely separated from PLS. Insufficient contact during the cycling causes polarization and more potential loss.

To further examine the cycling stability of three PEO-based membranes on the LLTO pellets, Figure 4.8 compares the resistance of symmetric Li cells before and after cycling at room temperature. The high-frequency semicircle corresponds to the total resistance of symmetric Li cells with coated-LLTO. Overall, there is a significant drop of total resistance for three gel coated-LLTO, proving the effectiveness of polymer-based coatings in improving interfacial contact. The large resistance of Li|PEO coated-LLTO|Li before galvanostatic cycling in Figure 4.8(A) might be ascribed to ineffectively interfacial contact between PEO and Li. PEO polymer is highly crystalline at room temperature, thus resulting in considerable impedance for $Li^+$ transport.[43] During the cycling at 60 ˚C, moderating the modulus of the soft-phase regions for PEO could be moderated, which helps to decrease the total resistance.[44] However, the total resistance of the cell is still relatively high after cycling, which may be owing to PEO degradation (e.g., the change of crystallization conditions) and its instability (e.g., the deterioration of physical properties) against Li metal.[45,46,47] The total resistance for PL coated-LLTO (accessed from in Figure 4.8(B)) after

cycling is subtly larger than PLS coated-LLTO (as seen in Figure 4.8(C)), possibly because the PLS membrane itself has lower resistance.

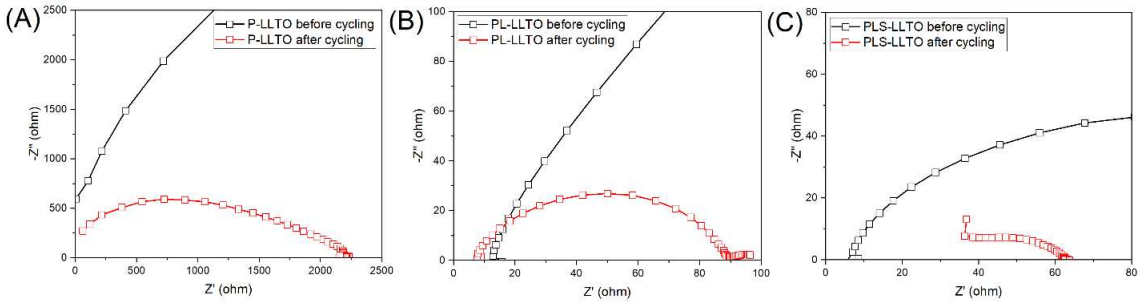


**Figure 4.8.** AC impedance symmetric Li|PEO-based coated-LLTO|Li cell before and after cycling (tested at room temperature): (A) PEO coated-LLTO; (B) PL coated-LLTO; and (C) PLS coated-LLTO.

Table 6 and Table A8 summarize the total polarization resistance and ionic conductivity of coated LLTO in symmetric Li cells. Stable potential is the average voltage window (the plus between positive potential and the absolute negative potential). The observed potential from all cells includes polarization losses from interfaces and ohmic losses from the LLTO pellet. The volume change of Li anode during cycling may be the origin of the overpotential change. The alignment of both Li foils may affect the polarization resistance with coating layers.[47] $R_{total}$ (ohm) is calculated from ohm's law (R = V/I, where V represents the stable potential (mV) and I represents the current density (mA $cm^{-2}$)). $R_{total}$ contains $R_{bulk}$ (the resistance of the LLTO pellet), $R_{interface1}$ (the polarization resistance between PEO-based layers and Li metal), and $R_{interface2}$ (the interfacial resistance between coated layers and LLTO pellet). $R_1$ (ohm $cm^{-2}$) is $R_{total\ /surface\ area(cm2)}$ and $R_2$ (ohm $cm^{-1}$) is $R_{total/\ thickness\ (cm)}$. The fitting circuit is $(R_{bulk})(R_{interface1}CPE1)(R_{interface2}CPE2)$.

**Table 6.** Summary of the total ionic conductivity for LLTO coated by three interfaces in symmetric Li cell (tested at 60 ˚C, with decreased current density).

| Interface | Current density (mA $cm^{-2}$) | Stable Potential (mV) | $R_{total}$ (ohm) | $R_1$(ohm $cm^{-2}$) | $R_2$(ohm $cm^{-1}$) | $\boldsymbol{\sigma_{total}}$(mS $cm^{-1}$) |
|---|---|---|---|---|---|---|
| PEO | 0.04 | 84.5 | 3755.56 | 2125.21 | 50074.07 | 0.011 |
| | 0.02 | 32 | 2844.45 | 1609.63 | 37925.93 | 0.015 |

| | | | | | | |
|---|---|---|---|---|---|---|
| | 0.01 | 13.5 | 2400 | 1358.12 | 32000 | 0.018 |
| PL | 0.04 | 1.55 | 68.89 | 38.98 | 810.46 | 0.70 |
| | 0.02 | 0.7 | 62.22 | 35.21 | 732.03 | 0.77 |
| | 0.01 | 0.35 | 62.22 | 35.21 | 732.03 | 0.77 |
| PLS | 0.04 | 7.25 | 322.22 | 182.34 | 3790.85 | 0.15 |
| | 0.02 | 5.1 | 453.33 | 256.53 | 5333.33 | 0.11 |
| | 0.01 | 2.35 | 417.78 | 236.41 | 4915.03 | 0.12 |

During the cycling process, when the current density is decreased from 0.04 mA $cm^{-2}$ to 0.01 mA $cm^{-2}$, the voltage profile of symmetric Li cells is relatively stable. For PL coated-LLTO, it is clearly observed that the total resistance ($R_{total}$) almost remains unchanged with the decreasing current density. This represents that the applied current density of these three cells does not affect ionic conductivity for these three cells.[47] The smaller polarization voltage verifies the reduction of concentration polarization.[41] Compared with PEO, LiTFSI in PEO builds more $Li^+$ conductive pathways that promote rapid $Li^+$ diffusion from the pellet to Li metal. PLS gel membranes show expansion during the stripping and plating process. This phenomenon is most likely the cause of the formation and disappearance of voids at the surface of ceramic pellets.[48] Produced voids or insufficient contacts would influence the value shift of the resistance. Among three gel membranes, PL has relatively stable resistance at different current densities, corresponding to a constant ionic conductivity of around 2 mS $cm^{-1}$ at 60 ˚C. The ionic conductivity of PLS-LLTO cell during the cycling is lower than PL-LLTO, which may be owing to phase transition of SN over 40 ˚C.

Polymer gel membranes as interfaces could fulfill all voids on the surface and tend to infiltrate into the grain boundary regions of LLTO. Coating provides a relatively flat surface contact with Li metal and PL or PLS coated-LLTO could maintain the original white color after cycling. Furthermore, softer PL or PLS could effectively permeate into the cracks of LLTO pellets and prevent direct exposure of LLTO from Li-metal. Moreover, the total ionic conductivity of the LLTO pellet is improved by optimizing the conductivity of polymer membranes. For the PLS membrane itself, the addition of SN dissociates Li ions from LiTFSI and further maximizes the

total ionic conductivity of LLTO pellets at 60 ˚C. However, the large value of overpotential for PLS coated-LLTO in symmetric Li cells indicates that PLS has poor compatibility with Li metal that could be attributed to the poor chemical stability of nitriles towards chemical reduction by Li metal.

## 4.5 Conclusion

In summary, we have successfully fabricated highly dense LLTO pellets via uniaxial cold press followed by sintering. EIS results from the Nyquist plot indicate that the sintered LLTO pellets have the largest bulk ionic conductivity of $2.1\times10^{-4}$ S $cm^{-1}$ at room temperature. In a highly dense LLTO system, M-LLTO powder with smaller secondary particles fills the voids between the primary particles in G-LLTO and enhances the densification of sintered LLTO pellets. Eventually, a denser LLTO can be beneficial to decrease the total resistance of electrolytes and thus increases the ionic conductivity.

Additionally, we have demonstrated that the instability of bare sintered LLTO electrolytes when in contact with Li metal ($Ti^{4+}$ cation reduction), that is accompanied by visual color change, can be overcome by coating with an interfacial layer. Three types of polymeric interfacial layers have been investigated and their effects at the LLTO|Li metal interface have been deeply studied. Our study shows that PEO-LiTFSI (PL) and PEO-LiTFSI-SN (PLS) coated-pellets maintains original white color of LLTO after cycling with Li metal and effectively resolved the issue. PL or PLS gel membranes have a soft and flexible structure, effectively providing sufficient contacts with LLTO pellets. They also facilitate the assembly of the fragile, thin ceramic electrolytes in cells. Among three types of gel membranes, LLTO coated by PLS gel shows the smallest total resistance of 84.88 ohm $cm^{-2}$ and confirmed the excellent ionic conductivity of PLS gel. Nevertheless, the PLS membrane as the interface is less chemically stable in symmetric Li cell and brings on larger overpotential. Phase transition of SN at 60 ˚C possibly increases the resistance at the PLS/Li metal interface and prohibits lithium ions diffusion.

Our work proposes a novel microstructure of LLTO and hence enhances ceramic sinterability. Importantly, we have addressed the $Ti^{4+}$ cation reduction issue when Li metal is in contact with LLTO and opened a new window for utilizing LLTO with Li-metal by introducing interfacial layers on ceramic electrolytes. Therefore, we believe that this approach sheds a light on the safe assembly of thin-film ceramic electrolytes in lithium metal battery.

## 4.6 References


1. Hu, X.; Yan, G.; Cheng, X.; Malzbender, J.; Qiang, W.; Huang, B. Electrochemical and mechanical stability of LixLa0.557TiO3-δ perovskite electrolyte at various voltages. *Journal of the American Ceramic Society*. **2019**, *102*, 1953-1960.
2. Chen, L.; Fan, X.; Ji, X.; Chen, J.; Hou, S.; Wang, C. High-energy Li metal battery with lithiated host. *Joule*. **2019**, *3*, 732-744.
3. Tarascon, JM.; Armand, M. Issues and challenges facing rechargeable lithium batteries. *Nature*. **2001**, *414*, 359–367.
4. Xu, W.; Wang, J.; Ding, F.; Chen, X.; Nasybulin, E.; Zhang, Y.; Zhang, J. G. Lithium metal anodes for rechargeable batteries. *Energy & Environmental Science*. **2014**, *7*, 513-537.
5. Lv, F.; Wang, Z.; Shi, L.; Zhu, J.; Edström, K.; Mindemark, J.; Yuan, S. Challenges and development of composite solid-state electrolytes for high-performance lithium-ion batteries. *Journal of Power Sources*. **2019**, *441*, 227175.
6. Wang, M.J.; Wolfenstine, J.B.; Sakamoto, J. Mixed Electronic and Ionic Conduction Properties of Lithium Lanthanum Titanate. *Advanced Functional Materials*. **2020**, *30*, 1909140.
7. Lotsch, B. V.; Maier, J. Relevance of solid electrolytes for lithium-based batteries: A realistic view. *Journal of Electroceramics*. **2017**, *38*, 128-141.
8. Wang, Q.; Zhang, J.; He, X.; Cao, G.; Hu, J.; Pan, J.; Shao, G. Synergistic effect of cation ordered structure and grain boundary engineering on long-term cycling of Li0. 35La0.

55TiO3-based solid batteries. *Journal of the European Ceramic Society*. **2019**, *39*, 3332-3337.

9. Yin, Y.; Jiang, C.S.; Guthrey, H.; Xiao, C.; Seitzman, N.; Ban, C.; Al-Jassim, M. Improved stability and cyclability of ceramic solid electrolyte by coating polymer. *Journal of The Electrochemical Society*. **2020**, *167*, 020519.
10. Jonson, R. A.; McGinn, P. J. Tape casting and sintering of Li7La3Zr1.75Nb0.25Al0.1O12 with Li3BO3 additions. *Solid State Ionics*. **2018**, *323*, 49-55.
11. Li, Y.; Yang, W.; Wang, L.; Zhu, J.; Meng, W.; He, Z.; Dai, L. Improvement of sinterability of BaZr0.8Y0.2O3-δ for H2 separation using Li2O/ZnO dual-sintering aid. *Ceramics International*. **2018**, *44*, 15935-15943.
12. Le, S.; Zhu, S.; Zhu, X.; Sun, K. Densification of Sm0.2Ce0.8O1.9 with the addition of lithium oxide as sintering aid. *Journal of Power Sources*. **2013**, *222*, 367-372.
13. Fu, K. K.; Gong, Y.; Liu, B.; Zhu, Y.; Xu, S.; Yao, Y.; Luo, W.; Wang, C.; Lacey, S.D.; Dai, J.; Chen, Y. Toward garnet electrolyte–based Li metal batteries: An ultrathin, highly effective, artificial solid-state electrolyte/metallic Li interface. *Science Advances*. **2017**, *3*, e1601659.
14. Shen, Y.; Zhang, Y.; Han, S.; Wang, J.; Peng, Z.; Chen, L. Unlocking the energy capabilities of lithium metal electrode with solid-state electrolytes. *Joule*. **2018**, *2*, 1674-1689.
15. Xu, L.; Tang, S.; Cheng, Y.; Wang, K.; Liang, J.; Liu, C.; Cao, Y.C.; Wei, F.; Mai, L. Interfaces in solid-state lithium batteries. *Joule*. **2018**, *2*, 1991-2015.
16. Tsai, C. L.; Roddatis, V.; Chandran, C. V.; Ma, Q.; Uhlenbruck, S.; Bram, M.; Heitjans, P.; Guillon, O. Li7La3Zr2O12 interface modification for Li dendrite prevention. *ACS Applied Materials & Interfaces*. **2016**, *8*, 10617-10626.

17. Luo, W.; Gong, Y.; Zhu, Y.; Li, Y.; Yao, Y.; Zhang, Y.; Fu, K.; Pastel, G.; Lin, C.F.; Mo, Y.; Wachsman, E.D. Reducing interfacial resistance between garnet-structured solid-state electrolyte and Li-metal anode by a germanium layer. *Advanced Materials*. **2017**, *29*, 1606042.

18. Han, X.; Gong, Y.; Fu, K. K.; He, X.; Hitz, G. T.; Dai, J.; Pearse, A.; Liu, B.; Wang, H.; Rubloff, G. Mo,; Mo, Y. Negating interfacial impedance in garnet-based solid-state Li metal batteries. *Nature Materials*. **2017**, *16*, 572-579.

19. Wang, C.; Gong, Y.; Liu, B.; Fu, K.; Yao, Y.; Hitz, E.; Li, Y.; Dai, J.; Xu, S.; Luo, W.; Wachsman, E.D.; Hu, L. Conformal, nanoscale ZnO surface modification of garnet-based solid-state electrolyte for lithium metal anodes. *Nano Letters*. **2017**, *17*, 565-571.

20. Shao, Y.; Wang, H.; Gong, Z.; Wang, D.; Zheng, B.; Zhu, J.; Lu, Y.; Hu, Y.S.; Guo, X.; Li, H.; Chen, L. Drawing a soft interface: an effective interfacial modification strategy for garnet-type solid-state Li batteries. *ACS Energy Letters*. **2018**, *3*, 1212-1218.

21. Jiang, Z.; Wang, S.; Chen, X.; Yang, W.; Yao, X.; Hu, X.; Han, Q.; Wang, H. Tape-Casting $Li_{0.34}La_{0.56}TiO_3$ Ceramic Electrolyte Films Permit High Energy Density of Lithium-Metal Batteries. *Advanced Materials*. **2020***, 32,* 1906221.

22. Chi, S. S.; Liu, Y.; Zhao, N.; Guo, X.; Nan, C. W.; Fan, L. Z. Solid polymer electrolyte soft interface layer with 3D lithium anode for all-solid-state lithium batteries. *Energy Storage Materials*. **2019**, *17*, 309-316.

23. Zhou, W.; Wang, S.; Li, Y.; Xin, S.; Manthiram, A.; Goodenough, J. B. Plating a dendrite-free lithium anode with a polymer/ceramic/polymer sandwich electrolyte. *Journal of the American Chemical Society*. **2016**, *138*, 9385-9388.

24. Yin, Y.; Jiang, C. S.; Guthrey, H.; Xiao, C.; Seitzman, N.; Ban, C.; Al-Jassim, M. Improved Stability and Cyclability of Ceramic Solid Electrolyte by Coating Polymer. *Journal of The Electrochemical Society*. **2020**, *167*, 020519.

25. Liu, Y.; Sun, Q.; Zhao, Y.; Wang, B.; Kaghazchi, P.; Adair, K. R.; Li, R.; Zhang, C.; Liu, J.; Kuo, L.Y.; Sun, X. Stabilizing the interface of NASICON solid electrolyte against Li metal with atomic layer deposition. *ACS Applied Materials & Interfaces*. **2018**, *10*, 31240-31248.

26. Liu, B.; Gong, Y.; Fu, K.; Han, X.; Yao, Y.; Pastel, G.; Yang, C.; Xie, H.; Wachsman, E.D.; Hu, L. Garnet solid electrolyte protected Li-metal batteries. *ACS Applied Materials & Interfaces*. **2017**, *9*, 18809-18815.

27. Cheng, X. B.; Zhao, C. Z.; Yao, Y. X.; Liu, H.; Zhang, Q. Recent advances in energy chemistry between solid-state electrolyte and safe lithium-metal anodes. *Chem*. **2019**, *5*, 74-96.

28. Al-Salih, H.; Huang, A.; Yim, C. H.; Freytag, A. I.; Goward, G. R.; Baranova, E.; Abu-Lebdeh, Y. A Polymer-Rich Quaternary Composite Solid Electrolyte for Lithium Batteries. *Journal of The Electrochemical Society*. **2020**, *167*, 070557.

29. Echeverri, M.; Kim, N.; Kyu, T. Ionic conductivity in relation to ternary phase diagram of poly (ethylene oxide), succinonitrile, and lithium bis (trifluoromethane) sulfonimide blends. *Macromolecules*. **2012**, *45*, 6068-6077.

30. Yan, S.; Yim, C.H.; Pankov, V.; Bauer, M.; Baranova, E.; Weck, A.; Merati, A.; Abu-Lebdeh, Y. Perovskite solid-state electrolytes for lithium metal batteries. *Batteries*. **2021**, *7*, 75.

31. Li, R.; Liao, K.; Zhou, W.; Li, X.; Meng, D.; Cai, R.; Shao, Z. Realizing fourfold enhancement in conductivity of perovskite Li0. 33La0. 557TiO3 electrolyte membrane via a Sr and Ta co-doping strategy. *Journal of Membrane Science*. **2019**, *582*, 194-202.

32. Yu, K.; Tian, Y.; Gu, R.; Jin, L.; Ma, R.; Sun, H.; Xu, Y.; Xu, Z.; Wei, X. Ionic conduction, colossal permittivity and dielectric relaxation behavior of solid electrolyte Li3xLa2/3-xTiO3 ceramics. *Journal of the European Ceramic Society*. **2018**, *38*, 4483-4487.

33. Cheng, L.; Wu, C. H.; Jarry, A.; Chen, W.; Ye, Y.; Zhu, J.; Kostecki, R.; Persson, K.; Guo, J.; Salmeron, M.; Doeff, M. Interrelationships among grain size, surface composition, air stability, and interfacial resistance of Al-substituted Li7La3Zr2O12 solid electrolytes. *ACS Applied Materials & Interfaces*. **2015**, *7*, 17649-17655.
34. Wagner, C. D.; Naumkin, A. V.; Kraut-Vass, A.; Allison, J. W.; Powell, C. J.; Rumble Jr, J. R. NIST standard reference database 20, Version 3.4 (Web version). *National Institute of Standards and Technology: Gaithersburg*. **2003***, MD*, 20899.
35. Biesinger, M. C.; Payne, B. P.; Hart, B. R.; Grosvenor, A. P.; McIntryre, N. S.; Lau, L. W.; Smart, R. S. Quantitative chemical state XPS analysis of first row transition metals, oxides and hydroxides. Journal of Physics: Conference Series. **2008**, *100*, 012025.
36. Biesinger, M. C.; Payne, B. P.; Grosvenor, A. P.; Lau, L. W.; Gerson, A. R.; Smart, R. S. C. Resolving surface chemical states in XPS analysis of first row transition metals, oxides and hydroxides: Cr, Mn, Fe, Co and Ni. *Applied Surface Science*. **2011**, *257*, 2717-2730.
37. Polu, A. R.; Rhee, H. W.; Kim, D. K. New solid polymer electrolytes (PEO20–LiTDI–SN) for lithium batteries: structural, thermal and ionic conductivity studies. *Journal of Materials Science: Materials in Electronics*. **2015**, *26*, 8548-8554.
38. Chen, L.; Huang, Z.; Pang, W.; Jin, Z.; Li, Y.; Wang, C.A. Dual interface layers for solid-state Li metal battery with low interfacial resistance and small polarization based on garnet electrolyte. *Electrochimica Acta*. **2020**, *330*, 135352.
39. Ulissi, U.; Agostini, M.; Ito, S.; Aihara, Y.; Hassoun, J. All solid-state battery using layered oxide cathode, lithium-carbon composite anode and thio-LISICON electrolyte. *Solid State Ionics*. **2016**, *296*, 13-17.
40. Seitzman, N.; Guthrey, H.; Sulas, D. B.; Platt, H. A.; Al-Jassim, M.; Pylypenko, S. Toward all-solid-state lithium batteries: three-dimensional visualization of lithium migration in β-Li3PS4 ceramic electrolyte. *Journal of the Electrochemical Society*. **2018**, *165*, A3732.

41. Chen, K. H.; Wood, K. N.; Kazyak, E.; LePage, W. S.; Davis, A. L.; Sanchez, A. J.; Dasgupta, N. P. Dead lithium: mass transport effects on voltage, capacity, and failure of lithium metal anodes. *Journal of Materials Chemistry A*. **2017**, *5*, 11671-11681.
42. Zhang, K.; Wu, F.; Wang, X.; Weng, S.; Yang, X.; Zhao, H.; Guo, R.; Sun, Y.; Zhao, W.; Song, T.; Wang, X. 8.5 μm-Thick Flexible-Rigid Hybrid Solid–Electrolyte/Lithium Integration for Air-Stable and Interface-Compatible All-Solid-State Lithium Metal Batteries. *Advanced Energy Materials*. **2022**, *12*, 2200368.
43. Lyu, W.; He, G.Liu, T. PEO-LITFSI-SiO2-SN system promotes the application of polymer electrolytes in all-solid-state lithium-ion batteries. *ChemistryOpen*. **2020**, *9*, 713-718.
44. Korley, L.T.J.; Pate, B.D.; Thomas, E.L.; Hammond, P.T. Effect of the degree of soft and hard segment ordering on the morphology and mechanical behavior of semicrystalline segmented polyurethanes. *Polymer*. **2006**, *47*, 3073-3082.
45. Scheirs, J.; Bigger, S.W.; Delatycki, O. Characterizing the solid-state thermal oxidation of poly (ethylene oxide) powder. *Polymer*. **1991**, *32*, 2014-2019.
46. Li, D.; Chen, L.; Wang, T.; Fan, L.Z. 3D fiber-network-reinforced bicontinuous composite solid electrolyte for dendrite-free lithium metal batteries. *ACS Applied Materials & Interfaces*. **2018**, *10*, 7069-7078.
47. Zhang, J.; Lei, L.; Li, H.; Chen, F.; Han, M. A practical approach for identifying various polarization behaviors of redox-stable electrodes in symmetrical solid oxide fuel cells. *Electrochimica Acta*. **2021**, *384*, 138340.
48. Koshikawa, H.; Matsuda, S.; Kamiya, K.; Miyayama, M.; Kubo, Y.; Uosaki, K.; Hashinoto, K.; Nakanishi, S. Dynamic changes in charge-transfer resistance at Li metal/Li7La3Zr2O12 interfaces during electrochemical Li dissolution/deposition cycles. *Journal of Power Sources*. **2018**, *376*, 147-151.

# Chapter 5

# Revealing the role of liquid electrolytes in cycling of garnet-based solid-state lithium metal batteries

This chapter has been adapted from a research paper published in *Journal of Physical Chemistry C* (doi: 10.1021/acs.jpcc.2c02074).

## 5.1 Abstract

Solid-State lithium metal batteries (SS-LMBs) suffer from the very high resistance at the garnet electrolyte|cathode interface that hampers their commercialization. Herein, a carbonate-based liquid electrolyte (LE) is introduced at the interface of $Li_{6.5}La_{2.9}Ba_{0.1}Zr_{1.4}Ta_{0.6}O_{12}$ (LLBZTO) garnet|$LiNi_{0.6}Mn_{0.2}Co_{0.2}O_2$ (NMC 622) cathode to lower the interfacial resistance and improve the battery performance. In this work, we conducted a thorough study on the role of liquid electrolytes at the interface using Scanning Transmission X-ray Microscopy (STXM) associated with X-ray Absorption Spectroscopy (XAS). As a result, we have shown new data relating to the formation and the chemical composition of the two formed interphases: a solid-liquid electrolyte interphase (SLEI) and the cathode-electrolyte interphase (CEI). Furthermore, we have presented evidence that LE decomposes during cycling into fluoride species including LiF and $LaF_3$, oxides like $Li_2O$, and carbonates (e.g., $Li_2CO_3$) as the main components of *in situ*–formed SLEI. Based on the synergy between SLEI and CEI, we demonstrate that Li|garnet|LE|NMC 622 cells cycled with an initial discharge capacity of 168 mAh $g^{-1}$ and capacity retention of ~82% after 28 cycles. We expect our study of SLEI will accelerate the implementation of a new hybrid electrolyte (solid garnet and liquid electrolyte) approach in SSLMBs.

## 5.2 Introduction

Solid-State lithium metal batteries (SS-LMBs) enable higher power density and excellent safety compared to traditional lithium-ion batteries with flammable liquid-state electrolytes.[1] Inorganic solid-state electrolytes (SSEs) (e.g., perovskites, garnets, NASICON-type, etc.) are promising candidates that may provide high ionic conductivity and improved energy density. In particular, garnet-type $Li_7La_3Zr_2O_{12}$ (LLZO) SSEs have a high ionic conductivity in excess of 1 mS $cm^{-1}$ at room temperature and a wide electrochemical widow (~6 V vs. $Li/Li^+$).[1,2]

One of the formidable challenges is the large interfacial resistance between the garnet SSE and cathode material due to the rigidity of ceramics.[3,4] Poor solid-solid interface results in a decreased electrochemical contact area and insufficient interdiffusion of $Li^+$ ions, which leads to rapid capacity fade and battery failure.[3] The use of liquid electrolytes (LEs) in small quantities has been suggested as a possible solution either at the garnet SSE|cathode interface or as a component in the quasi-solid hybrid electrolytes to improve ionic transport in bulk or at the interface.[5,6,7,8] LEs can effectively fill and penetrate through the pores of the cathode material and SSEs.[9] Moreover, LEs could react either with the cathode to form the cathode-electrolyte interface (CEI) or with SSEs to build the solid-liquid electrolyte interface (SLEI).[10] The decomposition products at the SSE|LE interface appears as an additional contribution to the overall battery resistance, representing a major barrier to the implementation of hybrid solid-liquid batteries. SLEI also plays a significant role in regulating interfacial stability and $Li^+$ transportation, and profoundly influences the morphology and structural stability of electrodes.[11] Therefore, a stable CEI and SLEI could minimize the interfacial resistance and stabilize the $Li^+$ transportation between electrodes.[12] To date, some works have studied the composition and properties of SLEI.[13,14,15] The consensus is that SLEI promotes $Li^+$ transport at the interface and is closely linked to electrochemical performances.[13,14] Interestingly, Xu et al. highlighted the role of n-BuLi as an additive in $LiPF_6$ EC/DEC (50:50 v/v%)

that could retard the decomposition reaction of LEs and suppress the $Li^+/H^+$ exchange at the interface.[16]

To better understanding the role of LE in impacting the SLEI evolution and SS-LMBs performance during the cycling, therefore, we sought to elucidate the formation and stability of SLEI between $Li_{6.5}La_{2.9}Ba_{0.1}Zr_{1.4}Ta_{0.6}O_{12}$ (LLBZTO) garnet electrolyte and $LiNi_{0.6}Mn_{0.6}Co_{0.2}O_2$ (NMC 622) cathode material with Scanning Transmission X-ray Microscopy (STXM) and X-ray Absorption Spectroscopy (XAS). To the best of our knowledge, there is no report in the literature on the use of STXM, a nanoscale chemical imaging technique, to examine the composition and working mechanism of CEI and SLEI. We demonstrated that the coordination of CEI and SLEI stabilized the interfaces during the charge/discharge process. Moreover, we further explored and analyzed the formation, composition, and evolution of SLEI. The LE started to decompose and an ultrathin SLEI formed after the first cycle. More LE decompose with cycle increase, leading to increased values of total resistance and overpotential of the cell. The formation of SLEI functions similarly as well-known solid-electrolyte interphase in Li-ion batteries, tending to suppress the decomposition of LLBZTO SSEs and maintaining good conductivity within the cell.

## 5.3 Experimental section

### 5.3.1 Synthesis and characterization of garnet

*Synthesis*

Ba/Ta-doped garnet with the nominal composition of $Li_{6.5}La_{2.9}Ba_{0.1}Zr_{1.4}Ta_{0.6}O_{12}$ (LLBZTO), was prepared by conventional solid-state synthesis in air using stoichiometric amounts of the precursors. The precursor materials were $LiNO_3$ (99%), $La_2O_3$ (99.99%), Ba $(NO_3)_3$ (99.5%), $Ta_2O_5$ (99.5%), and $ZrO_2$ (99%) with a mass ratio of 38:36.4:2:10:13.8 were mixed by ball-milling (Pulverisette, Fritsch, Germany) at 200 rpm for 6h in 2-propanol. All chemicals were from Alfa Aesar. An excess of 10 wt.% $LiNO_3$ was added to the mixture to compensate for the $Li_2O$ volatilization during high temperature treatment.

After ball-milling, the mixture was dried in an oven at 120 °C to remove 2-propanol followed by a heat-treatment at 700 °C for 6h. The dried powder was ball-milled again in 2-propanol for 6h. The dried samples were ground using a mortar and pestle until a fine powder was obtained without agglomerations. Then the material was pressed into pellets using an isostatic press. The pellets were covered with mother powder (excess amount of pristine powder) in an alumina crucible and were sintered initially at 900 °C for 24h. Afterwards, the pellets were crushed, and ball milled. Finally, the sample was ground into fine powders and pressed into pellets under 180 kN for 1 min followed by annealing at 1100 °C/6h covered with the mother powder. The heating/cooling rate was kept at 10 ºC $min^{-1}$ for all the heat-treatments. Pellets were stored in an Argon-filled glove box to avoid the formation of $Li_2CO_3$.

*Material characterization*

The phase purity of garnet powder and electrolytes were identified using a Bruker D8 powder X-ray diffractometer (PXRD) with Cu-Kα radiation. The morphology and elemental analysis of the garnet surface was studied by scanning electron microscopy (Gemini 500) with EDX.

*Ionic conductivity of garnet electrolyte*

Conductive Au-epoxy paste was painted using brush on both sides of a garnet pellet as blocking electrodes (in ~5 μm thick) and then it was cured at 700 ˚C for 1h in air. Electrochemical impedance spectroscopy (EIS) was measured with an AC amplitude of 10 mV and frequency range from $10^4$ Hz to 0.1 Hz using a Solartron 1260 impedance analyzer. The EIS spectra were obtained from room temperature to 141 ˚C. The size of the pellet was ~10.7 mm in diameter and ~1.3 mm thick. The total ionic conductivity was calculated using $\sigma$ = L/RS, where L is the thickness of SSEs, R is the total resistance from EIS plot and S is the surface area.

### 5.3.2 Cell assembly and electrochemical characterization

*Cathode preparation*

To prepare the $LiNi_{0.6}Mn_{0.2}Co_{0.2}O_2$ (NMC 622) cathode laminate, NMC 622 powder, PVDF, and carbon black were dispersed in 1-methyl-2-pyrrolidinone (NMP) at a weight ratio of 90:5:5 and stirred using magnetic stirring overnight at room temperature. The slurry was coated on an aluminum foil with an active material loading of about 3 mg $cm^{-2}$. The cathode was dried at 85 °C under vacuum overnight to remove the solvent.

*Li|garnet|LE|NMC 622 cell assembly*

The Li foil was melted on one side of the garnet electrolyte pellet at 200 ˚C. Liquid electrolyte made of 20 $\mu$L of 1M $LiPF_6$ in EC/DEC (50:50 v/v %) was added between garnet and NMC 622 cathode. The cell was assembled into a 2032-type coin cell. Galvanostatic cycling was performed between 3 V-4.2 V at room temperature with different C rates using a Neware BTS4000 testing station. In contrast, cells assembled without the addition of liquid electrolyte cannot be cycled due to the large cell resistance.

### 5.3.3 Interfaces (CEI and SLEI) analysis

*STXM sample preparation*

The STXM samples were prepared using a Zeiss NVision 40 FIB-SEM by the same conventional lift-out and thinning preparation methods for TEM samples. However, due to the thickness of the layers (over 25 $\mu$m), the extractions needed to be significantly taller than a typical FIB-prepared TEM lamella, and this required extra clearance for a deeper undercut, a thicker top protection layer, careful adjustment of the over-tilt angle during thinning, and extra care to reduce warping and hole formation as the ion beam broadens over the longer distance of the sample height during thinning. The porosity of the sample and dis-similar sputtering rates of the various phases also add to the challenges of thinning these tall extractions. Thick support frames on the sides and bottom of the lamella were utilized to help maintain structural integrity of the extraction. The thinning was performed with the Ga ion beam acceleration voltage at 30 kV using milling lines of progressively

smaller beam currents down to 40 pA. Final cleaning steps were performed with the ion beam voltage at 10 kV and 5 kV using a glancing angle raster box with the stage tilted 8 degrees below the tilt angle of the thinning step.

*STXM data collection and analysis*

Experiments were carried out using the ambient STXM at the 10ID-1 SM beamline of the Canadian Light Source (CLS). The sample used in the experiment was a thin section of cathode electrode and LLZO of 200 nm thick prepared by the FIB milling as being descript in the above session. Chemical mapping was conducted by Principal Component Analysis-Cluster Analysis (PCA-CA) with the open-source software aXis2000 (McMaster University, Canada). This method will identify natural groups of spectra, and then calculate the average spectra and display the thickness maps associated with these spectra.

## 5.4 Results and discussion

### 5.4.1 Material characterizations of garnet powder and pellet

PXRD pattern of the LLBZTO is presented in Figure 5.1, showing a good agreement with the PXRD of $Li_5La_3Nb_2O_{12}$ with a cubic structure (space group $Ia\bar{3}d$) and no secondary phase. For comparison, cubic garnet-type structured $Li_5La_3Nb_2O_{12}$ is shown (PDF card No.: 00-045-0109). Besides, there is no peak of $Li_2CO_3$ at 23 degrees, proving the absence of $Li_2CO_3$ on the surface of LLBZTO.[17]

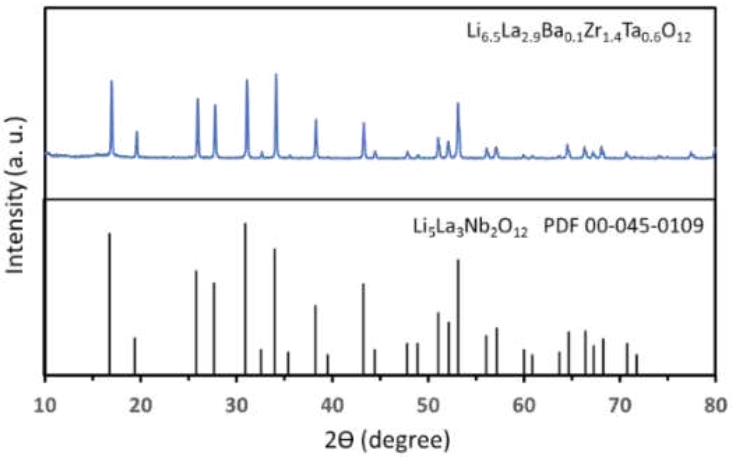


**Figure 5.1.** PXRD pattern of the final pellet.

The top view and cross-sectional SEM image and high-resolution EDX mapping of the LLBZTO pellet are shown in Figure 5.2 and Figure A10.1. Figure 5.2(a) confirms good densification (the average apparent density is 4.13 g $cm^{-3}$ as calculated in Table A9). A homogeneous distribution of core elements for LLBZTO are observed in Figure 5.2(b-f).

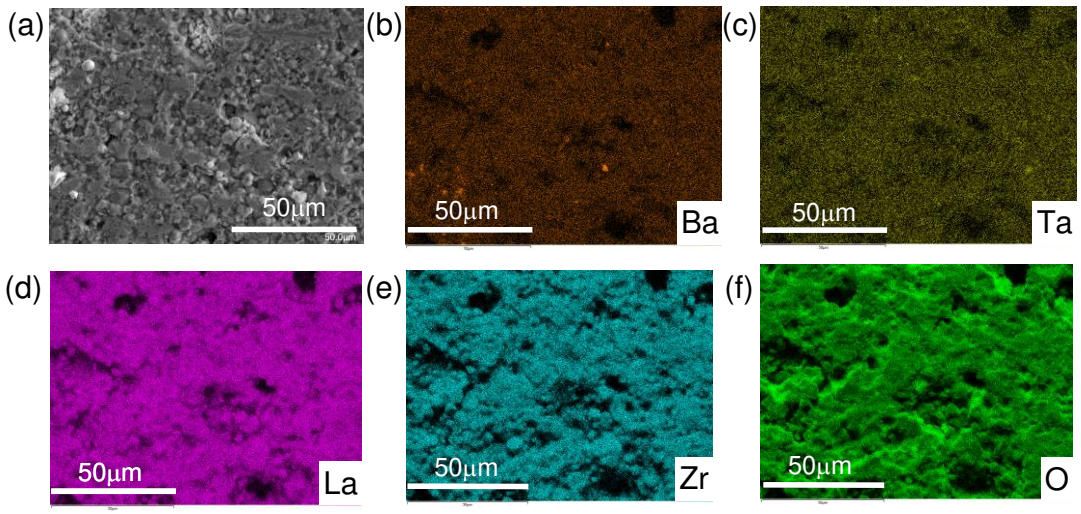


**Figure 5.2.** (a) SEM for the surface of LLBZTO SSEs; and (b-f) EDX analysis of Ba, Ta, La, Zr, and O elements.

### 5.4.2 Ionic conductivity of garnet electrolyte

The Nyquist plots of the Au|garnet|Au cell obtained at 24 ˚C -141 ˚C are shown in Figure 5.3(a). The total resistance (R) can be calculated from the intercept of the low-frequency tail. The total

ionic conductivity increases from $2\times10^{-4}$ S cm$^{-1}$ at room temperature to $6.27\times10^{-3}$ S cm$^{-1}$ at 141˚C, an impressive bulk $Li^+$ conductivity as reported previously.[18] The temperature-conductivity relationship can be expressed using an Arrhenius equation as plotted in Figure 5.3(b) and the activation energy has been calculated from the slope to be 0.35 eV which is in the range of other reported values for garnet-type SSEs.[19,20]

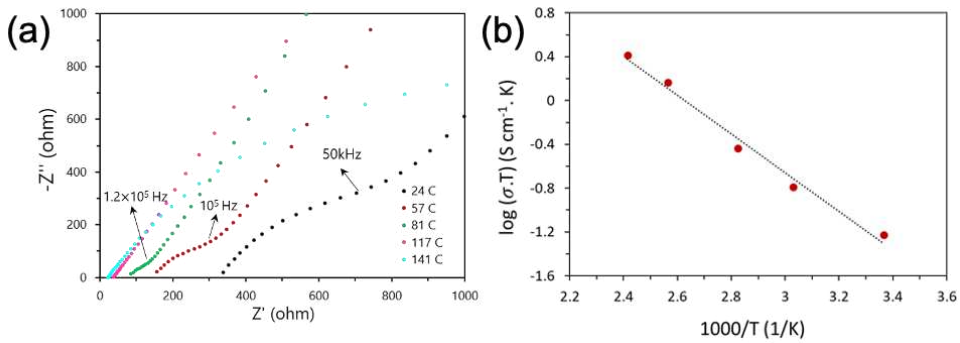


**Figure 5.3.** (a) The Nyquist plots of Au|garnet|Au cell at different temperatures; and (b) Temperature-dependence of Li ion conductivity in LLBZTO in the range of 24 ˚C -141 ˚C. Fitting circuit is (R1CPE1)(CPE2). R and CPE represent the resistor and the constant phase element, respectively.

### 5.4.3 Cycling performance of Li|LLBZTO|LE|NMC 622 cell

Figure 5.4(a) delineates the cycling performance of the Li|LLBZTO|LE|NMC 622 cell at a current density of ~0.05C (1C = 180 mAh g$^{-1}$). The initial discharge capacity is ~168 mAh g$^{-1}$ with a 1$^{st}$ cycle Coulombic efficiency (CE) of 90%. The specific capacity gradually decreases over cycling maintaining a capacity retention of around 82% calculated from 28 charge/discharge cycles and the cell failed at 29$^{th}$ cycle. Charge/discharge profiles of the cell is presented in Figure 5.4(b) with a working voltage at around 3.7 V. The electrochemical performance of the cell at higher current rates is shown in Figure 5.4(c). The discharge capacity drops to 160, 153, and 146 mAh g$^{-1}$ when the current density is increased to 0.1C, 0.15C, and 0.2C, respectively.

The oxidation of carbonate solvents (especially EC) always causes impedance increase and battery failure at a high operating voltage.[21] An excellent initial CE after the 1$^{st}$ cycle reflects a stable $Li^+$

transportation between electrodes. The lower CE and much higher voltage polarization for 28 cycles with capacity decay suggest that larger resistance is developed at the electrode interfaces because of the decomposition of electrolyte solvent.[21] However, increased overpotential and total resistance may be related to the formation of SLEI and CEI interfaces during the cycling process, as discussed in later sections.[14]

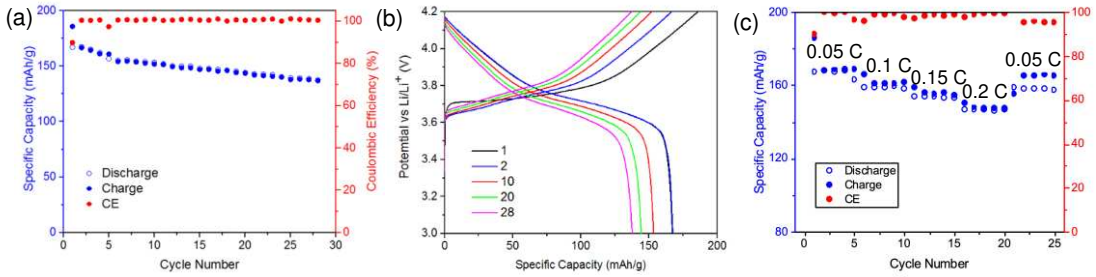


**Figure 5.4.** (a) Cycling performance at ~0.05C; (b) Galvanostatic charge/discharge curves at ~0.05C; and (c) Rate performance at different C rates.

### 5.4.4 The formation of SLEI interface at different discharge states

To investigate the SLEI formation at the interface for different cycles of charge/discharge, two slices consisting of LLBZTO pellets and NMC 622 cathode was extracted from the cell. The extracted two slices were washed in DEC by dipping to remove the precipitation of electrolyte salts. Furthermore, two thin sections containing NMC 622 and LLBZTO were lifted out along the electrode thickness direction via FIB and were characterized via SEM. Slice 1 and slice 2 were scrutinized at the discharged state after 1 (S_01) and 28 (S_02) cycles, respectively. There is not LE residue in the opened cell, as confirmed in Figure S2. To identify the differences in morphological features, cross-sectional view SEM images were taken over both slices.

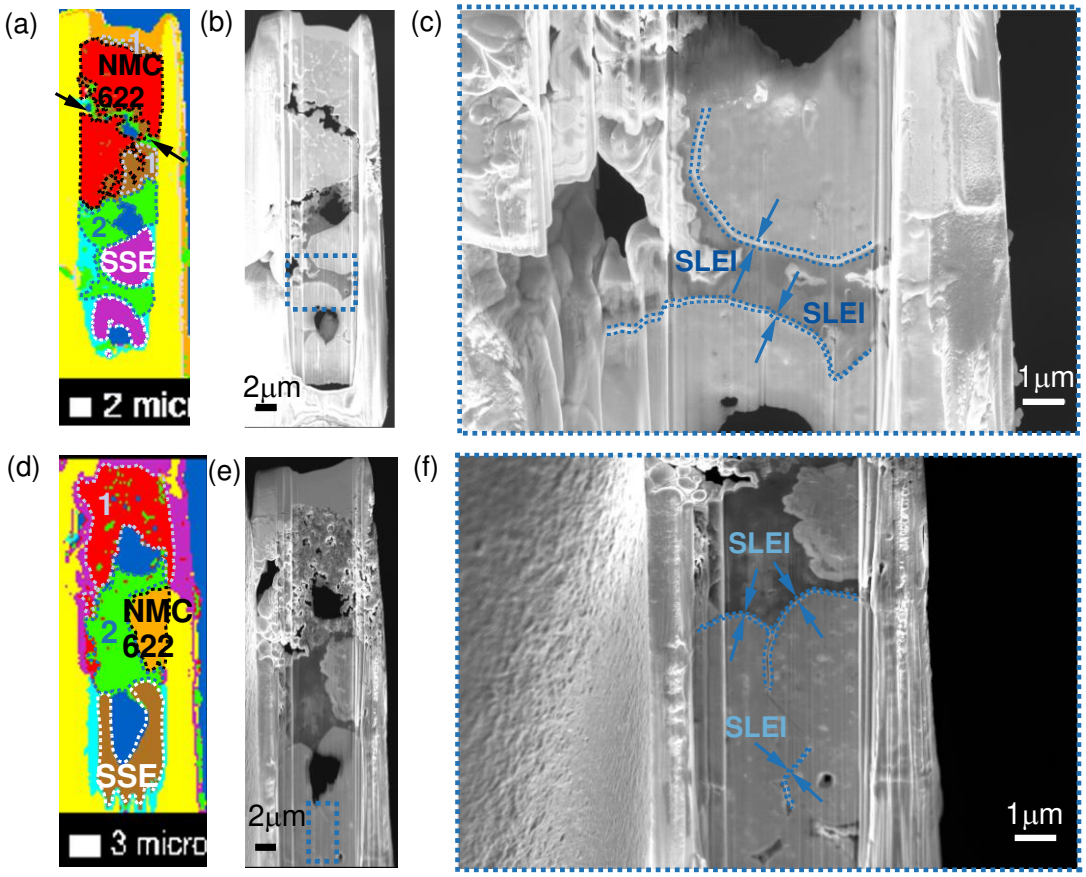


**Figure 5.5.** STXM and FIB-SEM images for NMC 622|LE|LLBZTO at the different charge states of: (a-c) after 1 cycle: (c) is zoomed-in region marked by a white dotted rectangle from FIB-SEM Figure 5.5(b); and (d-f) after 28 cycles: (f) is zoomed-in region marked by a white dotted rectangle from FIB-SEM Figure 5.5(e).

S_01 and S_02 were analyzed by as shown in STXM in Figure 5.5 and XAS method to probe the local chemistry for each region as indicated in Figure 5.6. In the STXM image with XAS spectra for both slices, different colors represent different chemical phases with different oxidation states of transition metal (TM) cations, accompanying with specific peaks for each colorful region. The STXM image (in Figure 5.5(a)) labels the region of the secondary particle of NMC 622. The peak at ~851 eV for SSE and region 2 (the interface between NMC 622 and SSE) is due to La $M_4$-edge transition cations.[22] Compared to the interface regions for S_01 and S_02, SSE has relatively higher intensity of La elements. Specifically, the spectrum of F K-edge at ~691.4 eV is only shown in the interface (numbered as region 2 in Figure 5.5(a)) where LE was added. We will get more insights

into this interface in the Section 5.4.5. Then region 1 is claimed as the surface of the bulk NMC 622 cathode in contact with LE.

In Figure 5.5(b) and (c), the clear contrast difference on the surface of NMC 622 and secondary LLBZTO particles (zoomed-in regions with arrows in Figure 5.5(c)) demonstrates that the existence of SLEI and CEI (in Figure A10.2). A thin SLEI (~several nm thick) forms after the first cycle of discharge. The growth and expansion of SLEI grew with increase of charge/discharge cycles, as evidenced by a thicker SLEI on the surface of LLBZTO and even boundaries in Figure 5.5(d-f).

The core elements, Mn and Ni, of NMC 622 are visible in spectra of Figure 5.6(a), supporting the distinguish of NMC 622 in Figure 5.6(a). In Figure 5.6(b), F K-edge at ~691.4 eV is identified in region 1 that might be attributed to the decomposed product of LE at the current collector side as supported by Figure A10.3.[23,24] The specific peaks of Mn $L_3$-edge (at ~633 eV) and Ni L-edge (at ~853 eV) confirms the presence of NMC 622 secondary particles as highlighted in Figure 5.5(c). A careful comparison of Mn $L_3$ and Ni $L_3$ between NMC after 1 cycle and NMC after 28 cycles shows the reduction of Mn and Ni in NMC after longer cycling. Reduced elements indicate that the structural change is caused by electrochemical cycling.[25]

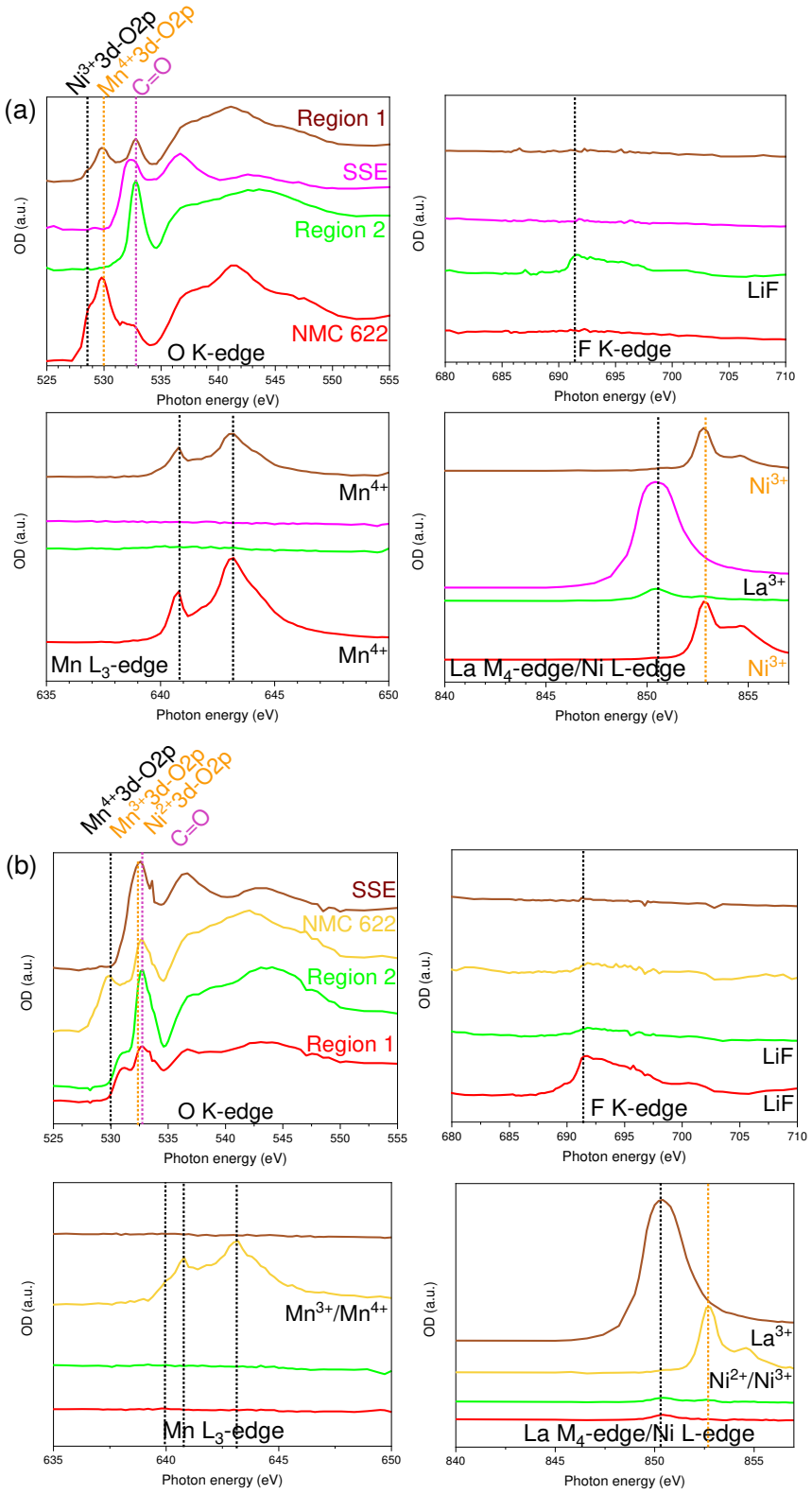


**Figure 5.6.** XAS spectra of O, Mn, F, La, Ni in different regions extracted from STXM results for: (a) S_01; and (b) S_02.

### 5.4.5 Components and mechanism analysis of the SLEI

To investigate the components of SLEI, XAS analysis was performed for S_01 and S_02 as plotted in Figure 5.7. The comparisons of chemical elements among interfaces in both slices help trace the composition of SLEI. Specific photon energy of O 1s at ~533 eV featured a sharp peak as shown in the interface of Figure 5.7(a) and (b), could from trace water of LE and during sample preparation. A good matching of standard LiF peak in Figure 5.7(c) suggests (F K-edge at~691.4 eV) that a more abundant LiF distributes in SLEI. Moreover, small LiF peak on the surface of LLBZTO verifies the wettability of LE on SSEs and decomposition of $LiPF_6$ happened even after 1 cycle. On the other hand, a higher signal of LiF in SLEI after 28 cycles (in Figure 5.7(d), F K-edge) reveals that more LiF species precipitate with increased cycles. The peak at ~851 eV in Figure 5.7(e) and (f) proves the existence of $La^{3+}$ species in SSE.

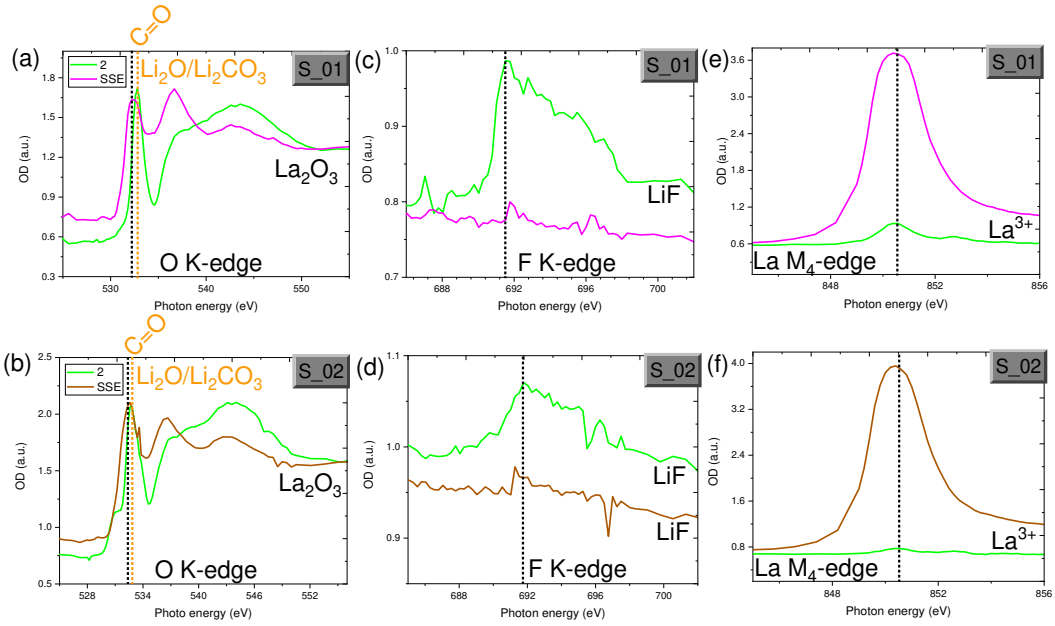


**Figure 5.7.** Detailed comparison by XAS analysis for SLEI at different discharge states of S_01 and S_02 among consecutive series of: (a-b) O K-edge; (c-d) F K-edge; and (e-f) La $M_4$-edge.

The known LiF formation reactions from decomposition of $LiPF_6$-based LEs are:

$$LiPF_6 + H_2O \rightarrow LiF + POF_3 + 2HF$$[23]

$$LiPF_6 \rightarrow LiF + PF_5$$[24]

The generated LiF layer will continue to grow until it is thick and dense enough to prevent the internal SSEs from further attack by LE.[13] In addition, oxygen (not fluorine) is enriched in the interfaces, in which the results validates the presence of oxides (e.g., $Li_2O$) at the interface.[26] This claim further evidenced by the absence of the peak around 531 eV (corresponds to $Li_2O_2$ formation) in Figure 5.7(a) and (b) of O K-edge.

Small quantities of LE at the SSE|cathode interface that penetrate into SSEs can function as an ionic conduit for fast Li-ion transfer kinetics. $LiPF_6$ tends to decompose to LiF, which could penetrate through the LLBZTO pellet. This trend signifies that dissociated LiF as a contributor to evolve denser and thicker SLEI during the cycling process. One characteristic of LLBZTO is its decomposition when in contact with LE. When LLBZTO garnets are in contact with LE, a SLEI may form due to electrolyte decomposition.[14] Decomposed $La^{3+}$ arises from LLBZTO agglomerated on the surface and tends to diffuse into SLEI. Besides, $La^{3+}$ may have reacted with the LE and is oxidized to produce $LaF_3$ and $La_2O_3$ in SLEI. These poor Li-ion conductors (e.g., $La_2O_3$) in the SLEI might increase interfacial resistance over time.[9] Strong Lewis acids possibly activate decomposition reactions in the SSEs, such as Li ions.[27]

The schematic in Figure 5.8 depicts a possible SLEI formation and evolution process accompanying with LE depletion during the cycle life. As illustrated in Figure 5.8(a), LE spreads to wet the surface of LLBZTO SSEs and enhances the interfacial contact with the NMC 622 cathode after cell assembly. Additionally, uneven surfaces on the SSEs become relatively flat when LE is immersed into micro voids. In Figure 5.8(b), after the first cycle, $LiPF_6$ decomposes to LiF, and LiF in turn sustains on the SSE to participate in the preliminary SLEI construction. In addition, LLBZTO is unstable and has a tendency to dissociate upon contact with LE.[28] Released $La^{3+}$ oxidizes on the surface of the LLBZTO particle and participate in the evolution of SLEI. Figure 5.8(c) exhibits the SLEI grows and expands along the whole grain boundaries of SSE after 28 cycles. Note that LE completely dries that suggests a transformation in the dominate compositions

of the SSE|cathode interface. Increased LiF and $Li_2O$ validates higher contents of inorganic species in a thicker SLEI that enables better interface compatibility and long-term battery cycling. Finally, SLEI consisting of fluorides, $La_2O_3$, $LaF_3$, and $Li_2O$ plus LE decomposition residuals ensure a contact at SSE|cathode interface.

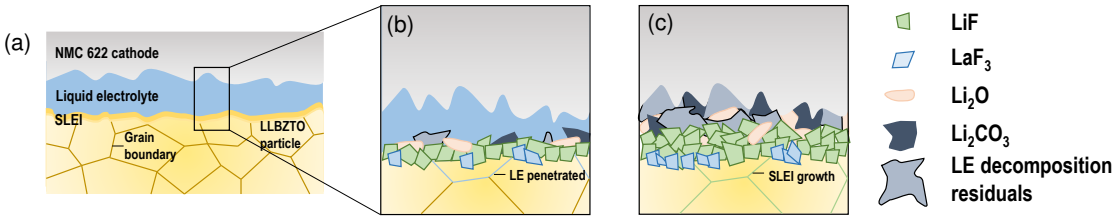


**Figure 5.8.** Schematic that illustrates the formation and expansion of SLEI: (a) Added LE effectively wetted the LLBZTO|NMC 622 interface after cell assembly; (b) LE remained at the interface after 1 cycle; and (c) LE exhausted and a thicker SLEI build-up after 28 cycles.

### 5.4.6 The reaction between LE and NMC 622 after 1 cycle

According to Figure 5.5(a), regions 1 are supposed to be where the LE contacts and reacts with near-surface NMC 622 secondary particles. In Figure 5.6(a) the O K-edge spectra at ~528.5 eV in NMC 622 region corresponds to the $Ni^{3+}$ 3*d*-O2*p* hybridized state. A relatively broader peak at ~530 eV could be attributed to the $Mn^{4+}$ 3*d*-O2*p* hybridization. The peak at ~532 eV arises primarily from the $Mn^{3+}$ and $Ni^{2+}$ 3*d*-O2*p* and indicates $Mn^{4+}$ and $Ni^{3+}$ in the pristine NMC622 was reduced at the surface after 28 cycles. In the interface, the sharp peak at ~533 eV indicates the existence of oxygen species in this region. It could be assigned to O 1s to $\pi^*$ (C=O) transition because no significant amount of 3*d* transition metal is detectable in this region, which is contradicted to that in region 1 in Figure 5.5.[29] The existence of $\pi^*$ (C=O) transition indicates the presence of carbonate in SLEI.[29,30]

Surface etching starts at the beginning of cycling and tends to take place along the grain boundary of the NMC 622 particle.[31] The primary grains of the NMC particle are closely packed but one obvious crack where one arrow pointed out in Figure 5.5(a) appears along the middle line of the

secondary NMC 622 particle. The morphology change of the cathode surface indicates a reaction with the LE and the formation of a CEI.

Propagated cracks may induce to inhomogeneous lithiation/delithiation and result in battery failure.[32] The larger intensity of O K-edge in the interface of SSE|NMC 622 in Figure 5.6(b) corresponds to more oxides produced during the cycling process.[29,30,33] The poor oxidation stability of 1M $LiPF_6$ in EC/DEC may cause more LE to remain in the cathode interphase.[33]

Figure 5.9 compares the different composition of the bulk NMC 622 and near-surface regions after 1 cycle. Figure 5.9(a) indicates the transition state of core elements in NMC 622, Ni and Mn, with O elements. Specifically, F (bump of slope feature at ~685 eV) can infiltrate into the secondary NMC 622 and trigger the formation of transition metal fluoride (TM-F) in Figure 5.9(b).[33,36] The permeation of LEs into the cathode material would retard the serious reduction of $Mn^{4+}$ and suppress the voltage fade.[25] This describes that TM-F bonds can not only raise the energy barrier of the EC ring-opening reactions, but positively affect the electrochemical performance of the NMC with EC-based electrolyte.[37] Core elements of NMC 622 are also visible in Figure 5.9(c) and (d).

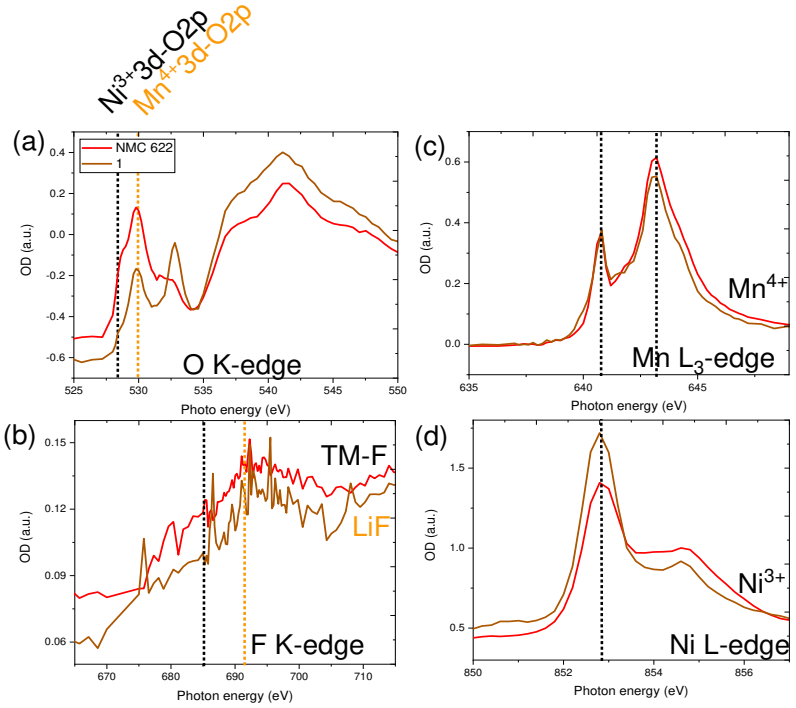

**Figure 5.9.** Detailed comparison by XAS analysis among NMC region: (a) O K-edge; (b) F K-edge; (c) Mn $L_3$-edge; and (d) Ni L-edge.

## 5.5 Conclusions

Our work has studied the role of small quantities of $LiPF_6$-based liquid electrolytes at the interface between garnet SSEs and NMC 622 cathode. We firstly conducted high resolution STXM with the XAS analysis to explore this interface after different cycles. The results verified the formation of a SLEI at the solidified interface resulting from the decomposition products of the LE. SLEI began to be established after the first cycle and became thicker during cycling process. No residual LE was found by visual inspection at 28 cycles of the cell. A SLEI dominantly consists of LiF, $LaF_3$, $Li_2CO_3$, and $Li_2O$.

The battery failure after 28 cycles might be mainly attributed to the LE decomposition during the cycling process. Possible inhomogeneous contact between the SSE and the cathode could result from the LE decomposition. Furthermore, the contact loss at the interface may be responsible for the high internal resistance of the cycled battery. In the future work, to maintain sufficient contact at the SSE|cathode interface, it is essential to investigate the proper amount of LE addition that would minimize the interface resistance at the same time. Additionally, further optimizations of LE (e.g., high salt/solvent molar ratio or with additives) are required to improve the chemical stability of SLEI.[38-42] Hence, we believe that the hybrid electrolyte approach to form a more robust SLEI could resolve the interfacial issues and enable a long-term performance of solid-state lithium metal batteries.

## 5.6 References

1. Han, X.; Gong, Y.; Fu, K. K.; He, X.; Hitz, G. T.; Dai, J.; Pearse, A.; Liu, B.; Wang, H.; Rubloff, G.; Mo, Y.; Hu, L. Negating interfacial impedance in garnet-based solid-state Li metal batteries. *Nature Materials*. **2017**, *16*, 572-579.

2. Pervez, S. A.; Cambaz, M. A.; Thangadurai, V.; Fichtner, M. Interface in solid-state lithium battery: challenges, progress, and outlook. *ACS Applied Materials & Interfaces*. **2019**, *11*, 22029-22050.
3. Barai, P.; Rojas, T.; Narayanan, B.; Ngo, A. T.; Curtiss, L. A.; Srinivasan, V. Investigation of Delamination-Induced Performance Decay at the Cathode/LLZO Interface. *Chemistry of Materials*. **2021**, *33*, 5527-5541.
4. Fu, K. K.; Gong, Y.; Liu, B.; Zhu, Y.; Xu, S.; Yao, Y.; Lup, W.; Wang, C.; Lacey, S.D.; Dai, J.; Chen, Y.; Hu, L. Toward garnet electrolyte–based Li metal batteries: An ultrathin, highly effective, artificial solid-state electrolyte/metallic Li interface. *Science Advances*. **2017**, *3*, e1601659.
5. Xie, Z.; Wu, Z.; An, X.; Yoshida, A.; Wang, Z.; Hao, X.; Abudula, A.; Guan, G. Bifunctional ionic liquid and conducting ceramic co-assisted solid polymer electrolyte membrane for quasi-solid-state lithium metal batteries. *Journal of Membrane Science*. **2019**, *586*, 122-129.
6. Zhai, Y.; Yang, G.; Zeng, Z.; Song, S.; Li, S.; Hu, N.; Tang, W.; Wen, Z.; Lu, L.; Molenda, J. Composite Hybrid Quasi-Solid Electrolyte for High-Energy Lithium Metal Batteries. *ACS Applied Energy Materials*. **2021**, *4*, 7973-7982.
7. Ji, Y.; Zhou, C.; Lin, F.; Li, B.; Yang, F.; Zhu, H.; Duan, J.; Chen, Z. Submicron-sized Nb-doped lithium garnet for high ionic conductivity solid electrolyte and performance of quasi-solid-state lithium battery. *Materials*. **2020**, *13*, 560.
8. Qiu, G.; Sun, C. A quasi-solid composite electrolyte with dual salts for dendrite-free lithium metal batteries. *New Journal of Chemistry*. **2020**, *44*, 1817-1824.
9. Wang, C.; Sun, Q.; Liu, Y.; Zhao, Y.; Li, X.; Lin, X.; Banis, M.N.; Li, M.; Li, W.; Adair, K.R.; Wang, D.; Sun, X. Boosting the performance of lithium batteries with solid-liquid

hybrid electrolytes: Interfacial properties and effects of liquid electrolytes. *Nano Energy*. **2018**, *48*, 35-43.

10. Tang, J.; Wang, L.; Tian, C.; Huang, T.; Zeng, L.; Yu, A. Comparative performance of LiFePO4 and LiNi0. 6Co0. 2Mn0. 2O2 cathode materials for lithium batteries with solid–liquid hybrid electrolytes. *Journal of Power Sources*. **2021**, *515*, 230639.
11. Li, X.; Cong, L.; Ma, S.; Shi, S.; Li, Y.; Li, S.; Chen, S.; Zheng, C.; Sun, L.; Liu, Y.; Xie, H. Low Resistance and High Stable Solid–Liquid Electrolyte Interphases Enable High-Voltage Solid-State Lithium Metal Batteries. *Advanced Functional Materials*. **2021**, *31*, 2010611.
12. Zhao, C. Z.; Zhao, B. C.; Yan, C.; Zhang, X. Q.; Huang, J. Q.; Mo, Y.; Xu, X.; Li, H.; Zhang, Q. Liquid phase therapy to solid electrolyte–electrode interface in solid-state Li metal batteries: a review. *Energy Storage Materials*. **2020**, *24*, 75-84.
13. Leng, J.; Wang, H.; Li, Y.; Xiao, Z.; Wang, S.; Zhang, Z.; Tang, Z. Insight into The Solid-liquid Electrolyte Interphase between Li6. 4La3Zr1. 4Ta0. 6O12 and LiPF6-based Liquid Electrolyte. *Applied Surface Science*. **2021**, *575*, 151638.
14. Gupta, A.; Kazyak, E.; Dasgupta, N. P.; Sakamoto, J. Electrochemical and surface chemistry analysis of lithium lanthanum zirconium tantalum oxide (LLZTO)/liquid electrolyte (LE) interfaces. *Journal of Power Sources*. **2020**, *474*, 228598.
15. Liu, J.; Gao, X.; Hartley, G. O.; Rees, G. J.; Gong, C.; Richter, F. H.; Janek, J.; Xia, Y.; Robertson, A.W.; Johnson, L.R.; Bruce, P. G. The interface between Li6. 5La3Zr1. 5Ta0. 5O12 and liquid electrolyte. *Joule*. **2020**, *4*, 101-108.
16. Xu, B.; Duan, H.; Liu, H.; Wang, C. A.; Zhong, S. Stabilization of garnet/liquid electrolyte interface using superbase additives for hybrid Li batteries. *ACS Applied Materials & Interfaces*. **2017**, *9*, 21077-21082.

17. Huo, H.; Chen, Y.; Zhao, N.; Lin, X.; Luo, J.; Yang, X.; Liu, Y.; Guo, X.; Sun, X. In-situ formed Li2CO3-free garnet/Li interface by rapid acid treatment for dendrite-free solid-state batteries. *Nano Energy*. **2019**, *61*, 119-125.
18. Kammampata, S. P.; Yamada, H.; Ito, T.; Paul, R.; Thangadurai, V. The activation entropy for ionic conduction and critical current density for Li charge transfer in novel garnet-type Li6.5La2.9A0.1Zr1.4Ta0.6O12 (A= Ca, Sr, Ba) solid electrolytes. *Journal of Materials Chemistry A*. **2020**, *8*, 2581-2590.
19. Li, Y.; Han, J. T.; Wang, C. A.; Xie, H.; Goodenough, J. B. Optimizing Li+ conductivity in a garnet framework. *Journal of Materials Chemistry*. **2012**, *22*, 15357-15361.
20. Thangadurai, V.; Narayanan, S.; Pinzaru, D. Garnet-type solid-state fast Li ion conductors for Li batteries: critical review. *Chemical Society Reviews*. **2014**, *43*, 4714-4727.
21. Fan, X.; Chen, L.; Ji, X.; Deng, T.; Hou, S.; Chen, J.; Zheng, J.; Wang, F.; Jiang, J.; Xu, K.; Wang, C. Highly fluorinated interphases enable high-voltage Li-metal batteries. *Chem*. **2018**, *4*, 174-185.
22. Meyers, D. J. Engineering the Ground State of Complex Oxides. Ph.D. Dissertation, University of Arkansas, Fayetteville, **2015**.
23. Niu, K. Y.; Lin, F.; Fang, L.; Nordlund, D.; Tao, R.; Weng, T. C.; Doeff, M.M.; Zheng, H. Structural and chemical evolution of amorphous nickel iron complex hydroxide upon lithiation/delithiation. *Chemistry of Materials*. **2015**, *27*, 1583-1589.d
24. Alemu, T.; Wang, F. M. In situ electrochemical synchrotron radiation for Li-ion batteries. *Journal of Synchrotron Radiation*. **2018**, *25*, 151-165.
25. Sun, G.; Zhao, C.; Yu, F. D.; Yu, R.; Wang, J.; Zhou, J.; Shao, G.; Sun, X.; Wang, Z. B. In-situ surface chemical and structural self-reconstruction strategy enables high performance of Li-rich cathode. *Nano Energy*. **2021**, *79*, 105459.

26. Kim, M. S.; Zhang, Z.; Rudnicki, P. E.; Yu, Z.; Wang, J.; Wang, H.; Oyakhire, S.T.; Chen, Y.; Kin, S.C.; Zhang, W.; Boyle, D.T.; Cui, Y. Suspension electrolyte with modified Li+ solvation environment for lithium metal batteries. *Nature Materials*. **2022,** *21*, 445-454.
27. Busche, M. R.; Drossel, T.; Leichtweiss, T.; Weber, D. A.; Falk, M.; Schneider, M.; Reich, M.L.; Sommer, H.; Adelhelm, P.; Janek, J. Dynamic formation of a solid-liquid electrolyte interphase and its consequences for hybrid-battery concepts. *Nature Chemistry*. **2016**, *8*, 426-434.
28. Pervez, S. A.; Kim, G.; Vinayan, B. P.; Cambaz, M. A.; Kuenzel, M.; Hekmatfar, M.; Fichtner, M.; Passerini, S. Overcoming the interfacial limitations imposed by the solid–solid interface in solid-state batteries using ionic liquid-based interlayers. *Small*. **2020**, *16*, 2000279.
29. Besli, M. M.; Usubelli, C.; Metzger, M.; Pande, V.; Harry, K.; Nordlund, D.; Sainio, S.; Christensen, J.; Doeff, M.M.; Kuppan, S. Effect of liquid electrolyte soaking on the interfacial resistance of Li7La3Zr2O12 for all-solid-state lithium batteries. *ACS Applied Materials & Interfaces*. **2020**, *12*, 20605-20612.
30. Zhang, N.; Long, X.; Wang, Z.; Yu, P.; Han, F.; Fu, J.; Ren, G.; Wu, Y.; Zheng, S.; Huang, W.; Wang, C.; Liu, X. Mechanism study on the interfacial stability of a lithium garnet-type oxide electrolyte against cathode materials. *ACS Applied Energy Materials*. **2018**, *1*, 5968-5976.
31. Shi, T.; Zhang, Y. Q.; Tu, Q.; Wang, Y.; Scott, M. C.; Ceder, G. Characterization of mechanical degradation in an all-solid-state battery cathode. *Journal of Materials Chemistry A*. **2020**, *8*, 17399-17404.
32. Wu, H.: Qin, C.: Wang, K.: Han, X.; Sui, M.; Yan, P. Revealing two distinctive intergranular cracking mechanisms of Ni-rich layered cathode by cross-sectional scanning electron microscopy. *Journal of Power Sources*. **2021**, *503*, 230066.

33. Cheng, L.; Wu, C. H.; Jarry, A.; Chen, W.; Ye, Y.; Zhu, J.; Kostecki, R.; Persson, K.; Guo, J.; Salneron, M.; Chen, G.; Doeff, M. Interrelationships among grain size, surface composition, air stability, and interfacial resistance of Al-substituted Li7La3Zr2O12 solid electrolytes. *ACS Applied Materials & Interfaces*. ***2015***, *7*, 17649-17655.

34. Fan, X.; Chen, L.; Borodin, O.; Ji, X.; Chen, J.; Hou, S.; Deng, T.; Zheng, J.; Yang, C.; Liou, S.C.; Amine, K. Non-flammable electrolyte enables Li-metal batteries with aggressive cathode chemistries. *Nature Nanotechnology*. **2018**, *13*, 715-722.

35. Zhang, J. N.; Li, Q.; Wang, Y.; Zheng, J.; Yu, X.; Li, H. Dynamic evolution of cathode electrolyte interphase (CEI) on high voltage LiCoO2 cathode and its interaction with Li anode. *Energy Storage Materials*. **2018**, *14*, 1-7.

36. Li, Q.; Wang, Y.; Wang, X.; Sun, X.; Zhang, J. N.; Yu, X.; Li, H. Investigations on the fundamental process of cathode electrolyte interphase formation and evolution of high-voltage cathodes. *ACS Applied Materials & Interfaces*. **2019**, *12*, 2319-2326.

37. Xu, S.; Luo, G.; Jacobs, R.; Fang, S.; Mahanthappa, M. K.; Hamers, R. J.; Morgan, D. Ab initio modeling of electrolyte molecule ethylene carbonate decomposition reaction on Li (Ni, Mn, Co)O2 cathode surface. *ACS Applied Materials & Interfaces*. **2017**, *9*, 20545-20553.

38. Doi, T.; Masuhara, R.; Hashinokuchi, M.; Shimizu, Y.; Inaba, M. Concentrated LiPF6/PC electrolyte solutions for 5-V LiNi0.5Mn1.5O4 positive electrode in lithium-ion batteries. *Electrochimica Acta*. **2016**, *209*, 219-224.

39. Hagos, T. T.; Thirumalraj, B.; Huang, C. J.; Abrha, L. H.; Hagos, T. M.; Berhe, G. B.; Cherng, J.; Chiu, S.F.; Su, W.N.; Hwang, B. J. Locally concentrated LiPF6 in a carbonate-based electrolyte with fluoroethylene carbonate as a diluent for anode-free lithium metal batteries. *ACS Applied Materials & Interfaces*. **2019**, *11*, 9955-9963.

40. Beyene, T. T.; Jote, B. A.; Wondimkun, Z. T.; Olbassa, B. W.; Huang, C. J.; Thirumalraj, B.; Wang, C.H.; Su, W.N.; Dai, H.; Hwang, B. J. Effects of concentrated salt and resting protocol on solid electrolyte interface formation for improved cycle stability of anode-free lithium metal batteries. *ACS Applied Materials & Interfaces*. **2019**, *11*, 31962-31971.
41. Wotango, A. S.; Su, W. N.; Leggesse, E. G.; Haregewoin, A. M.; Lin, M. H.; Zegeye, T. A.; Cheng, J.H.; Hwang, B. J. Improved interfacial properties of MCMB electrode by 1-(trimethylsilyl) imidazole as new electrolyte additive to suppress LiPF6 decomposition. *ACS Applied Materials & Interfaces*. **2017**, *9*, 2410-2420.
42. Kawamura, T.; Okada, S.; Yamaki, J. I. Decomposition reaction of LiPF6-based electrolytes for lithium ion cells. *Journal of Power Sources*. **2006**, *156*, 547-554.

# Chapter 6

# Elucidating the origins of rapid capacity fade in hybrid garnet-based solid-state lithium metal batteries

This chapter has been adapted from a research paper published in *Journal of Physical Chemistry C* (doi: 10.1021/acs.jpcc.3c05419).

## 6.1 Abstract

Hybrid solid-state lithium metal batteries (SS-LMBs) incorporate small amounts of a liquid electrolyte (LE) to overcome interfacial instabilities between cathodes and solid-state electrolytes. However, hybrid SS-LMBs suffer from a rapid capacity fade after few cycles that are not yet fully understood. Here, to shed light on this phenomenon and mechanism, we report the use of *ex situ* post-mortem analysis of Li|$Li_{6.5}La_{2.9}Ba_{0.1}Zr_{1.4}Ta_{0.6}O_{12}$|LE|$LiNi_{0.6}Mn_{0.2}Co_{0.2}O_2$ (NMC 622) cells by scanning transmission X-ray microscopy (STXM) combined transmission with ptychography and X-ray absorption spectroscopy (XAS). We find that the mechanism is complex and that microstructural and chemical phase changes, oxygen vacancies formation associated with transition metal dissolution, as well as contributions from the cathode-electrolyte interphase (CEI) and solid-liquid electrolyte interphase (SLEI) play a key role in the deterioration of battery performance of hybrid SS-LMBs. We expect that our findings will help advance the development of hybrid SS-LMBs by further optimization of the liquid and solid electrolyte formulations and cell structure.

## 6.2 Introduction

Growing demand for energy storage in electronics and transportation have sparked widespread research in solid-state lithium metal batteries (SS-LMBs) as a safer and higher energy density alternative to conventional Li-ion batteries. Substituting an inorganic solid-state electrolyte (SSE) for an organic liquid electrolyte (LE) removes the risk of flammability even at elevated

temperatures. Garnet ($Li_7La_3Zr_2O_{12}$, LLZO) is chemically stable towards metallic Li.[1,2] A tiny amount ($\mu$L) of LE is added as the cathode interfacial layer to improve the interfacial contact while an *in situ* solid-liquid electrolyte interphase (SLEI) as a result of the reaction between the LE and the SSE during the charge/discharge process.[5,6,7,8,9,10]

SS-LMBs are projected to perform with improved energy density, especially when coupled with high capacity (200 mAh $g^{-1}$-250 mAh $g^{-1}$) cathodes (e.g., $LiNi_{1-x-y}Mn_xCo_yO_2$, 1-x-y≥0.5, NMC). Likewise, NMC cathodes go through considerable capacity degradation especially when being cycled at high voltages (>4.2 V versus $Li/Li^+$).[11,12] In the case of NMC in liquid Li-ion batteries, various mechanisms have been identified, such as surface chemical instability, mechanical destruction, transition metal (TM) dissolution, and side reactions between the cathode and LEs.[12,13,14,15] These inherent drawbacks, in combination with one another often lead to cell degradation and safety hazards. Additionally, the surface of NMC particles undergoes a phase transformation, typically accompanied by oxygen loss and a volumetric change in the lattice structure.[16,17] In comparison, the dominant causes of capacity loss in SS-LMBs are insufficient interfacial contact and large polarization at the SSE|electrodes interface.[18] Small elastic deformation of SSEs results in non-uniform accommodation of NMC cathode volume change during Li-ion extraction/re-insertion.[19] The micro stress created during cycling causes mechanical and structural cracking to the cathode materials (e.g., cracking).[20] Compared to LEs, SSEs cannot "infiltrate" into the cracks because of the slower kinetics of Li-ion diffusion, which leads to severe battery failure even at low cycling rates.[4] Besides, the robust and conformal in situ formation of a cathode electrolyte interphase (CEI) is another critical factor in stabilizing the NMC performance and hindering the side reactions with electrolytes during cycling.[21,22]

However, in the hybrid system, the formation of SLEI introduces extra complexity to distinguish the influences of interfacial stability on the cathode performance. Furthermore, it is vital to simultaneously monitor the microstructural and chemical phase change in the NMC particles and

correlated them to any battery performance degradation. To the best of our knowledge, there has been no systematic investigation of the capacity deterioration (capacity retention <80%) in the hybrid SS-LMBs using NMC cathodes. In this work, for the first time, scanning transmission X-ray microscopy (STXM) associated with ptychography and X-ray absorption spectroscopy (XAS) were applied to qualitatively evaluate the capacity fade in a hybrid garnet-based SS-LMB with the $LiNi_{0.6}Mn_{0.6}Co_{0.2}O_2$ (NMC 622) cathode at the nanoscale. The high-resolution STXM ptychography visualizes the microstructural evolution in the secondary and primary particles at different discharged states. In addition, using the direct principal component analysis (PCA) map of the phase distribution and XAS spectra for the NMC 622 particles, we disclose the chemical heterogeneity of TMs from the bulk to the particle edge and oxygen vacancies penetration into the primary particles. Furthermore, we hypothesize that another key factor in the capacity decay could be the formation of chemically resistive CEI and SLEI layers, corresponding to increased interfacial resistance of SSE|NMC 622 and cell overpotential. Our work highlights the role of the cathode in the hybrid SS-LMBs, revealing the mechanism underlying the poor cycling performance in the cell.

## 6.3 Methods

### 6.3.1 Li|garnet|LE|NMC 622 hybrid cell assembly and electrochemical characterization

The detailed preparation of the garnet electrolyte (thickness = 0.8 mm, diameter = 11 mm) has been reported elsewhere.[6] To make the NMC 622 cathode, a mixture of NMC 622 powder, PVDF, and carbon black was combined at a weight ratio of 90:5:5. The mixture was stirred using magnetic stirring overnight at room temperature in 1-methyl-2-pyrrolidinone (NMP). Subsequently, the resulting slurry was applied onto an aluminum foil with an active material loading of approximately 3 mg $cm^{-2}$, followed by vacuum drying at 85 °C overnight to eliminate the solvent. The film was used without any calendaring process. The Li foil was applied to one side of the garnet pellet at 200 ˚C. 20 $\mu$L of the commercial liquid electrolyte (1M $LiPF_6$ in EC/DEC, 50:50 v/v %) was added to wet the interface between the garnet and the NMC cathode. The cell was assembled into a 2032-

type coin cell. Galvanostatic cycling was carried out between 3 V to 4.2 V voltage window at room temperature with various C rates by a Neware BTS4000 testing station.

### 6.3.2 STXM sample preparation and X-ray ptychography analysis

Briefly, the same lift-out and thinning preparation approaches for TEM samples were used to prepare the STXM samples (Zeiss NVision 40 FIB-SEM). STXM experiments were performed using the 101d-1 SM beamline (under a vacuum pressure of $10^{-2}$ mbar) of the Canadian Light Source (CLS) at conventional transmission and ptychography mode with a higher spatial resolution of 10 nm. The X-ray beam is focused by a Fresnel zone plate (ZP) into a tiny spot that passes through an order sorting aperture (OSA) to choose the first order diffracted light and filter out the stray light. The beam is further irradiated on the sample at the focal point of the zone plate. Convention STXM was collected by a photomultiplier tube (PMT) to form a pixel in a 2D image which is realized by a raster scan of the sample. Ptychography STXM was gathered by recording X-ray scattering images of samples using a CMOS or CCD detector.[23] To extract the chemical phases and their associated transmission soft-XAS spectra, the built-in principal component analysis (PCA) module of the open-source software aXis2000 (Adam P. Hitchcock group, McMaster University) was used.

## 6.4 Results and discussion

### 6.4.1 Cyling performance of Li|garnet|LE|NMC 622 hybrid cell

The performance of the Li|garnet|LE|NMC 622 hybrid cell has been verified and the cell shows an initial discharge capacity of ~168 mAh $g^{-1}$ with a 1st Coulombic efficiency of 89.9%) in Figure A11.1, is similar to what has been reported previously.[6] After 28 charge/discharge cycles, the cell indicates a capacity retention of ~82% while the Coulombic efficiency remains at ~100%. It should be noted that the Coulombic efficiency is marginally greater than 100% in many cycles. While the exact reason is unclear, side reactions leading to excess discharge capacity, or measurement errors

are possible reasons for this observation. Although various degradation factors have an impact on the cell resistance increase, in this work, we specifically focus on the NMC degradation phenomena and mechanisms upon cycling.

### 6.4.2 Microstructural evolution of discharged NMC 622 after cycling

The hybrid cells were disassembled after cycling and electrodes were recuperated. Two thin slices from two cells (cycled after 1 and 28 times) were lifted out by FIB along the cathode thickness direction. Microstructural characterization was carried out using FIB-SEM and high-resolution STXM, which reveals the presence of micro-cracks in both slices (designated NMC_01 and NMC_28). Yellow arrows in Figure 6.1(a)-(b) show a void that appears to be traveling through the spherical-shape secondary particle (consists of agglomerated primary particles) as well as cracks (in Figure A11.2(a)) and may have developed during the fabrication of the cathode laminate. Moreover, as white arrows indicate in Figure 6.1(b) as well as Figure A11.2(b), the degree of cracking gradually declines away from the outer surface and the cracks propagate into the central regions of the secondary particle. One assumption of this microstructural damage at the particle level (associated with Figure A11.2(a)-(b)) could be produced during the synthesis before long-time cycling.[24] In particular, the particles stacking and forming localized stress would be higher for a high-loading and thick electrode.[25] As a result, the NMC cathode has cracked or even fractured into isolated and/or deactivated primary particles from the conducting network, resulting in a capacity loss in the first few cycles. Therefore, a certain cathode loading is required to suppress the particle cracking and fracture.[25] Single-crystalline structures of the NMC particles and atomic layer deposition coating are normally recommended in raw powders for cathode fabrication to minimize this effect.[26,27] However, in this case when the cell was disassembled, the electrode coating detached from the current collector, which suggests a micro-delamination may have already occurred.

The 1-cycled primary particles show no obvious cracks (in Figure 6.1(c)). In contrast, as seen in Figure 6.1(d)-(e) and Figure A11.3(a)-(b), no large porosity is observed in the secondary particles

from NMC_28. However, as specified by the white arrows in Figure 6.1(e), some narrow intergranular gaps initiate from the particle surface and spread along the grain boundaries into the interior of the particle. In the core region (in Figure 6.1(e)), more micro cracks were observed between differently oriented primary particles. The primary particles in the central regions exhibit more random crystal orientations compared with those in the outer surface, causing more non-uniform deformations and micro-cracks.[28,29] Poor electrochemical contact among primary particles can consequently deteriorate cell performance.[29] Additionally, primary particles are developing some intragranular cracks, as shown by yellow arrows in Figure 6.1(f). These microcracks may have formed as a synergetic result of ongoing oxygen losses, internal micro-strain, and anisotropic volume fluctuation during Li extraction/re-insertion.[30,31]

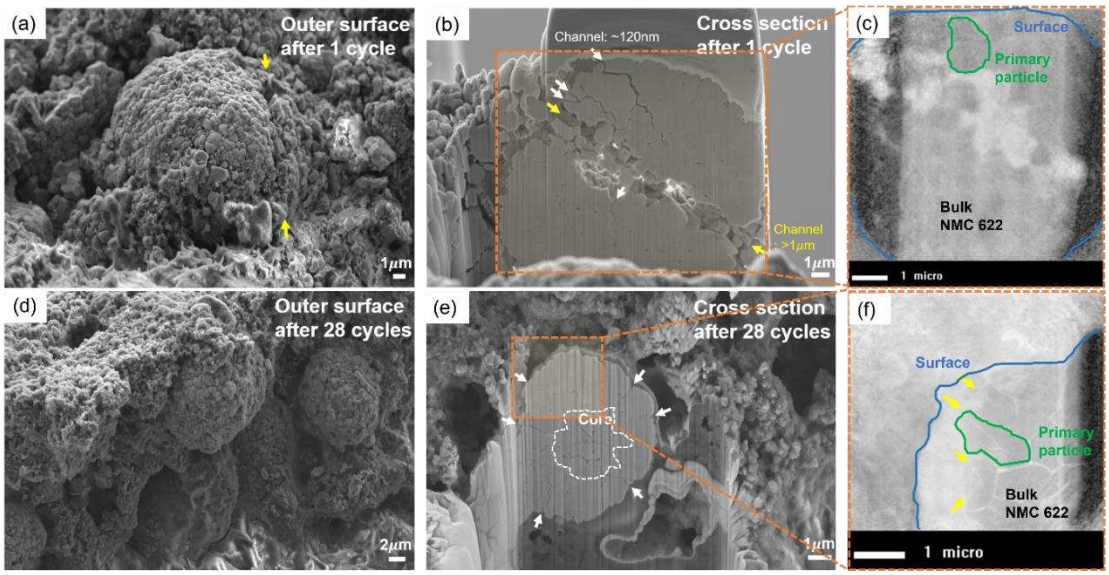


**Figure 6.1.** FIB-SEM and STXM images of NMC 622 secondary particles after different cycles. (a) Top-view NMC 622 secondary particles after 1 cycle. (b) Cross-sectional view NMC 622 secondary particles after 1 cycle. (c) Zoomed-in view of cross-sectional NMC 622 secondary particles from Figure 6.1(b) using high-resolution STXM. (d) Top-view NMC 622 secondary particles after 28 cycles. (e) Cross-sectional view NMC 622 secondary particles after 28 cycles. (f) Zoomed-in view of cross-sectional NMC 622 secondary particles from Figure 6.1(e) using high-resolution STXM. The "surface" as specified in Figure 6.1(c) and (f), is the regions around

the outer edge of cross-cut secondary particles. The exposed regions after FIB lift-out correspond to the internal bulk NMC 622.

### 6.4.3 Chemical phase evolution of discharged NMC 622 after cycling

To access the local chemistry in the bulk of secondary particles, STXM together with PCA was performed for both slices. Obtained STXM and XAS results for NMC_01 are displayed in Figure 6.2. Different colors (the right image in Figure 6.2(a)) reflect different chemical phases with different oxidation states of TM cations, correlating to specific peaks for each colorful region (Figure 6.2(b)). In Figure 6.2(c), the peak intensity of oxygen absorption is substantially different at the surface (red areas) and the bulk (green areas). The peaks of O K-edge at ~528.5 eV ($Ni^{3+}$*3d*-O*2p*) and ~530 eV ($Mn^{4+}$*3d*-O*2p*) almost vanish for the outer surface, indicating significant oxygen loss and the creation of oxygen vacancies on the particle surface. The lower Mn $L_3$ intensity (in Figure 6.2(d)) for the red spectrum further suggests that some surface $Mn^{4+}$ species are reduced and both $Mn^{3+}$ (at ~643 eV) along with $Mn^{2+}$ species (at ~641 eV) exist. The specific peak of F K-edge at ~691.4 eV can be assigned to LiF species from LE decomposition in the first cycle, as depicted in Figure 6.2(e), which exclusively originates at the surface region (including the exposed surface along the porosity). This result proves that the added LE can easily wet the cathode surface during the first cycle and penetrate the bulk region through the pores. In other words, the defective cathode directly exposed the particle surface to the LE and exhibited decreased TM contents.[12] As clearly observed in Figure A11.4, the Ni $L_3$-edge and Mn $L_3$-edge signal are detected at the interface between the garnet and the NMC 622 cathode, suggesting that the NMC cathode leaches out TMs after the initial cycle and would result in early-stage capacity attenuation. Figure 6.2(c) depicts a low-intensity peak O K-edge at ~533 eV ($Ni^{2+}$*3d*-O*2p*) inside the particle, which is matched by a low value of the Ni $L_3/L_2$ ratio in Figure 6.2(f). Both signatures show a decrease in the Ni valence state at the NMC 622 surface region after 1 cycle.

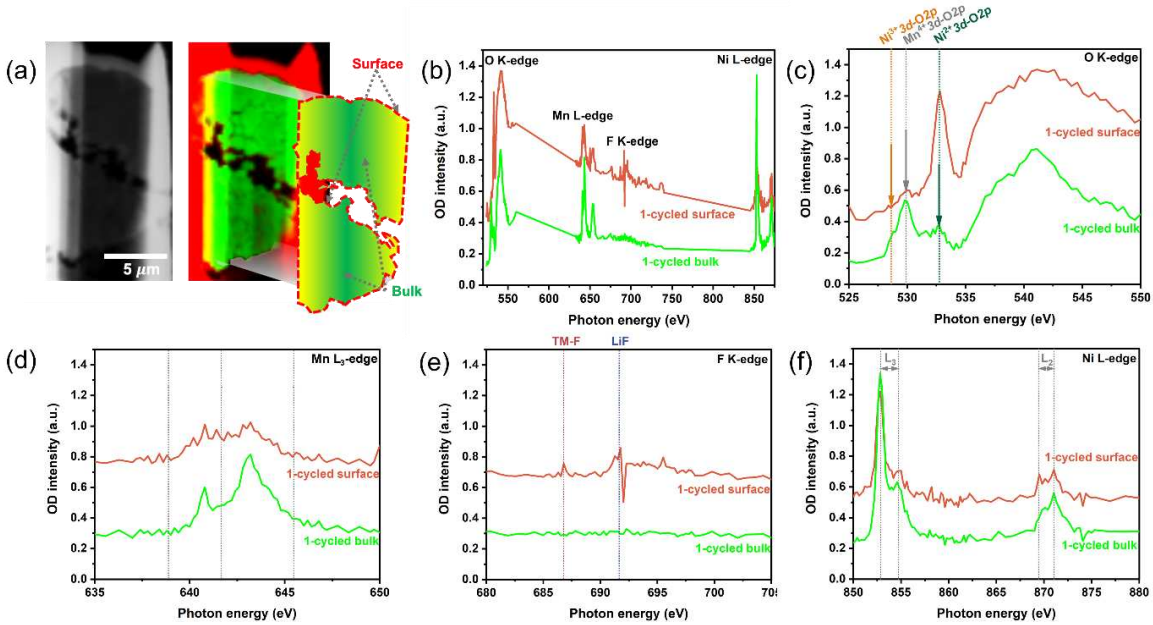


**Figure 6.2.** (a) STXM image and PCA map for the NMC 622 secondary particle from NMC_01. The "surface" is the regions around the outer edge of cross-cut secondary particles after 1 cycle (including the exposed surface along the porosity). The exposed regions after FIB lift-out correspond to the internal bulk NMC 622 as pointed out in Figure 6.2(a). (b)-(f) Comparison of the XAS spectra of (b) wide survey; (c) O K-edge; (d) Mn $L_3$-edge; (e) F K-edge; and (f) Ni L-edge, respectively, at the surface and bulk regions of the secondary particle as distinguished by the red and green colors in Figure 6.2(a).

Figure 6.3 shows the microstructural morphology of the 28-cycled secondary particle (STXM image in Figure 6.3(a)) and its local chemical distribution probed by XAS results (wide spectra in Figure 6.3(b)). A greater peak intensity of O K-edge at ~533 eV (in Figure 6.3(c)) indicates that more $Ni^{2+}$ species exist on the particle surface after 28 cycles, which is consistent with continuous oxygen loss from the bulk (green areas) to the surface (orange areas). With a higher Mn $L_3$ intensity for the orange spectrum in Figure 6.3(d), $Mn^{4+}$ with reduced $Mn^{3+}$ (high peak at ~643 eV) and $Mn^{2+}$ (low peak at ~641 eV) species are primarily maintained in the bulk region. As the cycle increases, more decomposed LE products, including $Li_2O$, $Li_2CO_3$, and LiF species are visible on the surface. LiF species (F K-edge at ~691.4 eV) are detected in the bulk region (in Figure 6.3(e)), probably due to LE localized decomposition in the fractured cathode particle. The signal of Ni L-edge in

Figure 6.3(f) is not apparent on the surface, which may be because the focused region consists of the SSE|NMC 622 interface.

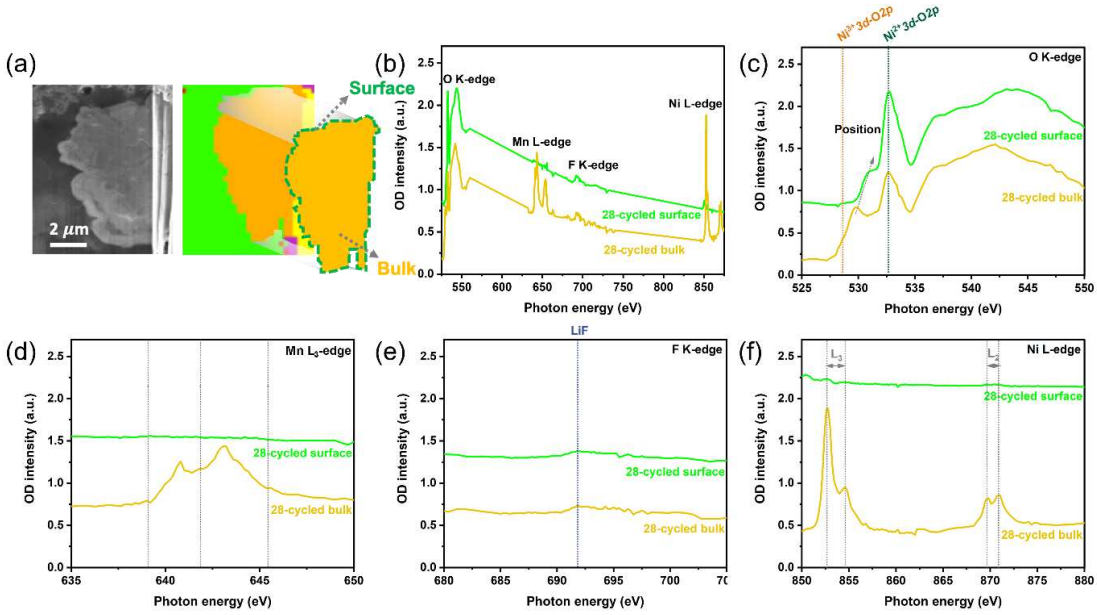


**Figure 6.3.** (a) STXM image and PCA map for the NMC 622 secondary particle from NMC_28. The "surface" is the regions around the outer edge of cross-cut secondary particles after 28 cycles. The exposed regions after FIB lift-out correspond to the internal bulk NMC 622 as pointed out in Figure 6.3(a). (b)-(f) Comparison of the XAS spectra of (b) wide survey; (c) O K-edge; (d) Mn $L_3$-edge; (e) F K-edge; and (f) Ni L-edge, respectively, at the surface and bulk regions of the secondary particle as distinguished by the green and orange colors in Figure 6.3(a).

Accompanied by the TM dissolution, the formation of the CEI after the initial cycle may block the Li-ion transport onto the surface, facilitating the surface degradation of the cracked cathode.[32] Besides, cracked cathode particles cannot maintain the CEI integrity; more LE thereby would be consumed to regenerate it. A thick CEI would decrease the ionic conductivity and simultaneously increase the interfacial resistance of the Li-ion re-insertion into the particle surface, leading to increased overpotential and total cell impedance. Capacity degradation could occur as a combined consequence of a net reduction reaction and crystal structural damage.[12] In terms of the cycling performance, a relatively low value of the 1$^{st}$ Coulombic efficiency (~90% as reported previously)

represents the irreversible capacity loss upon the early-stage cycling primarily owing to the formation of the chemically resistive CEI.[6]

The consensus from literatures suggests the oxidation state of Ni almost remain homogeneous in the pristine NMC 622 particles from the surface to the bulk.[33,34,35,36] To examine the distribution of chemical phases in the secondary particles from NMC_01, STXM combined with PCA qualitatively distinguished between $Ni^{3+}$ rich areas (green) and $Ni^{2+}$ rich areas (red) in Figure 6.4(a)-(b). Most primary particles are rich in $Ni^{3+}$; while minor particles are passivated by $Ni^{2+}$. More $Ni^{2+}$ species distribute along the exposed surface of the porosity, as supported by a higher-intensity peak of the $Ni^{2+}$*3d*-O2*p* (at ~533 eV) in Figure 6.4(c). This finding suggests that some primary particles are initially over delithiated and not restored to their fully lithiated state after 1 cycle, indicating the poor cycling stability and increased overpotential of the NMC 622 in the hybrid system.[33] Additionally, the chemical phase heterogeneity and the evolution of the internal strain might have exacerbated microstructural changes in the electrode.[38,39]

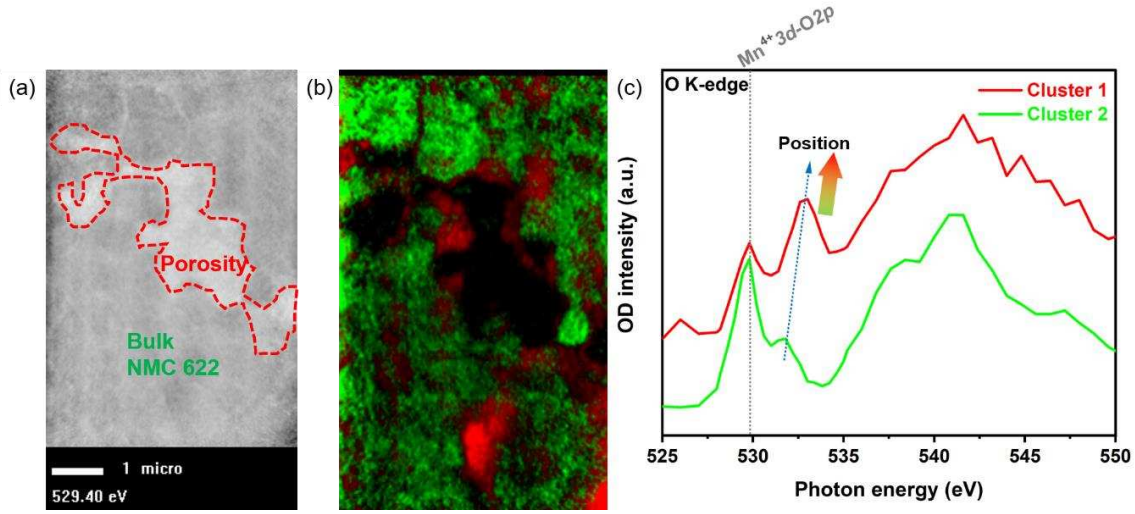


**Figure 6.4.** (a) STXM image for the large porosity from NMC_01. (b) PCA map with the Ni local element distribution for the same region in Figure 6.4(a). (c) XAS spectra of O K-edge in the distinguished regions from Figure 6.4(b). Cluster 1 is the spectrum for the exposed surface along the porosity. Cluster 2 is the spectrum for the bulk regions.

### 6.4.4 Heterogeneous phase distribution of discharged NMC 622 after 28 cycles

The bulk 1-cycled NMC shows homogeneous TM and TM-O distribution in Figure 6.1(a) and thus no further PCA is required. The STXM image with PCA map and the XAS spectra in Figure 6.5 display clear differences in chemical phase distribution inside the particles from NMC_28. XAS results from repeated STXM (Figure A11.5) demonstrate that there is no apparent radiation damage to the garnet and NMC particles. STXM imaging under specific X-ray energy can map out elemental distribution (i.e., more elements in the darker black regions in a ptychography STXM amplitude image). The bulk particles (represented by the darkest color in Figure 6.5(a) and the red color in Figure 6.5(b)) exhibit the highest-intensity peaks of both $Mn^{4+}$*3d*-O2*p* and $Ni^{2+}$*3d*-O2*p* in Figure 6.5(c). Reduced TM contents signify a considerable amount of oxygen loss in the primary particles that are agglomerated at the particle surface (cluster 3), which corresponds to the lowest signal of TM-O peaks in the blue region in Figure 6.5(b).

As illustrated in Figure 6.5(d)-(f), the greatest signal of TM-F (F K-edge at ~686.4 eV) and LiF (F K-edge at ~691.4 eV) peaks are visible at the cathode surface (especially concentrated on cluster 4). TM-F tends to accumulate at the cathode surface and diffuse into the cathode lattice in prolonged cycles.[23] The production of TM-F may increase the energy barrier for the EC ring-opening process and deteriorate the cell performance at prolonged cycles.[23] Furthermore, continuous oxygen loss produces results in the preferential TMs reduction and oxygen vacancies formation along the cracks.[40,41] The probability of parasitic reactions is increased by these fractured primary particles processing enlarged surface areas. Interestingly, grain-boundary regions between adjacent primary particles are quite clear, and more oxygen is released at the surface of the secondary particles (thickness of ~50 nm).

As supported by the darkest color in Figure 6.5(g), the Mn $L_3$-edge peak in cluster 1 of Figure 5(h) has the maximum intensity in Figure 6.5(i), which confirms that the Mn species was kept in a high-oxidation state ($Mn^{4+}$) in the bulk after 28 cycles. The Mn species in several primary particles are partially reduced at the surface and diffuse between the nearby particles, as implied by the lack of

visible grain boundaries observed in the green regions (cluster 2 in Figure 6.5(b)). As a result, the Mn reduction is concentrated at the outer particle surface (cluster 3 in Figure 6.5(h)), which also supports that oxygen release occurs simultaneously. The STXM in Figure 5(j) and PCA map in Figure 6.5(k) show that $Ni^{3+}/Ni^{2+}$ species are heterogeneously distributed in the primary particles close to the particle edge. According to a low-intensity peak of the blue region in Figure 6.5(l), $Ni^{3+}$ species aggregated at the surface are progressively reduced, which is accompanied by the creation of more oxygen vacancies that penetrate the individual primary particles. Compared with the surface and the outer edge regions, the Ni $L_3$-edge spectrum of the bulk exhibits a ~0.3 eV edge energy shift toward higher energy, which reflects an oxidation increase for Ni. A higher peak intensity ratio of $Ni^{3+}/Ni^{2+}$ indicates that the surface region has a deeper delithiatation level than other areas, corresponding to a serious delithiation heterogeneity in the 28-cycled cathode.

The lower oxidation state of the Ni at the outer surface may be due to more Mn being reduced here after 28 cycles, as evidenced by a high-intensity peak of cluster 2 in Figure 6.5(e). This allows Mn to compensate more charge during the delithation process, whereas less charge compensation is required from Ni cations. Based on these results, it is possible that the major oxygen release forms around Ni and that its reduction is more irreversible than Mn. We hypothesize that in the relatively short-term cycling, primary particles that had agglomerated at the outer surface had been over delithaited due to the LE attack and decomposition mainly after 1 cycle. Ni migration did not happen during the lithiation process in prolonged cycling.[42] Additionally, progressive oxygen release is invariably linked to the surface phase transformation and disordering of TM cations, which are related to irreversible capacity loss.[17] By accommodating lattice variation between neighboring primary particles, cation disordering may accelerate the generation of oxygen vacancy at the same time.[42]

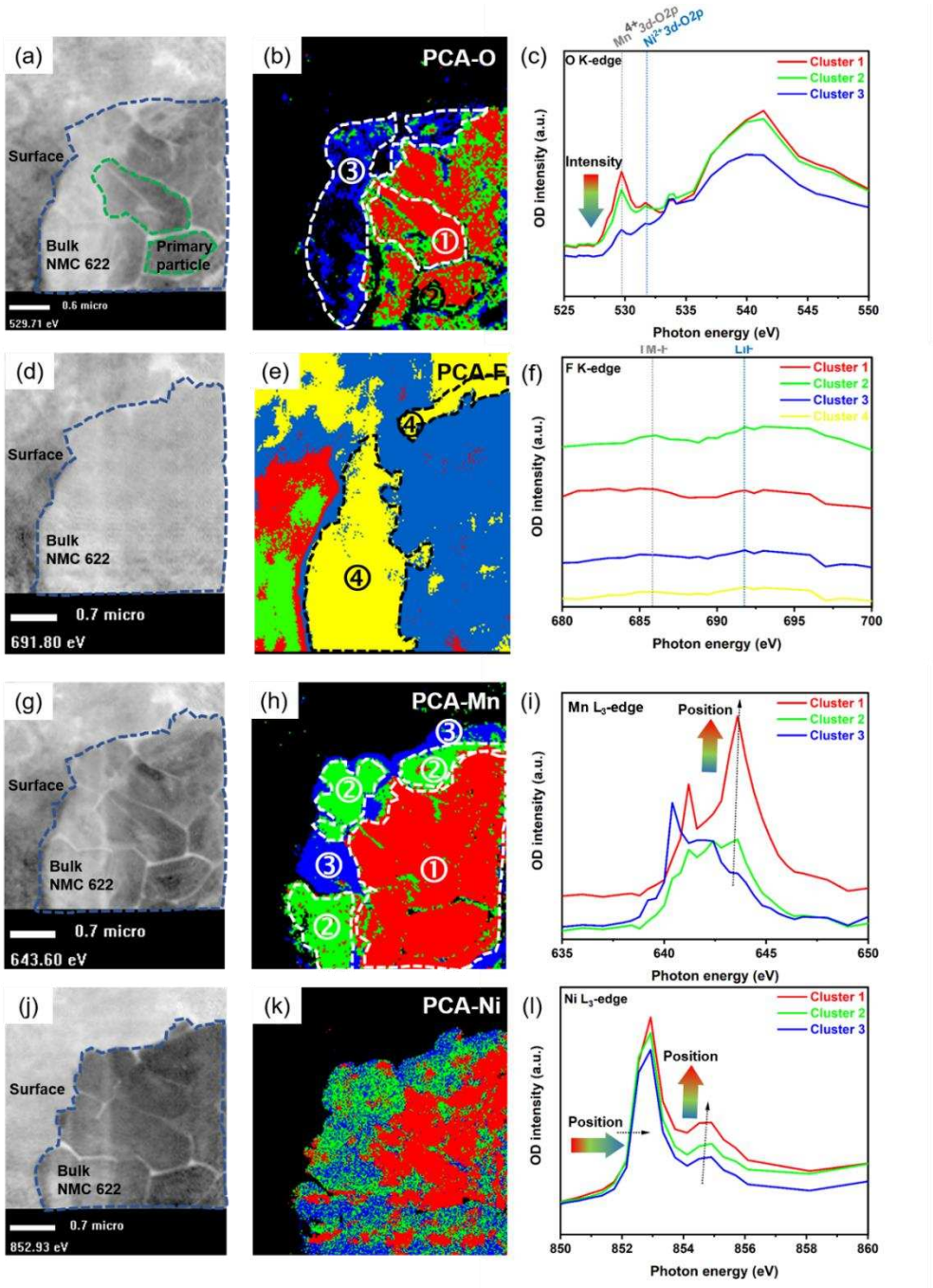


**Figure 6.5.** Ptychography STXM and XAS analysis of 28-cycled cathode from NMC_28 (a) Ptychography STXM amplitude image at the TM-O K-edge. (b) Elemental distribution mapping from Figure 6.5(a). (c) XAS spectra of the TM-O K-edge. (d) Ptychography STXM amplitude image at the F K-edge. (e) Elemental distribution mapping from Figure 6.5(d). (f) XAS spectra of the F K-edge. (g) Ptychography STXM amplitude image at the Mn $L_3$-edge. (h) Elemental distribution mapping from Figure 6.5(g). (i) XAS spectra of the Mn $L_3$-edge. (j) Ptychography

STXM amplitude image at the Ni $L_3$-edge. (k) Elemental distribution mapping from Figure 6.5(j). (l) XAS spectra of the Ni $L_3$-edge. The "surface" as specified Figure 6.5(a), (d), (g) and (j) is the regions around the outer edge of cross-cut secondary particles. The exposed regions after FIB lift-out correspond to the internal bulk NMC 622.

### 6.4.5 SLEI effects in discharged NMC 622 after cycling

For NMC_01, XAS results from the STXM (Figure 6.6(a)) and the specific photon energy of O K-edge in Figure 6.6(b) has a sharp peak at ~532.5 eV. A high-intensity peak signal at the interface suggests that oxygen is enriched between garnet and NMC 622, majorly resulting from the LE decomposition after the initial cycle. The generation of HF is known to occur from LE decomposition, and the presence of $H^+$ causes TM dissolution by attacking the cathode surface.[12] The identical peak intensities for the cathode surface and interface regions in Figure 6.6(c) provide evidence that La species dissolve from the garnet when in contact with LE. After 28 cycles, the SLEI on the garnet surface thickens and becomes increasingly enriched with decomposed LE byproducts (such as $Li_2O$ and $Li_2CO_3$ species) (as interpreted from the STXM and XAS spectra in Figure 6.6(d)-(f)). An increased value of the ratio O/La OD intensities (in Figure 6.6(g)-(h)) suggest that La species may re-deposit onto the SSE surface during the 1$^{st}$ cycle. Diffused $La^{3+}$ species were maintained at the interface region; whereas less $La^{3+}$ (a lower peak intensity indicated in Figure 6.6(f)) was dissociated from the garnet during the cycling, as confirmed by a higher value of the O/La ratio for NMC_28 (in Figure 6.6(g)-(h)). The fact that no detected La $M_4$-edge signal in Figure 6.2 and Figure 6.3 proves that no decomposed $La^{3+}$ from the SSE reaches the surface of the NMC cathode. Interestingly, TMs species are visible at the surface of SSE (in Figure A11.6). Such a chemically resistive SLEI with dissolute TMs would increase the interfacial resistance and partially affect the cathode performance.

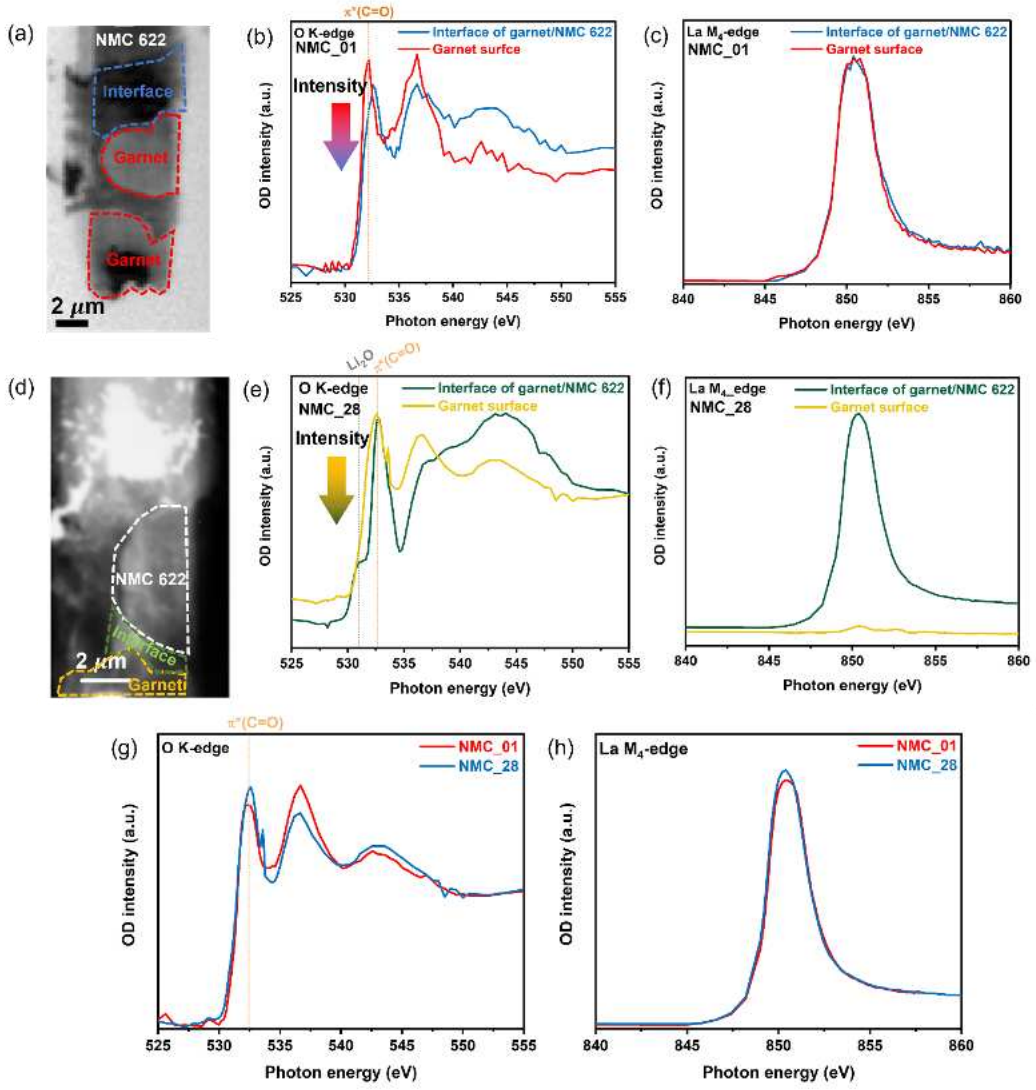


**Figure 6.6.** Comparison of STXM and XAS spectra between NMC_01 and NMC_28 (a) STXM image of NMC_01 (b)-(c) XAS spectra obtained from Figure 6.6(a) (including the surface and bulk regions) of O K-edge and La $M_4$-edge. (d) STXM image of NMC_28. (e)-(f) XAS spectra obtained from Figure 6.6(d) of O K-edge and La $M_4$-edge. (g) Comparisons of XAS spectra in O K-edge. (h) Comparisons of XAS spectra in La $M_4$-edge. The red spectra are for NMC_01 and the navy-blue spectra are for NMC_28 in Figure 6.6(g)-(h).

## 6.5 Conclusions

In conclusion, we investigated the origin of the rapid capacity fade of Li|$Li_{6.5}La_{2.9}Ba_{0.1}Zr_{1.4}Ta_{0.6}O_{12}$ (LLBZTO) garnet|LE|$LiNi_{0.6}Mn_{0.2}Co_{0.2}O_2$ (NMC 622) cathode hybrid SS-LMBs. The *ex situ* post-

mortem STXM study of cycled NMC 622 electrodes provided direct evidence for the existence of large voids in the NMC 622 secondary particles. We hypothesized that the voids worked as an open channel for LE to infiltrate the cathode, causing a decrease in TM contents and increased cation dissolution. More importantly, the defective cathode cannot maintain its structural and chemical stability leading to a capacity loss at the early-state of battery cycling. We also found that oxygen release occurs after the first cycle causing a heterogeneous $Ni^{3+}/Ni^{2+}$ phase distribution in the secondary particles. Besides, upon further cycling, the anisotropic volume change of NMC lattice and continuous oxygen loss initiate many intragranular cracks. It is supported by STXM with PCA map that the main oxygen release occurs around Ni and penetrates the bulk of the primary NMC 622 particles. In the meantime, the formation of a chemically-resistive SLEI with dissolute TMs and TM-F species on the cathode surface may block Li-ion re-reinsertion sites and eventually results in capacity fade. We believe that further optimization of LE and cathode design are essential to improve the overall performance of NMC cathodes in the hybrid SS-LMBs.

## 6.6 References


1. Thangadurai, V.; Pinzaru, D.; Narayanan, S.; Baral, A.K. Fast solid-state Li ion conducting garnet-type structure metal oxides for energy storage. *The Journal of Physical Chemistry Letters*. **2015**, *6*, 292-299.
2. Hou, A.Y.; Huang, C.Y.; Tsai, C.L.; Huang, C.W.; Schierholz, R.; Lo, H.Y.; Tempel, H.; Kungl, H.; Eichel, R.A.; Chang, J.K.; Wu, W.W. All-Solid-State Garnet-Based Lithium Batteries at Work–In Operando TEM Investigations of Delithiation/Lithiation Process and Capacity Degradation Mechanism. *Advanced Science*. **2023**, *10*, 2205012.
3. Kerman, K.; Luntz, A.; Viswanathan, V.; Chiang, Y.M.; Chen, Z. Practical challenges hindering the development of solid state Li ion batteries. *Journal of The Electrochemical Society*. **2017**, *164*, A1731.

4. Banerjee, A.; Wang, X.; Fang, C.; Wu, E.A.; Meng, Y.S. Interfaces and interphases in all-solid-state batteries with inorganic solid electrolytes. *Chemical reviews*. **2020**, *120*, 6878-6933.
5. Zhao, C.Z.; Zhao, B.C.; Yan, C.; Zhang, X.Q.; Huang, J.Q.; Mo, Y.; Xu, X.; Li, H.; Zhang, Q. Liquid phase therapy to solid electrolyte–electrode interface in solid-state Li metal batteries: a review. *Energy Storage Materials*. **2020**, *24*, 75-84.
6. Yan, S.; Abouali, S.; Yim, C.H.; Zhou, J.; Wang, J.; Baranova, E.A.; Weck, A.; Thangadurai, V.; Merati, A.; Abu-Lebdeh, Y. Revealing the role of liquid electrolytes in cycling of garnet-based solid-state lithium-metal batteries. *The Journal of Physical Chemistry C*. **2022**, *126*, 14027-14035.
7. Leng, J.; Wang, H.; Li, Y.; Xiao, Z.; Wang, S.; Zhang, Z.; Tang, Z. Insight into the solid-liquid electrolyte interphase between Li6. 4La3Zr1. 4Ta0. 6O12 and LiPF6-based liquid electrolyte. *Applied Surface Science*. **2022**, *575*, 151638.
8. Li, X.; Cong, L.; Ma, S.; Shi, S.; Li, Y.; Li, S.; Chen, S.; Zheng, C.; Sun, L.; Liu, Y.; Xie, H. Low resistance and high stable solid–liquid electrolyte interphases enable high-voltage solid-state lithium metal batteries. *Advanced Functional Materials*. **2021**, *31*, 2010611.
9. Sarkar, S.; Chen, B.; Zhou, C.; Shirazi, S.N.; Langer, F.; Schwenzel, J.; Thangadurai, V. Synergistic Approach toward Developing Highly Compatible Garnet-Liquid Electrolyte Interphase in Hybrid Solid-State Lithium-Metal Batteries. *Advanced Energy Materials*. **2023**, *13*, 2203897.
10. Xu, B.; Duan, H.; Liu, H.; Wang, C.A.; Zhong, S. Stabilization of garnet/liquid electrolyte interface using superbase additives for hybrid Li batteries. *ACS Applied Materials & Interfaces*. **2017**, *9*, 21077-21082.
11. Brandt, L.R.; Marie, J.J.; Moxham, T.; Förstermann, D.P.; Salvati, E.; Besnard, C.; Papadaki, C.; Wang, Z.; Bruce, P.G.; Korsunsky, A.M. Synchrotron X-ray quantitative

evaluation of transient deformation and damage phenomena in a single nickel-rich cathode particle. *Energy & Environmental Science*. **2020**, *13*, 3556-3566.

12. Ko, D.S.; Park, J.H.; Park, S.; Ham, Y.N.; Ahn, S.J.; Park, J.H.; Han, H.N.; Lee, E.; Jeon, W.S.; Jung, C. Microstructural visualization of compositional changes induced by transition metal dissolution in Ni-rich layered cathode materials by high-resolution particle analysis. *Nano Energy*. **2019**, *56*, 434-442.
13. Yan, P.; Zheng, J.; Gu, M.; Xiao, J.; Zhang, J.G.; Wang, C.M. Intragranular cracking as a critical barrier for high-voltage usage of layer-structured cathode for lithium-ion batteries. *Nature Communications*. **2017**, *8*, 14101.
14. Liu, T.; Yu, L.; Lu, J.; Zhou, T.; Huang, X.; Cai, Z.; Dai, A.; Gim, J.; Ren, Y.; Xiao, X.; Holt, M.V. Rational design of mechanically robust Ni-rich cathode materials via concentration gradient strategy. *Nature Communications*. **2021**, *12*, 6024.
15. Bartsch, T.; Strauss, F.; Hatsukade, T.; Schiele, A.; Kim, A.Y.; Hartmann, P.; Janek, J.; Brezesinski, T. Gas evolution in all-solid-state battery cells. *ACS Energy Letters*. **2018**, *3*, 2539-2543.
16. Teichert, P.; Eshetu, G.G.; Jahnke, H.; Figgemeier, E. Degradation and aging routes of Ni-rich cathode based Li-ion batteries. *Batteries*. **2020**, *6*, 8.
17. Liu, H.; Bugnet, M.; Tessaro, M.Z.; Harris, K.J.; Dunham, M.J.; Jiang, M.; Goward, G.R.; Botton, G.A. Spatially resolved surface valence gradient and structural transformation of lithium transition metal oxides in lithium-ion batteries. *Physical Chemistry Chemical Physics*. **2016**, *18*, 29064-29075.
18. Judez, X.; Eshetu, G.G.; Li, C.; Rodriguez-Martinez, L.M.; Zhang, H.; Armand, M. Opportunities for rechargeable solid-state batteries based on Li-intercalation cathodes. *Joule*. **2018**, *2*, 2208-2224.

19. Xu, R.; Sun, H.; de Vasconcelos, L.S.; Zhao, K. Mechanical and structural degradation of LiNixMnyCozO2 cathode in Li-ion batteries: an experimental study. *Journal of The Electrochemical Society*. **2017**, *164*, A3333.
20. Shi, T.; Zhang, Y.Q.; Tu, Q.; Wang, Y.; Scott, M.C.; Ceder, G. Characterization of mechanical degradation in an all-solid-state battery cathode. *Journal of Materials Chemistry A*. **2020**, *8*, 17399-17404.
21. Zhang, Z.; Yang, J.; Huang, W.; Wang, H.; Zhou, W.; Li, Y.; Li, Y.; Xu, J.; Huang, W.; Chiu, W.; Cui, Y. Cathode-electrolyte interphase in lithium batteries revealed by cryogenic electron microscopy. *Matter*. **2021**, *4*, 302-312.
22. Wu, Y.; Liu, X.; Wang, L.; Feng, X.; Ren, D.; Li, Y.; Rui, X.; Wang, Y.; Han, X.; Xu, G.L.; Wang, H. Development of cathode-electrolyte-interphase for safer lithium batteries. *Energy Storage Materials*. **2021**, *37*, 77-86.
23. Sun, T.; Sun, G.; Yu, F.; Mao, Y.; Tai, R.; Zhang, X.; Shao, G.; Wang, Z.; Wang, J.; Zhou, J. Soft X-ray ptychography chemical imaging of degradation in a composite surface-reconstructed Li-rich cathode. *ACS Nano*. **2020**, *15*, 1475-1485.
24. Mao, Y.; Wang, X.; Xia, S.; Zhang, K.; Wei, C.; Bak, S.; Shadike, Z.; Liu, X.; Yang, Y.; Xu, R.; Pianetta, P. High-voltage charging-induced strain, heterogeneity, and micro-cracks in secondary particles of a nickel-rich layered cathode material. *Advanced Functional Materials*. **2019**, *29*, 1900247.
25. Heenan, T.M.; Wade, A.; Tan, C.; Parker, J.E.; Matras, D.; Leach, A.S.; Robinson, J.B.; Llewellyn, A.; Dimitrijevic, A.; Jervis, R.; Quinn, P.D. Identifying the origins of microstructural defects such as cracking within Ni-rich NMC811 cathode particles for lithium-ion batteries. *Advanced Energy Materials*. **2020**, *10*, 2002655.

26. Liu, Y.; Harlow, J.; Dahn, J. Microstructural observations of “single crystal” positive electrode materials before and after long term cycling by cross-section scanning electron microscopy. *Journal of The Electrochemical Society*. **2020**, *167*, 020512.
27. Li, H.; Li, J.; Ma, X.; Dahn, J.R. Synthesis of single crystal LiNi0. 6Mn0. 2Co0. 2O2 with enhanced electrochemical performance for lithium ion batteries. *Journal of The Electrochemical Society*. **2018**, *165*, A1038-A1045.
28. Hu, J.; Li, L.; Hu, E.; Chae, S.; Jia, H.; Liu, T.; Wu, B.; Bi, Y.; Amine, K.; Wang, C.; Zhang, J. Mesoscale-architecture-based crack evolution dictating cycling stability of advanced lithium ion batteries. *Nano Energy*. **2021**, *79*, 105420.
29. Watanabe, S.; Kinoshita, M.; Hosokawa, T.; Morigaki, K.; Nakura, K. Capacity fade of LiAlyNi1−x−yCoxO2 cathode for lithium-ion batteries during accelerated calendar and cycle life tests (surface analysis of LiAlyNi1−x−yCoxO2 cathode after cycle tests in restricted depth of discharge ranges). *Journal of Power Sources*. **2014**, *258*, 210-217.
30. Xu, C.; Märker, K.; Lee, J.; Mahadevegowda, A.; Reeves, P.J.; Day, S.J.; Groh, M.F.; Emge, S.P.; Ducati, C.; Layla Mehdi, B.; Tang, C.C. Bulk fatigue induced by surface reconstruction in layered Ni-rich cathodes for Li-ion batteries. *Nature Materials*. **2021**, *20*, 84-92.
31. Preger, Y.; Barkholtz, H.M.; Fresquez, A.; Campbell, D.L.; Juba, B.W.; Romàn-Kustas, J.; Ferreira, S.R.; Chalamala, B. Degradation of commercial lithium-ion cells as a function of chemistry and cycling conditions. *Journal of The Electrochemical Society*. **2020**, *167*, 120532.
32. Liu, W.; Li, J.; Li, W.; Xu, H.; Zhang, C.; Qiu, X. Inhibition of transition metals dissolution in cobalt-free cathode with ultrathin robust interphase in concentrated electrolyte. *Nature Communications*. **2020**, *11*, 3629.

33. Tian, C.; Xu, Y.; Nordlund, D.; Lin, F.; Liu, J.; Sun, Z.; Liu, Y.; Doeff, M. Charge heterogeneity and surface chemistry in polycrystalline cathode materials. *Joule*. **2018**, *2*, 464-477.

34. Tan, C.; Leach, A.S.; Heenan, T.M.; Parks, H.; Jervis, R.; Weker, J.N.; Brett, D.J.; Shearing, P.R. Nanoscale state-of-charge heterogeneities within polycrystalline nickel-rich layered oxide cathode materials. *Cell Reports Physical Science*. **2021**, *2*, 100647.

35. Xu, Z.; Jiang, Z.; Kuai, C.; Xu, R.; Qin, C.; Zhang, Y.; Rahman, M.M.; Wei, C.; Nordlund, D.; Sun, C.J.; Xiao, X. Charge distribution guided by grain crystallographic orientations in polycrystalline battery materials. *Nature Communications*. **2020**, *11*, 83.

36. Tian, C.; Nordlund, D.; Xin, H.L.; Xu, Y.; Liu, Y.; Sokaras, D.; Lin, F.; Doeff, M.M. Depth-dependent redox behavior of LiNi0.6Mn0.2Co0.2O2. *Journal of the Electrochemical Society*. **2018**, *165*, A696-A704.

37. Ryu, H.H.; Park, N.Y.; Seo, J.H.; Yu, Y.S.; Sharma, M.; Mücke, R.; Kaghazchi, P.; Yoon, C.S.; Sun, Y.K. A highly stabilized Ni-rich NCA cathode for high-energy lithium-ion batteries. *Materials Today*. **2020**, *36*, 73-82.

38. Kalirai, S.; Lim, K.; Enders, B.; Hong, J.; Gent, W.E.; Deva, A.; Garcia, E.R.; Yu, Y.S.; Celestre, R.; Toney, M.F.; Shapiro, D.A. Understanding Chemomechanical Li-ion Cathode Degradation through Multi-Scale, Multi-Modal X-ray Spectromicroscopy. *Microscopy and Microanalysis*. **2018**, *24*, 426-427.

39. Lou, S.; Liu, Q.; Zhang, F.; Liu, Q.; Yu, Z.; Mu, T.; Zhao, Y.; Borovilas, J.; Chen, Y.; Ge, M.; Xiao, X. Insights into interfacial effect and local lithium-ion transport in polycrystalline cathodes of solid-state batteries. *Nature Communications*. **2020**, *11*, 5700.

40. Xu, S.; Luo, G.; Jacobs, R.; Fang, S.; Mahanthappa, M.K.; Hamers, R.J.; Morgan, D. Ab initio modeling of electrolyte molecule ethylene carbonate decomposition reaction on Li

(Ni, Mn, Co)O2 cathode surface. *ACS Applied Materials & Interfaces*. **2017**, *9*, 20545-20553.

41. Yang, F.; Liu, Y.; Martha, S.K.; Wu, Z.; Andrews, J.C.; Ice, G.E.; Pianetta, P.; Nanda, J. Nanoscale morphological and chemical changes of high voltage lithium–manganese rich NMC composite cathodes with cycling. *Nano Letters*. **2014**, *14*, 4334-4341.
42. Csernica, P.M.; Kalirai, S.S.; Gent, W.E.; Lim, K.; Yu, Y.S.; Liu, Y.; Ahn, S.J.; Kaeli, E.; Xu, X.; Stone, K.H.; Marshall, A.F. Persistent and partially mobile oxygen vacancies in Li-rich layered oxides. *Nature Energy*. **2021**, *6*, 642-652.

# Chapter 7

# Concentrated precipitation electrolyte for reviving ultrathin lithium metal anode

This chapter has been adapted from a research paper submitted to the *Journal of Power Sources*.

## 7.1 Abstract

Realizing high-performance lithium metal ($Li^0$) batteries requires the presence of a robust solid-electrolyte interphase (SEI) on the $Li^0$ surface that forms before or during operation. Herein, high concentrations of lithium bis(trifluoromethanesulfonyl)imide (LiTFSI) and lithium nitrite ($LiNO_3$) are employed to create a novel concentrated precipitation electrolyte (CPE) and form an inorganic-rich SEI. It is found that an ultrathin $Li^0$ anode (thickness of 25 μm) in the CPE remains highly reversible over 300 cycles with an average Coulombic efficiency (CE) of 97.21% in an asymmetric Cu|Li cell. The CPE enables superior stability to the $LiFePO_4$ cathode at a high mass loading of ~15 mg $cm^{-2}$ and reaches a capacity retention of 82.8% after 100 cycles with an average CE of 99.94%. This study elucidates the mechanism of both LiTFSI and $LiNO_3$ in enhancing the physiochemical properties of the SEI surface layer. It is believed that this design concept and the findings can be broadened in optimizing SEIs via electrolyte engineering for practical $Li^0$ batteries.

## 7.2 Introduction

Li metal ($Li^0$) as an optional anode material for boosting energy densities as graphite anode in commercially dominant Li-ion batteries cannot meet the steep requirements for cell energy densities greater than 300 Wh $kg^{-1}$. [1,2,3,4] An excess of $Li^0$ generally used to compensate for Li losses in most state-of-the-art $Li^0$ batteries (LMBs) decreases the practical volumetric capacity.[4] Therefore, in practical LMBs, a limited thickness of $Li^0$ anode coupled with a high mass loading cathode as well as a low negative to positive capacity ratio are necessary conditions to achieve

projected energy densities.[46] For instance, anode-free (or anode-less) batteries (N/P = 0) represent an effective strategy for maximizing energy densities by eliminating enough Li reservoir from the cells.[7,8]

The electrochemical performance of $Li^0$ relies on the formation of a solid-electrolyte interphase (SEI) upon the Li plating/stripping process.[9] A fragile SEI that initially establishes on the $Li^0$ surface cannot accommodate electrode volume change with repeated cycling, and fractured SEI could break the electrical contact and cause dendritic and/or "dead" Li production.[10] Accordingly, rationally inducing a mechanically robust and chemically stable SEI generation is essential for stabilizing $Li^0$ performance and restraining capacity loss over a long cycle life.[11] One strategy is to modify electrolyte components and construct functional interphases (e.g., inorganic-rich SEIs), such as highly-concentrated electrolytes (HCEs), localized highly-concentrated electrolytes (LHCEs), and suspension electrolytes.[11,12] Compared with organic-rich SEIs, inorganic-rich SEIs tend to effectively inhibit Li dendrite growth and stabilize $Li^+$ migration between electrodes.[13] As SEIs growth on $Li^0$ are directly linked with the $Li^+$ solvation environment, the other pathway is to modulate $Li^+$ solvation/de-solvation structure and/or strength (e.g., weakly solvating electrolytes) and adjust reaction kinetics.[14,15,16,17] For example, by increasing the number of components in the electrolytes, a wider distribution of diffusional barriers from diverse solvation structures could facilitate diffusional channels via the available percolation network.[18]

However, going beyond the features of principal chemical components in the electrolytes, the impacts of modifying phase behavior on electrolyte electrochemical performance and SEIs properties remain unclear. The diversity of local interactions among $Li^+$, anions, and solvents introduces extra complexity to clarify the kinetic characteristics commonly associated with the diffusivity and conductivity of concentrated electrolytes. Additionally, achieving >99% Coulombic efficiency (CE) without $Li^0$ excess at the negative electrode remains a challenge for most current liquid electrolytes.[5] Hence, we propose a dual-anion concentrated precipitation electrolyte

(designated as CPE) design for activating ion transport capabilities and improving reversibility of ultrathin $Li^0$ anodes (thickness of 25 μm). To the best of our knowledge, there is no literature on the formulation of the CPEs and investigation into the role of precipitation in influencing inorganic-rich SEI development. Both lithium bis(trifluoromethanesulfonyl)imide (LiTFSI) and lithium nitrite ($LiNO_3$) were used as additives in the ether-based CPEs, because of their ability to form a fluorine-rich and nitrogen-rich SEI that suppress the $Li^0$ anodes from undergoing side reactions. We demonstrate that a dual-anion CPE (4 M LiTFSI+2 wt.% $LiNO_3$ in 1,3-dioxolane (DOL) and 1,2-dimethoxyethane (DME), 50:50 v/v %) provides superior cycling reversibility when compared with single-salt dilute and concentrated electrolytes. The precipitation in the CPE serves as a reservoir of salting-out salts that saturate the $Li^0$ surface, and hence establishing a stable SEI and regulating Li deposition morphology during cycling.

## 7.3 Experimental section

### 7.3.1 Materials and synthesis

Free-standing ultrathin $Li^0$ anodes (thickness of 25 $\mu$m) and $LiFePO_4$ (LFP, mass loading of ~15 mg $cm^{-2}$) cathode material was supplied by MTI Corporation. The cathode sheets were punched into discs (12 mm in diameter) and dried at 85 ˚C under the vacuum.

Lithium bis(trifluoromethanesulfonyl)imide (LiTFSI) and lithium nitrile ($LiNO_3$) were purchased from Sigma-Aldrich and vacuum dried at 100 ˚C. All electrolytes were prepared by adding the specific amount of both salts in the battery-grade solvent 1,3-dioxolane (DOL) and 1,2-dimethoxyethane (DME) (50:50 v/v %) in an Argon-filled glovebox ($O_2$<0.1 ppm, $H_2O$<0.1 ppm). 1 mol $g^{-1}$ (M) LiTFSI+1 wt.% $LiNO_3$ (designated as 1+1 and the same for all electrolytes), 1 M LiTFSI+2 wt.% $LiNO_3$ (1+2), 2 M LiTFSI+2 wt.% $LiNO_3$ (2+2), 2 M LiTFSI+4 wt.% $LiNO_3$ (2+4), 4 M LiTFSI+2 wt.% $LiNO_3$ (4+2), and 4 M LiTFSI (4) electrolytes denote that the corresponding concentration of different salts were well mixed in the DOL/DME solvent at room temperature.

### 7.3.2 Electrochemical Measurements

Electrochemical cycling tests of all batteries were based on CR2325 coin-cell type assembled in an Argon-filled glovebox ($O_2$ < 0.1 ppm, $H_2O$ < 0.1 ppm). 74.8 µL laboratory-prepared electrolytes were injected into half cells (Li|LFP) with two layers of PP membrane (Celgard 2500) as separators, one LFP disc as a cathode, and one $Li^0$ foil as an anode. The anode-free (Cu|LFP) kept the same amount of liquid electrolyte without the usage of the $Li^0$ anode. Cu foil was washed up by freshly made 1 M hydrochloric acid (HCl) solution and vacuum dried at 85 ˚C before a usage. All coin cells were cycled between 2.5 V and 4.0 V (versus $Li/Li^+$) at 0.05C (1C = 170 mAh $g^{-1}$) using a multi-channel battery cycler (Arbin BT2000) at room temperature.

Li plating and stripping of laboratory-prepared electrolytes in Cu|Li cells with free-standing ultrathin $Li^0$ anodes (thickness of 25 $\mu$m) were monitored by time (1 h) and voltage (1 V) at a rate of 0.5 mA $cm^{-2}$. The average Coulombic efficiency (CE) was gained by dividing the total stripping capacity by the plating capacity.[19] Cu foil was used as the working electrode and $Li^0$ was used as the reference electrode. Cyclic voltammetry (CV) of Cu|Li and Li|LFP cells with selected electrolytes was separately conducted at a scan rate of 0.2 mV $s^{-1}$ from 0 V to 2 V and from 2 V to 4.5 V versus $Li/Li^+$.

Electrochemical impedance spectroscopy (EIS) of Li|LFP cells with $Li^0$ was measured after 1, 3, 5, and 10 cycles at a frequency range from 1 MHz to 0.01 Hz with a perturbation amplitude of 20 mV using a BioLogic Science instrument with a frequency response analyzer. 10 cycles were chosen to sustain a relatively stable electrochemical performance.[20]

Lithium transference numbers ($t_{Li^+}$) were determined via the Bruce-Vincent method:

$$t_{Li^+} = \frac{I^{ss}(\Delta V - I^0 R_{el}^0)}{I^0(\Delta V - I^{ss} R_{el}^{ss})}$$

$$I^0 = \frac{\Delta V}{R_b^0 + R_{el}^0}$$

According to the two formulas above, $t_{Li^+}$ was calculated as follows:

$$t_{Li^+} = \frac{I^{ss}R_b^0}{\Delta V - I^{ss}R_{el}^{ss}}$$

Where ΔV is the potential applied to the sample during the polarization process, $I^0$ is the initial current, $I^{ss}$ is the steady-state current, $R_b^0$ is the initial solution resistance, $R_{el}^0$ is the initial interfacial resistance and $R_{el}^{ss}$ is the steady-state interfacial resistance. The polarization potential ($\Delta V$) of 10 mV were used for symmetric Li|Li cells with various electrolytes until the polarization currents reached a steady state. The corresponding EIS data were collected before and after the polarization. All tests were performed at room temperature.

### 7.3.3 Materials characterizations

Morphology characterization of $Li^0$ anodes was performed by field emission scanning electron morphologies microscope (SEM) with a Hitachi SU5000 microscope. X-ray photoelectron spectroscopy (XPS) analyses of elemental composition on the $Li^0$ were carried out using an Axis Ultra DLD spectrometer (Kratos Analytical, Manchester, UK) with monochromatized Al K$\alpha$ X-rays. Peaks were fitted using CasaXPS software (version 2.3.25) with Shirley BG type and all spectra were calibrated with respect to C 1s (at 285.0 eV). The above morphology and composition characterization were performed with Li|LFP cells in selected electrolytes and respectively cycled for 1, 3, 5, and 10 cycles. Ultrathin $Li^0$ anodes were disassembled and carefully rinsed with the DOL/DME solvent (50:50 v/v %) three times to remove residual electrolytes, followed by slowly drying in the anti-chamber of an Argon-filled glovebox ($O_2$<0.1 ppm, $H_2O$<0.1 ppm) at room temperature to remove remaining solvent. Dried $Li^0$ electrodes were further transferred into a customized box filled with Argon for the XPS measurements to minimize the air exposure.

Raman spectrometer equipped with a 12 mW 532 nm pump laser and all electrolytes were tightly sealed in quartz cuvettes with Argon atmosphere. Differential scanning calorimeter (DSC) was analyzed in an $N_2$ atmosphere with a heating rate of 5˚C $min^{-1}$ ranging from -90 ˚C to 40 ˚C. X-ray

diffraction (XRD) was performed using a Bruker AXS D8 diffractometer equipped with an Al K$\alpha$ beam (1486.6 eV).

In a Li|LFP coin-cell assembly with 4+2 CPE, one piece of lacey-carbon TEM grid (TED PELLA, INC.) was applied above the $Li^0$ anode for deposited Li nanostructure study after initial Li plating/stripping. To minimize air exposure, TEM grids were mounted on the specimen holder in the glovebox, carried to the TEM measurement in a hermetically sealed argon tube, and quickly inserted into the TEM column in less than 30 seconds. To acquire both high-resolution Transmission Electron Microscope (HRTEM) bright-field and annular dark-filed (ADF) pictures, an FEI Titan$^3$ 80-300 TEM operated at 300 keV and equipped with a CEOS aberration corrector for the probe forming lens and a monochromated field emission gun. ADF images were collected in Scanning Transmission Electron Microscopy (STEM) mode using a high-angle annular dark-field (HAADF) Fischione detector. Energy-dispersive X-ray analysis (EDX) spectrometer (EDAX Analyzer, DPP-II) is also included with the TEM instrument. EDX spectra were gathered with the sample titled at 15 degrees.[19]

## 7.4 Results and discussion

### 7.4.1 Physical and electrochemical properties of precipitation electrolyte

As shown in Figure 7.1 (a), up to 2 wt.% $LiNO_3$ salt easily dissolves in DOL/DME with 1 M LiTFSI. However, when the salt concentration of LiTFSI is raised to 2 M, either 2 wt.% $LiNO_3$ or 4 wt.% $LiNO_3$ (in Figure A12.1) cannot be entirely dissolved at room temperature and eventually obtains a concentrated precipitation electrolyte (CPE). This interesting phenomenon might be described as the salting-out process of salts in the mixed-solvent system.[21] The addition of a second solute or solvent alters the solubility of the dissolved substance. With the increase of the concentrations for LiTFSI up to 4 M but keeping the relatively low mass ratio of $LiNO_3$ (2 wt.%), the solution becomes more suspended after being well mixed. Differential scanning calorimeter (DSC) was applied to reveal distinct glass transition temperatures, which indicates in Figure 7.1(b)

that all the electrolytes are glass-forming liquids, and their glass transition temperatures shift from low to high with increasing salt concentrations.[13]

Raman spectroscopy was conducted to explore the effects of different chemical components on the local environment of $Li^+$ solvation structure in the electrolytes (in Figure 7.1(c)). The signals of free DME and DOL molecules decrease with the increase of salt concentrations and almost diminish for CPEs (2+2 and 4+2). Moreover, the C=O stretching modes of DME (800-880 $cm^{-1}$) shift more than that of DOL (920-950 $cm^{-1}$) in all electrolytes, which suggests that $Li^+$ solvation by DME is stronger than by DOL, and the peak shift is also affected by salt concentrations.[21] The S-N stretching band of $TFSI^-$ at 730-780 $cm^{-1}$ is broader than the range reported by Wahyudi et al., implying the involvement of $TFSI^-$ in the solvation structure.[22a)] The slight shift could also correspond to a strong impact of aggregate ion pairs $Li^+$-$TFSI^-$ coordination (peak at ~747 $cm^{-1}$) than $TFSI^-$ free ion pairs in the precipitation solutions. It has been well known that $TFSI^-$ has a lower binding energy with $Li^+$, implying a lower de-solvation energy and a rapid kinetic.[21]. Moreover, the S-N band slightly shifts to a high wavenumber in the CPEs compared to the low-concentration electrolytes (1+1 and 1+2), suggesting a significant increase in $Li^+$-$TFSI^-$ coordination and a decrease in $TFSI^-$ free ion population in CPEs. The aggregate ion pairs have been previously reported to be a unique $Li^+$ coordination that appear in the HCEs and are beneficial for $Li^+$ transport.[22b)-c)] Figure 7.1(d) displays the ionic conductivity at room temperature for the electrolyte solutions of LiTFSI and $LiNO_3$ in DOL/DME solvent. After being sufficiently mixed, 5 mol $g^{-1}$ of $LiNO_3$ cannot be completely dissolved in the solvent at room temperature. It is evident that the ionic conductivity of LiTFSI in DOL/DME decreases as salt concentrations increase beyond its apparent $C_{max}$, the concentration of highest conductivity, at 1 M (mol $g^{-1}$). In contrast, the ionic conductivity of $LiNO_3$ rises linearly in DOL/DME without reaching a $C_{max}$ due to solubility limit.[22d)] Therefore, controlling the ratio of LiTFSI/$LiNO_3$ salt to the DOL/DME solvent is a key factor to preserve those electrolytes that have good ionic conductivity. The value of Li-ion

transference number ($t_{Li^+}$) for the 4+2 CPE is 0.08 (in Table A10), which is way lower than that of traditional liquid electrolytes (e.g., 0.2-0.3).[13] This feature may be attributed to distinct kinetics and the unique structure of the dual-anion solvation shells, which would necessitate further modelling and theoretical studies. One assumption for ion transport mechanism is that the $Li^+$ needs to "jump" from one $Li^+$-$TFSI^-$ coordination to another (similar to a hopping-like behavior in the HCEs) in the CPE and the number of associate states is sufficiently high to ensure close proximity among them.[23]

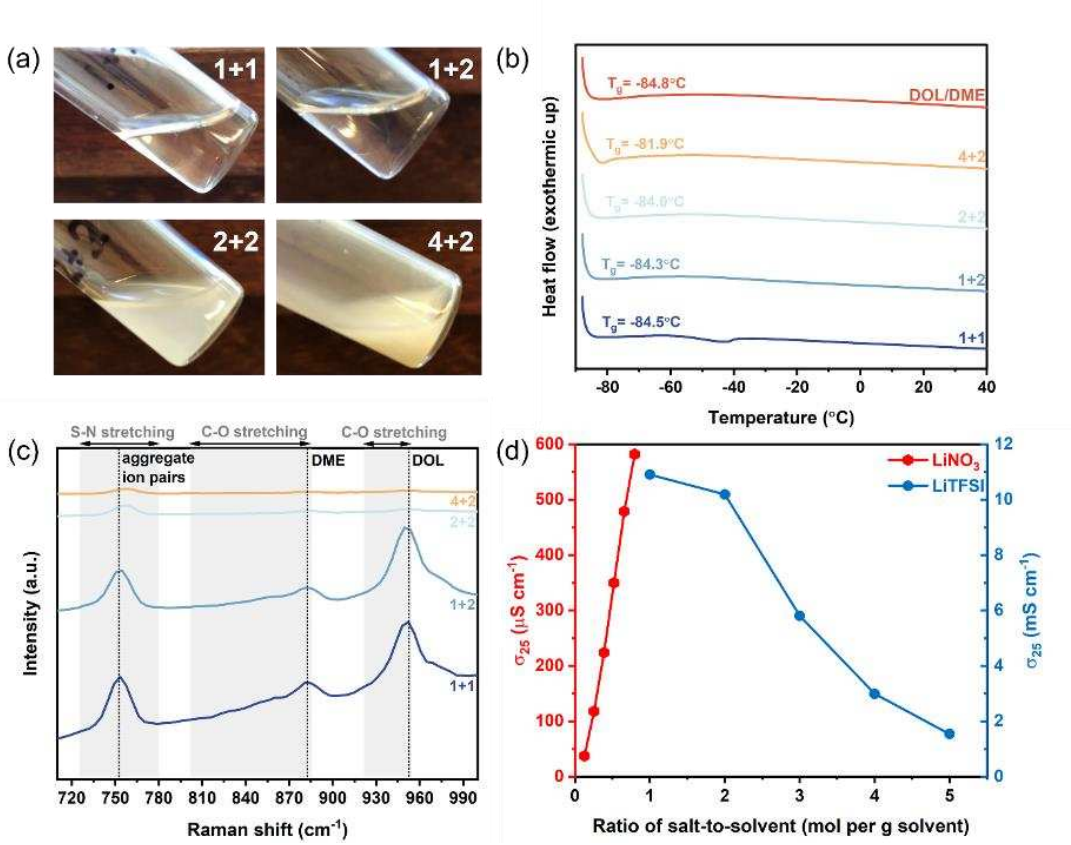


**Figure 7.1.** (a) The dissolution state after being well mixed at room temperature: 1 M LiTFSI+1 wt.% $LiNO_3$ (1+1), 1 M LiTFSI+2 wt.% $LiNO_3$ (1+2), 2 M LiTFSI+2 wt.% $LiNO_3$ (2+2), and 4 M LiTFSI+2 wt.% $LiNO_3$ (4+2); (b) DSC traces of the aforementioned electrolytes; (c) Raman spectra of various electrolytes: S-N stretching in $TFSI^-$ (730-780 $cm^{-1}$), C=O stretching in DME (800-880 $cm^{-1}$), and C=O stretching in DOL (920-950 $cm^{-1}$); (d) Room-temperature ionic conductivity as a function of ratios of salt-to-solvent (mol per g solvent) for $LiNO_3$ and LiTFSI.

### 7.4.2 Electrochemical performance of concentrated precipitated electrolyte

Figure 7.2(a) presents voltage profiles of Cu|Li cells with various electrolytes after initial Li plating. In the case of the Cu|4+2|Li cell, the lowest voltage spike (~114 mV at 0.5 mA $cm^{-2}$) of Li nucleation implies that larger Li nuclei was formed on the Cu current collector, and these nuclei is expected to promote dense Li growth during the initial Li deposition. We will further discuss the Li deposition morphologies on the $Li^0$ anode with 4+2 CPE in the Section 7.4.3. The precipitated 4+2 electrolyte contributes to well-overlapped Li plating/stripping profiles for 300 cycles with an overpotential of 57 mV as evidenced in Figure 7.2(b). According to Figure 7.2(c-e), the Cu|4+2|Li cell cycles steadily for over 750 h (after resting at the open-circuit voltage for 12 h) and exhibits a stable voltage profile with low electrode polarization that is comparable with the low-concentration electrolytes. For the cells containing diluent 4 and precipitated 2+4 electrolytes, the voltage lowers drastically and irreversibly which typically owing to the formation of a thick and unstable SEI and a dendrite-induced short circuit in the cell.[23] In addition, the average CE reaches 97.21% from 0 to 300 cycles in the 4+2 CPE (in Figure 7.2(f)). This endorses the fact that a stable SEI formation could improve the interfacial compatibility, allowing highly reversible Li deposition/dissolution.[23] Figure 7.2(g) depicts the observed reduction behavior of LiTFSI, $LiNO_3$, and DOL/DME in the Cu|4+2|Li cell. In the first CV cycle, there is a deep cathodic peak beginning at ~1.81 V vs $Li/Li^+$ that could be ascribed to the reduction of $NO_3^-$, and it disappears in the subsequent cycles.[4,11] The easy reduction of $NO_3^-$ in ether electrolytes serves as the frontier reaction during SEI nucleation and growth and is critical for the physiochemical properties of the SEI.[11] A tiny peak starting from around 1.43 V could be assigned to $TFSI^-$ reduction.[24] The absence of similar salt reduction peaks in the subsequent cycles implies an electrochemically stable inorganic-rich SEI formation.

To access the electrochemical performance of 4+2 CPE, anode-free (Cu|LFP) cells were assembled and tested, as exhibited in Figure A12.2. The Cu|4+2|LFP cell outperforms other electrolytes with the largest initial discharge capacity of 116.31 mAh $g^{-1}$ and a CE of 99.63% after 100 cycles. The

voltage hysteresis for the cell with the 4+2 CPE is relatively steady within 50 cycles, indicating the potential of a stable SEI growth.

A slight excess of Li has been suggested as an effective solution to stabilize Li plating process.[19] Herein, an ultrathin $Li^0$ foil was applied in half cells (Li|LFP). The compatibility of all electrolytes with LFP electrodes (mass loading of 15 mg $cm^{-2}$) was evaluated by CV. The CV curves (in Figure A12.3) reveal a high anodic stability over 4.0 V (versus $Li/Li^+$) with a more stable redox overpotential of the 4+2 CPE compared to the low-concentration 1+1 electrolyte, demonstrating a superior compatibility of the CPE with the high-loading LFP cathodes.

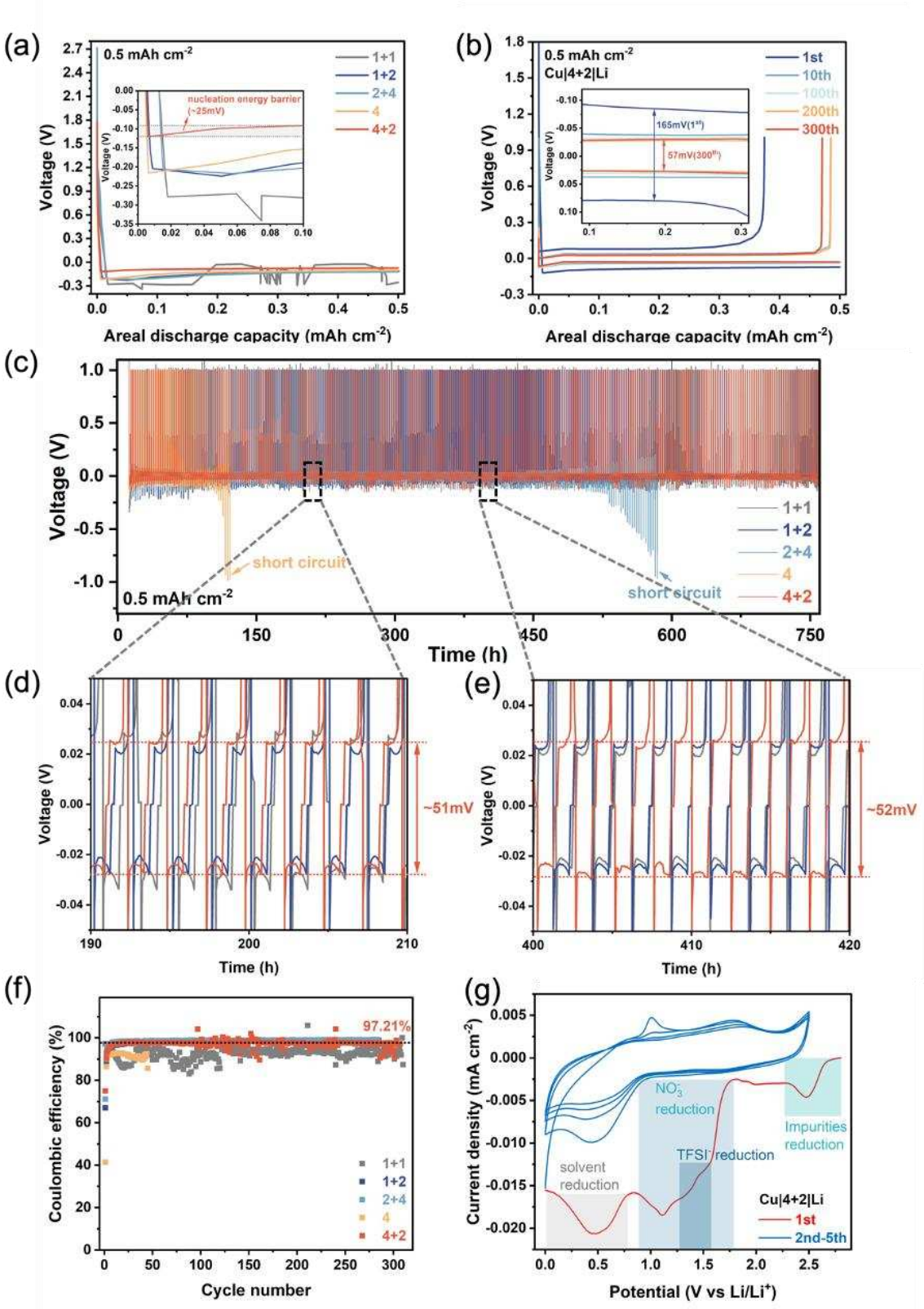
(a)
0.5 mAh cm-2
1+1
1+2
2+4
4
4+2
nucleation energy barrier (~25mV)
Voltage (V)
Areal discharge capacity (mAh cm-2)
(b)
0.5 mAh cm-2
Cu|4+2|Li
1st
10th
100th
200th
300th
165mV(1st)
57mV(300th)
Voltage (V)
Areal discharge capacity (mAh cm-2)
(c)
short circuit
short circuit
0.5 mAh cm-2
1+1
1+2
2+4
4
4+2
Voltage (V)
Time (h)
(d)
~51mV
Voltage (V)
Time (h)
(e)
~52mV
Voltage (V)
Time (h)
(f)
97.21%
1+1
1+2
2+4
4
4+2
Coulombic efficiency (%)
Cycle number
(g)
NO3- reduction
Impurities reduction
TFSI- reduction
solvent reduction
Cu|4+2|Li
1st
2nd-5th
Current density (mA cm-2)
Potential (V vs Li/Li+)

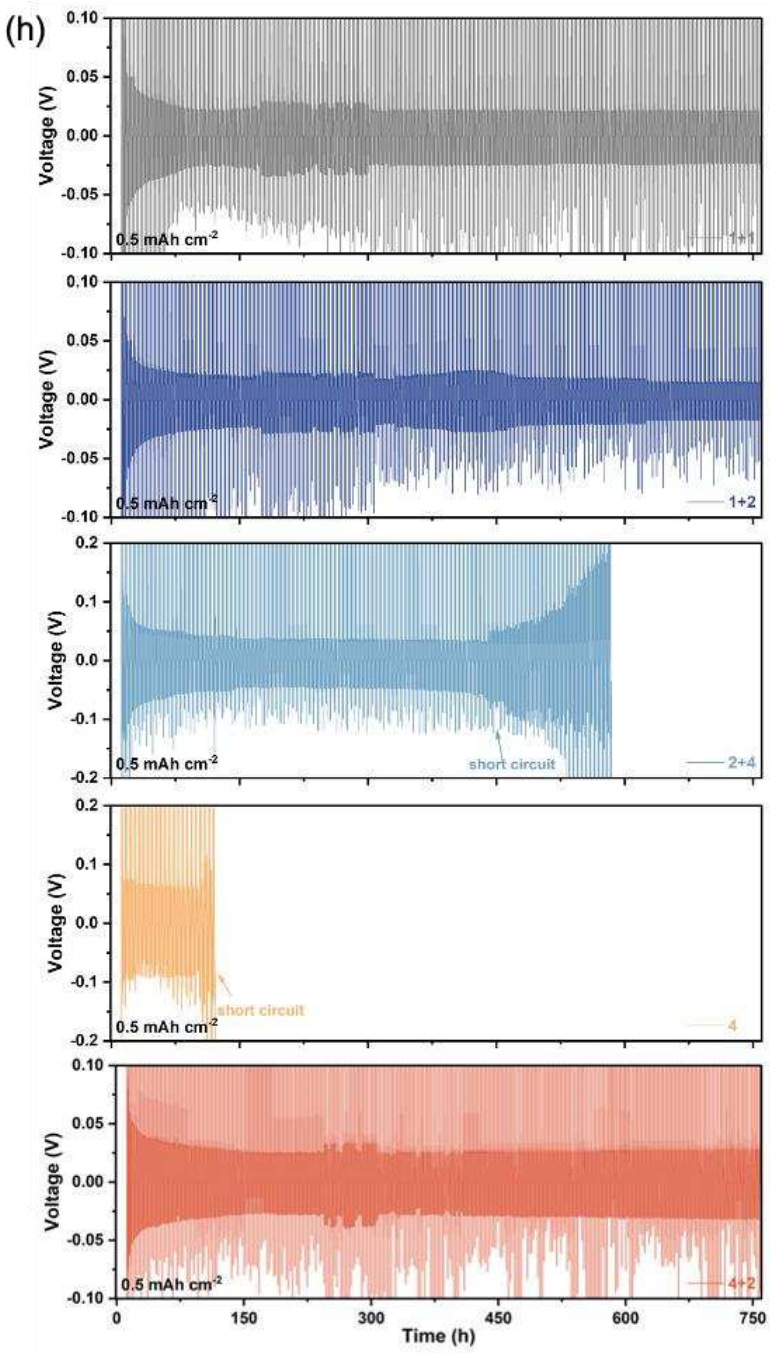


**Figure 7.2.** (a) Voltage profiles of the initial Li depositions in Cu|Li cells with 1+1, 1+2, 2+4, 4, and 4+2 electrolytes at a current density of 0.5 mA $cm^{-2}$. The inset shows the nucleation energy barrier for the 4+2 CPE. (b) Galvanostatic curves of Cu|4+2|Li cell after charge/discharge at 0.5 mA $cm^{-2}$. The inset shows the comparison of overpotentials after different cycles. (c) Long-term galvanostatic voltage profiles of Cu|Li cells with 1+1, 1+2, 2+4, 4, an 4+2 electrolytes at a current density of 0.5 mA $cm^{-2}$. (d-e) Zoom-in regions from Figure 7.2(c). (f) CEs of Cu|Li cell

with various electrolytes at 0.5 mA $cm^{-2}$. (g) CV profiles of Cu|4+2|Li cell after 5 cycles (at a scan rate of 0.2 mV $s^{-1}$). (h) Detailed spectra of plots in Figure 7.2(c).

As shown in Figure 7.3(a), the employment of 4+2 CPE results in a stable cycling performance for 100 cycles with a capacity reteintion of around 82.8% (an average CE of 99.94% in Figure 7.3(b)). The Li|4+2|LFP cell has an initial discharge capacity of 147.11 mAh $g^{-1}$, which is slightly lower than that of 1+1 electrolyte. More contact ion pairs are preferentially reduced at the $Li^0$ surface during the initial cycling and the cell with the 4+2 CPE which leads to a stable and compact SEI.[20] Furthermore, the voltage polarization of the Li|4+2|LFP cell begins at a low value (≈ 90 mV from Figure 7.3(c)) and increases slowly over 100 cycles, implying that the 4+2 CPE has enhanced electrochemical dynamics. In addition, the Li|4+2|LFP cell delivers superior rate performance from 0.05C to 0.2C, sustaining around 70% of the specific capacity with a tiny polarization after recovering to 0.05C (in Figure 7.3(d)).

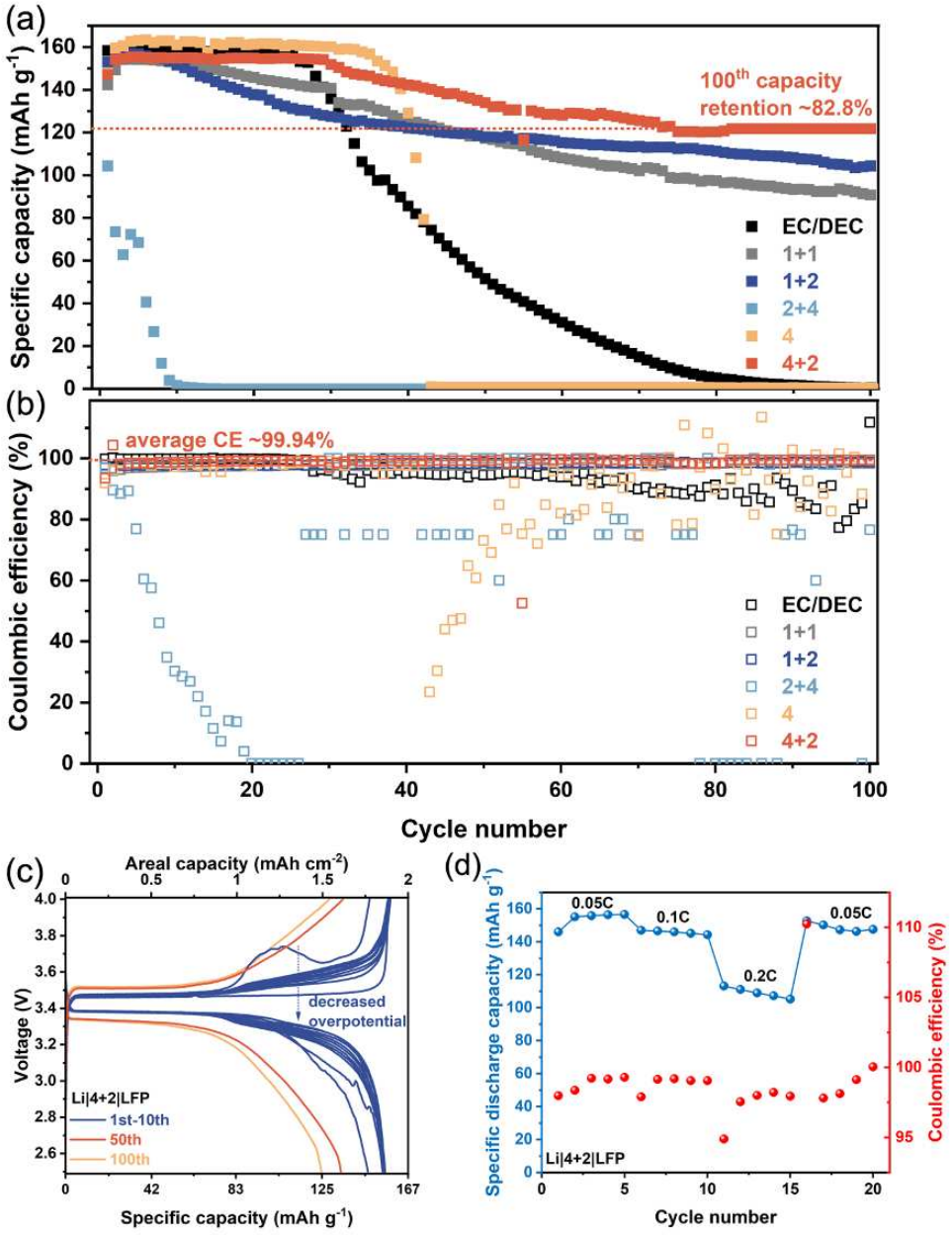


**Figure 7.3.** (a) Cycling performance and (b) Coulombic efficiency of Li|LFP cell with 1 M $LiPF_6$ in EC/DEC (50:50 vol.%), 1+1, 1+2, 2+4, 4, and 4+2 electrolytes at 0.05C. (c) Galvanostatic charge-discharge curves of Li|4+2|LFP cell at 0.05C. (d) Rate performances of Li|4+2|LFP cell at elevated rates from 0.05C to 0.2C.

### 7.4.3 Li deposition morphology evolution after cycling

To evaluate the morphology of the electrodeposited Li with the 4+2 CPE, post-mortem top-scanning electron microscopy (SEM) characterization was performed as shown in Figure 7.4(a)

and Figure A12.4. While the deposited Li on the $Li^0$ surface in the 1+1 electrolyte after the initial cycle shows an aggregate spiky-like appearance, those in the 1+2, 2+4, and 4+2 electrolytes exhibit a mossy-like Li morphology with increased size of Li nuclei. As the salt concentration increases, the morphology of deposited Li gradually changes from spike aggregates to granular and finally into a relatively regular spherically shaped aggregates, matching the findings reported by Chen et al.[23] This difference after the initial Li plating could be closely associated with the ability of $LiNO_3$ in the ether-based electrolytes, to regulate the Li deposition at an early stage.[11] After 3 cycles, the whiskers are scattered in large aggregates for 1+1 and 1+2 electrolytes, which suggest that Li nucleation sites are unevenly distributed. Such porous surface accounts for their low CEs and unstable Li plating/stripping cycling process. For the 2+4 CPE, smaller spherical Li nuclei with a small amount of Li spike is observed, which is consistent with a low discharge capacity and poor cycling stability in the Li|LFP cells. Surprisingly, uniform disc-like and spherical morphologies are obtained in the 4+2 CPE with a rather neat surface, along with the highest average CE and stable electrochemical performance. With cycling, the Li nuclei density and uniformity increases with well-connected deposits for the 4+2 CPE, allowing efficient stripping and suppressing the formation of inactive $Li^0$. Combing with these results support that when a higher concentration of $LiNO_3$ is employed for the 4+2 CPE, a denser deposited Li layer is originally produced at the early stage and maintains its stability during extended cycles.

To characterize the structure and composition of SEI, transmission electron microscopy (TEM) was implemented for the full cell with the 4+2 CPE after the initial charge/discharge process. Figure 7.4(b) shows the TEM images of deposited Li on TEM Cu mesh in the 4+2 CPE. The large size of ~2 $\mu$m spherical nuclei show excellent nucleation behavior. Figure 7.4(c) illustrates the EDX spectra of F, C, S that may originate from the SEI and the “noisy” signals (Fe, P, Cl, and Cu) probably coming from the TEM holders. The detailed SEI composition will be discussed in the following section.

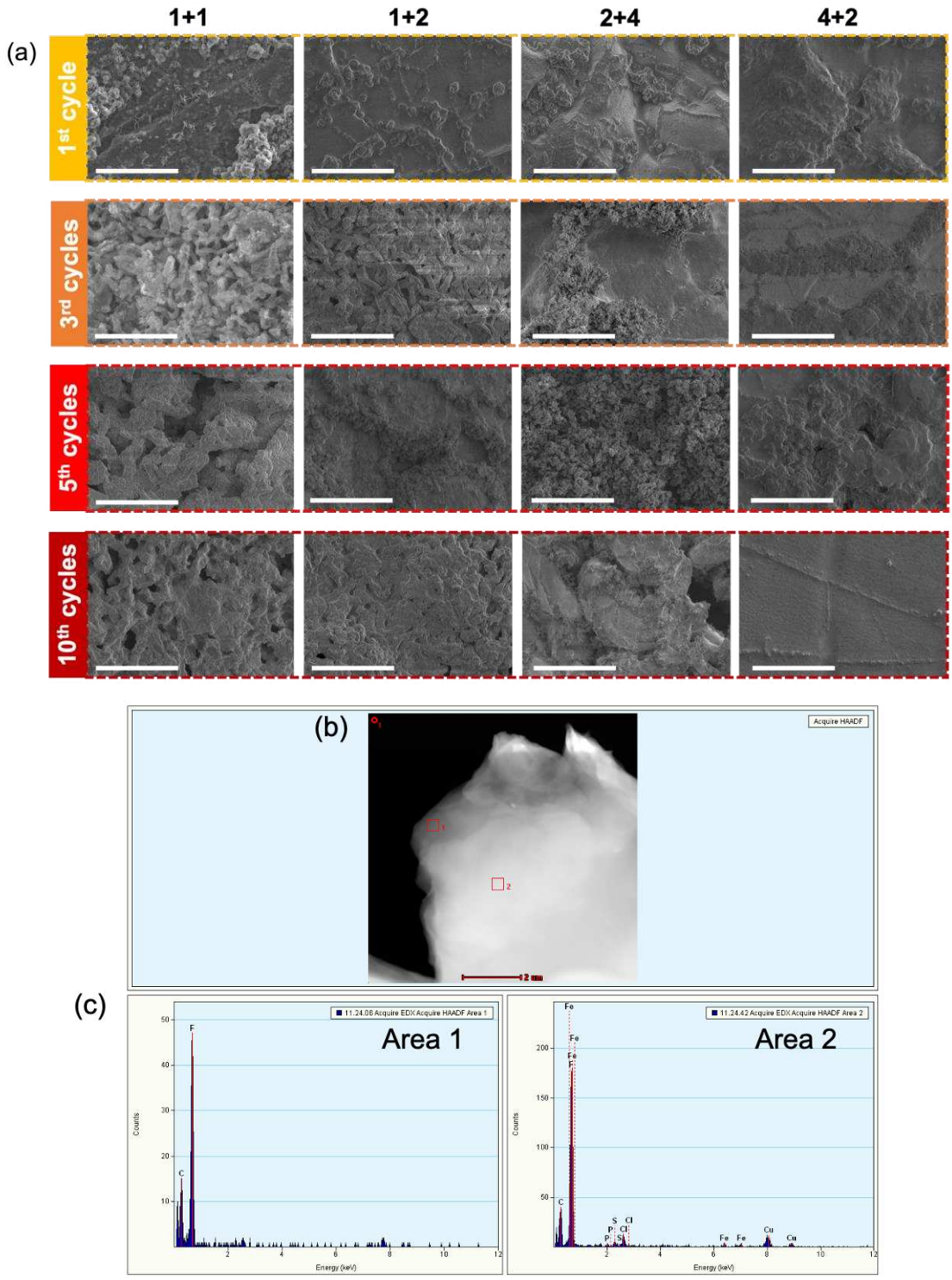


**Figure 7.4.** (a) Top-view SEM images of Li deposited on $Li^0$ foils in Li|LFP cells with 1+1, 1+2, 2+4, and 4+2 after 1, 3, 5, and 10 cycles at a current density of 0.05C (the scale bar is 10 μm). (b)

STEM images of the remaining Li nucleation on Cu mesh after the discharge process in Li|LFP with the 4+2 CPE. (c) EDX analysis from different areas (area 1 and 2) in Figure 7.4(b).

### 7.4.4 SEI composition analysis

To reveal the synergistic effect of dual anions ($TFSI^-$ and $NO_3^-$) on the SEI components, X-ray photoelectron spectroscopy (XPS) was carried out on cycled $Li^0$ anodes with the 4+2 CPE after being respectively cycled for 1, 3, 5, and 10 times. No obvious increased content of all elements suggests a chemically stable SEI formation. Figure 7.5(a) shows C 1s spectra and demonstrates the presence of $CF_x$ peak (at 293.1 eV) that originate from $TFSI^-$ anions. Organic species such as C-C/C-H, C-O (ethers), and C=O (carbonates) are detected for initial and evolved SEIs within 10 cycles. The presence of the organic C species may imply that there is a lower polymerization or other side reactions linked with the solvent reduction.[20] Regarding F 1s spectra as plotted in Figure 7.5(b)), peaks at 686.7 eV and at 688.9 eV are respectively assigned to $CF_x$ and $TFSI^-$ species, suggesting the existence of salting-out LiTFSI salts. The position of the peak at 685.4 eV coincides with the defluorination of $TFSI^-$ to produce LiF.[25] With cycle increases, the content of LiF remains almost unchanged for the 4+2 CPE only (in Figure A12.5). LiF has stronger adhesion to the $Li^0$ surface, benefiting in the formation of a robust SEI layer and effectively preventing further side reactions.[10] While without adding $LiNO_3$, LiTFSI as the single salt continuously decompose into LiF and may generate a thick SEI layer (in Figure A12.6).

The SEI film formed on ultrathin $Li^0$ with 4+2 CPE exhibits three peaks in high-resolution N 1s spectrum due to its strong oxidizing nature (in Figure 7.5(c)) at 399.9 eV, 403.7 eV, and 407.7 eV, corresponding to $Li_3N$, $LiNO_2$, and $LiNO_3$, respectively.[26] The existence of $Li_3N$, $LiNO_2$, and $LiNO_3$ enhances the ionic conductivity as well as the interphase stability, which could partially contribute to uniform and rapid depositions of $Li^+$ on the $Li^0$.[26] $LiN_3$ remains almost constant with cycle increase. The reaction mechanisms of the $LiNO_3$ decomposition are aligned with what was known as below:

$$NO_3^- + 2Li \rightarrow NO_2^- + Li_2O$$

$$NO_2^- + 6Li + Li^+ \rightarrow Li_3N + 2Li_2O$$

In Figure 7.5(d), the Li 1s spectrum verifies two peaks in the SEI film after 1 cycle at 53.8 eV and 55.6 eV, corresponding to $Li_2O$ and LiF species, respectively. The relative intensities for both peaks maintain constantly during 10 cycles, indicating a chemically stable SEI evolution. Such a LiF-$Li_3N$-rich SEI film in the 4+2 CPE improves the stability of $Li^0$ anode.

In S 2p spectra (in Figure A12.7), two peaks of S-N (163.7/164.9 eV, for $2p^{3/2}/2p^{1/2}$) and $SO_3^{2-}$ (165.6 eV/166.8 eV) are derived from the original $TFSI^-$ (-$SO^2CF_3$ group) and partially decomposed salt after 1 cycle. Upon cycling, the appearance of $SO_4^{2-}$ (170.0 eV/170.2 eV) corresponds to further decomposition of $TFSI^-$ after 3 cycles. The peak of S-N is visible after 5 cycles. After 10 cycles, the peaks of $SO_3^{2-}$ (166.1 eV/167.2 eV) and $SO_4^{2-}$ (167.9 eV/169.1 eV) represent complete decomposition of $TFSI^-$. The S-N in the LiTFSI can interact with Li ions directly. The introduction of $NO_3^-$ thereby regulates the interactions between Li ions and $TFSI^-$ and results in polarization of $TFSI^-$.[27]

The presence of $LiNO_3$ only in the liquid systems is considered as a "sacrificial electrolyte additive" since it is continuously reacting with deposited $Li^0$ in each cycle. Surprisingly, with cycling, the content of $Li_3N$ keeps nearly persistent in the 4+2 CPE compared with that of the 2+4 (in Figure A12.8). A relatively small amount of $LiNO_3$ dissolved in the 4+2 CPE is preferably reduced on the $Li^0$ surface but the salting-out of LiTFSI may help maintain a nearly saturated solution of $LiNO_3$. In this way, the beneficial effect of the LiF-$Li_3N$-rich SEI layer on the $Li^0$ anode is maintained. This key finding is supported by the work of Manthiram's group that the competitive reactivity between dual anions could slow down the reaction rate of one anion.[28]

Relatively higher F/C, F/O, N/C, and N/O ratios and a lower C/O ratio were obtained for the SEI of 4+2 CPE compared to that for 1+1 electrolyte (in Figure A12.9). These ratios confirm that more anions were decomposed in the SEI than the solvents, which validates higher contents of inorganics species (e.g., LiF, $LiN_3$, and $Li_2O$) involved in SEI for the 4+2 CPE on the $Li^0$ surface.[12]

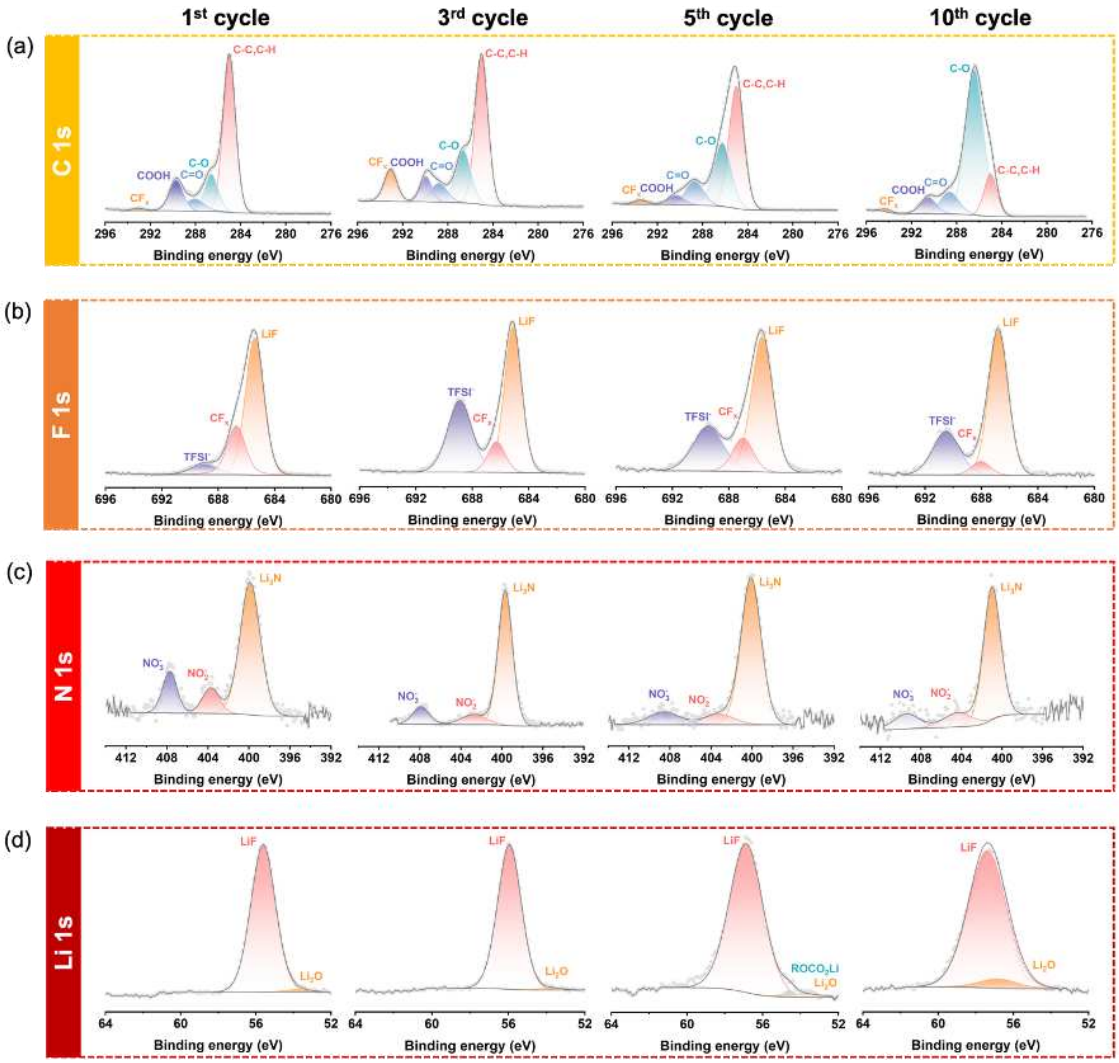


**Figure 7.5.** XPS profiling of the SEI layer on ultrathin $Li^0$ with the 4+2 CPE after 1, 3, 5, and 10 cycles: (a) C *1s*; (b) F *1s*; (c) N *1s*; (d) Li *1s*.

### 7.4.5 Electrolyte/electrode resistance evolution after cycling

To uncover the mechanism of better cycling performance of Li|4+2|LFP, electrochemical impedance spectroscopy (EIS) was performed after open-circuit rest of 12 h and being cycled for 1, 3, 5, and 10 times, respectively. A Nyquist plot is composed of a semicircle in the high-to-middle-frequency region and a Warburg tail in the low-frequency region. The semicircle in the high-to-middle-frequency region is interpreted as the interface between the 4+2 CPE and electrode.[11] The bulk resistance of all electrolytes including the 4+2 CPE in the cells is quite low

compared with the low-concentration electrolytes. After the initial cycle, the cell with 1+2 electrolyte could establish a less resistive interface than the one with 1+1 (in Figure 7.6(a) and (b)). While the cell with precipitated 4+2 CPE indicates the smallest interfacial resistance (the smallest semi-circle) compared to the other three electrolytes, and it remains relatively stable within 10 cycles than the one with 2+4 electrolyte (in Figure 7.6(c) and (d)), indicating a stable and less-resistive interface (including SEI). The increased charge-transfer resistance might be due to the special Li solvation/de-solvation structure at the $Li^0$|4+2 CPE interface.[12]

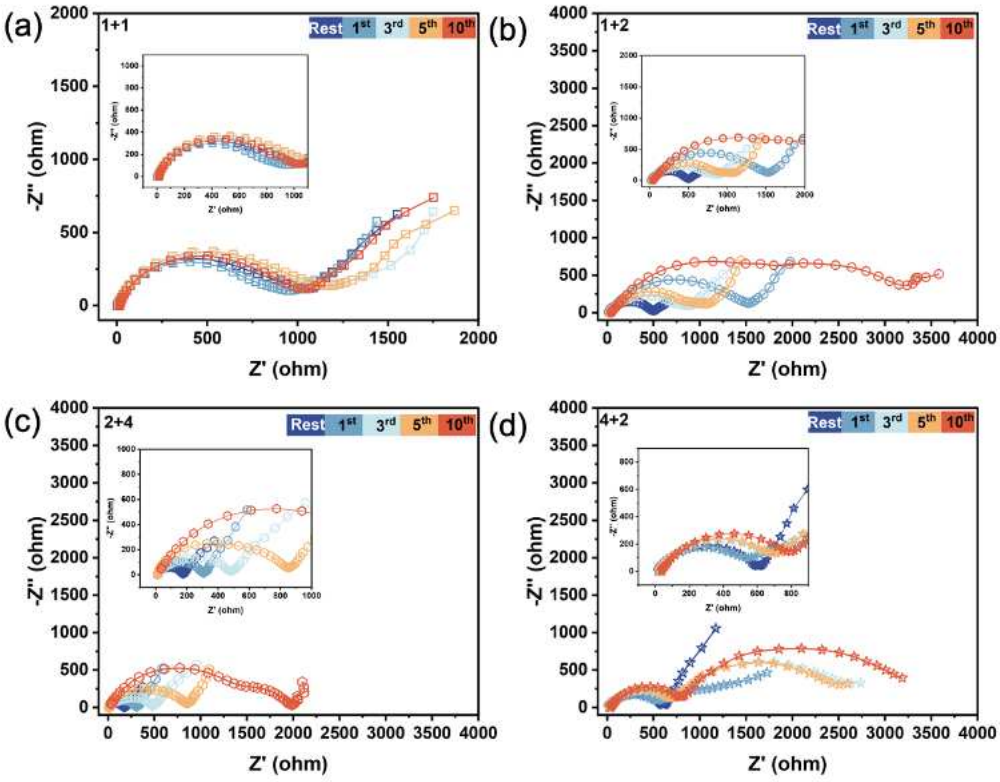


**Figure 7.6.** (a-d) Nyquist plots of Li|LFP cells with 1+1, 1+2, 2+4, and 4+2 after 1, 3, 5, and 10 cycles at a current density of 0.05C.

## 7.5 Conclusions

In conclusion, we introduced a concentrated precipitation electrolyte (CPE) by combining 4 M LiTFSI and 2 wt.% $LiNO_3$ (4+2) in the ether-based system to boost the electrochemical

performance of the ultrathin $Li^0$ anode (thickness of 25 μm). The distinct ion solvation environment in the 4+2 CPE induces a mechanically robust and chemically stable SEI. The uniform and compact $Li^0$ depos morphologies are obtained in the 4+2 CPE. Consequently, the highest average CE of 99.94% and a stable electrochemical performance (capacity retention of 82.8%) is attained after 100 cycles in the Li|4+2|LFP (mass loading of ~15mg $cm^{-2}$) cell. Upon cycling, the precipitation in the 4+2 CPE works as a reservoir for salting-out salts during cycling, leading to stabilization of the LITFSI and $LiNO_3$ reduction on the $Li^0$ surface. The formed LiF-$Li_3N$-rich SEI significantly improves the reversibility of the ultrathin $Li^0$ anode. Unlike all diluent and concentrated electrolytes so far, the 4+2 CPE with modified $Li^+$ solvation structure activates $Li^+$ transport kinetics and guides a stable SEI with enhanced physicochemical features in LMBs.

## 7.6 References


1. Thackeray, M. M.; Wolverton, C.; Isaacs, E. D. Electrical energy storage for transportation—approaching the limits of, and going beyond, lithium-ion batteries. *Energy & Environmental Science*. **2012,** *5*, 7854-7863.
2. Gür, T. M. Review of electrical energy storage technologies, materials and systems: challenges and prospects for large-scale grid storage. *Energy & Environmental Science*. **2018,** *11*, 2696-2767.
3. Liu, J.; Bao, Z.; Cui, Y.; Dufek, E.J.; Goodenough, J.B.; Khalifah, P.; Li, Q.; Liaw, B.Y.; Liu, P.; Manthiram, A.; Meng, Y.S. Pathways for practical high-energy long-cycling lithium metal batteries. *Nature Energy*. **2019**, *4*, 180-186.
4. Holoubek, J.; Liu, H.; Wu, Z.; Yin, Y.; Xing, X.; Cai, G.; Yu, S.; Zhou, H.; Pascal, T.A.; Chen, Z.; Liu, P. Tailoring electrolyte solvation for Li metal batteries cycled at ultra-low temperature. *Nature Energy*. **2021,** *6*, 303-313.
5. a) Stuckenberg, S.; Bela, M.M.; Lechtenfeld, C.T.; Mense, M.; Küpers, V.; Ingber, T.T.K.; Winter, M.; Stan, M.C. Influence of LiNO3 on the Lithium Metal Deposition Behavior in

Carbonate-Based Liquid Electrolytes and on the Electrochemical Performance in Zero-Excess Lithium Metal Batteries. *Small*. **2023**, 2305203. ; b) Yim, C. H.; Houache, M. S.; Baranova, E. A.; Abu-Lebdeh, Y. Understanding key limiting factors for the development of all-solid-state-batteries. *Chemical Engineering Journal Advcances*. **2023**, *13*, 100436. ; c) Weber, R.; Genovese, M.; Louli, A. J.; Hames, S.; Martin, C.; Hill, I. G.; Dahn, J. R. Long cycle life and dendrite-free lithium morphology in anode-free lithium pouch cells enabled by a dual-salt liquid electrolyte. *Nature Energy*. **2019**, *4*, 683-689. ; d) Hobold, G.M.; Lopez, J.; Guo, R.; Minafra, N.; Banerjee, A.; Shirley Meng, Y.; Shao-Horn, Y.; Gallant, B.M. Moving beyond 99.9% Coulombic efficiency for lithium anodes in liquid electrolytes. *Nature Energy*. **2021,** *6*, 951-960.

6. Shi, P.; Zhang, X.Q.; Shen, X.; Zhang, R.; Liu, H.; Zhang, Q. A review of composite lithium metal anode for practical applications. *Advanced Materials Technologies*. **2020,** *5*, 1900806.
7. Lee, Y.G.; Fujiki, S.; Jung, C.; Suzuki, N.; Yashiro, N.; Omoda, R.; Ko, D.S.; Shiratsuchi, T.; Sugimoto, T.; Ryu, S.; Ku, J.H. High-energy long-cycling all-solid-state lithium metal batteries enabled by silver–carbon composite anodes. *Nature Energy*. **2020,** *5,* 299-308.
8. Kwon, H.; Lee, J.H.; Roh, Y.; Baek, J.; Shin, D.J.; Yoon, J.K.; Ha, H.J.; Kim, J.Y.; Kim, H.T. An electron-deficient carbon current collector for anode-free Li-metal batteries. *Nature Communications*. **2021,** *12*, 5537.
9. a) Peled, E. The electrochemical behavior of alkali and alkaline earth metals in nonaqueous battery systems—the solid electrolyte interphase model. *Journal of The Electrochemical Society*. **1979,** *126*, 2047. ; b) Aurbach, D.; Daroux, M.L.; Faguy, P.W.; Yeager., E. Identification of surface films formed on lithium in propylene carbonate solutions. *Journal of The Electrochemical Society*. **1987,** *134*, 1611. ; c) Aurbach, D.; Ein-Ely, Y.; Zaban, A. The surface chemistry of lithium electrodes in alkyl carbonate solutions. *Journal of The*

*Electrochemical Society*. **1994,** *141*, L1. ; d) Peled, E.; Golodnitsky, D.; Ardel., G. Advanced model for solid electrolyte interphase electrodes in liquid and polymer electrolytes. *Journal of The Electrochemical Society*. **1997,** *144*, L208.

10. a) Lin, D.; Liu, Y.; Cui, Y. Reviving the lithium metal anode for high-energy batteries *Nature Nanotechnology*. **2017,** *12*, 194-206. ; b) Fang, C.; Li, J.; Zhang, M.; Zhang, Y.; Yang, F.; Lee, J.Z.; Lee, M.H.; Alvarado, J.; Schroeder, M.A.; Yang, Y.; Lu, B. Quantifying inactive lithium in lithium metal batteries. *Nature*. **2019,** *572*, 511-515.
11. a) Liu, Y.; Lin, D.; Li, Y.; Chen, G.; Pei, A.; Nix, O.; Li, Y.; Cui, Y. Solubility-mediated sustained release enabling nitrate additive in carbonate electrolytes for stable lithium metal anode. *Nature Communications*. **2018,** *9*, 3656. ; b) Jagger, B.; Pasta, M. Solid electrolyte interphases in lithium metal batteries. *Joule*. **2023,** *7*, 2228-2244.; c) Pham, T.D.; Bin Faheem, A.; Chun, S.Y.; Rho, J.R.; Kwak, K.; Lee, K.K. Synergistic effects on lithium metal batteries by preferential ionic interactions in concentrated bisalt electrolytes. *Advanced Energy Materials*. **2021,** *11*, 2003520.
12. Beyene, T.T.; Bezabh, H.K.; Weret, M.A.; Hagos, T.M.; Huang, C.J.; Wang, C.H.; Su, W.N.; Dai, H.; Hwang, B.J. Concentrated dual-salt electrolyte to stabilize Li metal and increase cycle life of anode free Li-metal batteries. *Journal of The Electrochemical Society*. **2019,** *166*, A1501-A1509.
13. a) Gu, Y.; Wang, W.W.; Li, Y.J.; Wu, Q.H.; Tang, S.; Yan, J.W.; Zheng, M.S.; Wu, D.Y.; Fan, C.H.; Hu, W.Q.; Chen, Z.B. Designable ultra-smooth ultra-thin solid-electrolyte interphases of three alkali metal anodes. *Nature Communications*. **2018,** *9*, 1339. ; b) Liu, W.; Liu, P.; Mitlin, D. Review of emerging concepts in SEI analysis and artificial SEI membranes for lithium, sodium, and potassium metal battery anodes. *Advanced Energy* Materials. **2020,** *10*, 2002297. ; c) Liu, S.; Ji, X.; Piao, N.; Chen, J.; Eidson, N.; Xu, J.; Wang, P.; Chen, L.; Zhang, J.; Deng, T.; Hou, S. An inorganic-rich solid electrolyte

interphase for advanced lithium-metal batteries in carbonate electrolytes. *Angewandte Chemie International Edition*. **2021,** *60*, 3661-3671. ; d) Ma, Q.; Fang, Z.; Liu, P.; Ma, J.; Qi, X.; Feng, W.; Nie, J.; Hu, Y.S.; Li, H.; Huang, X.; Chen, L. Improved Cycling Stability of Lithium-Metal Anode with Concentrated Electrolytes Based on Lithium (Fluorosulfonyl)(trifluoromethanesulfonyl) imide. *ChemElectroChem* **2016,** *3*, 531-536.

14. Chen, S.; Zheng, J.; Mei, D.; Han, K.S.; Engelhard, M.H.; Zhao, W.; Xu, W.; Liu, J.; Zhang, J.G. High-voltage lithium-metal batteries enabled by localized high-concentration electrolytes. *Advanced Materials*. **2018**, *30*,1706102.
15. Ren, X.; Chen, S.; Lee, H.; Mei, D.; Engelhard, M.H.; Burton, S.D.; Zhao, W.; Zheng, J.; Li, Q.; Ding, M.S.l Schroeder, M. Localized high-concentration sulfone electrolytes for high-efficiency lithium-metal batteries. *Chem.* **2018,** *4*, 1877-1892.
16. a) Kim, M.S.; Zhang, Z.; Rudnicki, P.E.; Yu, Z.; Wang, J.; Wang, H.; Oyakhire, S.T.; Chen, Y.; Kim, S.C.; Zhang, W.; Boyle, D.T. Suspension electrolyte with modified Li+ solvation environment for lithium metal batteries. *Nature Materials*. **2022,** *21*, 445-454. ; b) Kim, M.S.; Zhang, Z.; Wang, J.; Oyakhire, S.T.; Kim, S.C.; Yu, Z.; Chen, Y.; Boyle, D.T.; Ye, Y.; Huang, Z.; Zhang, W. Revealing the multifunctions of Li3N in the suspension electrolyte for lithium metal batteries. *ACS nano*. **2023,** *17*, 3168-3180.
17. a) Yamada, Y.; Usui, K.; Sodeyama, K.; Ko, S.; Tateyama, Y.; Yamada, A. Hydrate-melt electrolytes for high-energy-density aqueous batteries. *Nature Energy*. **2016,** *1*, 1-9. ; b) Yao, Y.X.; Chen, X.; Yan, C.; Zhang, X.Q.; Cai, W.L.; Huang, J.Q.; Zhang, Q. Regulating interfacial chemistry in lithium-ion batteries by a weakly solvating electrolyte. *Angewandte Chemmie International Edition*. **2021,** *60*, 4090-4097. ; c) Holoubek, J.; Liu, H.; Wu, Z.; Yin, Y.; Xing, X.; Cai, G.; Yu, S.; Zhou, H.; Pascal, T.A.; Chen, Z.; Liu, P. Tailoring electrolyte solvation for Li metal batteries cycled at ultra-low temperature. *Nature Energy*. **2021,** *6*, 303-313. ; d) Yu, Z.; Rudnicki, P.E.; Zhang, Z.; Huang, Z.; Celik, H.; Oyakhire,

S.T.; Chen, Y.; Kong, X.; Kim, S.C.; Xiao, X.; Wang, H. Rational solvent molecule tuning for high-performance lithium metal battery electrolytes. *Nature Energy*. **2022,** *7*, 94-106. ; e) Kwon, H.; Choi, H.J.; Jang, J.K.; Lee, J.; Jung, J.; Lee, W.; Roh, Y.; Baek, J.; Shin, D.J.; Lee, J.H.; Choi, N.S. Weakly coordinated Li ion in single-ion-conductor-based composite enabling low electrolyte content Li-metal batteries. *Nature Communications*. **2023,** *14*, 4047.

18. a) Ma, Y.; Ma, Y.; Wang, Q.; Schweidler, S.; Botros, M.; Fu, T.; Hahn, H.; Brezesinski, T.; Breitung, B. High-entropy energy materials: challenges and new opportunities. *Energy Environmental Science*. **2021,** *14*, 2883-2905. ; b) Wang, Q.; Zhao, C.; Wang, J.; Yao, Z.; Wang, S.; Kumar, S.G.H.; Ganapathy, S.; Eustace, S.; Bai, X.; Li, B.; Wagemaker, M. High entropy liquid electrolytes for lithium batteries. *Nature Communications*. **2023,** *14*, 440. ; c) Kim, S.C.; Wang, J.; Xu, R.; Zhang, P.; Chen, Y.; Huang, Z.; Yang, Y.; Yu, Z.; Oyakhire, S.; Zhang, W.; Greenburg, L. High-entropy electrolytes for practical lithium metal batteries. *Nature Energy*. **2023,** *8*, 814-826. ; d) Wang, Q.; Zhao, C.; Yao, Z.; Wang, J.; Wu, F.; Kumar, S.G.H.; Ganapathy, S.; Eustace, S.; Bai, X.; Li, B.; Lu, J. Entropy-driven liquid electrolytes for lithium batteries. *Advanced Materials*. **2023,** *35*, 2210677.
19. a) Couillard, M.; Tyo, D.D.; Kingston, D.M.; Patarachao, B.; Zborowski, A.; Ng, S.; Mercier, P.H. Structure and Mineralogy of Hydrophilic and Biwettable Sub-2 μm Clay Aggregates in Oil Sands Bitumen Froth. *Minerals*. **2020**, *10*, 1040. ; b) Qiu, F.; Li, X.; Deng, H.; Wang, D.; Mu, X.; He, P.; Zhou, H. A concentrated ternary-salts electrolyte for high reversible Li metal battery with slight excess Li. *Advanced Energy Materials*. **2019,** *9*, 1803372.
20. Cavers, H.; Steffen, J.; Gogoi, N.; Adelung, R.; Hartke, B.; Hansen, S. Investigation of the Impact of High Concentration LiTFSI Electrolytes on Silicon Anodes with Reactive Force Field Simulations. *Liquids*. **2023,** *3*, 132-158.

21. a) Lee, L.L. A molecular theory of Setchenov's salting-out principle and applications in mixed-solvent electrolyte solutions. *Fluid Phase Equilibria*. **1997**, *131*, 67-82. ; b) Galvão, A.C.; Jiménez, Y.P.; Justel, F.J.; Robazza, W.S.; Donatti, F.S. Salting-out precipitation of NaCl, KCl and NH4Cl in mixtures of water and methanol described by the modified Pitzer model. *The Journal of Chemical Thermodynamics*. **2020,** *150*, 106202.

22. a) Wahyudi, W.; Ladelta, V.; Tsetseris, L.; Alsabban, M.M.; Guo, X.; Yengel, E.; Faber, H.; Adilbekova, B.; Seitkhan, A.; Emwas, A.H.; Hedhili, M.N. Lithium-ion desolvation induced by nitrate additives reveals new insights into high performance lithium batteries. *Advanced Functional Materials*. **2021,** *31*, 2101593. ; b) Su, H.; Chen, Z.; Li, M.; Bai, P.; Li, Y.; Ji, X.; Liu, Z.; Sun, J.; Ding, J.; Yang, M.; Yao, X. Achieving Practical High-Energy-Density Lithium-Metal Batteries by a Dual-Anion Regulated Electrolyte. *Advcanced Materials.* **2023,** *35,* 2301171. ; c) Seo, D.M.; Boyle, P.D.; Sommer, R.D.; Daubert, J.S.; Borodin, O.; Henderson, W.A. Solvate structures and spectroscopic characterization of LiTFSI electrolytes. *Journal of Physical Chemistry B*. **2014**, *118*, 13601-13608. ; d) Al-Salih, H.; Baranova, E.A.; Abu-Lebdeh, Y. Unraveling the phase diagram-ion transport relationship in aqueous electrolyte solutions and correlating conductivity with concentration and temperature by semi-empirical modeling. *Communications Chemistry*. **2023**, *6*, 195.

23. a) Chen, Y.; Li, M.; Liu, Y.; Jie, Y.; Li, W.; Huang, F.; Li, X.; He, Z.; Ren, X.; Chen, Y.; Meng, X. Origin of dendrite-free lithium deposition in concentrated electrolytes. *Nature Commun.* **2023,** *14*, 2655. ; b) Yim, C. H.; Tam, J.; Soboleski, H.; Abu-Lebdeh, Y. On the correlation between free volume, phase diagram and ionic conductivity of aqueous and non-aqueous lithium battery electrolyte solutions over a wide concentration range. *Journal of The Electrochemical Society*. **2017**, *164*, A1002.

24. Venezia, E.; Salimi, P.; Liang, S.; Fugattini, S.; Carbone, L.; Zaccaria, R.P. Comparative Study of Lithium Halide-Based Electrolytes for Application in Lithium-Sulfur Batteries. *Inorganics*. **2023,** *11*, 86.

25. a) Liu, P.; Ma, Q.; Fang, Z.; Ma, J.; Hu, Y.S.; Zhou, Z.B.; Li, H.; Huang, X.J.; Chen, L.Q. Concentrated dual-salt electrolytes for improving the cycling stability of lithium metal anodes. *Chinese Physics B*. **2016,** *25*, 078203. ; b) Andersson, E.K.; Sångeland, C.; Berggren, E.; Johansson, F.O.; Kühn, D.; Lindblad, A.; Mindemark, J.; Hahlin, M. Early-stage decomposition of solid polymer electrolytes in Li-metal batteries. *Journal of Materials Chemistry A*. **2021,** *9*, 22462-22471. ; c) Yu, W.; Yu, Z.; Cui, Y.; Bao, Z. Degradation and speciation of Li salts during XPS analysis for battery research. *ACS Energy Letters.* **2022,** *7*, 3270-3275.

26. A) Yan, C.; Yao, Y.X.; Chen, X.; Cheng, X.B.; Zhang, X.Q.; Huang, J.Q.; Zhang, Q. Lithium nitrate solvation chemistry in carbonate electrolyte sustains high-voltage lithium metal batteries. *Angewandte Chemie International Edition.* **2018,** *57*, 14055-14059. ; b) Yao, Y.X.; Zhang, X.Q.; Li, B.Q.; Yan, C.; Chen, P.Y.; Huang, J.Q.; Zhang, Q. A compact inorganic layer for robust anode protection in lithium-sulfur batteries. *InfoMat.* **2020**, *2*, 379-388.

27. Zhang, X.Q.; Chen, X.; Hou, L.P.; Li, B.Q.; Cheng, X.B.; Huang, J.Q.; Zhang, Q. Regulating anions in the solvation sheath of lithium ions for stable lithium metal batteries. *ACS Energy Letters.* **2019,** *4*, 411-416.

28. Zhang, X.; Cui, Z.; Manthiram, A. Long-Life Lithium-Metal Batteries with an Ultra-High-Nickel Cathode and Electrolytes with Bi-Anion Activity. *Advanced Functional Materials.* **2023**, 2309591.

# Chapter 8

## Conclusions and future recommendations

This PhD dissertation has been majorly concerned with addressing solid-solid and solid-liquid interfaces and/or interphases issues between electrolyte and battery electrodes in lithium batteries. Solid-state lithium metal batteries (SS-LMBs) with ceramic-based oxide electrolytes hold great promise as the next-generation lithium batteries due to their reliable safety, high-energy densities, and excellent mechanical and thermal stabilities. However, attaining practical SSBs remains challenging because of the point-by-point interface contact between electrolytes and electrodes.

The first part of this work had resolved the $Ti^{4+}$ cation reduction issue of perovskite-type (LLTO) electrolytes towards Li-metal anodes. It was found that $Ti^{4+}$-ions reduction leads to increased interfacial resistance of Li-ion migration at the LLTO|Li-metal interface in symmetric Li|LLTO|Li cells. The use of solid-gel hybrid approach effectively prevented $Ti^{4+}$ cations reduction and decreased interfacial resistance while in contact with Li metals by coating PEO-LiTFSI-SN (35:30:35, wt.%) gel on the surface of LLTO pellets. The flexible gel at the interface acted as a buffer layer to alleviate SSEs stacking pressure during the battery assembly. It was recommended that a design of SSBs with a flexible coating may beneficial to avoiding severe SSEs cracking from assembly.

Aside from the anode interface approach in SSBs, this thesis had significantly improved the SSEs|cathode interfacial contact when using solid-liquid hybrid approach. It was found that the addition of liquid electrolyte (LE) improves the initial physical contact between garnet-type (LLZO) SSEs and NMC 622 cathode and enable the cycling of SSBs. Synchrotron-based X-ray technique (e.g., scanning transmission X-ray microscopy associated with X-ray absorption microscopy) was applied to identify unique interphases in hybrid SSBs. After the 1$^{st}$ charge/discharge process, liquid electrolyte was decomposed and reacted with LLZO to form a

new-identified interphase designated as solid-liquid electrolyte interphase (SLEI). At the same time, a 50 nm thick cathode-electrolyte interphase (CEI) was observed on the outer edge of NMC 622 cathode by ptychography-mode STXM (with a spatial resolution of ~10 nm).

The last part of this work had designed a novel type of concentrated liquid electrolyte to establish a robust SEI in LIBs. Detailed chemical and structural insights into SEI evolution on Li-meal anodes needs to be carefully monitored. The developed LE may be adapted to acts as the interfacial additives in SSBs.

Overall, we found that hybrid solid-state electrolyte synergistically combined the advantages of SSEs and liquids and enabled improved electrochemical performance of SS-LMBs. There are a few promising avenues to advance hybrid solid-state electrolytes in the future as a solution for implementation of practical SSBs.

One area of improvement is to optimize the quantity of liquid additives and their chemical compositions to promote the formation of a chemically stable, thin, and efficient SLEI. It is recommended that surface coating and microstructural design (e.g., core-shell structure) of Ni-rich NMC cathodes are necessary to prohibit battery failure. Moreover, the phase change of liquid electrolyte in hybrid SS-LMBs should be evaluated in real-time during the battery operation using advanced *in operando* techniques. It would be essential to clarify the consumption of LE at different charge/discharge stages and reveal their influences on the capacity degradation in the cells.

Another area of improvement is to combine the surface structuring of SSEs with the usage of liquid additives at the SSEs|battery electrode interfaces. It is recommended that the surface contact area between SSEs and battery electrodes could be further increased by structuring the surface of SSEs (e.g., laser processing and three-dimensional printing) with micro-/nano-patterns. In this way, more pathways for Li-ion migration at the interfaces are provided that could lead to improved battery performance of hybrid SSBs.

When developing a concentrated precipitation electrolyte (CPE), a theoretical understanding of its $Li^+$ solvation/de-solvation structure (e.g., molecular dynamics simulation and density functional theory) could help with electrolyte composition adjustments to further improve the battery performance. Furthermore, the CEI structure and composition should be evaluated to guide the use of high-capacity cathode chemistries (e.g., Ni-rich cathodes) with CPEs.

# Chapter 9

# Appendix 1: Supporting information for Chapter 4

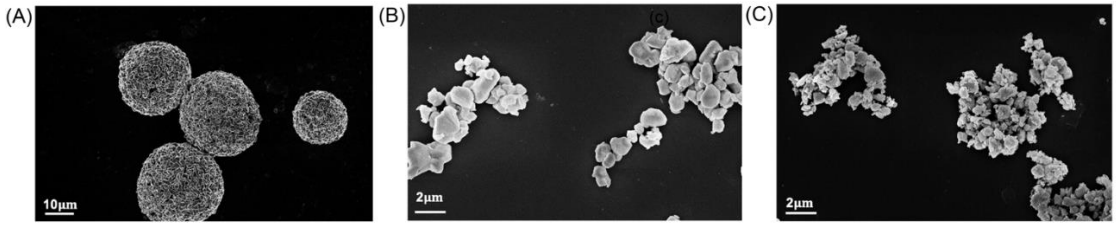


**Figure A9.1.** SEM pictures of pristine LLTO powders: (A) granular LLTO; (B) milled LLTO; and (C) mixed LLTO.

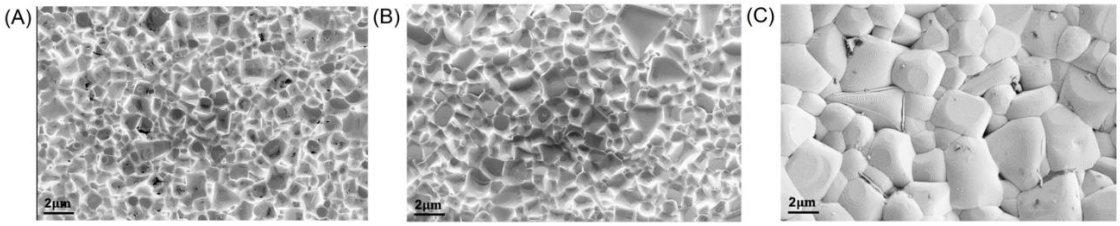


**Figure A9.2.** SEM pictures of the surface morphology for sintered mixed pellets with different weight ratio between G-LLTO and M-LLTO: (A) 60:40; (B) 65:35; and (C) 70:30.

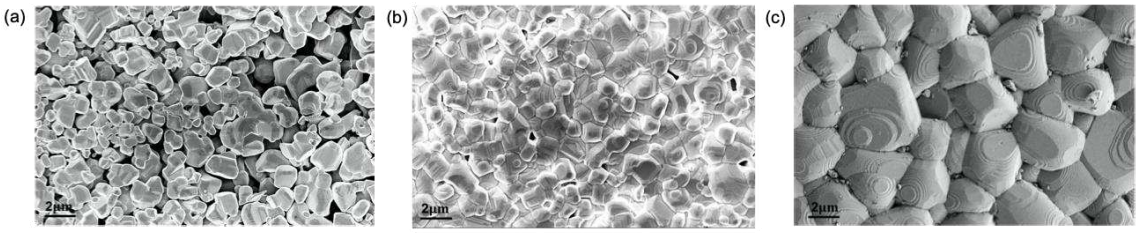


**Figure A9.3.** SEM pictures of the surface morphology for sintered mixed pellets in air at: (A) 960 ˚C; (B) 1050 ˚C; and (C) 1170 ˚C.

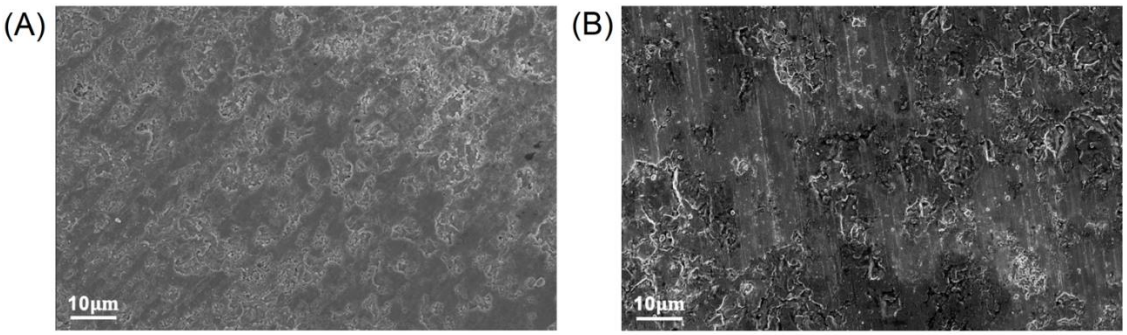

**Figure A9.4.** SEM pictures of cut-off sintered pellets: (A) white LLTO; and (B) black LLTO (color change after contacting with Li).

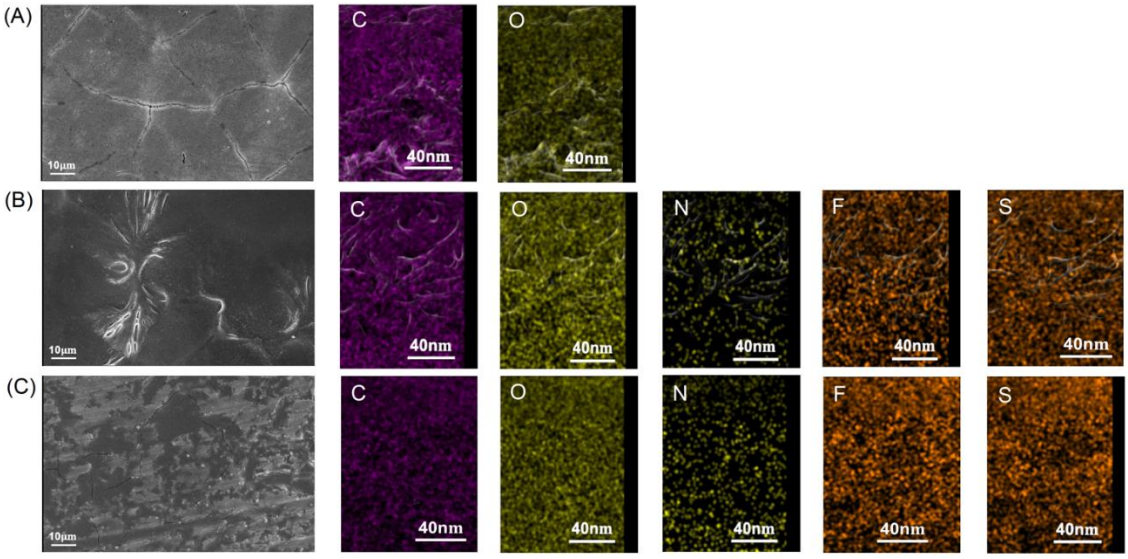


**Figure A9.5.** SEM pictures for the surface coated LLTO pellets by: (A) PEO; (B) PEO-LiTFSI; and (C) PEO-LiTFSI-SN and EDX mapping of C, O, N, F, S elements for each coated LLTO.

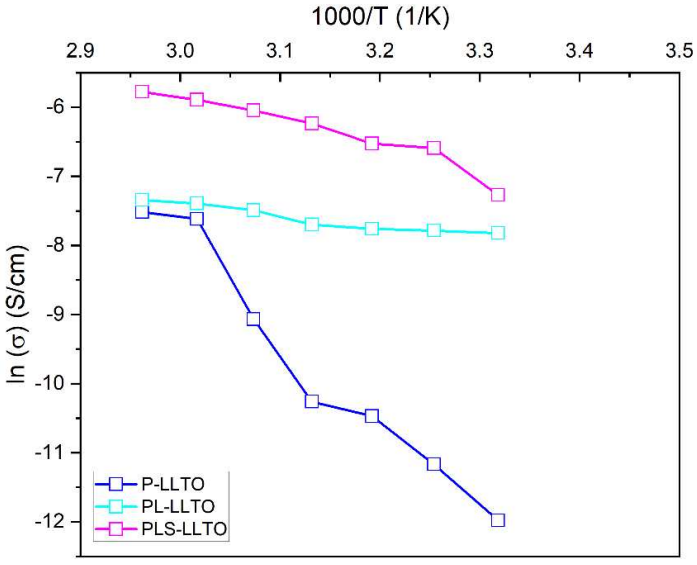


**Figure A9.6.** Arrhenius plots for coated pellet during 30 ˚C-60 ˚C.

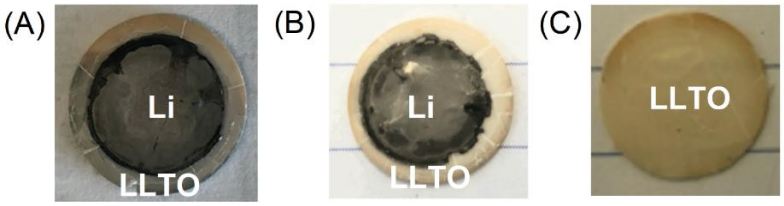

**Figure A9.7.** Photographs of LLTO pellets after cycling coated by: (A) PEO; (B) PEO-LiTFSI; and (C) PEO-LiTFSI-SN.

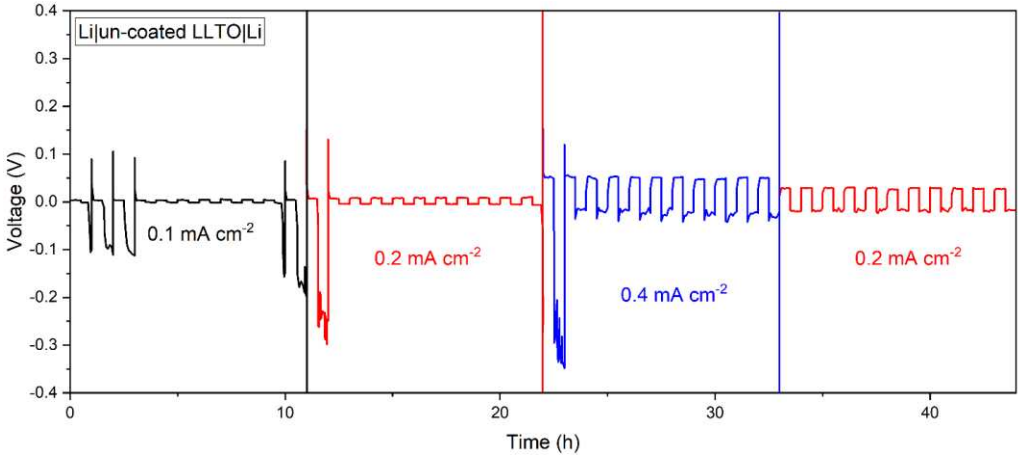


**Figure A9.8.** Cycling performance of symmetric Li | un-coated LLTO | Li cell at different current densities (tested at 60 ˚C).

**Table A7.** Summary of activation energy for coated-LLTO electrolytes.

| **Interfaces** | **Activation energy (kJ mol$^{-1}$)** |
|---|---|
| **PEO** | 131.06 |
| **PL** | 14.85 |
| **PLS** | 22.30 |

**Table A8.** Summary of the total ionic conductivity for LLTO coated by six interfaces in symmetric Li cell (tested at 60 ˚C, increased current density). $R_{total}$ contains $R_{bulk}$ (the resistance of the LLTO pellet), $R_{interface1}$ (the polarization resistance between PEO-based layers and Li metal), and $R_{interface2}$ (the interfacial resistance between coated layers and LLTO pellet). $R_1$ (ohm cm$^{-2}$) is $R_{total}$/surface area(cm$^2$) and $R_2$ (ohm cm$^{-1}$) is $R_{total}$/thickness (cm).

| **Interface** | **Current density (mA cm$^{-2}$)** | **Stable potential (mV)** | **$R_{total}$ (ohm)** | **$R_1$(ohm cm$^{-2}$)** | **$R_2$(ohm cm$^{-1}$)** | **$\sigma_{total}$(mS cm$^{-1}$)** |
|---|---|---|---|---|---|---|
| **PEO** | 0.01 | 50 | 2829.42 | 1601.13 | 37725.62 | 0.015 |
| | 0.02 | 46.85 | 1325.58 | 750.13 | 17674.45 | 0.032 |
| | 0.04 | 84.5 | 1195.43 | 676.48 | 15939.07 | 0.036 |
| **PL** | 0.01 | 0.45 | 25.46 | 14.41 | 363.78 | 1.89 |
| | 0.02 | 0.8 | 22.64 | 12.81 | 323.36 | 2.13 |
| | 0.04 | 1.55 | 21.93 | 12.41 | 313.26 | 2.19 |

| | | | | | | |
|---|---|---|---|---|---|---|
| **PLS** | 0.01 | 0.7 | 39.61 | 22.42 | 565.88 | 1.21 |
| | 0.02 | 2.85 | 80.64 | 45.63 | 1151.98 | 0.60 |
| | 0.04 | 7.25 | 102.57 | 58.04 | 1465.24 | 0.47 |

# Appendix 2: Supporting information for Chapter 5

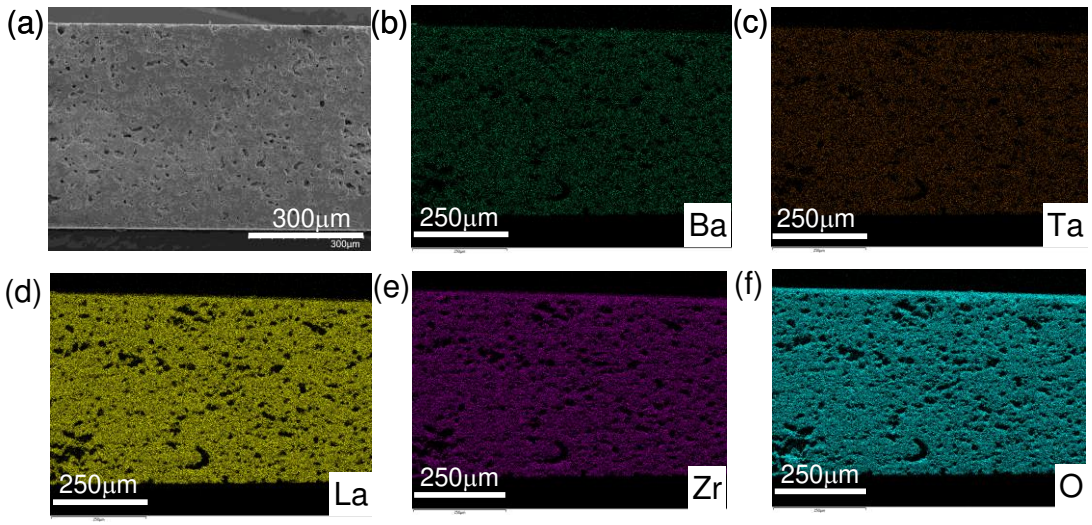


**Figure A10.1.** (a) SEM for the cross-section of LLBZTO SSEs; and (b-f) EDX analysis of Ba, Ta, La, Zr, and O elements.

In Figure A11.2, the top-view digital image of opened cell indicated that the active cathode completely separated from current collector and certain residual retained on the LLBZTO surface. No liquid was found in the cell after 28 cycles after being dissembled in an Argon-filled glovebox.

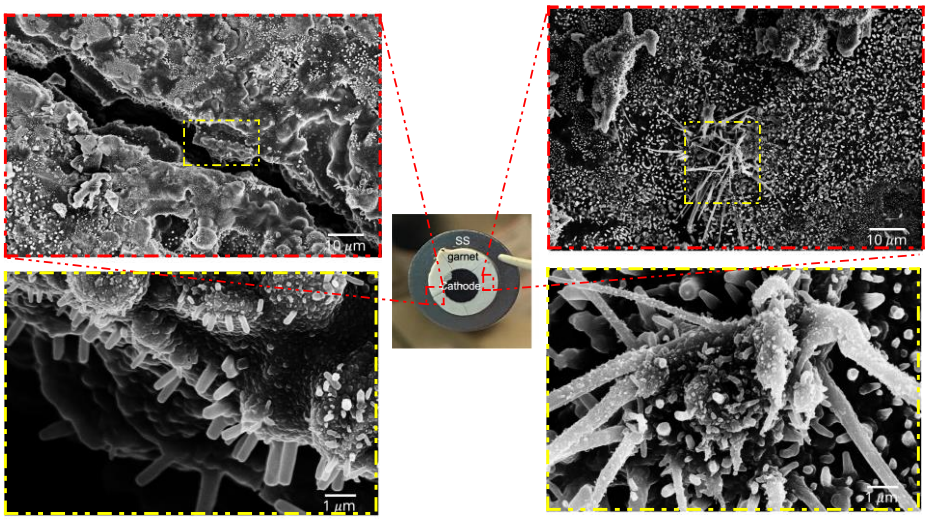


**Figure A10.2.** Top-view digital image of un-washed LLBZTO SSEs with remained NMC cathode (middle) and SEM images for the surface of LLBZTO SSEs.

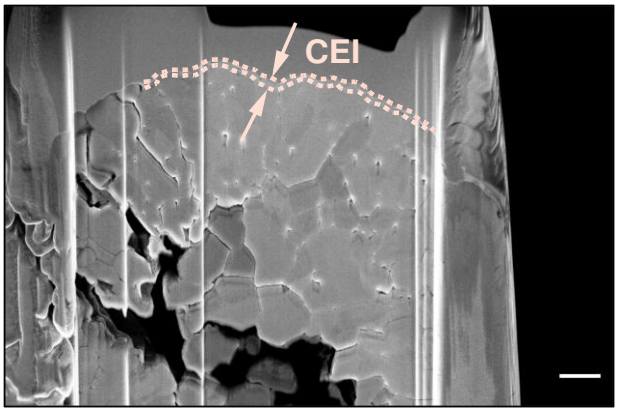


**Figure A10.3.** Zoomed-in NMC 622 region of S_01 (scale is 1 µm).

**Table A9.** Apparent density of garnet electrolytes.

| Sample numbers | Diameter (cm) | Thickness (mm) | Dry weight (g) | Density (g $cm^{-3}$) |
|---|---|---|---|---|
| **#1** | 1.02 | 0.881 | 0.2975 | 4.132576 |
| **#2** | 1.03 | 0.84 | 0.2869 | 4.099085 |
| **#3** | 1.02 | 0.818 | 0.2771 | 4.145653 |
| **Average value** | 1.02 | 0.85 | 0.29 | 4.13 |

# Appendix 3: Supporting information for Chapter 6

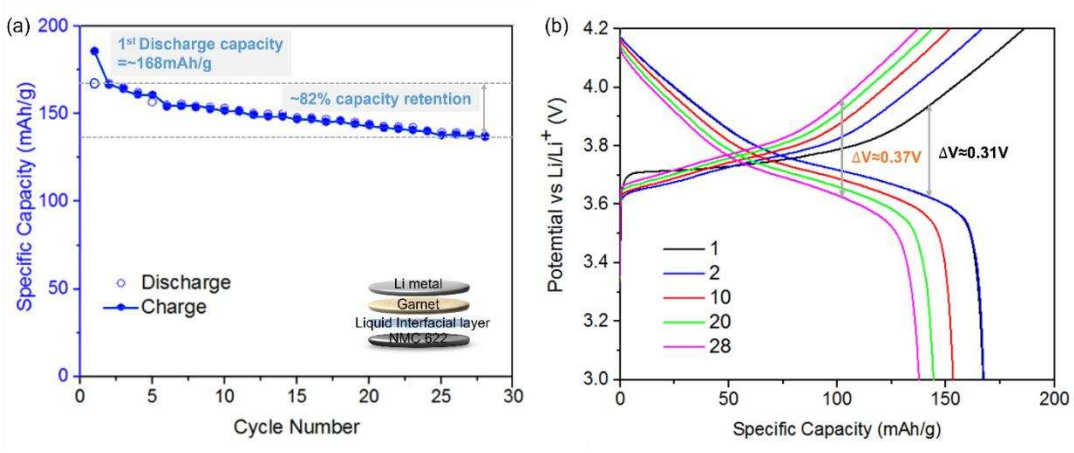


**Figure A11.1.** (a) Cycling performance at ~0.05C. (b) Galvanostatic charge/discharge curves at ~0.05C.

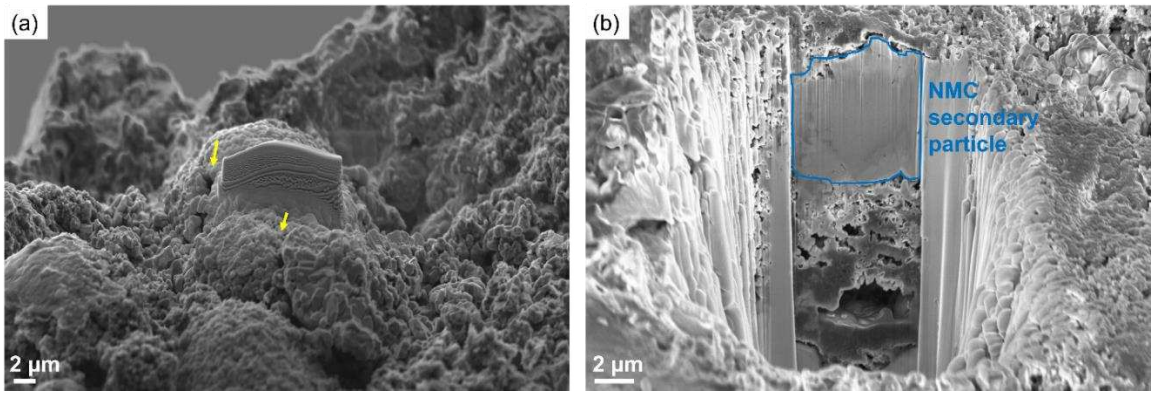


**Figure A11.2.** FIB-SEM image of NMC 622 secondary particles after 1 cycle. (a) Top view. Yellow arrows show various locations of cracks. (b) Cross-sectional view. The region highlighted in navy blue is one NMC 622 secondary particle.

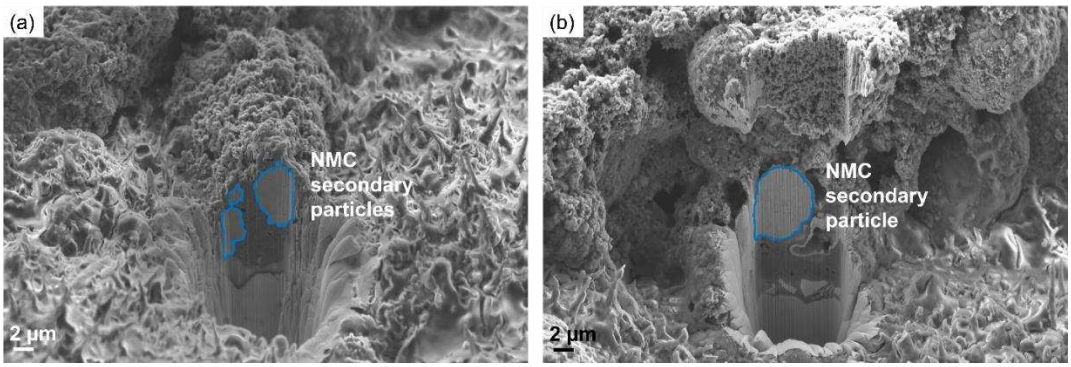

**Figure A11.3.** (a)-(b) Cross-sectional view FIB-SEM images of NMC 622 secondary particles from different spots after 28 cycles. The regions highlighted in navy blue are NMC 622 secondary particles.

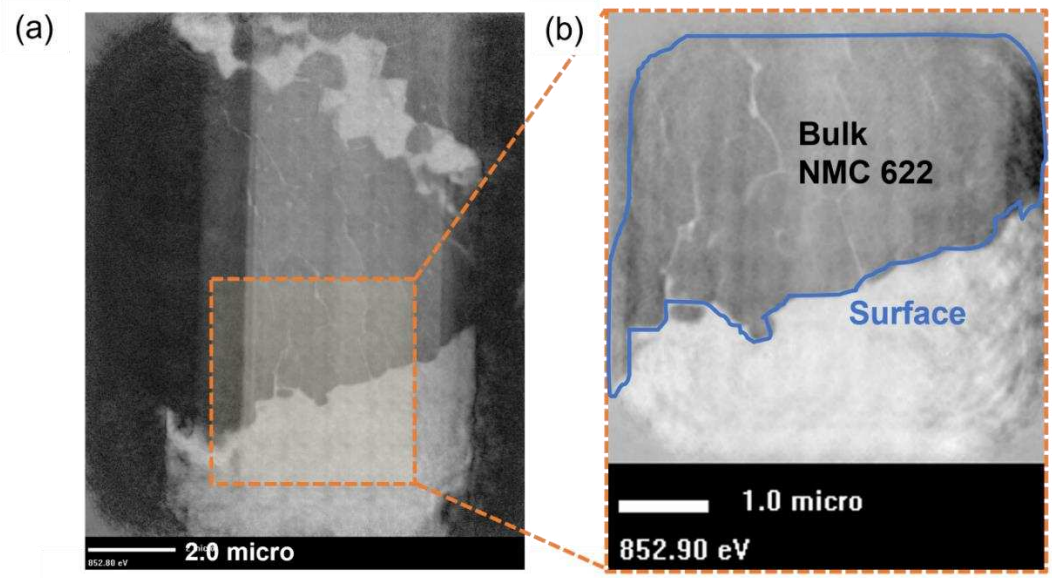


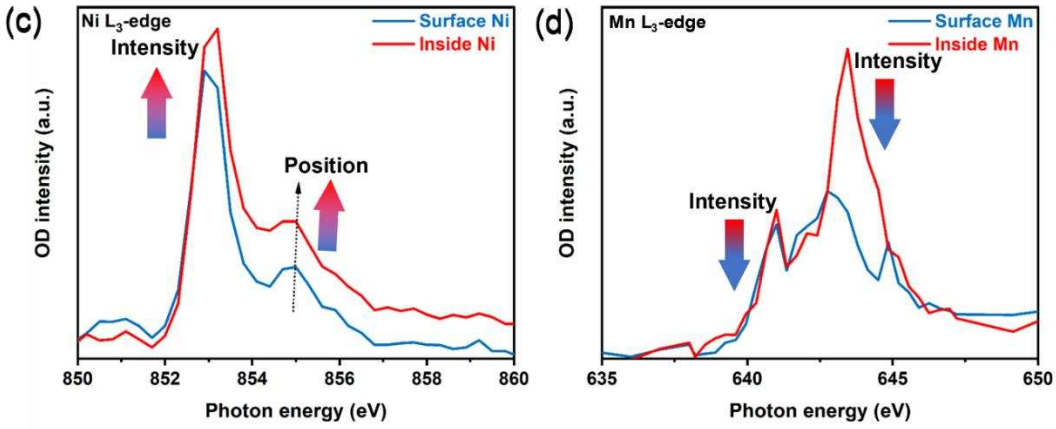


**Figure A11.4.** (a)-(b) Ptychography STXM amplitude images for surface and inside (bulk) of 1-cycled NMC 622 secondary particles. (c)-(d) XAS spectra for surface and inside (bulk) of 1-cycled NMC 622 secondary particles.

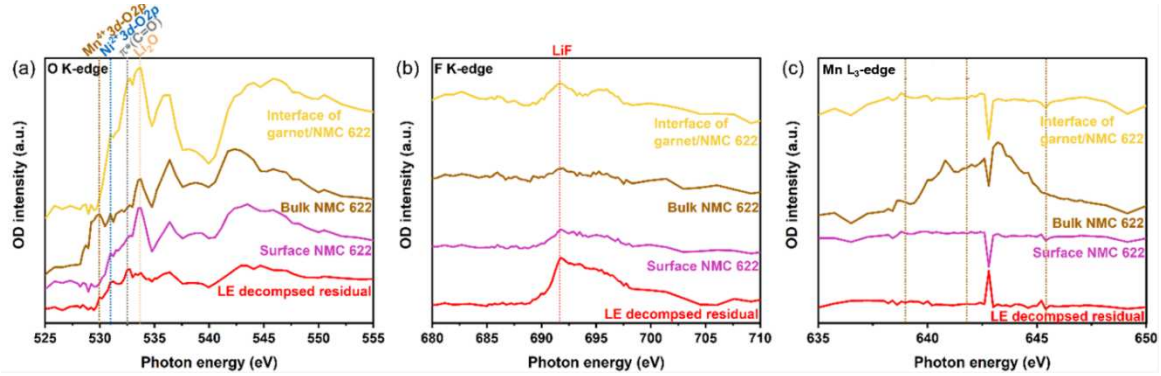


**Figure A11.5.** XAS spectra for NMC_28. (a) O K-edge; (b) F K-edge; (c) Mn $L_3$-edge from repeated STXM mapping of the same sample region.

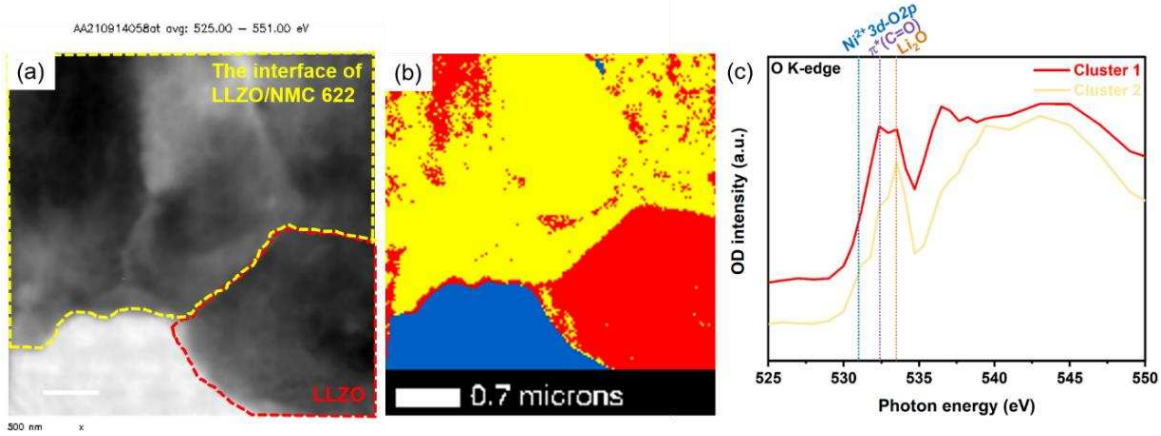


**Figure A11.6.** (a) Ptychography STXM amplitude image. (b) Elemental distribution mapping at the O K-edge of the region between the 28-cycled cathode and the garnet electrolyte. (c) XAS spectra of the O K-edge.

# Appendix 4: Supporting information for Chapter 7

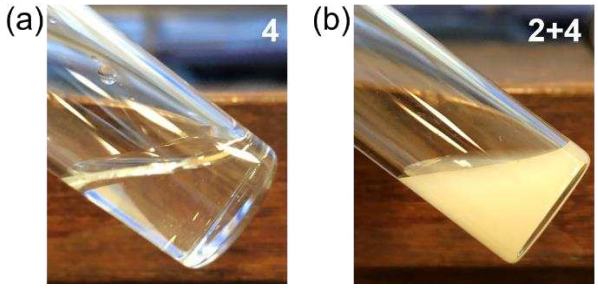


**Figure A12.1.** Photo of the dissolution state for (a) 4 M LiTFSI (4) and (b) 2 M LiTFSI+4 wt.% $LiNO_3$ (2+4) electrolytes after being well mixed at room temperature.

**Table A10.** Li-ion transference number of 1+1, 1+2, 2+2, and 4+2 electrolyte.

| **Electrolytes** | $I^{ss}[\mu A]$ | $R_b^0[ohm]$ | $R_{el}^0[ohm]$ | $R_{el}^{ss}[ohm]$ | $t_{Li^+}$ |
|---|---|---|---|---|---|
| **1+1** | 1.69 | 39.86 | 33.73 | 1885.49 | 0.01 |
| **1+2** | 3.24 | 21.39 | 5.09 | 2516.89 | 0.03 |
| **2+2** | 9 | 13.6 | 10.2 | 1811.8 | 0.02 |
| **4+2** | 8.1 | 38.18 | 16.67 | 743.61 | 0.08 |

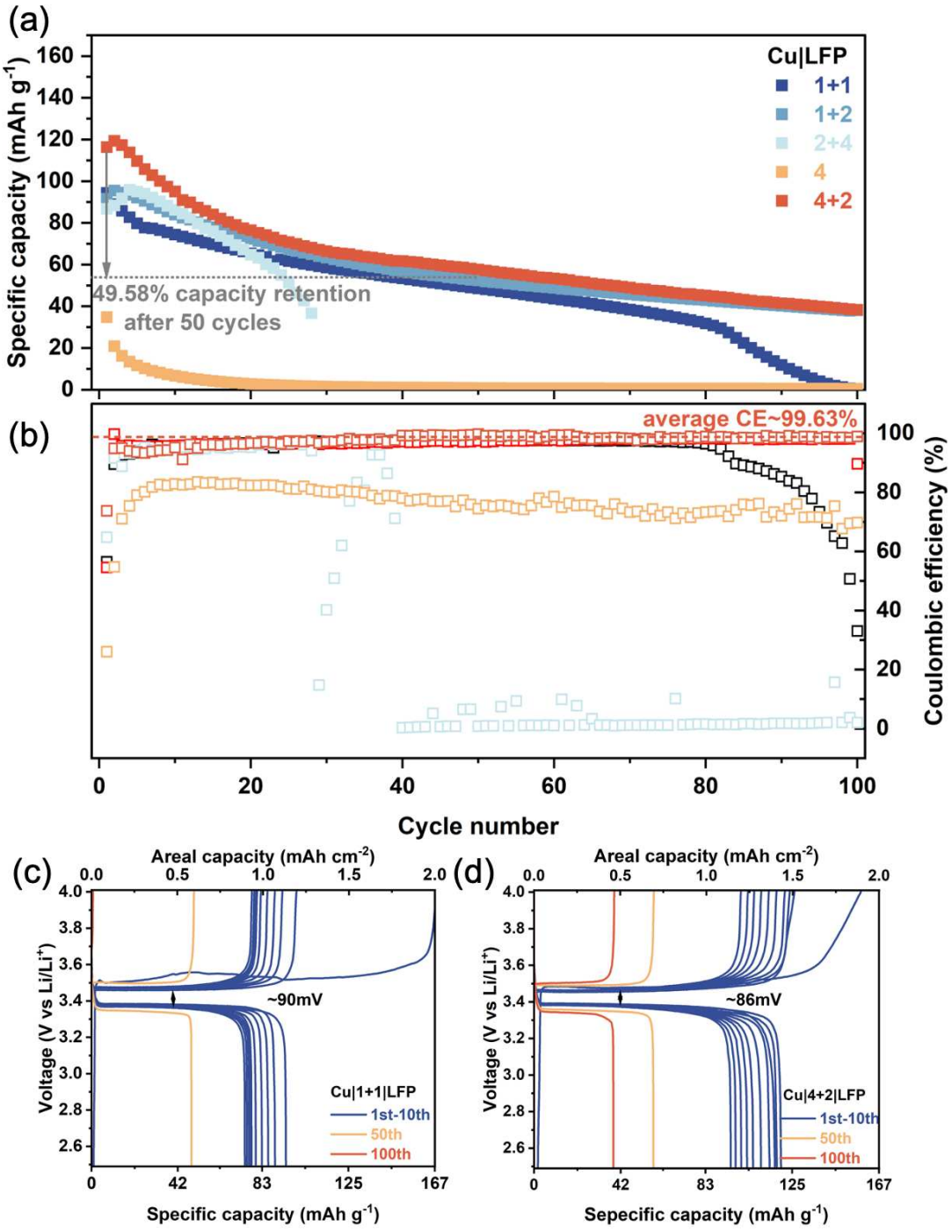


**Figure A12.2.** a) Cycling performance and (b) Coulombic efficiency of Cu|LFP cells with 1+1, 1+2, 2+4, 4, and 4+2 electrolytes at 0.05C. Galvanostatic charge-discharge curves of Cu|LFP cells at 0.05C with (c) 1+1 and (d) 4+2 electrolytes.

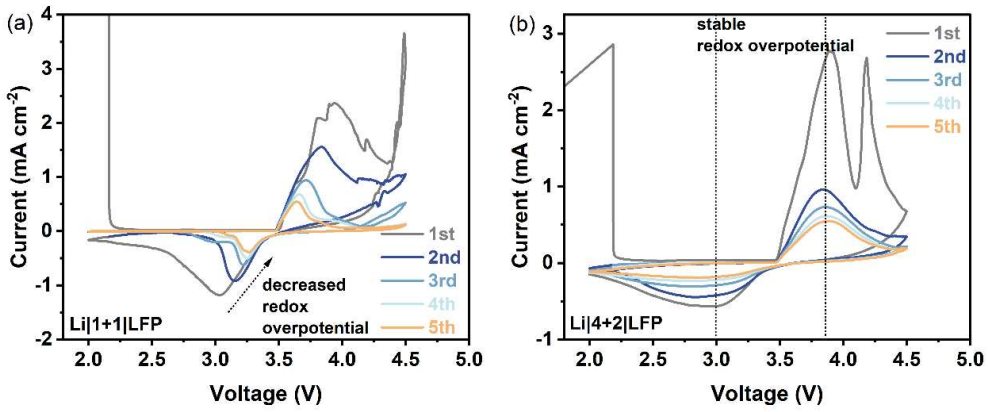


**Figure A12.3.** CV spectra of (a) 1+1 and (b) 4+2 electrolytes in Li|LFP cells at a scan rate of 0.2 mV $s^{-1}$.

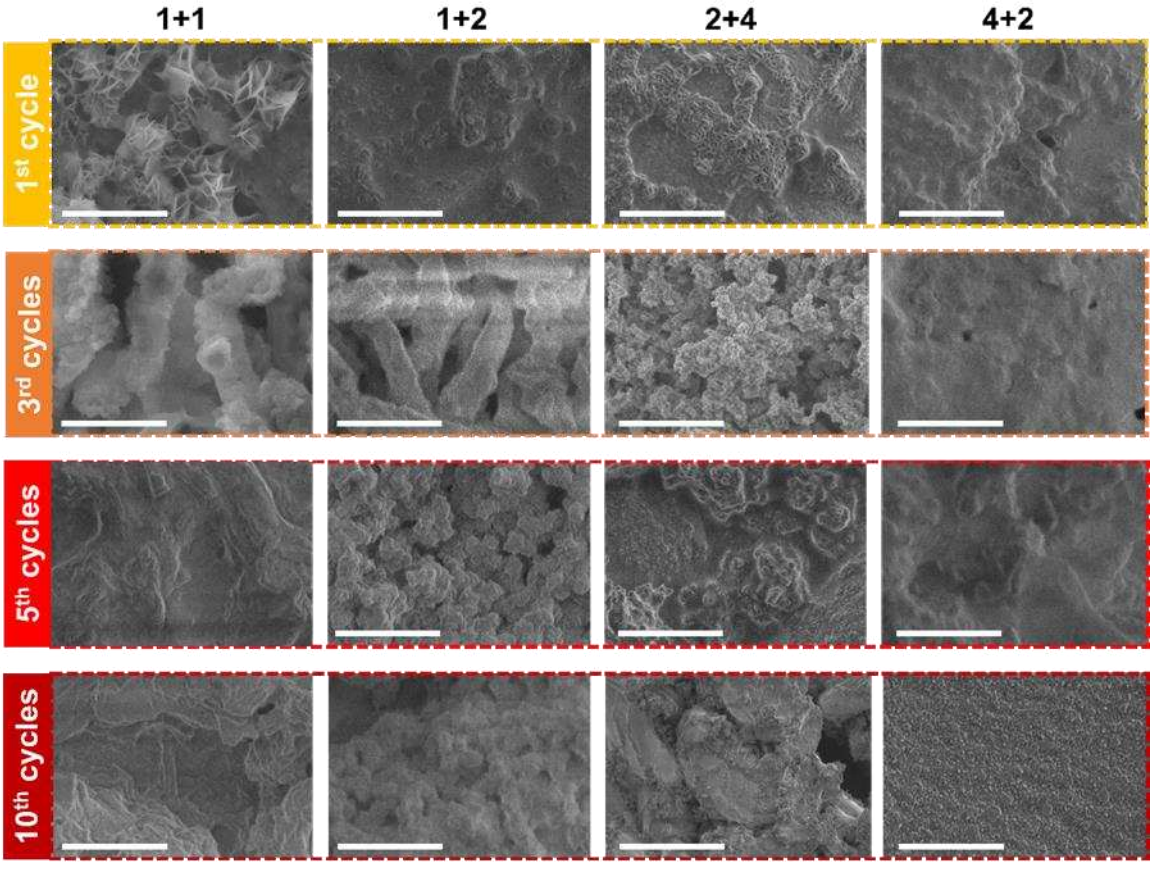


**Figure A12.4.** Top-view SEM images of Li deposited on Li0 foils in Li|LFP cells with 1+1, 1+2, 2+4, and 4+2 after 1, 3, 5, and 10 cycles at a current density of 0.05C (the scale bar is 2µm).

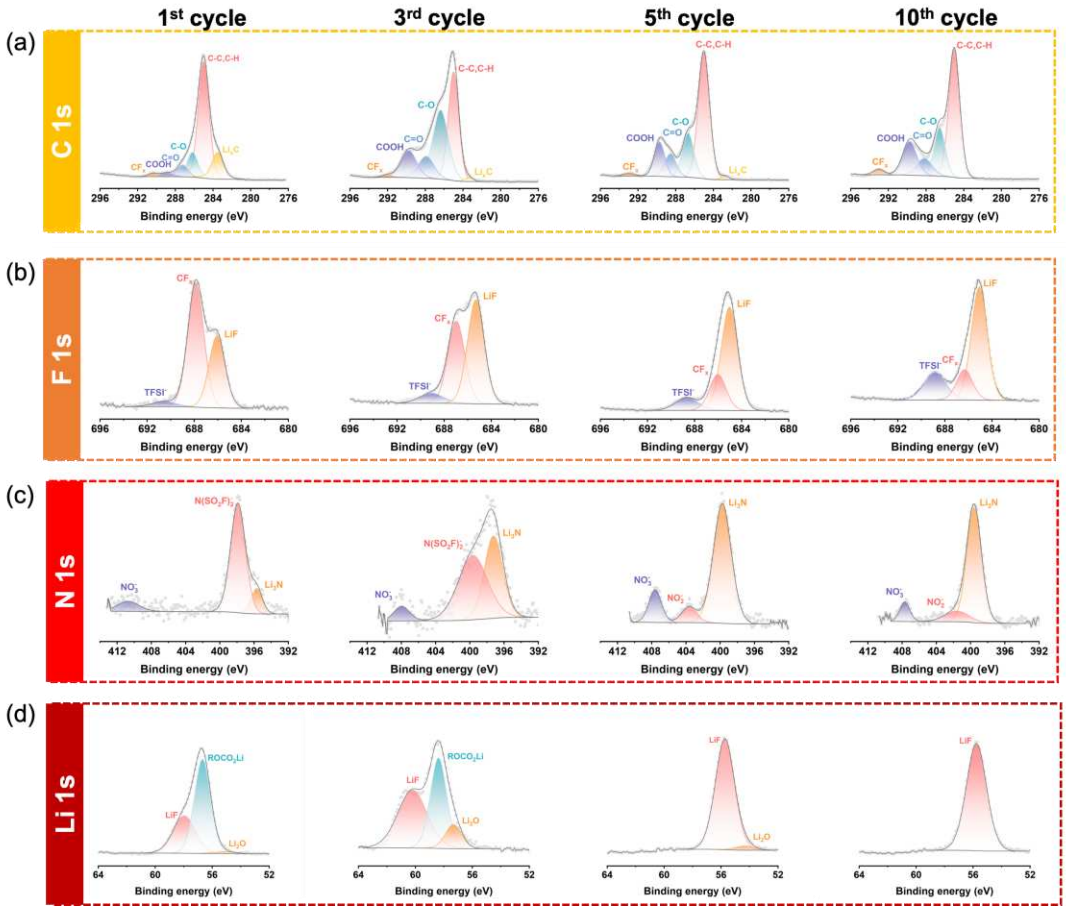


**Figure A12.5.** XPS profiling of the SEI layer on ultrathin $Li^0$ with the 1+1 electrolyte after 1, 3, 5, and 10 cycles: (a) C *1s*; (b) F *1s*; (c) N *1s*; (d) Li *1s*.

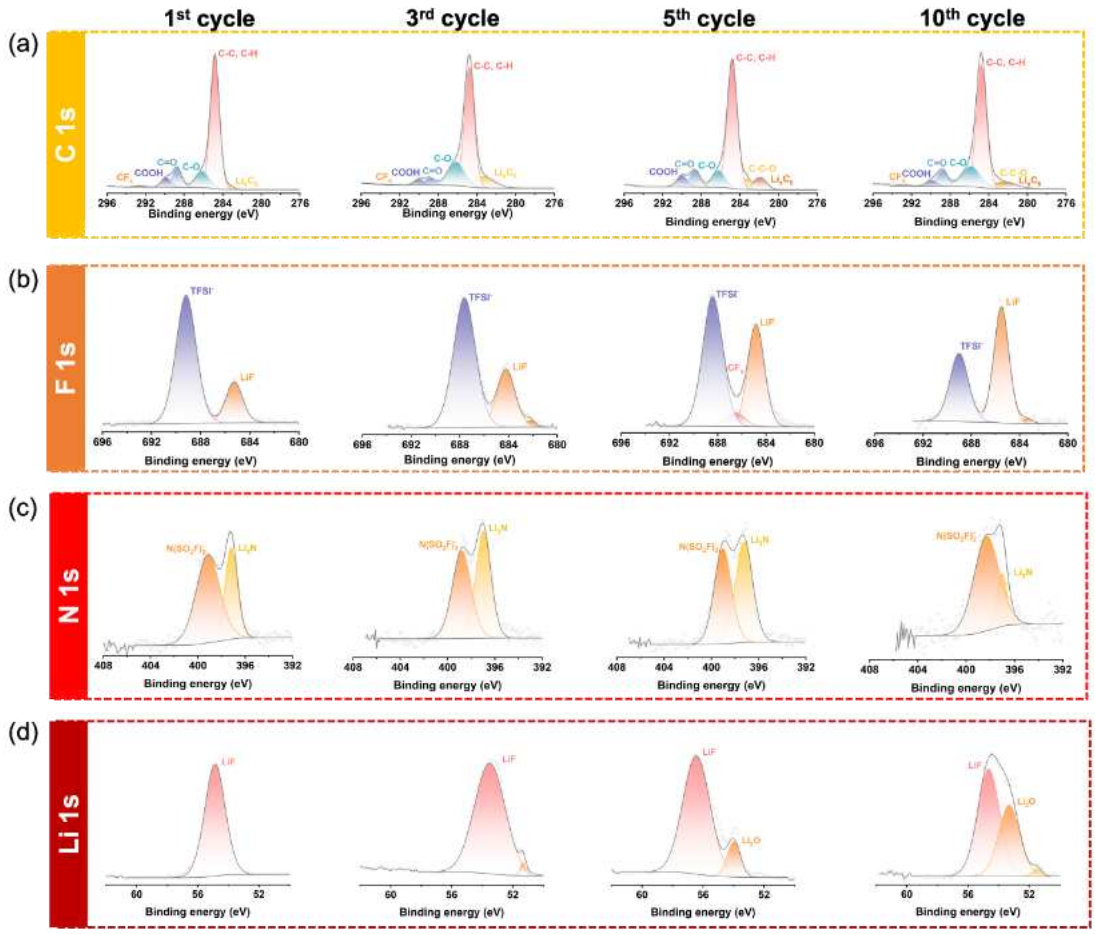


**Figure A12.6.** XPS profiling of the SEI layer on ultrathin $Li^0$ with the 4 electrolyte after 1, 3, 5, and 10 cycles: (a) C *1s*; (b) F *1s*; (c) N *1s*; (d) Li *1s*.

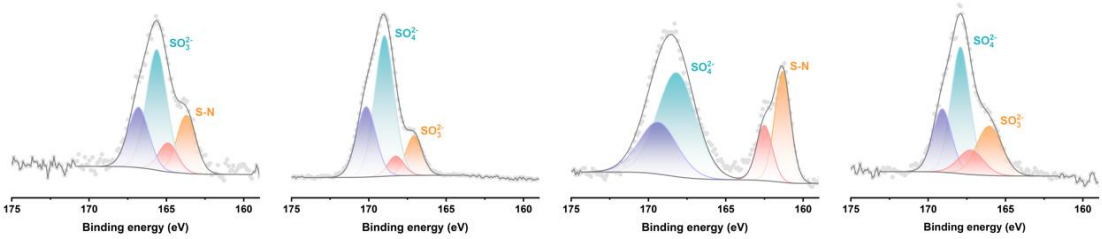


**Figure A12.7.** S *2p* XPS profiling of the SEI layer on ultrathin $Li^0$ with the 4+2 CPE after 1, 3, 5, and 10 cycles.

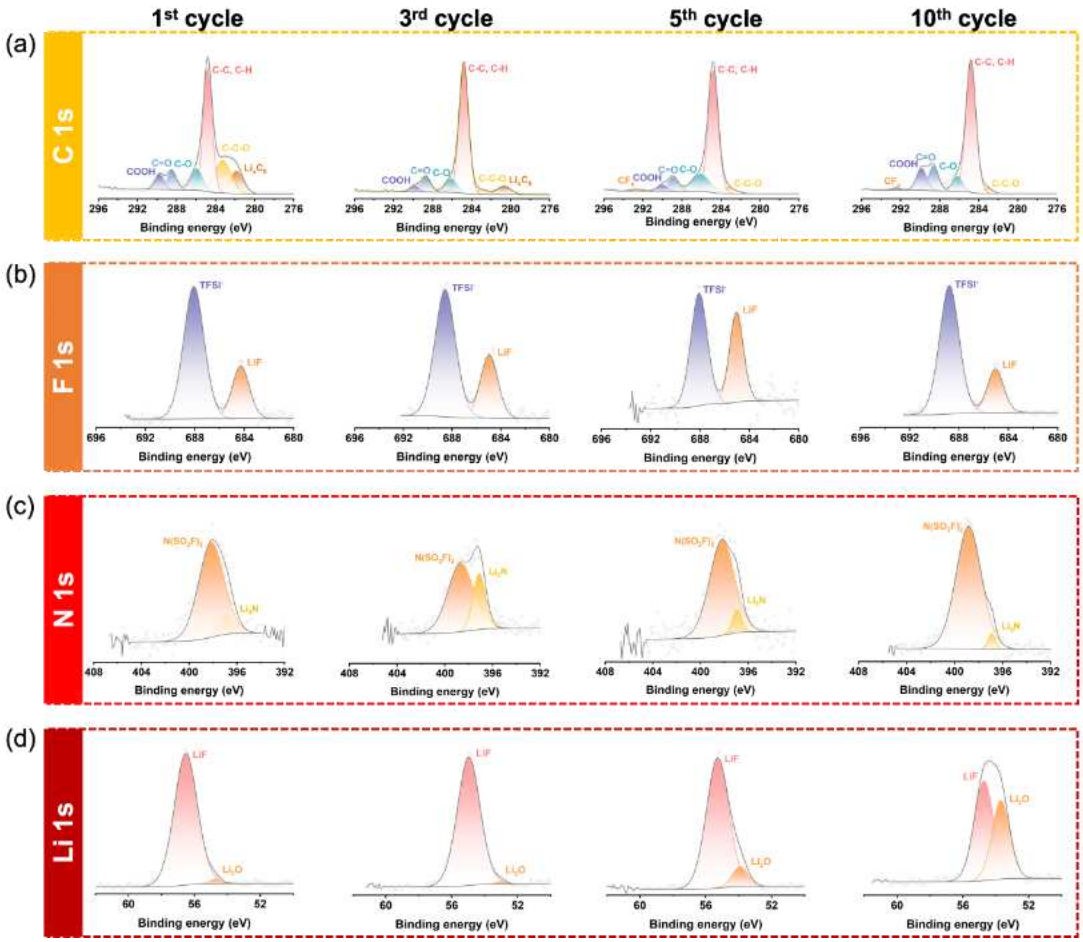


**Figure A12.8.** XPS profiling of the SEI layer on ultrathin $Li^0$ with the 2+4 CPE after 1, 3, 5, and 10 cycles: (a) C *1s*; (b) F *1s*; (c) N *1s*; (d) Li *1s*.

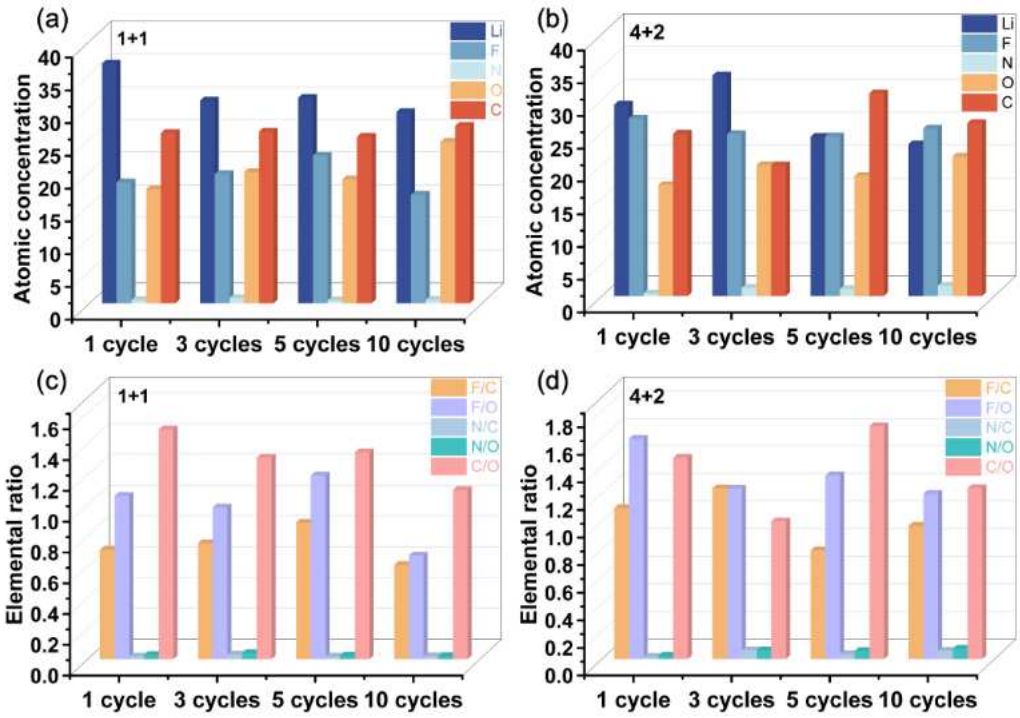


**Figure A12.9.** Atomic concentration of C *1s*, F *1s*, N *1s*, O *1s*, and Li *1s* on the SEI layer of (a)1+1; (b) 4+2; F/C, F/O, N/C, N/O, and C/O on the SEI layer of (c)1+1; (b) 4+2.

# Appendix 5: List of publications and conferences and awards

- **List of publications**

**Peer-reviewed publications**

*(published)*

1. **Yan, S.**; Yim, C.H.; Zhou, J.; Wang, J.; Abouali, S.; Baranova, E.A.; Weck, A.; Thangadurai, V.; Merati, A.; Abu-Lebdeh, Y. Elucidating the Origins of Rapid Capacity Fade in Hybrid Garnet-Based Solid-State Lithium Metal Batteries. *The Journal of Physical Chemistry C*. **2023**, *127*, 24641-24650.
2. **Yan, S.**; Abouali, S.; Yim, C.H.; Zhou, J.; Wang, J.; Baranova, E.A.; Weck, A.; Thangadurai, V.; Merati, A.; Abu-Lebdeh, Y. Revealing the Role of Liquid Electrolytes in Cycling of Garnet-Based Solid-State Lithium-Metal Batteries. *The Journal of Physical Chemistry C*. **2022***, 126*, 14027-14035.
3. **Yan, S.**; Al-Salih, H.; Yim, C.H.; Merati, A.; Baranova, E.A.; Weck, A.; Abu-Lebdeh, Y. Engineered Interfaces between Perovskite $La_{2/3x}Li_{3x}TiO_3$ Electrolyte and Li Metal for Solid-State Batteries. *Journal of Frontiers in Chemistry*. **2022**, *10*, 966274.
4. Al-Salih, H.; Cui, M.; Yim, C.H.; Sadighi, Z.; **Yan, S.**, Karkar, Z.; Goward, G.R.; Baranova, E.A.; Abu-Lebdeh, Y. A Ceramic Rich Quaternary Composite Solid-State Electrolyte for Solid-State Lithium Metal Batteries. *Journal of The Electrochemical Society*. **2022**, *169*, 080510.
5. Panaritis, C.; **Yan, S.**; Couillard, M.; Baranova, E.A. Electrochemical study of the metal-support interaction between $FeO_x$ nanoparticles and cobalt oxide support for the reverse water gas shift reaction. *Journal of $CO_2$ Utilization*. **2022**, *56*, 101824.
6. **Yan, S.**; Yim, C.H.; Pankov, V.; Bauer, M.; Baranova, E.; Weck, A.; Merati, A.; Abu-Lebdeh, Y. Perovskite Solid-State Electrolytes for Lithium Metal Batteries. *Batteries*. **2021**, *7*, 75.

*(under review)*

7. **Yan, S.**; Houache, M.S.E.; Weck, A.; Baranova, E.A.; Merati, A.; Yim, C.H.; Abu-Lebdeh, Y. Concentrated Precipitation Electrolyte for Reviving Ultrathin lithium Metal Anode. *Journal of Power Sources*. **2024**.

*(non-peer-reviewed publications)*

8. Guo, D.L.; **Yan, S.**; Merati, A.; Jodoin, B., Weck. A. **2024**. "Laser-textured solid-state batteries: a high energy density solution for E-aviation", Internal technical report; LTR-SMM-2024-0031, P. 54.
9. Yan, S.; Merati, A.; Pankov, V. **2022**. Fabrication and Optimization of Ceramic Electrolytes for Solid-State Lithium Metal Batteries", Internal technical report; LTR-SMM-2022-0144, P. 50.
10. Abouali, S.; **Yan, S.**; Thangadurai, V.; Yim, C.H., Y.; Abu-Lebdeh, Y. **2022**. "Material for solid-state lithium batteries - Garnet-based solid-state electrolyte", Internal technical report; LTR-SMM-2022-0118, P. 67.

- **Conferences**

*(oral presentation)*

1. **Yan, S.**, Houache M., Yim, C-H., Merati, A., Baranova, E., Weck, A., Abu-Lebdeh, Y. "Concentrated precipitation electrolyte for reviving ultrathin lithium metal anode", 245$^{th}$ ECS Meeting, oral presentation, San Francisco/USA, **May 2024**.
2. **Yan, S.**, Yim, C-H., Merati, A., Baranova, E., Weck, A., Abu-Lebdeh, Y. "X-ray spectromicroscopy: qualitative evaluation of degradation phenomena in solid-state lithium batteries", Canadian Chemistry Conference and Exhibition (CSC 2023), oral presentation, Vancouver/Canada, **June 2023**.
3. **Yan, S.**, Guo, D.L., Yim, C-H., Merati, A., Baranova, E., Weck, A., Abu-Lebdeh, Y. "Cycling efficiency improvement of solid-state batteries-laser textured interfaces", 243rd

ECS Meeting with the 18th international symposium on solid oxide fuel cells, oral presentation, Boston/USA, **May 2023**.

4. **Yan, S.**, Houache M., Yim, C-H., Merati, A., Baranova, E., Weck, A., Abu-Lebdeh, Y. "Concentrated electrolyte for stable lithium metal anode", 243rd ECS Meeting with the 18th international symposium on solid oxide fuel cells, oral presentation, Boston/USA, **May 2023**.
5. **Yan, S.**, Merati, A., Yim, C-H., Baranova, E., Weck, A., Abu-Lebdeh, Y. "Hybrid Interfacial Approach in Cycling of Solid-State Lithium Metal Batteries", CPR-SMM-2022-0138, Canadian Chemical Engineering Conference (CCEC), oral presentation, Vancouver/Canada, **October 2022**.
6. **Yan, S.**, Merati, A., Yim, C-H., Baranova, E., Weck, A., Abu-Lebdeh, Y. "Ceramic Battery for Electrically Powered Aircraft", 9th International Conference & Exhibition on Advanced & Nano Materials (ICANM2022), oral presentation, virtual meeting, **October 2022**.
7. **Yan, S.**, Merati, A., Yim, C-H., Baranova, E., Weck, A., Abu-Lebdeh, Y. "Liquid Solution for a Solid-State Lithium Battery", AB-SMM-2022-0052, 21st International Meeting on Lithium Batteries (Hybrid), oral presentation, virtual meeting, **July 2022**.
8. **Yan, S.**, Weck, A., Merati, A., Yim, C-H., Baranova, E., Abu-Lebdeh, Y. "Polyethylene oxide Membranes as an Interface between Perovskite-type Electrolytes and Li-metal Anode", Canadian Chemistry Conference and Exhibition (CCCE), AB-SMM-2022-0050, oral presentation, virtual meeting, **June 2022**.
9. **Yan, S.**, Merati, A., Yim, C-H., Baranova, E., Weck, A., Abu-Lebdeh, Y. "Interfacial Solutions for Solid-State Lithium Metal Batteries with Ceramic Electrolytes", AB-SMM-2022-0051, 33rd Canadian Materials Science Conference (CMSC), oral presentation, Toronto/Canada, **June 2022**.

10. **Yan, S.**, Merati, A., Yim, C-H., Baranova, E., Weck, A., Abu-Lebdeh, Y. "Understanding the Role of Liquid Electrolytes in Performance Improvement of Solid-State Lithium Metal Batteries", 241st ECS Meeting, oral presentation, virtual meeting, **May 2022**.
11. **Yan, S.**, Merati, A., Yim, C-H., Baranova, E., Weck, A., Abu-Lebdeh, Y. "Reducing interfacial resistance between perovskite-structured electrolytes and Li-metal anode", Canadian Chemical Engineering Conference (CCEC 2021), oral presentation, virtual meeting, **October 2021**.
12. **Yan, S.**, Merati, A., Yim, C-H., Baranova, E., Weck, A., Abu-Lebdeh, Y. "Perovskite-ceramic electrolytes with enhanced microstructure and interface for solid-state lithium batteries", IUPAC|CCEC 2021 conference, oral presentation, virtual meeting, **August 2021**.
13. **Yan, S.**, Merati, A., Yim, C-H., Baranova, E., Weck, A., Abu-Lebdeh, Y. "perovskite-type Electrolyte for Ceramic Lithium Batteries: Enhanced Microstructure and Bulk Ionic Conductivity", 239$^{th}$ ECS Meeting with the 18$^{th}$ International Meeting on chemical sensors, oral presentation, virtual meeting, **June 2021**.

*(poster presentation)*

1. **Yan, S.**, Abouali, S., Yim, C.H., Zhou, J., Wang, J., Baranova, E.A., Weck, A., Thangadurai, V., Merati, A. and Abu-Lebdeh, Y. "Elucidating the Origins of Rapid Capacity Fade in Hybrid Garnet-Based Solid-State Lithium Metal Batteries", Celebrating the Success of Women in STEM Symposium, poster, virtual meeting (invited panel discussion), **February 2024**.
2. **Yan, S.**, Abouali, S., Yim, C.H., Zhou, J., Wang, J., Baranova, E.A., Weck, A., Thangadurai, V., Merati, A. and Abu-Lebdeh, Y. "Elucidating the Origins of Rapid Capacity Fade in Hybrid Garnet-Based Solid-State Lithium Metal Batteries", 5$^{th}$ battery and energy storage conference, Chicago/USA, poster, **November 2023**.

3. **Yan, S.**, Guo, D.L., Yim, C-H., Merati, A., Baranova, E., Weck, A., Abu-Lebdeh, Y. "Electrode/electrolyte interface contact improvement using a laser texturing approach", COM 2023, poster, Toronto/Canada, **August 2023**.
4. **Yan, S.**, Yim, C-H., Merati, A., Baranova, E., Weck, A., Abu-Lebdeh, Y. "Interfacial challenge for solid-state lithium batteries-liquid addition", 243rd ECS Meeting with the 18$^{th}$ international symposium on solid oxide fuel cells, poster, Boston/USA, **May 2023**.
5. **Yan, S.**, Abouali, S., Yim, C.H., Zhou, J., Wang, J., Baranova, E.A., Weck, A., Thangadurai, V., Merati, A. and Abu-Lebdeh, Y. "Hybrid electrolyte approach for solid-state lithium batteries", poster presentation, ECS Canada Section, Queen's University, Kingston/Canada, **April 2023**.
6. **Yan, S.**, Yim, C.H., Baranova, E.A., Weck, A., Merati, A. and Abu-Lebdeh, Y. "Hybrid electrolyte approach for solid-state lithium batteries", poster competition, Engineering and Computer Science Graduate Poster Competition, Ottawa/Canada, **March 2023**.
7. **Yan, S.**, Merati, A., Yim, C.H., Baranova, E.A., Weck, A., Abu-Lebdeh, Y. "Membrane Interlayers of Ceramic Electrolyte and Lithium Metal Anode", Celebrating the Success of Women in STEM Symposium: 100 years of women's research across Canada, poster, virtual meeting, **February 2023**.
8. **Yan, S.**, Merati, A., Yim, C-H., Baranova, E., Weck, A., Abu-Lebdeh, Y. "Polymeric Membrane Interlayers of Ceramic Electrolyte and Lithium Metal Anode", CPR-SMM-2022-0137, Conference of Metallurgists (COM), poster, Montréal/Canada, **August 2022**.
9. **Yan, S.**, Merati, A., Yim, C-H., Baranova, E., Weck, A., Abu-Lebdeh, Y. "Electrically powder airplane with safe all-ceramic battery', TechX 2021, poster, virtual meeting, **November 2021**.
10. **Yan, S.**, Merati, A., Yim, C-H., Baranova, E., Weck, A., Abu-Lebdeh, Y. "Electrically Powered Flight-safe ceramic", CASI AERO, poster, virtual meeting, **June 2021**.

- **Awards**

1. 3rd place, 5th Battery and Energy Storage Conference Poster Session, **November 2023**.
2. 1st place, Women in Science and Engineering | Engineering and Computer Science Graduate Poster Competition, **March 2023**.
3. 3rd place, Emerging Materials and Processes: Design and Development | Engineering and Computer Science Graduate Poster Competition, **March 2023**.
4. Appeared in NRC's Echo Newsletter in recognition of outstanding research achievement, **December 2022**.
5. 3rd place, 3-Minute Pitch Competition | Canadian Chemical Engineering Conference 2022, **October 2022**.
6. Best paper presentation, Energy Symposium | Canadian Chemical Engineering Conference 2022, **October 2022**.
7. "Highly-cited Articles in 2021". (Yan, S. et al. 2021. *Batteries*, 7, 75).